

Higher-Order Topology in Quantum Matter

Dissertation

zur

**Erlangung der naturwissenschaftlichen Doktorwürde
(Dr. sc. nat.)**

vorgelegt der

Mathematisch-naturwissenschaftlichen Fakultät

der

Universität Zürich

von

Frank Schindler

aus

Deutschland

Promotionskommision

Prof. Dr. Titus Neupert (Vorsitz)

Prof. Dr. Johan Chang

Prof. Dr. Ronny Thomale

Zürich, 2020

Abstract

In condensed matter physics, one of the defining features of a topological phase of matter is that it realizes a bulk-boundary correspondence: For instance, in the context of topological insulators, a topologically nontrivial gapped bulk electronic band structure implies a gapless boundary spectrum when the system is terminated in a manner that preserves all relevant symmetries. Initially, all known examples of a bulk-boundary correspondence related a d -dimensional bulk to its $(d - 1)$ -dimensional boundary.

In the first half of this thesis, we introduce higher-order topological phases of matter that instead show a correspondence between the d -dimensional bulk and boundary segments of co-dimension larger than 1. After detailing the theoretical underpinnings of such quantum phases of matter in the context of electronic band structures, we report on the experimental discovery of higher-order topology in elementary bismuth. We then discuss further means of characterizing three-dimensional higher-order topological insulators via their novel response to crystalline lattice defects and magnetic fluxes.

The second half of the thesis treats a range of related topics. After explaining how higher-order topology can be realized in classical electric circuit systems, we show how its proper definition in two-dimensional quantum crystals requires the concept of corner charge fractionalization. Motivated by the position-space picture of topological insulators, we then explore how a similar perspective can shed light on (higher-order) topological superconductors. We finish our survey of higher-order topology by discussing its generalization to interacting bosonic models.

Dedicated to my sister.

God made the bulk in heaven, the boundary however was invented by the devil.
Wolfgang Ernst Pauli

Contents

I Preliminaries	1
1 Introduction and literature review	3
2 Overview of topological band theory	13
2.1 Wilson loop perspective on first-order topological phases	13
2.2 Survey of invariants for higher-order topological phases	29
2.3 Systematic construction of \mathcal{I} -symmetric topological phases	35
List of publications	43
II Core concepts	47
3 Theory of higher-order topological insulators	49
3.1 Chiral higher-order topological insulator	50
3.2 Helical higher-order topological insulator	53
3.3 Material candidates and experimental setup	56
4 Experimental realization in elementary bismuth	61
4.1 Topology of \mathcal{I} - and \mathcal{C}_3 -symmetric insulators	63
4.2 Bulk-boundary correspondence	65
4.3 Scanning tunneling microscopy experiment	67
4.4 Transport experiment	69
5 Defect and flux response of higher-order topological insulators	73
5.1 Mapping topology from momentum space to position space	74
5.2 Edge and screw dislocations	87
5.3 Magnetic fluxes and flux tubes	107

III Extensions	117
6 Higher-order topology in classical electric circuits	119
6.1 Linear circuit theory and topology	121
6.2 Electric circuit with corner states	123
6.3 Experimental circuit realization	126
6.4 Physical interpretation of corner modes	127
7 Fractional corner charges in two-dimensional systems	129
7.1 Charge quantization in time-reversal symmetric insulators	130
7.2 Identification of two-dimensional obstructed atomic limits	135
7.3 Material candidates with corner charge fractionalization	151
8 Position-space perspective on topological superconductors	155
8.1 p -wave superconductor in particle-hole basis	157
8.2 p -wave superconductor in Majorana basis	160
8.3 Chiral superconductor and generalization to higher dimensions	162
9 Toy models for interacting higher-order topological phases	165
9.1 One-dimensional first-order model with local symmetry	165
9.2 Two-dimensional second-order model with crystalline symmetry	166
IV Conclusions and outlook	169
V Appendices	175
A More on higher-order topological insulators	177
B More on bismuth	195
C More on topoelectrical circuits	209
D More on fractional corner charges	219
E More on superconductors	223
Bibliography	254

Part I

Preliminaries

Chapter 1

Introduction and literature review

The study of topological phases of matter currently represents one of the focal points of condensed matter physics. One of its main achievements is the theoretical prediction and experimental discovery of topological insulators in two and three dimensions. Electronic insulators are characterized by an energy gap between valence and conduction bands. Two insulators are classified as topologically equivalent if they can be deformed into one another without closing this gap, while certain symmetries are respected. If time-reversal symmetry (TRS) is respected in this deformation process, three-dimensional (3D) insulators fall into two disconnected topological classes: trivial and nontrivial [1, 2, 3, 4, 5, 6, 7]. The latter are called topological insulators (TIs).

What makes this mathematical classification highly relevant experimentally is the so-called bulk-boundary correspondence of TIs: the two-dimensional (2D) surface of a 3D TI hosts conducting states, with the dispersion of a non-degenerate Dirac cone, which cannot be gapped or localized without breaking TRS (or inducing interacting instabilities such as superconductivity or topological order). In general, a d -dimensional topological insulator is defined via the presence of $(d-1)$ -dimensional topologically protected gapless boundary states. When, in addition, the spatial symmetries of the crystal are preserved during this deformation process, such as mirror reflections or rotations, one speaks of topological crystalline insulators [8, 9, 10, 11, 12, 13].

As crystalline symmetries extend the number of known topological phases significantly, they also call for a sharper definition of what is *topological*. In particular, the atomic limit, which is defined as a gapped ground state where all electrons can be exponentially localized in position space, is not a unique trivial reference point

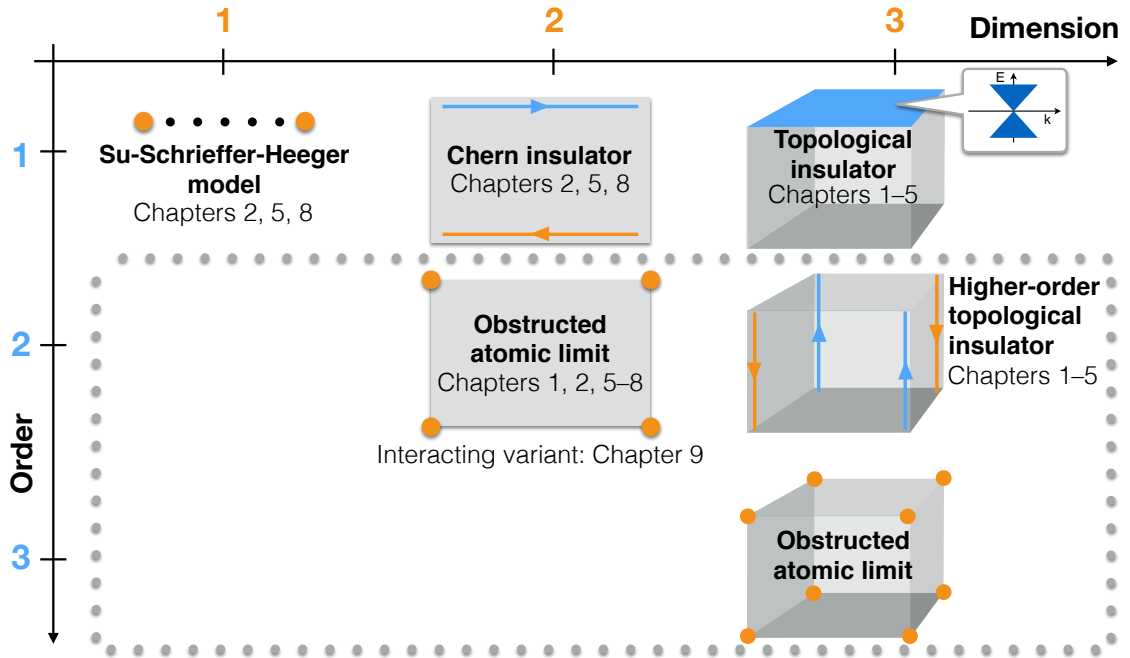


Figure 1.1: Overview of insulating topological phases of matter with representative examples and chapters where they appear in the thesis. Higher-order topological phases are encircled by the dotted line. This introduction and Chapters 3–5 focus on second-order 3D topological insulators (higher-order topological insulators). Chapters 6, 7 treat classical and quantum second-order 2D phases, respectively, while Chapter 8 discusses the superconducting counterparts of the Su-Schrieffer-Heeger model (p -wave superconductor), Chern insulator (chiral superconductor), and obstructed atomic limit (Majorana obstructed atomic limit). Finally, Chapter 9 presents an interacting bosonic model of a second-order 2D phase.

anymore [14]. With spatial symmetries, several atomic limits exist that cannot be adiabatically deformed into one another. The physical reference point for an actual material is the atomic limit that corresponds to the physical location of ions. A situation where electronic charge centers (so-called Wannier function centers) of the occupied bands of an insulator correspond to a different atomic limit is referred to as an obstructed atomic limit [14].

We distinguish between three types of (spatial) symmetry-protected phases: (1) phases that cannot be adiabatically transformed to any atomic limit, which we refer to as strong topological, (2) phases that correspond to an obstructed atomic limit, and (3) phases with fragile topology [15, 16, 17, 18, 19, 20, 21, 22] that are not adiabatically deformable to an atomic limit, but can be deformed to one upon the addition of bands that correspond to an atomic limit.

In this thesis, we further extend the notion of topological phases of matter by what we call higher-order topological phases, which in the context of insulators describes materials which have $(d - k)$ -dimensional topologically protected gapless boundary states while the bulk and all higher-dimensional boundaries are gapped. Higher-order topological phases come in all guises (1), (2), (3), but the most relevant case with respect to experiments and potential applications is of type (1) and is realized by the choice $d = 3$, $k = 2$ (see Figure 1.1 for an overview). It is therefore simply termed three-dimensional higher-order topological insulator (HOTI).

In the remainder of this introductory chapter, we sketch out the theoretical and experimental characteristics of HOTIs in broad strokes, and review the relevant literature. For a more rigorous treatment and explicit model Hamiltonians, see Chapter 3.

Readers who are unfamiliar with topological band theory might first want to take a look at Chapter 2, where we pedagogically introduce the topological indices and phases that are most relevant to this thesis, with a special focus on momentum space Wilson loops.

HOTIs: Concept

The electronic band structure of a HOTI is characterized by a gapped three-dimensional (3D) bulk, gapped two-dimensional (2D) surfaces, and topologically enforced gapless one-dimensional (1D) hinges [23, 24, 25, 26]. Such a phase necessarily requires spatial (crystalline) symmetries in addition to a spectral gap for its topological protection. Several caveats apply to this definition. In particular, using the Bloch description of crystalline systems, it is only necessary to maintain a direct gap at every Bloch momentum in order to define the topological properties of a HOTI. Furthermore, not all surfaces need to be gapped (some may be necessarily gapless due to symmetry requirements), but all generic surfaces (those not invariant under any of the crystalline symmetries) have to be. Finally, the gapless 1D states of a HOTI could not be localized at the hinges of the 3D sample geometry (one may even consider spherical or cylindrical samples without any hinges), but generally hinge localization will be energetically favorable.

There are two general construction schemes for HOTIs: (1) A HOTI can be obtained from coupling two 3D first-order topological insulators (TIs) in a way that preserves a crystalline (or spatio-temporal) symmetry. The latter symmetry needs to be chosen so that any symmetric surface Dirac mass, which gaps out the two surface Dirac cones resulting from the original TIs, has domain walls, thus inducing

1D hinge states [24, 27, 28]. The simplest symmetry that fulfills this requirement is 3D spatial inversion symmetry \mathcal{I} . Since an \mathcal{I} -symmetric TI can be obtained by band-inverting a single Kramers pair with respect to an atomic limit [5], an inversion-symmetric HOTI is characterized by a double band inversion [29, 30, 31]. (2) A HOTI can be obtained from 2D second-order topological insulators – which are either fragile phases or obstructed atomic limits with corner filling anomalies [32] (see also Chapter 7) – by a pumping procedure in which these phases are tuned from topological to trivial along a third momentum quantum number k_z [23, 25, 33, 34]. The pumping implies that the 0D corner states of the 2D insulator traverse the bulk gap as k_z flows from 0 to 2π , thus resulting in 1D hinge states. Interestingly, some of the simplest HOTIs correspond to a pumping cycle of 2D fragile phases (which become Wannierizable upon the addition of trivial bands [15]), thus elevating the fragile 2D topology to a stable 3D topological phase (which is never Wannierizable) by dimensional enhancement [19]. When the 2D insulator is supplemented by trivial bands to form an obstructed atomic limit with corner filling anomaly, the HOTI realizes 2D Wannier center pumping along a third direction, akin to how a 2D Chern insulator realizes 1D Wannier center pumping along a second direction [35]. Both construction schemes, (1) and (2), allow for time-reversal (\mathcal{T}) preserving and non-preserving variants of HOTIs. In the \mathcal{T} -broken case, the hinge states are chiral (uni-directionally dispersing modes along a given hinge). In the \mathcal{T} -symmetric case, the hinge states are helical (anti-propagating modes that are protected from back-scattering by the Kramers theorem). In general, HOTIs do not require electron-electron interactions to be stable ground states of local Hamiltonians, and can therefore be realized in simple tight-binding models [36, 37, 38, 39, 40, 41].

Bulk-boundary correspondence

To ensure the presence of hinge states in a HOTI, the bulk gap is required to stay open and the relevant bulk crystalline symmetries need to be preserved. Note that these conditions for establishing a bulk-boundary correspondence are sometimes supplemented by the additional prohibition of surface phase transitions (surface gap closings), allowing for a wider range of HOTI phases to be stable [in fact, from this point of view, a HOTI constructed by placing a 3D topological insulator in a static magnetic field [42, 27, 28] is \mathbb{Z} classified, while allowing for surface transitions reduces the classification to \mathbb{Z}_2]. However, in this thesis we take the point of view that for characterizing a true 3D phase of matter – which should not be trivializable by attaching non-anomalous 2D insulators to its sample boundaries – only the bulk gap and symmetries should play a role. This has the benefit of

establishing a one-to-one correspondence between bulk topological invariants and the presence of hinge states, and in particular one that is stable to arbitrary surface manipulations that preserve the overall crystalline symmetry.

Role of crystalline symmetry

Any finite sample of a HOTI necessarily features an equal number of right- and left-moving hinge modes due to total momentum conservation (in the \mathcal{T} -broken case, the total chirality is zero, while in the \mathcal{T} -symmetric case, the total helicity is zero). If crystalline symmetries were not enforced, these modes could be brought together in real space and annihilated via surface manipulations that do not close the bulk gap. In order to stabilize HOTI phases, crystalline symmetries are therefore a necessary requirement. The simplest of these is inversion symmetry \mathcal{I} , which inverts all three space coordinates, and already allows for the stabilization of one kind of HOTI [43, 30]. Further examples are mirror \mathcal{M} and n -fold rotational symmetries \mathcal{C}_n , which leave real-space planes and lines invariant, respectively. In addition to crystalline symmetries, the zoo of HOTIs is enlarged by the inclusion of local symmetries, the most physically relevant one being time-reversal symmetry \mathcal{T} . There also exist HOTI phases protected by spatio-temporal symmetries that are a combination of rotation or inversion with time-reversal (discussed in Section 3.1 of this thesis), or non-symmorphic symmetries that involve fractional translations [44, 45, 46]. While it is possible to have all surfaces gapped in HOTIs protected by \mathcal{I} symmetry, since none of them are left invariant under spatial inversion on their own, this is not the case for the other point-group symmetries (or combinations of these with local symmetries). For instance, in $\mathcal{C}_n\mathcal{T}$ -symmetric axion insulators, a subclass of HOTIs, surfaces that have their normal along the \mathcal{C}_n axis are topologically enforced to be gapless (since the $\mathcal{C}_n\mathcal{T}$ symmetry leaves them invariant and imposes additional degeneracies in their surface band structure). They are connected by 1D hinge modes running along the sample [44, 31], justifying the label of HOTI. Next to \mathcal{I} symmetry, non-symmorphic crystalline symmetries allow for arbitrary surface-gapped sample terminations, as long as they combine point-group symmetries with fractional translations that are broken on the surface.

Classification of HOTIs

Topological band structures that are protected by local symmetry operations such as time-reversal symmetry and particle hole conjugation have been fully classified via the tenfold way [47, 48]. In contrast, the classification of topological crystalline insulators (TCIs), of which HOTIs form a part, is much more difficult

AZ label	Symmetry			Order	
	\mathcal{T}^2	\mathcal{P}^2	\mathcal{S}^2	1st	2nd
A	0	0	0	0	\mathbb{Z}_2
AIII	0	0	1	\mathbb{Z}_2	0
AI	1	0	0	0	0
BDI	1	1	1	0	0
D	0	1	0	0	\mathbb{Z}_2
DIII	-1	1	1	\mathbb{Z}_2	\mathbb{Z}_2
AII	-1	0	0	\mathbb{Z}_2	\mathbb{Z}_2
CII	-1	-1	1	\mathbb{Z}_2	0
C	0	-1	0	0	\mathbb{Z}_2
CI	1	-1	1	\mathbb{Z}_2	0

Table 1.1: Classification of 3D topological insulators protected by inversion (\mathcal{I}) symmetry. The first column indicates the Altland-Zirnbauer label, and the next three columns indicate the presence (± 1) or absence (0) of time-reversal (\mathcal{T}) and particle-hole (\mathcal{P}) symmetries distinguishing the cases of $\mathcal{T}^2, \mathcal{P}^2 = \pm 1$ as well as the presence (1) or absence (0) of chiral symmetry $\mathcal{S} = \mathcal{TP}$. The next two columns give the classification of inversion-protected 3D first and second-order topological insulators, respectively. (Table adapted from Reference [43].)

to obtain. Symmetry-indicated TCIs (which allow for simple topological invariants in terms of the symmetry transformation properties of occupied Bloch states, see also Section 2.3.3) were classified in all 230 non-magnetic and 1651 magnetic space groups [29, 14, 49]. For general, potentially non-symmetry-indicated 3D TCIs, a full classification was achieved for systems with point-group symmetries [50, 51, 52, 53, 54, 55].

In most cases, the classification results for 3D systems are with respect to bulk topology, and do not pay special attention to the presence of protected boundary states. This means that they treat phases with gapless surfaces, HOTIs, and also phases without any stable boundary states on equal footing, and need to be refined when restricting to HOTIs. There are two main approaches to distill a classification of HOTIs: (1) One classifies all possible stable hinge state configurations, and then infers the HOTI bulk classification under the assumption of a bulk-boundary correspondence [24, 27, 43, 30, 56]. For instance, consider a $\mathcal{C}_n\mathcal{T}$ -symmetric HOTI with chiral hinge states. Since an even number of hinge states can be trivialized upon attaching 2D Chern insulators to the surfaces in a symmetry-preserving fashion, it is only the parity of the number of hinge states that is invariant, giving a \mathbb{Z}_2 .

classification (see the discussion and Figures in Section 3.1). (2) Another strategy is to classify the possible types of band inversions in the bulk that give rise to gapped surfaces via stacked Dirac Hamiltonians [50, 51, 52, 57]. Hinge states are then induced by symmetry-enforced domain walls in the real-space dependence of the respective Dirac mass term. For instance, consider a \mathcal{I} -symmetric HOTI built from two coupled TIs (in general, the number of TIs needs to be even because the system is otherwise guaranteed to have gapless surfaces). The band inversion of a single TI can be captured by a massive bulk Dirac Hamiltonian. The sign of the Dirac mass of the two TIs making up the HOTI can be equal or opposite. Since the equal-sign case can be explicitly checked to give hinge states, while the opposite-sign case is necessarily trivial (it corresponds to the sum of the occupied and unoccupied subspace of a single TI), one again obtains a \mathbb{Z}_2 classification. See Table 1.1 for the classification of \mathcal{I} -symmetric HOTIs with additional anti-unitary symmetries [43].

In fact, it can be easily seen that in systems without mirror symmetry, the classification of HOTIs is always either trivial or given by \mathbb{Z}_2 . Given a Hamiltonian that features hinge states (either chiral or helical), this is because one may always consider the doubled system, whose two copies of hinge states can be gapped out with each other without breaking any symmetry. The only exception are mirror symmetries, since they are the only spatial symmetries that can map a hinge to itself. In this case, hinge states are labelled by mirror eigenvalues $\pm i$ and can thus be symmetry-protected from hybridization as long as antipropagating modes reside in different mirror eigenvalue sectors. The number of hinge states in each mirror sector is therefore unconstrained, giving a $\mathbb{Z} \times \mathbb{Z}$ classification without \mathcal{T} symmetry and a \mathbb{Z} classification with \mathcal{T} symmetry (since in this case the two mirror subspaces $\pm i$ are not independent due to the anti-unitary nature of time-reversal). For more detail, see Section 3.2.

Material realizations of HOTIs

We now proceed to discuss the appearance of HOTIs in realistic materials. We first describe the material candidates that have been proposed so far, and then summarize the status of experiments.

Predictions

As explained in Section 2.2.2, a nonzero even mirror Chern number $C_{\mathcal{M}}$ indicates hinge modes for surface terminations involving surfaces that are not mirror-

symmetric on their own. One can therefore take over material realizations for HOTIs from the TCI literature, with prominent examples given by tin telluride SnTe [9, 58] and jacutingaite Pt_2HgSe_3 [59]. The case of SnTe is discussed in more detail in Section 3.3.

Transition metal dichalcogenides have long provided fertile grounds for the realization of topological phases of matter. In particular, MoTe_2 is known to host bulk Weyl points that induce surface Fermi arcs [60, 61]. However, spectroscopy experiments revealed additional slightly gapped surface states whose nature remained somewhat of a mystery before the identification of spin-orbit-coupled $\beta - \text{MoTe}_2$ as an inversion-symmetry-indicated HOTI candidate with \mathbb{Z}_4 index $z_4 = 2$ [62, 63]. One caveat is that MoTe_2 is not bulk-insulating (this does not impede its topological characterization as a \mathbb{Z}_4 -nontrivial insulator since it has a direct gap at every Bloch momentum).

Rotation-anomaly TCIs have gapless surfaces perpendicular to the rotation axis, and otherwise gapped generic surfaces that harbor hinge states [44, 31, 64]. They thus qualify as HOTIs, and have been predicted to be realized in Zintl compounds, including the materials $\text{Ba}_3\text{Cd}_2\text{As}_4$, $\text{Ba}_3\text{Zn}_2\text{As}_4$, and $\text{Ba}_3\text{Cd}_2\text{Sb}_4$ [65].

Another class of materials with hinge states are axion insulators, which are time-reversal symmetry-breaking HOTIs with a nonzero and quantized magnetoelectric polarization (see also Section 2.2.4). Compounds of the form $\text{Bi}_{2-x}\text{Sm}_x\text{Se}_3$ were predicted to realize inversion-symmetric axion insulators [66]. Bi_2Se_3 on its own is known to be a TI with gapless surfaces [67], doping with Sm introduces ferromagnetism that breaks time-reversal invariance and gaps out the TI surface Dirac cones to leave behind hinge states. Similarly, the magnetic material EuIn_2As_2 is predicted to be an axion insulator [68].

In addition to these case-by-case materials predictions, HOTIs can be identified via the symmetry indicator invariants discussed in Section 2.3.3 from ab-initio simulation results provided in extensive topological material databases [63], [69], [70].

Experiments

There have so far been two experimental confirmations of HOTI materials, elementary bismuth (Bi) and the van-der-Waals compound Bi_4Br_4 .

The first of these was motivated by the discovery of ballistic edge states in elementary bismuth [71], first interpreted as the 1D edge states of the topological insulator phase of 2D bismuth. This interpretation is tenuous as the bismuth sample used in the experiment was 300nm thick and thereby inherently three-dimensional, raising

the question of whether 3D bismuth itself might have topologically protected hinge states. 3D bismuth was previously used in some of the first TI compounds such as Bi_2Se_3 and Bi_2Te_3 [67], but thought to be topologically trivial on its own. The nontrivial second-order topological nature of bismuth can be confirmed theoretically by evaluating the \mathbb{Z}_4 index in Equation (2.38) for a realistic tight-binding model and also directly from ab-initio calculations, giving $z_4 = 2$ as expected for a HOTI. Further experiments using Josephson interferometry as well as scanning tunneling microscopy (STM) vindicated the presence of hinge states in 3D bismuth [72]. Bismuth is a semimetal, but has a direct gap at all crystal momenta, rendering its characterization as a HOTI well-defined. However, in principle one would expect the resultant energetic overlap of bulk states with hinge states to occlude probing the hinge states directly. That an observation of the characteristic HOTI physics was nevertheless possible is due to the strong disorder of experimental samples: Whereas the trivial bulk and surface states are subject to Anderson localization in the presence of disorder, the hinge states remain immune to localization by their topological nature and therefore dominate in transport experiments. These findings were challenged by STM experiments on crystal defects in bismuth, which hint at an interplay of various topological phenomena attributed to the proximity of bismuth to a topological phase transition [73]. For an in-depth treatment of higher-order topology in bismuth, see Chapter 4.

The second experimental realization of a HOTI followed the prediction of Bi_4Br_4 as a rotation-anomaly TCI with hinge states [74]. Bi_4Br_4 is a van-der-Waals material that can be stacked to form quasi-1D structures. Its topological index can be determined from ab-initio calculations to be equal to $z_4 = 2$ [75, 74, 63, 69, 70]. Since the Bi_4Br_4 nanowire band structure is remarkably clean and the band gap large, the presence of hinge states can be confirmed directly by angle-resolved photoemission spectroscopy experiments (ARPES) [76], a first for higher-order topological phases. Bi_4Br_4 , unlike bismuth, has an insulating bulk, making it an interesting platform for future spintronics applications.

Chapter 2

Overview of topological band theory

In preparation of the following chapters, we review the topological band theory of non-interacting insulators. We begin with the introduction of Wilson loop operators as general indicators of band topology and bulk-boundary correspondence, and use them to characterize first-order topological phases such as the 1D Su-Schrieffer-Heeger model, the 2D Chern insulator, and the 2D and 3D time-reversal invariant topological insulators. We then detail the definition of topological invariants for crystalline and higher-order topological insulators in 3D, in particular discussing the mirror Chern number, symmetry indicator invariants, and the magnetoelectric polarization.

2.1 Wilson loop perspective on first-order topological phases

We first provide a unified picture of topological bulk-boundary correspondences in any dimension by making use of Brillouin zone Wilson loops. To determine the topology of a given ground state, several topological invariants have been proposed, such as the Pfaffian invariant for 2D time-reversal symmetric systems [77]. However, they often require Bloch states to be provided in a smooth gauge across the whole momentum space, or Brillouin zone (BZ), for their evaluation, making them impractical for numerical calculations. In addition, most of them are specific to a certain dimension or symmetry class and thus do not generalize well.

Here, we employ non-abelian Wilson loops as a generalization of the 1D Berry phase to characterize topological properties in any dimension and any symmetry class. This provides a framework of topological invariants which makes direct contact with the protected boundary degrees of freedom of a given phase, and which we will use throughout this thesis as a versatile means of diagnosing translationally invariant phases of matter.

We begin by stating our conventions. We work in units where $\hbar = c = e = 1$ and denote by σ_i , $i = x, y, z$, the 2×2 Pauli matrices. We define $\sigma_0 = \mathbb{1}_{2 \times 2}$ for convenience. We express eigenfunctions of a translationally invariant single-particle Hamiltonian in the basis

$$\phi_{\mathbf{k},\alpha}(\mathbf{r}) = \frac{1}{\sqrt{N}} \sum_{\mathbf{R}} e^{i\mathbf{k}\cdot(\mathbf{R}+\mathbf{r}_\alpha)} \varphi_{\mathbf{R},\alpha}(\mathbf{r} - \mathbf{R} - \mathbf{r}_\alpha), \quad (2.1)$$

where $\varphi_{\mathbf{R},\alpha}$, $\alpha = 1, \dots, N$, are the orbitals chosen as basis for the finite-dimensional Hilbert space in each unit cell, labelled by the lattice vector \mathbf{R} , and \mathbf{r}_α is the center of each of these orbitals relative to the origin of the unit cell. Including \mathbf{r}_α in the exponent corresponds to a convenient choice of gauge when studying the response to external fields defined in continuous real space.

A general non-interacting Hamiltonian then has the Bloch matrix elements

$$\mathcal{H}_{\alpha,\beta}(\mathbf{k}) = \int d^d r \phi_{\mathbf{k},\alpha}^*(\mathbf{r}) \hat{H} \phi_{\mathbf{k},\beta}(\mathbf{r}), \quad (2.2)$$

as well as energy eigenstates

$$\psi_{\mathbf{k},n}(\mathbf{r}) = \sum_{\alpha}^N u_{\mathbf{k};n,\alpha} \phi_{\mathbf{k},\alpha}(\mathbf{r}), \quad (2.3)$$

where

$$\sum_{\beta} \mathcal{H}_{\alpha,\beta}(\mathbf{k}) u_{\mathbf{k};n,\beta} = \epsilon_n(\mathbf{k}) u_{\mathbf{k};n,\alpha}, \quad n = 1, \dots, N. \quad (2.4)$$

In the following, we are interested in situations where the system has an energy gap after the first $M < N$ bands, i.e., $\epsilon_M(\mathbf{k}) < \epsilon_{M+1}(\mathbf{k})$ for all \mathbf{k} .

2.1.1 Wilson loop and position operator

Introduced in 1984 by Sir Michael Berry, the so-called Berry phase describes a phase factor which arises in addition to the dynamical evolution $e^{i \int E[\lambda(t)] dt}$ of a quantum mechanical state in an adiabatic interpolation of the corresponding Hamiltonian

$\hat{H}[\lambda(t)]$ along a closed path $\lambda(t)$ in parameter space. It depends only on the geometry of the path chosen, and can be expressed as a line integral of the Berry connection, which we define below for the case where the parameter λ is a single particle momentum. If degeneracies between energy levels are encountered along the path, we have to consider the joint evolution of a set of eigenstates that may have degeneracies. If we consider M such states, the Berry phase generalizes to a $U(M)$ matrix, which can be expressed as the line integral of a non-abelian Berry connection, and is called non-abelian Wilson loop.

In the BZ, we may consider momentum \mathbf{k} as a parameter of the Bloch Hamiltonian $\mathcal{H}(\mathbf{k})$. The corresponding non-abelian Berry-Wilczek-Zee connection is then given by

$$\mathbf{A}_{m,n}(\mathbf{k}) = \langle u_{\mathbf{k},m} | \nabla_{\mathbf{k}} | u_{\mathbf{k},n} \rangle, \quad n, m = 1, \dots, M. \quad (2.5)$$

Note that it is anti-Hermitian, that is, it satisfies $\mathbf{A}_{n,m}^*(\mathbf{k}) = -\mathbf{A}_{m,n}(\mathbf{k})$. Using matrix notation, we define the Wilson loop, a unitary operator, as

$$W[I] = \overline{\exp} \left[- \int_I dI \cdot \mathbf{A}(\mathbf{k}) \right], \quad (2.6)$$

where I is a loop in momentum space and the overline denotes path ordering of the exponential, where operators at the beginning of the path occur to the right of operators at the end. This unitary operator acts on the occupied band manifold, and can be numerically evaluated with the formula

$$\begin{aligned} W_{n_f, n_1}[I] &= \lim_{R \rightarrow \infty} \sum_{n_2, \dots, n_R=1}^M \prod_{i=R}^1 \left[\exp [-(\mathbf{k}_{i+1} - \mathbf{k}_i) \cdot \mathbf{A}(\mathbf{k}_{i+1})] \right]_{n_{i+1}, n_i} \\ &= \lim_{R \rightarrow \infty} \sum_{n_2, \dots, n_R=1}^M \prod_{i=R}^1 \left[\delta_{n_{i+1}, n_i} - (\mathbf{k}_{i+1} - \mathbf{k}_i) \cdot \mathbf{A}_{n_{i+1}, n_i}(\mathbf{k}_{i+1}) \right] \\ &= \lim_{R \rightarrow \infty} \sum_{n_2, \dots, n_R=1}^M \prod_{i=R}^1 \left[\langle u_{\mathbf{k}_{i+1}, n_{i+1}} | u_{\mathbf{k}_{i+1}, n_i} \rangle \right. \\ &\quad \left. - (\mathbf{k}_{i+1} - \mathbf{k}_i) \cdot \langle u_{\mathbf{k}_{i+1}, n_{i+1}} | \nabla_{\mathbf{k}_{i+1}} | u_{\mathbf{k}_{i+1}, n_i} \rangle \right] \\ &= \lim_{R \rightarrow \infty} \sum_{n_2, \dots, n_R=1}^M \prod_{i=R}^1 \langle u_{\mathbf{k}_{i+1}, n_{i+1}} | u_{\mathbf{k}_i, n_i} \rangle \\ &= \langle u_{\mathbf{k}_f, n_f} | \lim_{R \rightarrow \infty} \prod_{i=R}^2 \left(\sum_{n_i}^M |u_{\mathbf{k}_i, n_i}\rangle \langle u_{\mathbf{k}_i, n_i}| \right) |u_{\mathbf{k}_1, n_1}\rangle \\ &= \sum_m^M V(\mathbf{G})_{n_f, m}^\dagger \langle u_{\mathbf{k}_1, m} | \lim_{R \rightarrow \infty} \prod_{i=R}^2 \left(\sum_{n_i}^M |u_{\mathbf{k}_i, n_i}\rangle \langle u_{\mathbf{k}_i, n_i}| \right) |u_{\mathbf{k}_1, n_1}\rangle, \end{aligned} \quad (2.7)$$

where we have identified $n_{R+1} = n_f$ and $\mathbf{k}_{R+1} = \mathbf{k}_f$, the path \mathcal{I} is sampled into R momenta \mathbf{k}_i , $i = 1, \dots, R$, and the limit $R \rightarrow \infty$ is taken such that the distance between any two neighboring momentum points goes to zero. Further, \mathbf{k}_1 and $\mathbf{k}_f = \mathbf{k}_1 + \mathbf{G}$, with \mathbf{G} a reciprocal lattice vector, are the initial and final momenta along the loop, respectively, on which the Wilson loop matrix depends. Note that in general $|u_{\mathbf{k}_1,n}\rangle$ and $|u_{\mathbf{k}_f,n}\rangle$ are not equal but differ by a gauge transformation $|u_{\mathbf{k}_f,n}\rangle = \sum_m V(\mathbf{G})_{n,m} |u_{\mathbf{k}_1,m}\rangle$.

By the last line of Equation (2.7) it becomes clear that $W[\mathcal{I}]$ is gauge *covariant*, that is, transforms as an operator under a general gauge transformation $S(\mathbf{k}) \in U(M)$ of the occupied subspace given by $|u_{\mathbf{k}}\rangle \rightarrow S(\mathbf{k})|u_{\mathbf{k}}\rangle$, only for a closed loop \mathcal{I} (the case where \mathcal{I} is non-contractible is also referred to as the Zak phase): in this case $V(\mathbf{G})$ exists, and we can choose a labelling convention where it is diagonal. However, the Wilson loop *eigenvalues* for a closed loop are gauge *invariant*, that is, they are not affected by gauge transformations (note that they also do not depend on the choice of $\mathbf{k}_i = \mathbf{k}_f$) and may therefore carry physical information. We will show that this is indeed the case: the Wilson loop eigenvalues are related to the eigenvalues of the position operator projected into the space of occupied bands.

To proceed, we consider a geometry where the loop \mathcal{I} is parallel to the x coordinate axis, and winds once around the BZ. Let \vec{k} denote the $(d - 1)$ dimensional vector of remaining good momentum quantum numbers. Then $W(\vec{k})$ is labelled by these remaining momenta. Denote by $\exp(i\theta_{\alpha,\vec{k}})$, $\alpha = 1, \dots, M$, the eigenvalues of $W(\vec{k})$. The set of phases $\{\theta_{\alpha,\vec{k}}\}$ forms a band structure in the $(d - 1)$ dimensional BZ and is referred to as the Wilson loop spectrum. Let us add that all $\theta_{\alpha,\vec{k}}$ are only defined modulo 2π , making the Wilson loop spectrum inherently different from the spectrum of a physical Bloch Hamiltonian.

The spectral equivalence relates the eigenvalues of the operator $(-i/2\pi) \log[W(\vec{k})]$ with those of the projected position operator

$$P(\vec{k}) \hat{x} P(\vec{k}), \quad (2.8)$$

where the projector $P(\vec{k})$ onto all occupied band eigenstates along \mathcal{I} (i.e., all states with wave vector \vec{k}) is given by

$$P(\vec{k}) = \sum_n^M \int_{-\pi}^{\pi} \frac{dk_x}{2\pi} |\psi_{k,n}\rangle \langle \psi_{k,n}|, \quad (2.9)$$

while the states $|\psi_{k,n}\rangle$ are given by Equation (2.3). The eigenvalues of the projected position operator have the interpretation of the charge centers in the ground state

of the Hamiltonian, while the eigenstates are known as hybrid Wannier states, being localized in the x -direction and plane waves perpendicular to it [78].

To prove the equivalence, we start with the eigenfunctions of $P(\vec{k})\hat{x}P(\vec{k})$, which satisfy

$$\left[P(\vec{k})\hat{x}P(\vec{k}) - \frac{\tilde{\theta}_{\vec{k}}}{2\pi} \right] |\Psi_{\vec{k}}\rangle = 0. \quad (2.10)$$

Note that there are M eigenvectors, and that the form of the corresponding eigenvalues $\tilde{\theta}_{\alpha,\vec{k}}/(2\pi)$, $\alpha = 1, \dots, M$ has been chosen for later convenience and in particular has not yet been logically connected to the $\theta_{\alpha,\vec{k}}$ making up the Wilson loop spectrum (however, we will do so shortly). An eigenfunction can be expanded as

$$|\Psi_{\vec{k}}\rangle = \sum_n^M \int dk_x f_{\vec{k},n}(k_x) |\psi_{\vec{k},n}\rangle, \quad (2.11)$$

where the coefficients $f_{\vec{k},n}$ satisfy the equation

$$\begin{aligned} \langle \psi_{\vec{k},n} | P(\vec{k})\hat{x}P(\vec{k}) | \Psi_{\vec{k}} \rangle &= \sum_m \int d\tilde{k}_x \langle \psi_{\vec{k},n} | (i\partial_{\tilde{k}_x}) f_{\vec{k},m}(\tilde{k}_x) | \Psi_{\vec{k},m} \rangle \\ &= \sum_m \int d\tilde{k}_x i \frac{\partial f_{\vec{k},m}(\tilde{k}_x)}{\partial \tilde{k}_x} (\delta_{m,n} \delta_{\tilde{k}_x, k_x}) \\ &\quad + \sum_m \int d\tilde{k}_x f_{\vec{k},m}(\tilde{k}_x) \int \frac{dx}{2\pi} \langle u_{\vec{k},n} | e^{-ik_x x} (i\partial_{\tilde{k}_x}) e^{i\tilde{k}_x x} | u_{\vec{k},m} \rangle \\ &= i \frac{\partial f_{\vec{k},n}(k_x)}{\partial k_x} - f_{\vec{k},n}(k_x) \int \frac{dx}{2\pi} x \\ &\quad + i \sum_m \int d\tilde{k}_x f_{\vec{k},m}(\tilde{k}_x) \int \frac{dx}{2\pi} e^{-i(k_x - \tilde{k}_x)x} \langle u_{\vec{k},n} | \partial_{\tilde{k}_x} | u_{\vec{k},m} \rangle \\ &= i \frac{\partial f_{\vec{k},n}(k_x)}{\partial k_x} + i \sum_m f_{\vec{k},m}(k_x) \langle u_{\vec{k},n} | \partial_{\tilde{k}_x} | u_{\vec{k},m} \rangle \\ &= i \frac{\partial f_{\vec{k},n}(k_x)}{\partial k_x} + i \sum_m A_{x;n,m}(\vec{k}) f_{\vec{k},m}(k_x). \end{aligned} \quad (2.12)$$

(Note that we have to assume an appropriate regularization to make the term $\int dx x$ vanish in this continuum calculation, reflecting the ambiguity in choosing the origin of the coordinate system.) Then, integrating the resulting Equation (2.10) for $f_{\vec{k},n}(k_x)$, we obtain

$$f_{\vec{k},n}(k_x) = e^{-i(k_x - k_x^0)\tilde{\theta}_{\vec{k}}/(2\pi)} \sum_m^M \overline{\exp} \left[- \int_{k_x^0}^{k_x} d\tilde{k}_x A_x(\tilde{k}_x, \vec{k}) \right]_{n,m} f_{\vec{k},m}(k_x^0). \quad (2.13)$$

We now choose $k_x = k_x^0 + 2\pi$. Periodicity of $f_{\vec{k},m}(k_x^0)$ as $k_x^0 \rightarrow k_x^0 + 2\pi$ yields (choosing $k_x^0 = \pi$ without loss of generality)

$$\sum_m^M W(\vec{k})_{n,m} f_{\vec{k},m}(\pi) = e^{i\tilde{\theta}_{\vec{k}}} f_{\vec{k},n}(\pi), \quad (2.14)$$

showing that the expansion coefficients of an eigenstate of $P(\vec{k})\hat{x}P(\vec{k})$ with eigenvalue $\tilde{\theta}_{\vec{k}}/(2\pi)$ form eigenvectors of $W(\vec{k})$ with eigenvalues $e^{i\tilde{\theta}_{\vec{k}}}$. This establishes the spectral equivalence $\tilde{\theta}_{\vec{k}} = \theta_{\vec{k}}$.

Note that there are M eigenvalues of the Wilson loop, while the number of eigenvalues of $P(\vec{k})\hat{x}P(\vec{k})$ is extensive in the system size. Indeed, for each occupied band (i.e., every Wilson loop eigenvalue $\theta_{\alpha,\vec{k}}$, $\alpha = 1, \dots, M$) there exists a ladder of eigenvalues of the projected position operator

$$\frac{\theta_{\alpha,\vec{k},X}}{2\pi} = \frac{\theta_{\alpha,\vec{k}}}{2\pi} + X, \quad X \in \mathbb{Z}, \quad \alpha = 1, \dots, M. \quad (2.15)$$

We have set the lattice spacing in the x -direction to 1 for convenience here and in the following.

The eigenstates of the projected position operator are hybrid Wannier states that are maximally localized in x direction, but take on plane wave form in the perpendicular directions. The eigenvalues, which coincide with the Wilson loop spectrum, correspond to the x -coordinates of the Wannier function charge centers (Wannier centers) [78] upon a suitable rescaling – we will make use of this correspondence extensively in Chapter 7. Since the eigenvalues of $W(\vec{k})$ along any non-contractible loop of \vec{k} in the BZ define a map $S^1 \rightarrow U(1) \cong S^1$, their winding number, which is necessarily an integer, can – given additional crystalline symmetries – provide a topological invariant that cannot be changed by smooth deformations of the system’s Hamiltonian. To familiarize the reader with the concepts introduced above, we now present the properties of Wilson loop spectra in the context of three simple models.

2.1.1.1 Su-Schrieffer-Heeger model: polarization and winding number

One of the simplest examples of a topological phase is exemplified by the Su-Schrieffer-Heeger (SSH) model, initially devised to model polyacetylene [79]. It describes electrons hopping on a 1D dimerized lattice with two sites A and B in its unit cell [see Figure 2.1 (a)]. In momentum space, the Bloch Hamiltonian reads

$$\mathcal{H}(k) = \begin{pmatrix} 0 & t + t'e^{ik} \\ t + t'e^{-ik} & 0 \end{pmatrix}. \quad (2.16)$$

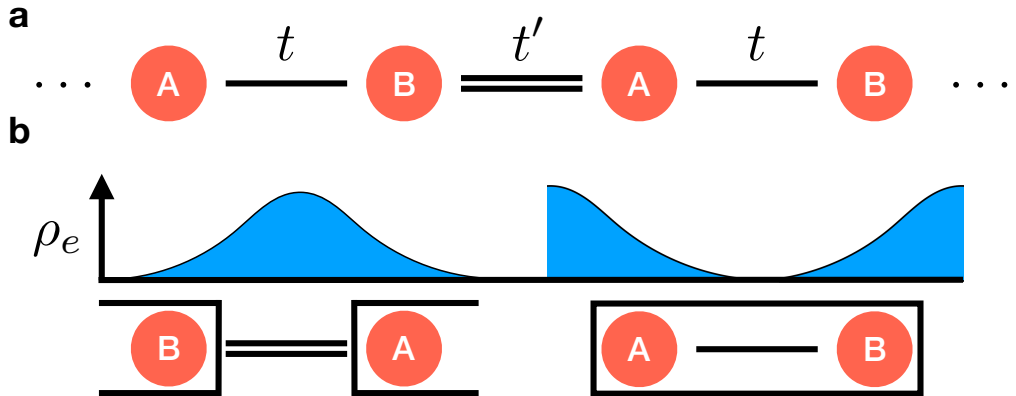


Figure 2.1: Su-Schrieffer-Heeger model. (a) The model consists of electrons hopping on a dimerized chain with alternating hopping strengths t and t' . For the case of $t' > t$, the model is in its topological phase, which is adiabatically connected to the special case $t' \neq 0, t = 0$. In this limit, the presence of gapless edge modes is evident when the chain is cut after a full unit cell. (b) The polarization is a measure of where charges sit in the unit cell. Shown is the case $P = 1/2$, where the charge center (Wannier center) is displaced by exactly half a lattice spacing. When cutting the system after a full unit cell, the edge hosts a state of charge $1/2$. This is the simplest example of charge fractionalization in topological condensed matter systems.

The model has an inversion symmetry $\mathcal{I}\mathcal{H}(k)\mathcal{I}^{-1} = \mathcal{H}(-k)$, with $\mathcal{I} = \sigma_x$. Since the Hamiltonian does not couple sites A to A or B to B individually, it furthermore enjoys a chiral or sublattice symmetry $\mathcal{C}\mathcal{H}(k)\mathcal{C}^{-1} = -\mathcal{H}(k)$ with $\mathcal{C} = \sigma_z$. [Notice some abuse of language here: the chiral symmetry is not a “symmetry” in the sense of a commuting operator on the level of the first quantized Bloch Hamiltonian. Still, as a mathematical fact, this chiral symmetry can be helpful to infer and protect the existence of topological boundary modes.] While a standard discussion of the SSH model would focus on the chiral symmetry and its role in protecting topological phases, here we will first consider the implications of the crystalline inversion symmetry (see also the general discussion of \mathcal{I} -symmetric models in Section 2.3). It will be useful to point out that the spectrum is given by $E = \pm\sqrt{t^2 + t'^2 + 2tt'\cos k}$ with a gap closing at $k = \pi$ for $t = t'$ and at $k = 0$ for $t = -t'$.

Let us start by calculating the Wilson loop for the case where $(t, t') = (0, 1)$. The eigenvectors of $\mathcal{H}(k)$ are then given by

$$|u_{k,1}\rangle = \frac{1}{\sqrt{2}} \begin{pmatrix} -e^{ik} \\ 1 \end{pmatrix}, \quad |u_{k,2}\rangle = \frac{1}{\sqrt{2}} \begin{pmatrix} e^{ik} \\ 1 \end{pmatrix}, \quad (2.17)$$

with energies -1 and $+1$, respectively. Since the occupied subspace is one-dimensional in this case, the Berry connection $A(k) = \langle u_{k,1} | \partial_k | u_{k,1} \rangle = i/2$ is abelian and given by just a purely imaginary number (remember that it is anti-Hermitian in general). We thus obtain

$$P \equiv -\frac{i}{2\pi} \log W = -\frac{i}{2\pi} \int_0^{2\pi} A(k) dk = \frac{1}{2}. \quad (2.18)$$

Recalling that the Wilson loop spectrum is closely related to the Wannier centers, we recognize P as the electric polarization. Specifically, the physical interpretation of P is expounded within the modern theory of polarization (see Reference [80] for a pedagogical introduction) as that of a bulk electrical dipole moment, which is naturally only defined modulo 1 since the coordinate of a center of charge on the lattice is only defined up to a lattice translation (remember that we have chosen the lattice spacing $a = 1$). The rescaling by 2π makes sure that the periodicity of the charge centers defined in this way is that of the real-space lattice. See also Figure 2.1 (b).

The result $P = 1/2$ is by no means accidental: since the inversion symmetry reverses the path of integration in W , but leaves inner products such as $A(k)$ invariant, the Wilson loop eigenvalues of an inversion symmetric system satisfy $e^{i\theta} = e^{-i\theta}$ (see also Section 2.1.1.3 below). This requires that P is quantized to 0 ($\theta = 0$) or $1/2$ ($\theta = \pi$) in the abelian case. This is a first example where a crystalline symmetry such as inversion, which acts non-locally in space, protects a topological phase by enforcing the quantization of a topological invariant to values that cannot be mapped into one another by an adiabatic evolution of the corresponding Hamiltonian. Since the eigenstates for the parameter choice $(t, t') = (1, 0)$ do not depend on k , we immediately obtain $P = 0$ for this topologically trivial case.

By these considerations it is clear that the full parameter regime $t < t'$ is topological, while the regime $t > t'$ is trivial. This is because it is possible to perform an adiabatic interpolation from the specific parameter choices $(t, t') \in \{(0, 1), (1, 0)\}$ considered above to all other values as long as there is no gap closing and no breaking of inversion symmetry, which is true provided that the line $t = t'$ is avoided in parameter space.

In general, a topological phase comes with topologically protected gapless boundary modes on boundaries which preserve the protecting symmetry. For inversion symmetry, however, there are no boundaries satisfying this requirement. Even though the model at $(t, t') = (0, 1)$ has zero-mode end states [since in this case, $\mathcal{H}(k)$ does not act at all on the A (B) site in the unit cell at the left (right) edge of the

sample], these modes can be removed from zero energy by generic local perturbations even without a bulk gap closing. To protect the end modes, we need to invoke the chiral symmetry, implying that an eigenstate at any energy E is paired up with an eigenstate at energy $-E$. Eigenstates of the chiral symmetry can then only appear at $E = 0$. A spatially and spectrally isolated boundary mode at $E = 0$ can not be removed by perturbations that retain the chiral symmetry. In conclusion, topological crystalline phases in 1D have no protected boundary degrees of freedom as long as we do not include further local symmetries. We will, however, explain in Chapter 5 how some notion of a topological boundary signature survives in the form of a filling anomaly.

In the presence of chiral symmetry, the above discussion can be generalized to arbitrary 1D models. In the eigenbasis of \mathcal{C} , we can write any Hamiltonian with chiral symmetry in the form

$$\mathcal{H}(k) = \begin{pmatrix} 0 & q(k) \\ q^\dagger(k) & 0 \end{pmatrix}, \quad (2.19)$$

where for the SSH model the matrix $q(k)$ was given by just a complex number, and in general we choose it to be a unitary matrix by an adiabatic deformation of the Hamiltonian. The chiral symmetry allows for the definition of a winding number

$$\nu = \frac{i}{2\pi} \int dk \text{Tr} [q(k)\partial_k q^\dagger(k)] \in \mathbb{Z}. \quad (2.20)$$

This winding number is only a valid topological invariant when chiral symmetry is present. We can make contact with the overarching concept of Wilson loops by calculating the connection

$$A = \frac{1}{2}q(k)\partial_k q^\dagger(k). \quad (2.21)$$

Thus the Wilson loop eigenvalues $e^{i\theta_\alpha}$ satisfy

$$\frac{1}{2\pi} \sum_\alpha \theta_\alpha = \frac{\nu}{2} \bmod 1. \quad (2.22)$$

In particular, in the abelian case, chiral symmetry thus implies the quantization of P to half-integer values, just as inversion symmetry did it above. An important distinction to be made is that with inversion symmetry, we have a \mathbb{Z}_2 topological classification (P can be either 0 or 1/2), while with chiral symmetry the winding number allows for a \mathbb{Z} classification.

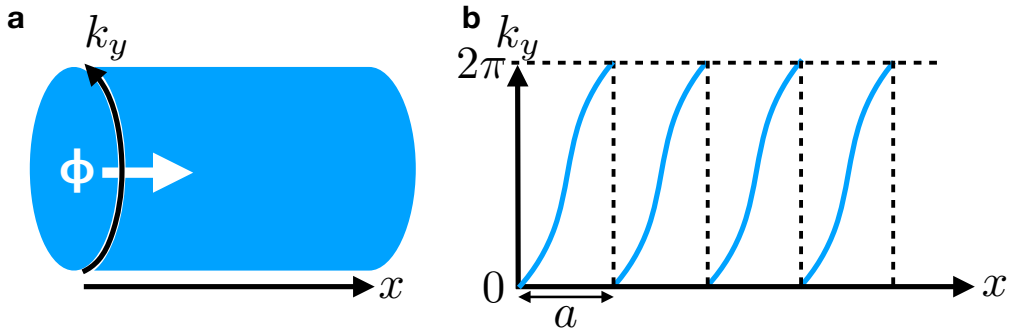


Figure 2.2: Chern insulator geometry and charge center flow. (a) To calculate the Hall conductivity, we consider a gedanken experiment where the y -direction of 2D space is compactified while we retain open boundary conditions in the x -direction. In particular, the translational symmetry along y allows for the introduction of the momentum k_y as a good quantum number to label blocks of the Hamiltonian and eigenstates. The Hall conductivity is then equal to the amount of charge transported along the y -direction in a single adiabatic cycle of flux insertion, where the inserted flux ϕ varies over time from 0 to 2π . (b) Charge center flow corresponding to a Chern number $C = 1$. Since one cycle of flux insertion corresponds to tuning k_y from 0 to 2π , we see that in one such cycle the charge center crosses exactly one unit cell.

2.1.1.2 Wilson loop spectrum of the Chern insulator

Another paradigmatic example of a topologically protected phase is given by the (integer) quantum Hall effect of electrons subject to a perpendicular magnetic field in 2D continuous space. Here, we study its lattice realization, also called the quantum anomalous Hall effect or Chern insulator. We consider a 2D square lattice with open boundary conditions in x -direction and periodic boundary conditions in y -direction, retaining the momentum k_y as good quantum number.

To find an expression for the Hall conductivity for any Hamiltonian we could put on this lattice in terms of Wilson loops, let us perform a thought experiment where we roll up the y direction to form a cylinder of circumference L [see Figure 2.2 (a)]. Threading a magnetic flux ϕ along the x direction through this cylinder, amounts to the replacement $k_y \rightarrow k_y + \phi$ by a Peierls substitution [81]. Note that in our units $\phi = 2\pi$ denotes a single flux quantum.

We now consider a Wilson loop along x direction, labelled by k_y with eigenvalues $e^{i\theta_{\alpha,k_y}}$. The derivative $\partial_{k_y}\theta_{\alpha,k_y}$ of the α -th Wilson loop eigenvalue is by the interpretation in terms of the modern theory of polarization explained in the previous section simply the ‘velocity’ in x -direction of the α -th charge center at ‘time’ k_y . Integrating over k_y , i.e., adiabatically performing a flux insertion from $\phi = 0$

to $\phi = 2\pi$ (which brings the system back to its initial state), gives the full Hall conductivity as 2π (or, if e and \hbar are reinstated, e^2/h) times

$$C = \sum_{\alpha}^M \int \frac{dk_y}{2\pi} \partial_{k_y} \theta_{\alpha, k_y}, \quad (2.23)$$

where C is known as the Chern number. To see how this formula works, note that the Hall conductivity is equal to the amount of charge transported in y direction under the adiabatic insertion of a single flux quantum. Since we can only transport an integer number of charge around the cylinder in one such evolution (at least in the non-interacting systems we are considering here), C is necessarily quantized.

Making use of the relation $\sum_{\alpha}^M \theta_{\alpha, k_y} = i \int dk_x \text{Tr} A_x(k_x, k_y)$, which follows from Equation (2.6), and requiring C to be gauge invariant, we can generalize Equation (2.23) to

$$C = -\frac{i}{2\pi} \int d^2k [\partial_{k_x} \text{Tr} A_y(\mathbf{k}) - \partial_{k_y} \text{Tr} A_x(\mathbf{k})]. \quad (2.24)$$

The equality is directly seen in a gauge in which the integral of the first term $\partial_{k_x} \text{Tr} A_y(\mathbf{k})$ does not contribute, which we have implicitly been working in (\mathbf{A} here denotes the Berry connection, *not* the electromagnetic gauge field). The Chern number is thus the net number of charge centers crossing a given x position in the full k_y BZ. In the Wilson loop picture, it just corresponds to the winding number of the x -direction Wilson loop eigenvalues as k_y is varied along a non-contractible loop in the BZ, which is of course quantized [see Figure 2.2 (b)]. While the Chern number is normally defined by employing the concept of Berry curvature, we have shown here that it may be equivalently expressed in terms of the spectral flow of Wilson loop eigenvalues, or Wannier centers.

Note that as the $\theta_{\alpha}(\mathbf{k})$ are only defined modulo 2π , we can have unidirectional flow in the Wilson loop spectrum: in the case of a Chern insulator with $C = 1$, we have a single Wilson loop band which winds once along the θ -direction as k_y goes from 0 to 2π . This is in stark contrast to energy spectra, in which every unidirectionally dispersing band is paired up with a band going into the opposite direction so that the net chirality of the spectrum is always zero, a result which follows from the Nielsen-Ninomiya theorem under physically realistic circumstances such as locality [82].

2.1.1.3 Wilson loop spectrum of the 2D topological insulator

Here, we explore the constraints imposed by time-reversal or inversion symmetries on Wilson loops. These symmetries protect topological insulators in two and three

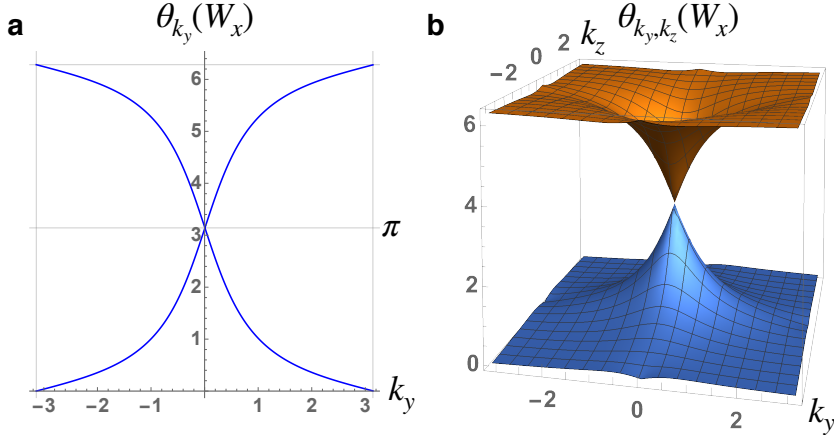


Figure 2.3: Wilson loop spectra of topological insulators in 2D and 3D. (a) A 2D topological insulator can be diagnosed by its gapless Wilson loop spectrum. The twofold degeneracies at $k_y = 0, \pi$ are protected by TRS. (b) A 3D topological insulator can be viewed as a topological-to-trivial tuning of a 2D insulator. Its Wilson loop spectrum is thereby enforced to be gapless and hosts a Dirac cone.

dimensions. In the presence of an anti-unitary time-reversal symmetry \mathcal{T} , a Wilson loop $W_{2\pi \leftarrow 0}(\mathbf{k})$ along the x -direction, with k_x running from 0 to 2π , transforms as

$$\begin{aligned} \mathcal{T}W_{2\pi \leftarrow 0}(\mathbf{k})\mathcal{T}^{-1} &= W_{0 \leftarrow 2\pi}^*(-\mathbf{k}) \\ &= W_{2\pi \leftarrow 0}^\text{T}(-\mathbf{k}) \\ \Rightarrow \quad \theta_\alpha(\mathbf{k}) &= \theta_\alpha(-\mathbf{k}). \end{aligned} \quad (2.25)$$

In particular, in a spinful system where $\mathcal{T}^2 = -1$, the representation of the time-reversal operation on the Wilson loop retains its property to square to -1 , so that there is a Kramers degeneracy not only in the energy spectrum, but also in the Wilson loop spectrum.

We thus recover the \mathbb{Z}_2 classification of time-reversal invariant 2D topological insulators from the spectral flow in the Wilson loop eigenvalues: either the bands emerging from individual Kramers pairs connect back to the same pairs as \mathbf{k} evolves along a non-contractible loop in the BZ, or they split up to connect to separate pairs. The latter scenario is realized in a 2D topological insulator, and is shown in Figure 2.3 (a)]. From this picture, it becomes clear that the 2D topological insulator can be viewed as two stacked Chern insulators, one with $C = +1$, and one with $C = -1$, which are mapped to each other by the action of TRS.

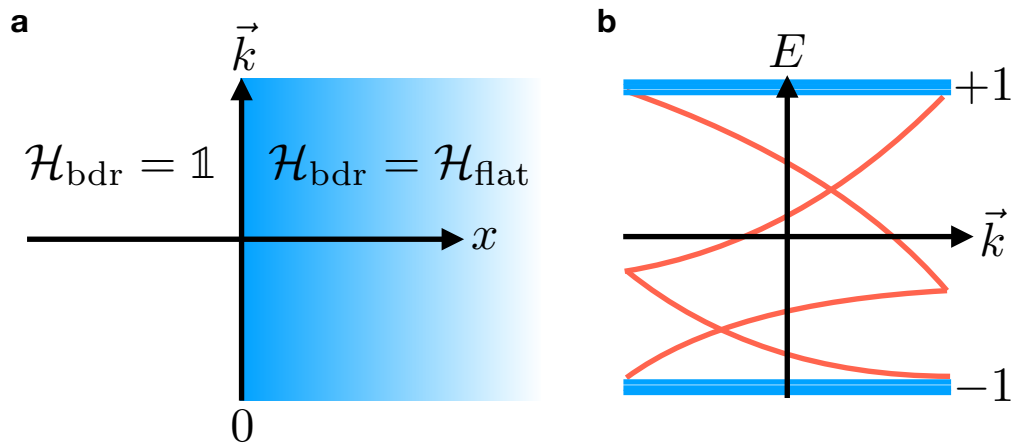


Figure 2.4: Real space setup and generic spectrum of \mathcal{H}_{bdr} . (a) For $V_0(x)$ as given by Equation (2.29), \mathcal{H}_{bdr} varies discontinuously from a trivial projector in the domain $x < 0$ to $\mathcal{H}_{\text{flat}}$ in the domain $x > 0$. Translational symmetry along x is thus broken, however it is preserved along all perpendicular directions, which still have good momentum quantum numbers \mathbf{k} . (b) The spectrum of \mathcal{H}_{bdr} has accumulation points at ± 1 , stemming from the semi-infinite regions to the left and right of the domain wall, and a discrete set of bands in between, coming from the finite domain wall region.

2.1.2 Bulk-boundary correspondence

Wilson loops not only provide a convenient formulation of many topological invariants, but are also in one-to-one correspondence with the boundary degrees of freedom of the system considered. We will now show that indeed the spectrum of a Hamiltonian in the presence of a boundary is smoothly connected to the spectrum of its Wilson loop along the direction perpendicular to the boundary. Note that since the Wilson loop is determined entirely by the bulk Bloch Hamiltonian, this relation provides an explicit realization of the bulk-boundary correspondence [83, 84, 85].

We consider a semi-infinite slab geometry with a single edge of the system at $x = 0$, while keeping \mathbf{k} as good quantum numbers. From a topological viewpoint, the actual energetics of the band structure are irrelevant, and we can always deform the Hamiltonian for the sake of clarity to a spectrally flattened Hamiltonian where all bands above and below the gap are at energy $+1$ and -1 , respectively, without closing the gap. It is therefore enough to work with

$$\mathcal{H}_{\text{flat}}(\mathbf{k}) = 1 - 2P(\mathbf{k}) \quad (2.26)$$

to model the bulk system. Here, $P(\mathbf{k})$ as defined in Equation (2.9), repeated here for convenience,

$$P(\mathbf{k}) = \sum_n^M \int_{-\pi}^{\pi} \frac{dk_x}{2\pi} |\psi_{\mathbf{k},n}\rangle \langle \psi_{\mathbf{k},n}|, \quad (2.27)$$

is the projector onto the occupied subspace for a given \mathbf{k} . Note that $\mathcal{H}_{\text{flat}}(\mathbf{k})$ actually has the same eigenvectors as the original Hamiltonian. To model a system with boundary, we use

$$\mathcal{H}_{\text{bdr}}(\mathbf{k}) = P(\mathbf{k})V_0(\hat{x})P(\mathbf{k}) + 1 - P(\mathbf{k}), \quad (2.28)$$

with

$$V_0(x) = \begin{cases} 1 & x < 0 \\ -1 & x > 0 \end{cases} \quad (2.29)$$

so that we have $\mathcal{H}_{\text{bdr}}(\mathbf{k}) \rightarrow \mathcal{H}_{\text{flat}}(\mathbf{k})$ for $x \rightarrow +\infty$ and $\mathcal{H}_{\text{bdr}}(\mathbf{k}) \rightarrow 1$ for $x \rightarrow -\infty$ [see Figure 2.4 (a)]. The latter limit corresponds to a description of the vacuum with the chemical potential chosen so that no electron states will be occupied, which we take to be the topologically trivial limit.

Since we take space to be infinitely extended away from the domain wall at $x = 0$, the spectrum of $\mathcal{H}_{\text{bdr}}(\mathbf{k})$ includes the spectrum of $\mathcal{H}_{\text{flat}}(\mathbf{k})$, given by ± 1 since $P^2(\mathbf{k}) = P(\mathbf{k})$, as well as that of the operator 1, trivially given by +1. The boundary region is of finite extent and can therefore contribute only a finite number of midgap states as the system has exponentially decaying correlations on either side of the boundary. There are therefore spectral accumulation points at ± 1 , but otherwise we are left with a discrete spectrum [see Figure 2.4 (b)]. We will focus on this part of the spectrum.

We will now deform the spectrum of $\mathcal{H}_{\text{bdr}}(\mathbf{k})$ to that of $(-i/2\pi) \log[W(\mathbf{k})]$ by considering an evolution that takes $P(\mathbf{k})V_0(\hat{x})P(\mathbf{k})$ to $P(\vec{k})\hat{x}P(\vec{k})$, the eigenvalues of which were previously shown to be directly related to those of $(-i/2\pi) \log[W(\mathbf{k})]$. The deformation is continuous in \mathbf{k} and therefore preserves both discreteness of the spectrum as well as its topological properties. An example for this interpolation is given by

$$V_t(x) = \begin{cases} -\frac{x}{t} & \text{for } |x| < t/(1-t) \\ -\frac{\text{sgn}(x)}{1-t} & \text{for } |x| \geq t/(1-t) \end{cases}, \quad 0 \leq t \leq 1. \quad (2.30)$$

Importantly, for any $t < 1$, $P(\mathbf{k})V_t(\hat{x})P(\mathbf{k})$ is a finite rank (finite support) perturbation of $(1-t)^{-1}P(\mathbf{k})V_0(\hat{x})P(\mathbf{k})$, so it will retain the property that the spectrum

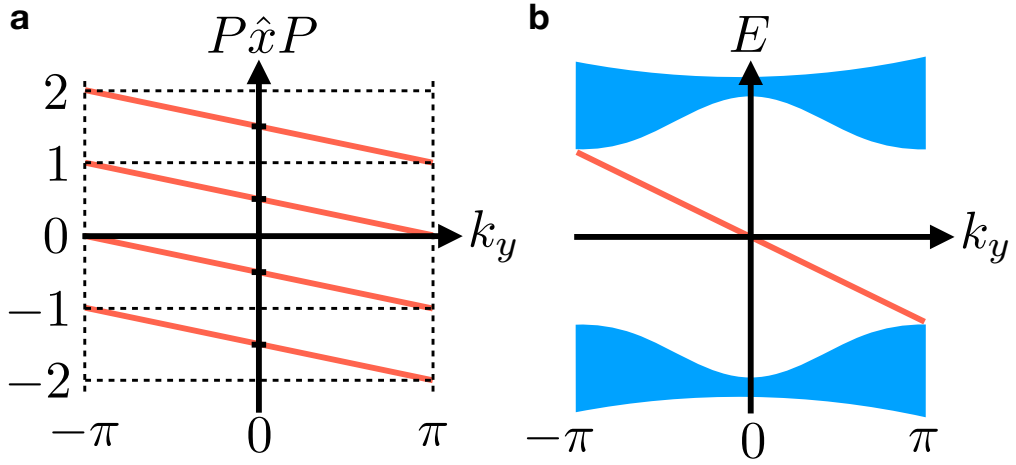


Figure 2.5: Projected position operator spectral flow and its implications for the boundary Hamiltonian of a Chern insulator. (a) The model in Equation (2.32) has two bands, therefore the Wilson loop is abelian. Due to $C = 1$, by the spectral equivalence derived in Section 2.1.1, the eigenvalues of the projected position operator $P \hat{x} P$ flow from an integer n back to $n - 1 = n \bmod 1$ exactly once as k_y is varied across a non-contractible loop in the BZ. (b) By the bulk-boundary correspondence derived in the present chapter, this implies a single chiral mode crossing the gapped bulk bands when the system is considered in the presence of a boundary termination.

is discrete. However, the point $t = 1$ deserves closer inspection, as $P(\vec{k})\hat{x}P(\vec{k})$ is not a bounded operator. However, we can handle this subtlety by defining

$$h(r) = \begin{cases} r & \text{for } -w < r < w \\ \text{sgn}(r)w & \text{else} \end{cases} \quad (2.31)$$

and considering $h[P(\mathbf{k})V_t(\hat{x})P(\mathbf{k})]$ for some large w . The spectrum evolves uniformly continuously from $h[P(\mathbf{k})V_0(\hat{x})P(\mathbf{k})]$ to $h[P(\mathbf{k})V_1(\hat{x})P(\mathbf{k})]$ for any finite w [83].

The topology of the Wilson loop spectrum and the physical boundary spectrum is thus identical. Protected spectral flow in the former implies gapless boundary modes in the latter, as long as the form of the boundary [i.e., $V(x)$] does not break a symmetry that protects the bulk spectral flow.

2.1.2.1 Chern insulator spectral flow

We can obtain a simple Hamiltonian for a Chern insulator in 2D from that of the 1D SSH model by tuning the latter from its topological to its trivial phase along a perpendicular direction k_y in the BZ. Along the way, we have to make sure that

the whole system stays gapped. One Hamiltonian that achieves this is given by [compare to Equation (2.16)]

$$\mathcal{H}(\mathbf{k}) = \begin{pmatrix} \sin k_y & -e^{ik_x} + (1 - \cos k_y) \\ -e^{-ik_x} + (1 - \cos k_y) & -\sin k_y \end{pmatrix}. \quad (2.32)$$

Here, the part proportional to $\sin k_y$ is the term we added to keep the system gapped at all points in the new 2D BZ. The Wilson loop we considered in Section 2.1.1.1, and with it the polarization P , now becomes a function of k_y . We know that $\mathcal{H}(k_x, 0)$ corresponds to a topological SSH chain, while $\mathcal{H}(k_x, \pi)$ corresponds to a trivial one, implying $P(0) = 1/2$ and $P(\pi) = 0$. Remembering that P is only defined up to an integer, there are two possibilities for the Wilson loop spectral flow as k_y is varied from $-\pi$ to $+\pi$: Either the Wilson loop bands connect back to themselves trivially after the cycle has come to a close, or they do so only modulo an integer given by the Chern number C in Equation (2.23). To infer which case applies to the model at hand, we can use the relation $\mathcal{H}(k_x, k_y) = -\sigma_3 \mathcal{H}(k_x, -k_y) \sigma_3$, which is a combination of chiral symmetry and y -mirror symmetry and must also hold in presence of a boundary (if the boundary potential is chosen such that it does not break this symmetry). It dictates that boundary spectra consist of *chiral* modes that connect the SSH spectra at $k_y = 0$ and $k_y = \pi$ as shown in Figure 2.5. (Note that invoking the combination of chiral and mirror symmetry is only a convenient way to infer the boundary mode connectivity. No symmetry is needed to protect chiral boundary modes.) This is consistent with the Chern number, which for the model at hand evaluates to $C = 1$.

2.1.2.2 3D topological insulator surface states

Similar to the construction of a Chern insulator from the SSH model by a tuning procedure, a 3D topological insulator (TI) can be obtained by tuning a 2D topological insulator from topological to trivial along a perpendicular direction k_z in the BZ. For instance, let $k_z = 0$ carry the 2D topological insulator and $k_z = \pi$ the trivial one ($k_z = 0, \pi$ are the only choices for BZ surfaces at fixed k_z that are time-reversal invariant on their own). This implies a corresponding tuning of the Wilson loop spectrum along k_z : Denote by $W_x(k_y, k_z)$ the Wilson loop along the x direction of the 3D TI, it is indexed by the good momentum quantum numbers k_y and k_z . Then the spectrum of $W_x(k_y, 0)$ will be gapless [it is that of the 2D topological insulator, shown in Figure 2.3 (a)] while the spectrum of $W_x(k_y, \pi)$ will be gapped (trivial), and the spectrum of $W_x(k_y, k_z)$ has to continuously interpolate between these two cases as k_z is tuned from 0 to π . This implies a splitting of the TRS-enforced degeneracy in the spectrum of $W_x(k_y, 0)$ away from $k_z = 0$, giving rise to a Dirac cone dispersion [shown in Figure 2.3 (b)].

Employing the relation of Wilson loop and boundary spectra, we can now immediately deduce that the surface band structure of a 3D TI is characterized by the presence of a gapless Dirac cone.

2.2 Survey of invariants for higher-order topological phases

We now discuss the kinds of topological invariants that are enabled by crystalline (spatial) symmetries in 3D systems, with a particular focus on the diagnosis of higher-order topological insulators.

2.2.1 Nested Wilson loops

Nested Wilson loops extend the concept of Wilson loops, and are used as topological invariants for higher-order topological insulators protected by crystalline symmetries. For instance, consider the Wilson loop in x -direction, which can be reformulated as [see second-to-last line of Equation (2.7)]

$$W_{mn}^x(k_y, k_z) = \langle u_m(2\pi, k_y, k_z) | \prod_{k_x}^{2\pi \leftarrow 0} P(\mathbf{k}) | u_n(0, k_y, k_z) \rangle, \quad (2.33)$$

where $|u_m(\mathbf{k})\rangle$ are the occupied eigenstates, $P(\mathbf{k}) = |u_m(\mathbf{k})\rangle \langle u_m(\mathbf{k})|$ projects onto the occupied subspace at \mathbf{k} , and summation over repeated indices is implied. As a unitary operator, $W^x(k_y, k_z)$ can be rewritten as $W^x(k_y, k_z) = e^{i\mathcal{H}_W(k_y, k_z)}$, where $\mathcal{H}_W(k_y, k_z)$ is a Hermitian operator called the Wilson loop Hamiltonian. $\mathcal{H}_W(k_y, k_z)$ can be interpreted as the Hamiltonian of a 2D system. As shown in 2.1.2, the spectrum of the Wilson loop Hamiltonian shares the topological properties of that of the slab Hamiltonian with surface normal along the loop direction. This implies that the Wilson loop spectrum of a HOTI is generically gapped (as the 2D surfaces of a HOTI are generically gapped), and allows for the definition of the nested Wilson loop.

To arrive at the nested Wilson loop for the example above, one computes the Wilson loop of the Wilson loop Hamiltonian $\mathcal{H}_W(k_y, k_z)$ [86]. That is, one first diagonalizes the Hamiltonian $\mathcal{H}_W(k_y, k_z)$ (which needs to be gapped in order for its “occupied” subspace, and thereby the nested Wilson loop, to be well-defined) and then evaluates a y -directed Wilson loop in its “occupied” subspace. The presence of gapless hinge states for a HOTI implies that its nested Wilson loop is gapless. As the Wilson loop eigenvalues can be related to the real-space centers

of hybrid Wannier functions that are exponentially localized along the direction of the loop [87, 88, 89], a gapless nested Wilson loop indicates the Wannier center pumping of HOTIs [23, 25, 33, 34]. See also the discussion in Appendix A.5, where we furthermore use nested entanglement spectra to diagnose HOTIs.

We find it adequate to briefly introduce the concept of Wannier function localization and Wannierizability. In general, one can obtain the real space-localized Wannier functions as the Fourier transforms of the momentum space-localized Bloch functions $\psi_{k,n}(\mathbf{r})$ [defined in Equation (2.3)]. The choice of gauge for the Bloch functions then corresponds to the varying degrees to which the Wannier functions are localized in real space – using the Paley-Wiener theorem, it can be shown that only a smooth (analytic) gauge across the whole Brillouin zone leads to exponentially localized Wannier functions. We refer to the ground state of an insulator as Wannierizable, or equivalently as an atomic limit, when all of its Wannier functions can be exponentially localized in a manner that respects the (crystalline) symmetries of the Bloch Hamiltonian, Equation (2.2). In this sense, the SSH model of Section 2.1.1.1 realizes an obstructed atomic limit (introduced at the beginning of Chapter 1) where the electronic Wannier functions are localized away from the atomic sites.

A gapless Wilson loop spectrum, such as that of 2D and 3D topological insulators shown in Figure 2.3, implies an irremovable flow of Wannier centers with the transverse momenta (k_y and k_z in the figure), and thereby an obstruction to full exponential localization – i.e., when taking the Fourier transform also with respect to the transverse momenta, the discontinuity in the Bloch eigenstates that is implied by the Wilson loop winding will prohibit a simultaneous exponential localization in the corresponding directions. The converse is however not true: we have explained above that HOTIs have a gapped Wilson loop spectrum, but they are not adiabatically connected to any atomic limit (as can for instance be seen by the presence of gapless hinge states at their boundaries). This implies that HOTIs realize novel band structures that are not simultaneously Wannierizable in all three directions while at the same time having a fully gapped Wilson loop spectrum [19]. Their Wannier obstruction can instead be observed in the spectrum of the nested Wilson loop.

2.2.2 Mirror Chern numbers

A general scheme to construct topological BZ invariants for systems protected by crystalline symmetries is the following: since a crystalline symmetry acts non-locally in space, it also maps different parts of the BZ onto each other. However,

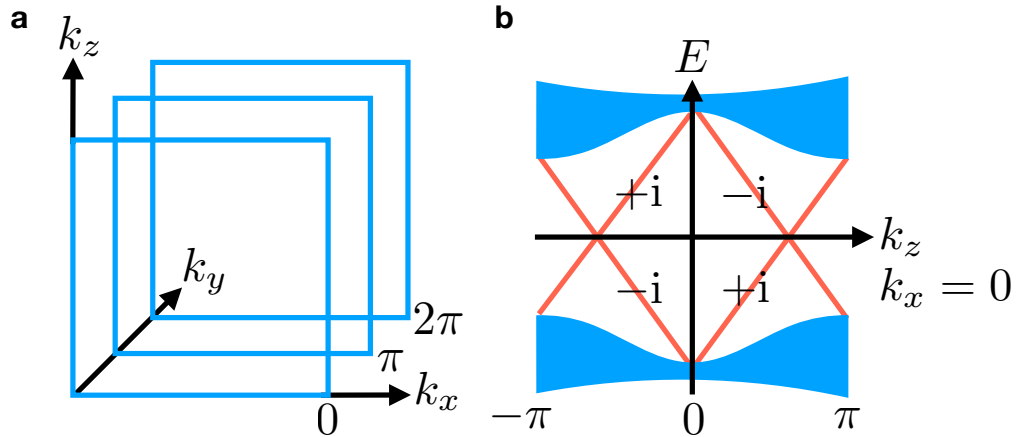


Figure 2.6: Mirror Chern planes in the BZ and schematic surface spectrum for a time-reversal topological crystalline insulator with $C_M = 2$. (a) For the mirror symmetry \mathcal{M} , there are two planes in the BZ which are left invariant by it and can therefore be used to define a mirror Chern number: the plane at $k_y = 0$ and the one at $k_y = \pi$. (b) A mirror Chern number $C_M = 2$ enforces the presence of two chiral left-movers and two chiral right-movers along mirror symmetric lines in the surface BZ of any surface mapped onto itself by the mirror symmetry. For \mathcal{M} , this is, e.g., the case for the surface obtained by terminating the bulk in x -direction and retaining k_y and k_z as momentum quantum numbers. At $k_y = 0$ all bands are eigenstates of the mirror symmetry with eigenvalues as shown, and thus prevented from gapping out. At finite k_y however, hybridization becomes possible and we are left with two Dirac cones in the surface BZ in the case at hand.

when there are submanifolds of the BZ which are left invariant by the action of the symmetry considered, we may evaluate a non-crystalline invariant on them, suited for the dimension and symmetry class of the corresponding submanifold, as long as we restrict ourselves to one of the symmetry's eigenspaces.

The most prominent example of this construction is the mirror Chern number C_M in three-dimensional systems. Since for a spinful system, mirror symmetry \mathcal{M} squares to $M^2 = -1$ its representation in this case has eigenvalues $\pm i$. Let Σ be a surface in the BZ which is left invariant under the action of \mathcal{M} , such as the surfaces shown in Figure 2.6 (a) for \mathcal{M} . Then, the eigenstates $|u_{\mathbf{k},n}\rangle$ of the Hamiltonian on Σ can be decomposed into two groups, $\{|u_{\mathbf{k},l}^+\rangle\}$ and $\{|u_{\mathbf{k},l}^-\rangle\}$, with mirror eigenvalues $+i$ and $-i$, respectively. Time-reversal symmetry maps one mirror subspace onto the other; if it is present, the two mirror eigenspaces are of the same dimension. We may define the Chern number in each mirror subspace as

$$C_{\pm} = -\frac{i}{2\pi} \int_{\Sigma} dk_x dk_z \text{Tr} [\mathcal{F}_{xz}^{\pm}(\mathbf{k})]. \quad (2.34)$$

Here

$$\mathcal{F}_{ab}^\pm(\mathbf{k}) = \partial_a \mathcal{A}_b^\pm(\mathbf{k}) - \partial_b \mathcal{A}_a^\pm(\mathbf{k}) + [\mathcal{A}_a^\pm(\mathbf{k}), \mathcal{A}_b^\pm(\mathbf{k})] \quad (2.35)$$

is the non-abelian Berry curvature field in the $\pm i$ mirror subspace, with $\mathcal{A}_{a,I,I'}^\pm(\mathbf{k}) = \langle u_{\mathbf{k},I}^\pm | \partial_a | u_{\mathbf{k},I'}^\pm \rangle$, and matrix multiplication is implied. Since $\text{Tr} [\mathcal{A}_a^\pm(\mathbf{k}), \mathcal{A}_b^\pm(\mathbf{k})] = 0$, this corresponds to Equation (2.24) restricted to a single mirror subspace. Note that in time-reversal symmetric systems we have $C_+ = -C_-$, and can thus define the mirror Chern number

$$C_M := (C_+ - C_-)/2. \quad (2.36)$$

A non-vanishing mirror Chern number implies that the Bloch Hamiltonian on Σ corresponds to a time-reversal pair of Chern insulators. Thus, the full model will host C_M Kramers pairs of gapless modes on an M -invariant line in any surface BZ corresponding to a real space boundary which is mapped onto itself under the mirror symmetry M . These Kramers pairs of modes will be generically gapped out away from the lines in the surface BZ which are invariant under the mirror symmetry, and therefore form surface Dirac cones. Indeed, when C_M is odd in a time-reversal symmetric system, this implies an odd number of Dirac cones in any surface BZ, since then the system realizes a conventional time-reversal invariant 3D TI with the Dirac cones located at time-reversal invariant surface momenta. When C_M is even, the surface Dirac cones exist only on mirror symmetric surfaces and are located at generic momenta along the mirror invariant lines of the surface BZ [see Figure 2.6 (b)]. This inherently crystalline case is realized in the band structure of tin telluride, SnTe [9].

A straightforward way to obtain a HOTI with hinge states is to start with a time-reversal symmetric TCI with nonzero mirror Chern number C_M , and cleave it along low-symmetry planes. Recall that a mirror Chern number induces gapless Dirac cones on all mirror-symmetric surfaces. Since mirror symmetry M protects these Dirac cones from gapping out, its matrix representation needs to anti-commute rather than commute with any Dirac mass. This implies that two surfaces which are not mirror symmetric themselves, but rather mapped to each other under M , have opposite Dirac masses and are joined together by a domain wall where the Dirac mass is zero. Along the domain wall (which lies in the mirror plane), the system is gapless and hosts $C_M/2$ helical hinge states (each Dirac cone contributes a chiral mode, two antipropagating chiral modes are paired to give a T -symmetric helical mode). As long as only generic (that is, not mirror-symmetric) surfaces terminations are chosen, any TCI with nonzero C_M has hinge states and qualifies as a HOTI (this argument is mathematically explicated in Section 3.2 of the thesis).

2.2.3 Symmetry indicators

The conceptually simplest topological invariants for TCIs are symmetry indicators [29, 14, 49, 30, 90, 91, 75]. They are inspired by the Fu-Kane formula [5], which relates the topological invariant of a TI to a product over the inversion eigenvalues of occupied Bloch eigenstates. Similar formulas of Fu-Kane type have been established for HOTIs [23]: For instance, when a HOTI protected by $\mathcal{C}_4\mathcal{T}$ symmetry is additionally invariant under \mathcal{IT} , the eigenvalues of the unitary combination $\mathcal{C}_4\mathcal{I}$ can be used to indicate nontrivial higher-order topology (see also Appendix A.3).

We now discuss the systematic construction of symmetry indicators. When the symmetries protecting the hinge modes of HOTIs are unitary, all occupied eigenstates at high-symmetry momenta can be labelled using their eigenvalues. In particular, given a symmetry \mathcal{S} that is realized on the Bloch Hamiltonian as $\mathcal{SH}(\mathbf{k})\mathcal{S}^\dagger = \mathcal{H}(S\mathbf{k})$, acting on the momenta as $\mathbf{k} \rightarrow S\mathbf{k}$, we can calculate its corresponding symmetry indicator topological invariants from the eigenvalues of the matrices

$$S_{mn} = \langle u_m(S\bar{\mathbf{k}}) | \mathcal{S} | u_n(\bar{\mathbf{k}}) \rangle, \quad (2.37)$$

where m, n run over the occupied subspace only and $\bar{\mathbf{k}} = S\bar{\mathbf{k}} + \mathbf{G}$ are high-symmetry points of the Brillouin zone that are left invariant by the symmetry \mathcal{S} , with \mathbf{G} a reciprocal lattice vector.

One can systematically enumerate the eigenvalue configurations that correspond to trivial atomic limits, the others then necessarily have to be topological. Of these, only a subclass correspond to HOTIs. The symmetry indicators that are compatible with a HOTI ground state can be found by matching the occupied symmetry eigenvalues of a few linearly independent reference models to the presence of hinge states in these models. Since both symmetry eigenvalues and hinge states form additive groups, all remaining configurations can then be analyzed by decomposition, allowing for the definition of indices that are linear in the occupation numbers of symmetry eigenvalues, and in correspondence with hinge states. A notable example is the \mathbb{Z}_4 index for nonmagnetic crystals with \mathcal{I} symmetry (see also the general discussion of \mathcal{I} -symmetric models in Section 2.3), which is proportional to sum of all occupied inversion eigenvalues and given by [30]

$$z_4 = \frac{1}{4} \sum_{\mathbf{k} \in \text{TRIMs}} (n_{\mathbf{k}}^+ - n_{\mathbf{k}}^-) \mod 4, \quad (2.38)$$

where $n_{\mathbf{k}}^+$ ($n_{\mathbf{k}}^-$) is the number of occupied eigenstates with inversion eigenvalue + (-) and TRIMs denotes the eight time-reversal invariant momenta in the Brillouin

zone. The index satisfies $z_4 = 2 \pmod{4}$ for a HOTI. Another import index is the \mathbb{Z}_8 index for nonmagnetic crystals with \mathcal{I} and C_4 symmetry, which satisfies $z_8 = 4 \pmod{8}$ for a HOTI [30, 91]. Although symmetry indicators are often more easily obtained than other topological invariants, one drawback is that they represent only necessary rather than sufficient conditions for the presence of hinge states. For instance, a nontrivial index $z_8 = 4 \pmod{8}$ could also be due to a nonzero mirror Chern number [92, 9] $C_M = 4$ rather than nontrivial second-order topology [91]. To uniquely identify a material as a HOTI, symmetry indicators therefore need to be supplemented by Wilson-loop or real-space calculations. Symmetry indicators are pedagogically reviewed in [93], and used extensively in Chapter 7 of this thesis.

2.2.4 Magnetoelectric polarization

One important class of magnetic (time-reversal breaking) TCIs are axion insulators, which are characterized by a quantized and non-vanishing magnetoelectric polarization that contributes to the effective action of an external electromagnetic field [26, 23, 25, 66, 43, 94, 62, 95, 49, 96, 97, 19, 98]. Expressed in electric and magnetic field components, the magnetoelectric polarization corresponds to the coefficient θ in an effective Lagrangian density of the form $\frac{\theta}{4\pi^2} \mathbf{E} \cdot \mathbf{B}$ (where the electric charge and the reduced Planck constant are set to unity $e = \hbar = 1$) [99], with θ given by the Brillouin zone integral

$$\theta = \frac{1}{4\pi} \int d\mathbf{k} \epsilon_{abc} \text{tr} \left[\mathcal{A}_a \partial_b \mathcal{A}_c + i \frac{2}{3} \mathcal{A}_a \mathcal{A}_b \mathcal{A}_c \right], \quad (2.39)$$

written in terms of the Berry gauge field $\mathcal{A}_{a;n,n'} = -i \langle u_n | \partial_a | u_{n'} \rangle$, where $|u_n\rangle$ are the Bloch eigenstates of the Bloch Hamiltonian, and n, n' are running over the occupied bands of the insulator. ∂_a is the partial derivative with respect to the momentum component k_a , $a = x, z, y$. The trace is performed with respect to band indices. Since the exponential of the electromagnetic action that appears in the path integral is invariant under the replacement $\theta \rightarrow \theta + 2\pi$ [100], a symmetry that invokes the sign switch $\theta \rightarrow -\theta$ quantizes θ to values $0, \pi$. The action stays invariant under a symmetry transformation, and so any such symmetry need also flip the sign of $\mathbf{E} \cdot \mathbf{B}$. Since \mathbf{E} is a vector that is even under time-reversal, and \mathbf{B} a pseudo-vector that is odd under time-reversal, this is for example the case for time-reversal \mathcal{T} or inversion \mathcal{I} symmetry, or combinations of rotational symmetries with inversion or time-reversal such as $C_n \mathcal{T}$ (see also Appendix A.2). In \mathcal{T} -symmetric systems, $\theta = \pi$ indicates a TI with gapless surface states. For all other symmetry classes, $\theta = \pi$ indicates a HOTI (an axion insulator) with chiral hinge states. This can be seen by noting that in this case a generic surface does not preserve the symmetry relevant

to the quantization of θ , and is therefore not subject to a symmetry impediment to becoming gapped. However, differently oriented surfaces are mapped to each other under the crystalline symmetry, and $\theta = \pi$ enforces their Hall conductivity to be quantized to $\pm 1/2$, with gapless domain walls between them at which the surface Hall conductivity switches sign. These domain walls bind hinge states, implying that axion insulators are HOTIs.

An alternative to calculate the magnetoelectric polarization via Equation (2.39) in $\mathcal{C}_4\mathcal{T}$ -symmetric systems is to use a generalized Pfaffian formula [101], akin to the original Pfaffian invariant of TIs. θ satisfies the relation

$$e^{i\theta} = \prod_{\mathbf{k} \in K^4} \frac{\text{Pf} M(\mathbf{k})}{\sqrt{\det B(\mathbf{k})}}, \quad (2.40)$$

with the sewing matrices

$$\begin{aligned} M_{mn}(\mathbf{k}) &= \langle u_m(\mathbf{k}) | \mathcal{C}_4\mathcal{T} + \mathcal{C}_4^{-1}\mathcal{T} | u_n(\mathbf{k}) \rangle / \sqrt{2} \\ B_{mn}(\mathbf{k}) &= \langle u_m(\mathcal{C}_4\mathcal{T}\mathbf{k}) | \mathcal{C}_4\mathcal{T} | u_n(\mathbf{k}) \rangle. \end{aligned} \quad (2.41)$$

This formula can be generalized to systems with $\mathcal{C}_3\mathcal{T}$ and \mathcal{IT} symmetry [101]. Note that both Equation (2.39) and Equation (2.40) require a smooth gauge of Bloch states $|u_m(\mathbf{k})\rangle$ for their numerical evaluation. Computationally efficient methods for calculating the magnetoelectric polarization without the need for a smooth gauge exist [102, 103, 98, 101].

2.3 Systematic construction of \mathcal{I} -symmetric topological phases

We conclude our overview of topological band theory with a unifying discussion of inversion-symmetric topological phases and their model Hamiltonians. Spatial inversion \mathcal{I} (which in d dimensions simply reverses all d coordinates and momenta) is the simplest symmetry that protects topological phases of any order. Here we discuss \mathcal{I} -symmetric first-order phases in 1D, 2D and 3D, while the remainder of the thesis will explore various aspects of higher-order topological phases protected by inversion or other crystalline symmetries. The elementary property $\mathcal{I}^2 = +1$ of the inversion operator implies that all eigenstates of inversion have eigenvalues ± 1 , giving rise to symmetry indicator invariants. This grading of eigenstates furthermore allows to introduce the notion of a band inversion as follows: the occupied Bloch states at high-symmetry points of the Brillouin carry inversion eigenvalues. The eigenvalue configurations belonging to all atomic limits can be enumerated. If

for a given ground state we need to exchange an eigenstate between the occupied and unoccupied subspace, with opposite inversion eigenvalues, in order to arrive at an (obstructed) atomic limit eigenvalue configuration, we speak of a band inversion. Similarly, n exchanges imply n band inversions. Only necessary exchanges are counted (for instance, swapping a state of eigenvalue $+1$ with one of eigenvalue -1 , and then reversing the exchange, amounts to zero band inversions rather than two). It follows from this definition that any ground state with a nonzero number of band inversions is topological (by which we mean that it cannot be adiabatically connected to an atomic limit).

2.3.1 Su-Schrieffer-Heeger model

We begin in one dimension, where the \mathcal{I} -symmetric SSH model introduced in Section 2.1.1.1 provides somewhat of a “hydrogen atom” system from which all models in higher dimensions can be derived (see Figure 2.7). For the choice of parameters $t \equiv M$ and $t' = -1$, its Bloch Hamiltonian [Equation (2.16)] can be recast as

$$\mathcal{H}(k) = (M - \cos k) \sigma_x + \sin k \sigma_y, \quad (2.42)$$

where σ_i , $i = 0, x, y, z$ are Pauli matrices indexing spinless valence s and conduction p orbitals in each unit cell. Inversion symmetry is represented by:

$$\mathcal{I} : \mathcal{H}(k) \rightarrow (-\sigma_x)\mathcal{H}(-k)(-\sigma_x). \quad (2.43)$$

At half-filling there is a single occupied band with the Bloch eigenstates $|u(k)\rangle$. At the two time-reversal symmetric momenta (TRIMs) $\bar{k} = 0, \pi$ of the 1D Brillouin zone, here defined by $\mathcal{I}\bar{k} = \bar{k}$ because \mathcal{T} symmetry is absent [104, 105], we can define the inversion eigenvalue $\lambda_{\bar{k}}$ of the occupied state $|u(\bar{k})\rangle$ as:

$$\mathcal{I}|u(\bar{k})\rangle = \lambda_{\bar{k}}|u(\bar{k})\rangle, \quad (2.44)$$

with $\lambda_{\bar{k}} = \pm 1$. For $|M| > 1$, the occupied subspace of Equation (2.42) is composed of a single band with equal inversion eigenvalues at both TRIM points. This corresponds to an atomic limit of s (for $M > 1$) or p (for $M < -1$) orbitals at the origin ($x = 0$) of each unit cell. In contrast, the regime $|M| < 1$ (which is separated by a gap closing at $|M| = 1$) has opposite occupied inversion eigenvalues at $k = 0$ and $k = \pi$, corresponding to an atomic limit of p orbitals at the boundary ($x = 1/2$) of each unit cell (we need to choose symmetric unit cells such that the positions $x = 0, 1/2$ are invariant under spatial inversion). (See Figure 2.7.) As both eigenvalue configurations are atomic limits, we find that there are no true inversion-protected topological insulators in 1D. In this sense, the 1D distinction

between trivial and topological that we previously employed, and which is often colloquially made use of in the literature, really refers to the distinction between two inequivalent atomic limits.

2.3.2 Chern insulator

We previously described how the 2D Chern insulator can be constructed from the 1D SSH model by a tuning procedure in Section 2.1.2.1. Here we analyze the so obtained model from the point of view of inversion symmetry.

Introducing the parameter M , the Bloch Hamiltonian in Equation (2.32) can be recast as

$$\mathcal{H}(\mathbf{k}) = (M - \cos k_x - \cos k_y) \sigma_x + \sin k_x \sigma_y + \sin k_y \sigma_z, \quad (2.45)$$

Inversion symmetry is represented by:

$$\mathcal{I} : \mathcal{H}(\mathbf{k}) \rightarrow (-\sigma_x)\mathcal{H}(-\mathbf{k})(-\sigma_x). \quad (2.46)$$

At half-filling there is a single occupied band. At the four TRIMs

$$\bar{\mathbf{k}} = (0, 0), (0, \pi), (\pi, 0), (\pi, \pi) \quad (2.47)$$

of the 2D Brillouin zone, we can again define inversion eigenvalues $\lambda_{\bar{\mathbf{k}}}$ similar to Equation (2.44). We see that the $C = 1$ Chern insulator phase $|M| < 2$ is characterized by a single band inversion at $\bar{\mathbf{k}} = (0, 0)$: there is no atomic limit that gives rise to the same configuration of \mathcal{I} eigenvalues (it can be easily confirmed that any atomic limit necessarily has an even number of negative \mathcal{I} eigenvalues), but upon flipping the sign of the \mathcal{I} eigenvalue at $\bar{\mathbf{k}} = (0, 0)$ we obtain an atomic limit of s orbitals at the origin of each unit cell. (See Figure 2.7.) The Chern insulator therefore represents a topological phase that is not Wannierizable. In fact, we know from the discussion in Section 2.1.2.1 that a Chern number does not require \mathcal{I} symmetry to stay quantized, however, \mathcal{I} symmetry allows to constrain the \mathbb{Z} -valued Chern number C via the formula

$$(-1)^C = \prod_{\bar{\mathbf{k}} \in \text{TRIMs}} \lambda_{\bar{\mathbf{k}}}, \quad (2.48)$$

which is computationally easier to evaluate than the Brillouin zone integral in Equation (2.24).

2.3.3 2D topological insulator

As discussed in Section 2.1.1.3, the 2D topological insulator can be constructed by TRS doubling the Chern insulator. Starting from Equation (2.45), we arrive at the Bloch Hamiltonian

$$\mathcal{H}(\mathbf{k}) = (M - \cos k_x - \cos k_y) \tau_z \sigma_x + \sin k_x \tau_z \sigma_y + \sin k_y \tau_z \sigma_z, \quad (2.49)$$

where τ_i , $i = 0, x, y, z$ are an additional set of Pauli matrices indexing physical spin in each unit cell, and we have abbreviated the Kronecker product $\tau_i \otimes \sigma_j$ by $\tau_i \sigma_j$. Inversion \mathcal{I} and time-reversal symmetry \mathcal{T} are represented by:

$$\begin{aligned} \mathcal{I} : \mathcal{H}(\mathbf{k}) &\rightarrow (-\tau_z \sigma_x) \mathcal{H}(-\mathbf{k}) (-\tau_z \sigma_x), \\ \mathcal{T} : \mathcal{H}(\mathbf{k}) &\rightarrow \tau_y \sigma_z \mathcal{H}^*(-\mathbf{k}) \tau_y \sigma_z. \end{aligned} \quad (2.50)$$

(Recall that \mathcal{T} is anti-unitary.) At half-filling there are two occupied bands with the Bloch eigenstates $|u^n(\mathbf{k})\rangle$, $n = 1, 2$. At the four TRIMs of the 2D Brillouin zone, we can define the inversion eigenvalue $\lambda_{\bar{\mathbf{k}}}$ of the occupied Kramers pair $\{|u^1(\bar{\mathbf{k}})\rangle, |u^2(\bar{\mathbf{k}})\rangle\}$ as:

$$\mathcal{I} |u^1(\bar{\mathbf{k}})\rangle = \lambda_{\bar{\mathbf{k}}} |u^1(\bar{\mathbf{k}})\rangle, \quad (2.51)$$

At each TRIM point, states appear in Kramers pairs with the same inversion (\mathcal{I}) eigenvalues, because the eigenvalues of \mathcal{I} are real ($\lambda_{\bar{\mathbf{k}}} = \pm 1$). For systems with TRS, it is conventional to slightly modify the notion of band inversion so that it refers to inverting Kramers pairs of states instead of individual states. In this sense, the topological insulator phase $|M| < 2$ is again characterized by a single band inversion [occurring at $\bar{\mathbf{k}} = (0, 0)$ for the model at hand] from an atomic limit. (See Figure 2.7.) In fact, the Fu-Kane symmetry indicator formula [5] mentioned in Section simply states that the \mathbb{Z}_2 invariant of topological insulators $\Delta_{2D} = 0, 1$ is given by the product over all occupied inversion eigenvalues:

$$(-1)^{\Delta_{2D}} = \prod_{\bar{\mathbf{k}} \in \text{TRIMs}} \lambda_{\bar{\mathbf{k}}}. \quad (2.52)$$

In 2D, inversion symmetry does not refine the \mathbb{Z}_2 classification of TRS topological insulators: it can be easily confirmed that two consecutive band inversions bring the system back to an (obstructed) atomic limit.

2.3.4 3D topological insulator

We explained in Section 2.1.2.2 how the 3D topological insulator (TI) can be constructed by tuning its 2D counterpart from topological to trivial along the z -direction. Starting from Equation (2.49), this tuning is achieved by the Bloch

Hamiltonian

$$\begin{aligned}\mathcal{H}(\mathbf{k}) = & (M - \cos k_x - \cos k_y - \cos k_z) \tau_z \sigma_x \\ & + \sin k_x \tau_z \sigma_y + \sin k_y \tau_z \sigma_z + \sin k_z \tau_x \sigma_0,\end{aligned}\quad (2.53)$$

Inversion \mathcal{I} and time-reversal symmetry \mathcal{T} are represented just as in Equation (2.50). At each of the eight TRIM point of the 3D BZ, given by

$$\bar{\mathbf{k}} = (0, 0, 0), (0, \pi, 0), (\pi, 0, 0), (\pi, \pi, 0), (0, 0, \pi), (0, \pi, \pi), (\pi, 0, \pi), (\pi, \pi, \pi), \quad (2.54)$$

we may again define inversion eigenvalues of Kramers pairs as in Equation (2.51). The TI parameter regime $1 < |M| < 3$ is then characterized by a single band inversion at $\bar{\mathbf{k}} = (0, 0, 0)$ with respect to an atomic limit of spinful s orbitals at the origin $x = (0, 0, 0)$ of the 3D unit cell. (See Figure 2.7.) In straightforward generalization of the Fu-Kane formula for 2D topological insulators, the 3D \mathbb{Z}_2 -valued TI invariant $\Delta = 0, 1$ is given by the product over all occupied inversion eigenvalues:

$$(-1)^\Delta = \prod_{\bar{\mathbf{k}} \in \text{TRIMs}} \lambda_{\bar{\mathbf{k}}}. \quad (2.55)$$

To conclude, we have shown that the 3D and 2D topological insulators, as well as the 2D Chern insulator with $C = 1$, can be obtained by a single (Kramers-paired with TRS) band inversion from atomic limit ground states. At the same time, the 1D SSH model realizes two inequivalent atomic limits that are related to each other by exchanging the occupied and unoccupied inversion eigenvalues at one TRIM. We have provided explicit model Hamiltonians for all of these phases by straightforwardly generalizing the SSH eigenvalue exchange, captured by Equation (2.42), to induce band inversions in higher-dimensional systems (possibly with TRS), and were thus able to explicitly construct some of the most relevant first-order topological phases by tuning and TRS doubling procedures.

However, inversion symmetry not only provides a convenient framework for tracking band inversions and thereby diagnosing known topological phases. More interestingly, it refines the \mathbb{Z}_2 classification of 3D TRS topological insulators: For instance, two consecutive band inversions at the same TRIM point $\bar{\mathbf{k}} = (0, 0, 0)$, which naively seem to give a trivial TI invariant $\Delta = 0$, cannot be identified with any 3D atomic limit [30]. Instead, they yield a higher-order topological insulator that is diagnosed by the inversion symmetry indicator z_4 of Equation (2.38). HOTIs, which are therefore characterized by a *double band inversion*, are extensively studied in the remainder of this thesis.

We close by noting that not only the bulk topology, but also the boundary physics can be deduced from the tuning and (TRS) doubling picture developed in this

section and illustrated in Figure 2.7. For this perspective, it is useful to consider a semi-infinite slab geometry that is open in one spatial direction (for instance, with one end at $x = 0$, and the other end infinitely far away) but closed and periodic in all other directions, retaining the respective good momentum quantum numbers. The chiral edge state of a $C = 1$ Chern insulator along the edge with normal in x -direction is then obtained from the zero-dimensional end state of the SSH model, which linearly disperses with k_y as the topological-to-trivial tuning of the SSH model along k_y induces a spectral flow between conduction and valence bands: To be explicit, consider the Chern insulator of Section 2.3.2, which we built by tuning a SSH model from its topological limit (at $k_y = 0$) to its trivial one (at $k_y = \pi$). Without loss of generality, let us assume that there are no edge potentials so that the zero-dimensional SSH end state at $k_y = 0$ is also a zero-energy state. Knowing that $k_y = \pi$ is trivial, this end state has to continuously move into either the valence or conductance band manifold as k_y is tuned from 0 to π . Furthermore, it has to connect valence and conductance bands as we tune k_y from $-\pi$ to π , since our tuning Hamiltonian [Equation (2.45)] enjoys the spectral symmetry $\mathcal{H}(k_x, k_y) = -\sigma_3 \mathcal{H}(k_x, -k_y) \sigma_3$. Note that this derivation closely mirrors that of the Wilson loop spectrum of the Chern insulator presented in Section 2.1.2.1.

Similarly, the helical edge states of the 2D topological insulator are simply two TRS-related copies of the chiral Chern insulator edge state, which avoid hybridization at the edge BZ TRIMs (specifically, at $k_y = 0$ in the example above) due to the Kramers theorem. In close correspondence to how we derived the Wilson loop spectrum of a 3D TI from that of a 2D topological insulator in Section 2.1.2.2, the 3D TI surface states are then readily seen to have a Dirac cone dispersion.

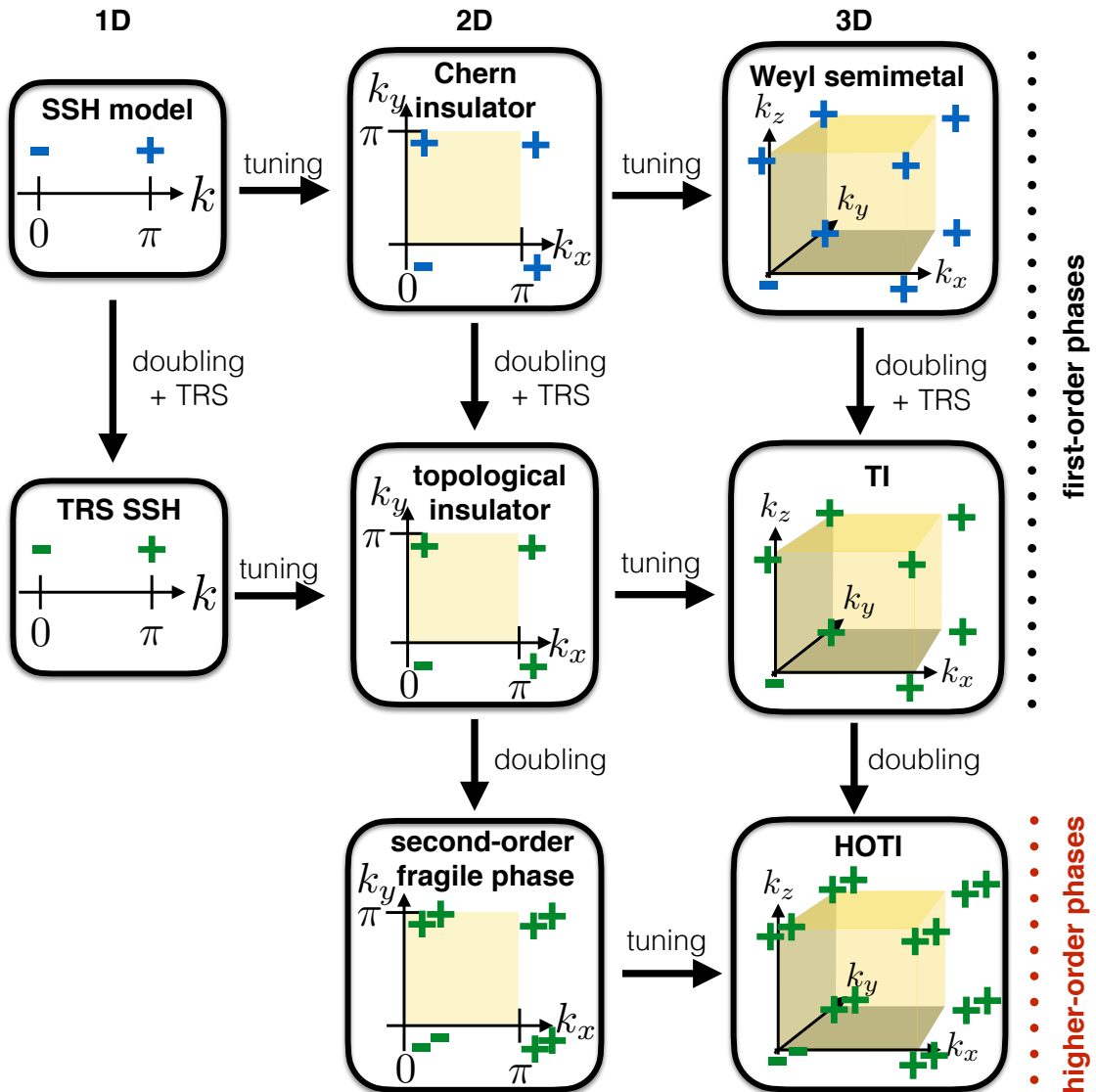


Figure 2.7: Overview of inversion-symmetric topological phases. For each phase, we show the Brillouin zone with the occupied inversion eigenvalues at all TRIMs (single eigenstates are shown in blue, and Kramers pairs are shown in green). All phases can be obtained by starting with the inversion-symmetric 1D SSH model and successively tuning (from topological to trivial parameter regimes along a transverse momentum coordinate) and doubling (by stacking copies, effectively forming the tensor sum of two copies of the original Hamiltonian, and possibly imposing TRS). The TRS SSH model and the second-order fragile phase, which features midgap corner states in open rectangular geometries, are treated in Chapter 5. Weyl semimetals are gapless and are not discussed in this thesis. By directly doubling Chern insulators and Weyl semimetals without imposing TRS, we obtain the TRS broken versions of second-order fragile phase and HOTI, respectively (not shown). The TRS-broken HOTI is an axion insulator.

List of publications

Publications discussed in this thesis:

Chapter 3: F. Schindler, A. M. Cook, M. G. Vergniory, Z.J. Wang, S. S. P. Parkin, B. A. Bernevig, T. Neupert: **Higher-order topological insulators**, Science Advances Vol. 4, no. 6, eaat0346 (2018)

Author contributions: F.S., A.M.C., B.A.B., and T.N. conceived the project and worked out the theoretical results, M.G.V. and Z.W. performed first-principles calculations, and S.S.P.P. contributed the experimental proposal for SnTe nanowires.

Chapter 4: F. Schindler, Z. J. Wang, M. G. Vergniory, A. M. Cook, A. Murani, S. Sengupta, A. Y. Kasumov, R. Deblock, S. Jeon, I. Drozdov, H. Bouchiat, S. Guéron, A. Yazdani, B. A. Bernevig, T. Neupert: **Higher-order topology in bismuth**, Nature Physics 14, 918–924 (2018)

Author contributions: F.S., A.M.C., B.A.B. and T.N. carried out the theoretical analysis and model calculations. Z.W. and M.G.V. performed the first-principles calculations and topological quantum chemistry analysis. A.M., S.S., A.Y.K., R.D., H.B., and S.G. conceived and carried out the transport experiments and crystal growth. S.J., I.D. and A.Y. conceived and carried out the STM experiments.

Chapter 6: S. Imhof, C. Berger, F. Bayer, J. Brehm, L. Molenkamp, T. Kiessling, F. Schindler, C. H. Lee, M. Greiter, T. Neupert, R. Thomale: **Topoelectrical circuit realization of topological corner modes**, Nature Physics 14, 925–929 (2018)

Author contributions: F.S., C.H.L., M.G., T.N., and R.T. conceived the project and developed the mapping from a Bloch Hamiltonian to topological circuitry. S.I., T.K., and F.S. performed numerical simulations. S.I., C.B., F.B., J.B., L.M., and T.K. were responsible for circuit implementation and measurements.

Chapter 7: F. Schindler, M. Brzezińska, W. A. Benalcazar, M. Iraola, A. Bouhon, S. S. Tsirkin, M. G. Vergniory, T. Neupert: **Fractional corner charges in spin-orbit coupled crystals**, Phys. Rev. Research 1, 033074 (2019)

Author contributions: F.S., M.B., W.A.B., A.B., and T.N. conceived the project and worked out the theoretical results, M.I., S.S.T., and M.G.V. performed first-principles calculations.

Chapter 8: F. Schindler, B. Bradlyn, M. H. Fischer, T. Neupert: **Pairing Obstructions in Topological Superconductors**, Phys. Rev. Letters (2020)

Author contributions: F.S., B.B., M.H.F., and T.N. conceived the project and worked out the theoretical results.

Chapter 9: T. Neupert, F. Schindler: **Lecture notes on topological crystalline insulators**, Springer Series in Solid-State Sciences, vol 190 (2018)

Author contributions: T.N. and F.S. worked out the theoretical results.

Further publications:

F. Schindler, A. S. Jermyn: **Algorithms for Tensor Network Contraction Ordering**, Machine Learning: Science and Technology (2020)

T. Hofmann, T. Helbig, F. Schindler, N. Salgo, M. Brzezińska, M. Greiter, T. Kiessling, D. Wolf, A. Vollhardt, A. Kabaši, C. H. Lee, A. Bilušić, R. Thomale, T. Neupert: **Reciprocal skin effect and its realization in a topoelectrical circuit**, Phys. Rev. Research 2, 023265 (2020)

B. Wan, F. Schindler, K. Wang, K. Wu, X. Wan, T. Neupert and H.-Z. Lu: **Theory for the negative longitudinal magnetoresistance in the quantum limit of Kramers Weyl semimetals**, Journal of Physics: Condensed Matter, Vol. 30, No. 50 (2018)

E. V. H. Doggen, F. Schindler, K. S. Tikhonov, A. D. Mirlin, T. Neupert, D. G. Polyakov, I. V. Gornyi: **Many-body localization and delocalization in large quantum chains**, Phys. Rev. B 98, 174202 (2018)

G. Chang, B. J. Wieder, F. Schindler, D. S. Sanchez, I. Belopolski, S.-M. Huang, B. Singh, D. Wu, T.-R. Chang, T. Neupert, S.-Y. Xu, H. Lin, M. Zahid Hasan: **Topological quantum properties of chiral crystals**, Nature Materials 17, 978-985 (2018)

L. Das, F. Forte, R. Fittipaldi, C. G. Fatuzzo, V. Granata, O. Ivashko, M. Horio, F. Schindler, M. Dantz, Y. Tseng, D. McNally, H. M. Rønnow, W. Wan, N. B. Christensen, J. Pelliciari, P. Olalde-Velasco, N. Kikugawa, T. Neupert, A. Vecchione, T. Schmitt, M. Cuoco, J. Chang: **Spin-orbital excitations in Ca₂RuO₄ revealed by resonant inelastic x-ray scattering**, Phys. Rev. X 8, 011048 (2018)

W.-L. Tu, F. Schindler, T. Neupert, D. Poilblanc: **Competing orders in the Hofstadter t-J model**, Phys. Rev. B 97, 035154 (2018)

C.-L. Zhang, F. Schindler, H. Liu, T.-R. Chang, S.-Y. Xu, G. Chang, W. Hua, H. Jiang, Z. Yuan, J. Sun, H.-T. Jeng, H.-Z. Lu, H. Lin, M. Z. Hasan, X. C. Xie, T. Neupert, and S. Jia: **Ultraquantum magnetoresistance in the Kramers-Weyl semimetal candidate β -Ag₂Se**, Phys. Rev. B 96, 165148 (2017)

F. Schindler, N. Regnault, T. Neupert: **Probing many-body localization with neural networks**, Phys. Rev. B 95, 245134 (2017)

Part II

Core concepts

Chapter 3

Theory of higher-order topological insulators

In this chapter, we present a more in-depth treatment of HOTIs than that of Chapter 1, discussing both time-reversal breaking and time-reversal preserving instantiations.

The topological properties of HOTIs are protected by symmetries that involve spatial transformations, possibly augmented by time reversal. They thus generalize topological crystalline insulators [8, 9], which have been encompassed in a recent exhaustive classification of topological insulators in Reference [14]. In this chapter, we treat two cases: (1) *chiral* HOTIs with hinge modes that propagate unidirectionally, akin to the edge states of a 2D quantum Hall effect [106], or Chern insulator [107]. We show that chiral HOTIs may be protected by the product $\mathcal{C}_4\mathcal{T}$ of time reversal \mathcal{T} and a \mathcal{C}_4 rotation symmetry. The existence of these hinge modes – but not the direction in which they propagate – is determined by the topology of the 3D bulk. By a $\mathcal{C}_4\mathcal{T}$ -respecting surface manipulation, the direction of all hinge modes can be reversed, but they cannot be removed. This constitutes a bulk \mathbb{Z}_2 topological classification. We also show that chiral HOTIs may have a bulk \mathbb{Z} topological classification protected by mirror symmetries which leave the hinges invariant when time reversal symmetry \mathcal{T} is broken. (2) *helical* HOTIs with Kramers pairs of counter-propagating hinge modes, akin to the edge states of a 2D quantum spin Hall effect [108, 109, 110, 111]. We show that helical HOTIs may occur when a system is invariant under time reversal \mathcal{T} and a \mathcal{C}_4 rotation symmetry. We further show that helical HOTIs can also be protected by \mathcal{T} and mirror symmetries which leave the hinges invariant. Any integer number of Kramers pairs is

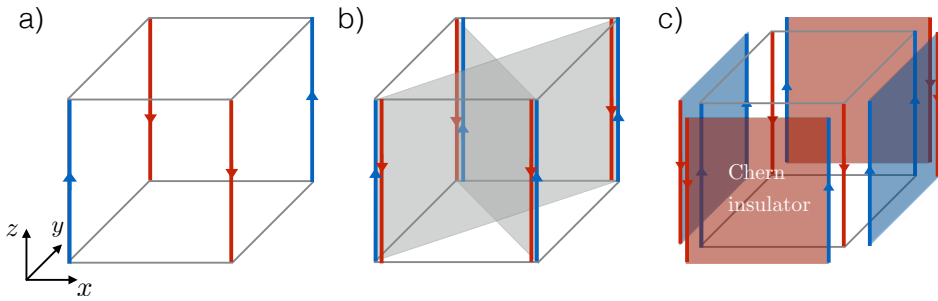


Figure 3.1: Topologically protected hinge excitations of second-order 3D TIs. (a) Time-reversal breaking model with chiral hinge currents running along the corners of a C_4^z -preserving bulk termination, were periodic boundary conditions in z -direction are assumed. (b) Time-reversal invariant model with anti-propagating Kramers pairs of hinge modes. Highlighted in gray are the planes invariant under the mirror symmetries M_{xy} and $M_{x\bar{y}}$ that protect the hinge states. (c) By supplementing each surface of the chiral HOTI in (a) with a Chern insulator with Hall conductivity $\sigma_{xy} = \pm e^2/h$, the number of chiral hinge modes can be changed by 2. The Hall conductivities of the additional Chern insulator layers alternate (blue for $+e^2/h$, red for $-e^2/h$) to comply with the $C_4^z T$ symmetry. The topology is therefore \mathbb{Z}_2 classified.

topologically protected against symmetry preserving surface manipulations, yielding a \mathbb{Z} classification.

For both cases, we show the topological bulk-surface-hinge correspondence, provide concrete lattice-model realizations, and provide expressions for the bulk topological invariants. The latter are given by the magnetoelectric polarization (Section 2.2.4) and mirror Chern numbers (Section 2.2.2), for chiral and helical HOTIs, respectively. For the case where a chiral HOTI also respects the product of inversion times time-reversal symmetry IT , we formulate a simplified topological index akin to the Fu-Kane formula for inversion symmetric TIs [1]. Finally, on the basis of tight-binding and ab-initio calculations, we explain how SnTe serves as a material realization for helical HOTIs. We also detail an explicit experimental setup to cleanly create hinge states in a topological SnTe coaxial cable. Chiral HOTIs, in contrast, may arise in 3D TI materials that exhibit noncollinear antiferromagnetic order at low temperatures.

3.1 Chiral higher-order topological insulator

We first give an intuitive argument for the topological nature of a chiral 3D HOTI. We consider a hypothetical but realizable electronic structure where gapless degrees of freedom are only found on the hinge. For concreteness, let us consider a system

with a square cross-section, periodic boundary conditions in z -direction and $\mathcal{C}_4^z\mathcal{T}$ symmetry that has a single chiral mode at each hinge, as sketched in Figure 6.1 (a). For these modes to be a feature associated with the 3D bulk topology of the system, they should be protected against any $\mathcal{C}_4^z\mathcal{T}$ preserving *surface* or *hinge* perturbation of the system. The minimal relevant surface perturbation of that kind is the addition of an integer quantum Hall (or Chern insulator) layer with Hall conductivity $\sigma_{xy} = e^2/h$ and $\sigma_{xy} = -e^2/h$ on the (100) surfaces and the (010) surfaces, respectively, which respects $\mathcal{C}_4^z\mathcal{T}$. As seen from Figure 6.1 (c), this adds to each hinge *two* chiral hinge channels. Repeating this procedure, we can change—via a pure surface manipulation—the number of chiral channels on each hinge by any even number. Hence, only the \mathbb{Z}_2 *parity* of hinge channels can be a topological property protected by the system's 3D bulk.

A concrete model of this phase is defined via the four-band Bloch Hamiltonian

$$\begin{aligned}\mathcal{H}_c(\mathbf{k}) = & \left(M + t \sum_i \cos k_i \right) \tau_z \sigma_0 + \Delta_1 \sum_i \sin k_i \tau_x \sigma_i \\ & + \Delta_2 (\cos k_x - \cos k_y) \tau_y \sigma_0,\end{aligned}\quad (3.1)$$

where σ_i and τ_i , $i = x, y, z$, are the three Pauli matrices acting on spin and orbital degree of freedoms, respectively (see Appendix A.1 for a real space representation of the model). For $\Delta_2 = 0$, $\mathcal{H}_c(\mathbf{k})$ represents the well-known 3D TI if $1 < |M| < 3$. Time-reversal symmetry is represented by $\mathcal{T}\mathcal{H}_c(\mathbf{k})\mathcal{T}^{-1} = \mathcal{H}_c(-\mathbf{k})$, with $\mathcal{T} \equiv \tau_0 \sigma_y K$, where K denotes complex conjugation. For $\Delta_2 = 0$, Hamiltonian (3.1) has a \mathcal{C}_4^z rotation symmetry $\mathcal{C}_4^z \mathcal{H}_c(\mathbf{k}) (\mathcal{C}_4^z)^{-1} = \mathcal{H}_c(D_{\mathcal{C}_4^z} \mathbf{k})$, where $\mathcal{C}_4^z \equiv \tau_0 e^{-i\frac{\pi}{4}\sigma_z}$ and $D_{\mathcal{C}_4^z} \mathbf{k} = (-k_y, k_x, k_z)$.

The term proportional to Δ_2 breaks both \mathcal{T} and \mathcal{C}_4^z individually, but respects the anti-unitary combination $\mathcal{C}_4^z\mathcal{T}$, which means that

$$\begin{aligned}(\mathcal{C}_4^z\mathcal{T}) \mathcal{H}_c(\mathbf{k}) (\mathcal{C}_4^z\mathcal{T})^{-1} &= \mathcal{H}_c(D_{\mathcal{C}_4^z\mathcal{T}} \mathbf{k}), \\ D_{\mathcal{C}_4^z\mathcal{T}} \mathbf{k} &= (k_y, -k_x, -k_z)\end{aligned}\quad (3.2)$$

is a symmetry of the Hamiltonian also when $\Delta_2 \neq 0$. Since $[\mathcal{C}_4^z, \mathcal{T}] = 0$, we have $(\mathcal{C}_4^z\mathcal{T})^4 = -1$, independent of the choice of representation.

The phase diagram of Hamiltonian (3.1) is shown in Figure 3.2 (a). For $1 < |M/t| < 3$ and $\Delta_1, \Delta_2 \neq 0$ the system is a chiral 3D HOTI. The spectrum in the case of open boundary conditions in x and y directions is presented in Figure 3.2 (c), where the chiral hinge modes (each 2-fold degenerate) are seen to traverse the bulk gap. Physically, the term multiplied by Δ_2 corresponds to orbital currents that break TRS oppositely in the x and y -directions. When infinitesimally small, its main effect

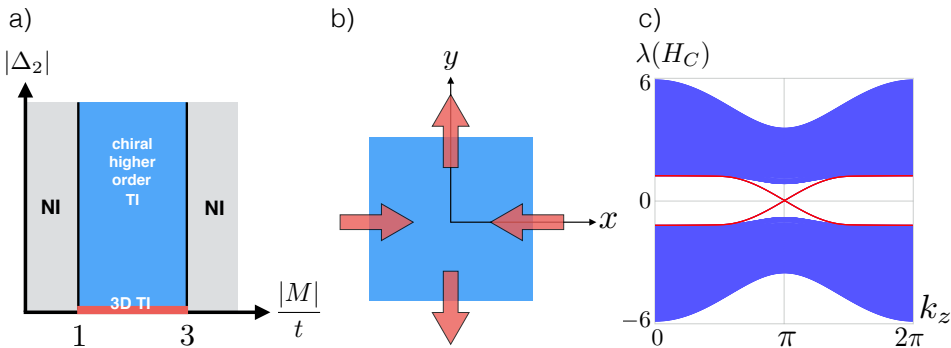


Figure 3.2: (a) Schematic phase diagram for model (3.1), where NI stands for normal insulator. (b) A unit cell of noncollinear magnetic order with $C_4^z\mathcal{T}$ symmetry. (c) Energy spectrum of model (3.1) with chiral hinge currents (red) in the geometry of Figure 6.1 (a). For a slab geometry, where the bulk is terminated in just one direction of space, there are in general no gapless modes.

is thus to open gaps with alternating signs for the surface Dirac electrons of the 3D TI (derived in Section 2.1.2.2) on the (100) and (010) surfaces. The four hinges are then domain walls at which the Dirac mass changes sign. It is well known [112, 113, 42, 94] that such a domain wall on the surface of a 3D TI binds a gapless chiral mode, which in the case at hand is reinterpreted as the hinge mode of the HOTI. [Another physical mechanism that breaks time-reversal symmetry and preserves $C_4^z\mathcal{T}$ would be $(\pi, \pi, 0)$ noncollinear antiferromagnetic order with a unit cell as shown in Figure 3.2 (b).] Note that even with finite Δ_2 , the (001) surface of the model remains gapless, since its Dirac cone is protected by the $C_4^z\mathcal{T}$ symmetry which leaves the surface invariant and enforces a Kramers-like degeneracy discussed in the Appendix. The gapless nature of the (001) surface in the geometry of Figure 6.1 is also required by current conservation, because the chiral hinge currents cannot terminate in a gapped region of the sample.

We turn to the bulk topological invariant that describes the \mathbb{Z}_2 topology. The topological invariant of 3D TIs is the theta angle, or magnetoelectric polarization θ (see Section 2.2.4), which is quantized by time-reversal symmetry to be $\theta = 0, \pi \bmod 2\pi$, with $\theta = \pi$ being the nontrivial case [114]. In fact, the very same quantity θ is the topological invariant of chiral HOTIs. What changes is that its quantization to values $0, \pi$ is not enforced by \mathcal{T} but by $C_4\mathcal{T}$ symmetry in this case. θ attains a new meaning in the second-order picture: it uniquely characterizes a different symmetry-protected topological phase which exhibits \mathcal{T} breaking, but $C_4\mathcal{T}$ preserving hinge currents instead of \mathcal{T} preserving gapless surface excitations. In the Appendix, Section A.2, we show the quantization of θ enforced by $C_4\mathcal{T}$ symmetry and explicitly evaluate $\theta = \pi$ for the model (3.1). We furthermore note that for a

nontrivial θ in the presence of $\mathcal{C}_4\mathcal{T}$ symmetry to uniquely characterize the presence of gapless hinge excitations, the bulk *and* the surfaces of the material which adjoin the hinge are required to be insulating. This constitutes the *bulk-surface-hinge* correspondence of chiral HOTIs.

The explicit evaluation of θ is impractical for ab-initio computations in generic insulators. This motivates the discussion of alternative forms of the topological invariant. The Pfaffian invariant [108, 115] used to define first-order 3D TIs rests on the group relation $\mathcal{T}^2 = -1$, it fails in our case where $(\mathcal{C}_4\mathcal{T})^4 = -1$. We may instead use a non-Abelian Wilson loop characterization of the topology, as discussed in Section 2.2.1 and rigorously detailed in Appendix A. There, we also discuss two further topological characterizations, one based on nested Wilson loop [86] and entanglement spectra [116, 117, 118], and one applicable to systems that are in addition invariant under the product \mathcal{IT} of inversion symmetry \mathcal{I} and \mathcal{T} [5].

3.2 Helical higher-order topological insulator

Helical higher-order TIs feature Kramers pairs of counter-propagating hinge modes. They are protected by time-reversal symmetry and a spatial symmetry. For concreteness, let us consider a system with a square (or rhombic) cross-section, periodic boundary conditions in z -direction, and two mirror symmetries \mathcal{M}_{xy} and $\mathcal{M}_{x\bar{y}}$ that leave, respectively, the $x = -y$ and the $x = y$ planes invariant, and with it a pair of hinges each [sketched in Figure 6.1 (b)]. We consider a hypothetical but realizable electronic structure where gapless degrees of freedom are only found on the hinge. At a given hinge, for instance one that is invariant under \mathcal{M}_{xy} , we can choose all hinge modes as eigenstates of \mathcal{M}_{xy} . We denote the number of modes that propagate parallel, R, (antiparallel, L) to the z direction and have \mathcal{M}_{xy} eigenvalue $i\lambda$, $\lambda = \pm 1$, by $N_{R,\lambda}$ ($N_{L,\lambda}$). We argue that the net number of helical hinge pairs $n \equiv N_{R,+} - N_{L,+}$ (which by time-reversal symmetry is equal to $N_{L,-} - N_{R,-}$) is topologically protected. In particular, n cannot be changed by any *surface or hinge* manipulation that respects both \mathcal{T} and \mathcal{M}_{xy} . First note that if both $N_{R,+}$ and $N_{L,+}$ are nonzero (assuming from now on that $N_{R,+} > N_{R,-}$), we can always hybridize $N_{L,+}$ right-moving modes with all $N_{L,+}$ left-moving modes within the $\lambda = +$ subspace without breaking any symmetry. Therefore, only the difference n is well defined and corresponds to the number of remaining pairs of modes.

The argument for their topological protection proceeds similar to the chiral HOTI case by considering a minimal symmetry-preserving surface perturbation. It consists of a layer of a 2D time-reversal symmetric TI and its mirror-conjugated partner added to surfaces that border the hinge under consideration. Each of the TIs

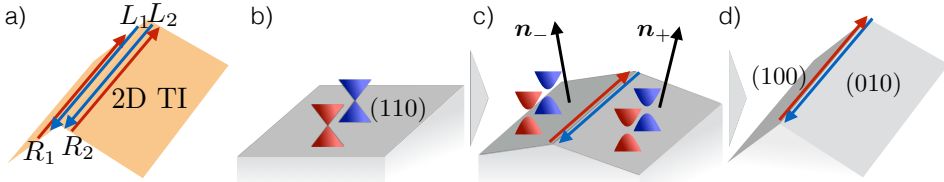


Figure 3.3: Bulk-surface-hinge correspondence of helical HOTIs. (a) Additional hinge modes obtained by decorating the surfaces with 2D time-reversal symmetric TIs in a mirror-symmetric fashion. They can always be combined in ‘bonding’ and ‘anti-bonding’ pairs $\{R_1+R_2, L_1+L_2\}$ and $\{R_1-R_2, L_1-L_2\}$, with mirror eigenvalues $+i$ and $-i$, respectively. Therefore, they do not change the net mirror chirality of the hinge. (b) Mirror-symmetry protected Dirac cones on a (110) surface. (c) Slightly tilting the surface normal out of the mirror plane gaps the Dirac cones and forms a Kramers pair of domain wall states between two surfaces with opposite tilting. The mirror eigenvalues of the hinge modes are tied to those of the Dirac cones, which in turn are related to a bulk topological invariant, the mirror Chern number C_M . (d) Further deforming the surface to the (100) and (010) orientation in a mirror-symmetry preserving manner does not change this correspondence.

contributes a single Kramers pair of boundary modes to the hinge so that $(N_{L,-} + N_{L,+})$ and $(N_{R,-} + N_{R,+})$ each increase by 2 [see Figure 3.3 (a)]. Since mirror symmetry maps the right-moving modes of the two Kramers pairs onto one another (and the same for the two left-moving modes) we can form a ‘bonding’ and ‘anti-bonding’ superposition with mirror eigenvalues $+i$ and $-i$ out of each pair. Thus each of $N_{L,+}$, $N_{L,-}$, $N_{R,+}$, and $N_{R,-}$ increase by 1 due to this minimal surface manipulation. This leaves n invariant, suggesting a \mathbb{Z} classification of the helical HOTI for each pair of mirror-invariant hinges. The case depicted in Figure 6.1 (b) with two mirror symmetries is then $\mathbb{Z} \times \mathbb{Z}$ classified. A more rigorous version of this argument can be found in the Appendix.

The topological invariant for the $\mathbb{Z} \times \mathbb{Z}$ classification of the helical HOTI is the set of mirror Chern numbers [92, 9] $C_M/2$ on the \mathcal{M}_{xy} and $\mathcal{M}_{x\bar{y}}$ mirror planes (see Section 2.2.2 for the definition of C_M). First observe that if C_M were odd, the system would be a strong 3D TI: the \mathcal{M}_{xy} mirror planes in momentum space include all time-reversal invariant momenta in the (110) surface Brillouin zone. Thus if C_M is odd, there is an odd number of Dirac cones on the (110) surface and time-reversal symmetry implies that such a system is a strong 3D TI. As the surfaces of a strong 3D TI cannot be gapped out with a time-reversal symmetric perturbation, we cannot construct a helical HOTI from it. We conclude that C_M is even for all systems of interest to us.

We now discuss the correspondence between the bulk topological invariant $C_{\mathcal{M}}/2$ and the existence of Kramers paired hinge modes. For this, we first consider the electronic structure of the (110) surface, which is invariant under \mathcal{M}_{xy} , and then that of a pair of surfaces with a normal $\mathbf{n}_{\pm} = (1 \pm \alpha, 1 \mp \alpha, 0)$ for small α , which are mapped into each other under \mathcal{M}_{xy} and form a hinge at their interface [see Figure 3.3 (b)–(d)].

A nonzero bulk mirror Chern number $C_{\mathcal{M}}$ with respect to the \mathcal{M}_{xy} symmetry enforces the existence of gapless Dirac cones on the (110) surface. These Dirac cones are pinned to the mirror invariant lines $k_1 = 0, \pi$ in the surface Brillouin zone of the (110) surface, where k_1 is the momentum along the direction with unit vector $\mathbf{e}_1 = (\mathbf{e}_x - \mathbf{e}_y)/\sqrt{2}$. If we consider the electronic structure along these lines in momentum space, see Figure 3.3 (b), each Dirac cone has an effective Hamiltonian $\mathcal{H}_D = v_1 \sigma_z(k_1 - k_1^{(0)}) + v_z \sigma_x(k_z - k_z^{(0)})$ when expanded around a Dirac point at $(k_1, k_z) = (k_1^{(0)}, k_z^{(0)})$ for $k_1^{(0)} = 0$ or $k_1^{(0)} = \pi$. The mirror symmetry is represented by $\mathcal{M}_{xy} = i\sigma_x$, preventing mass terms of the form $m\sigma_y$ from appearing. The sign of v_z is tied to the \mathcal{M}_{xy} eigenvalue ($i\text{sign } v_z$) of the eigenstate with positive group velocity in z direction (at $k_1 - k_1^{(0)} = 0$). Denoting the total number of Dirac cones with $v_z > 0$ ($v_z < 0$) by n_+ (n_-), the bulk-boundary correspondence of a topological crystalline insulator [8] implies

$$C_{\mathcal{M}} = n_+ - n_- \quad (3.3)$$

Consider now a pair of surfaces with slightly tilted normals \mathbf{n}_+ and \mathbf{n}_- , which are not invariant under the mirror symmetry but map into each other. Mass terms are allowed and the Hamiltonians on the surfaces with normal \mathbf{n}_{\pm} read

$$\mathcal{H}_{D,\pm} = v_1 \sigma_z(k_1 - k_1^{(0)} \pm \kappa\alpha) + v_z \sigma_x(k_z - k_z^{(0)}) \pm m\alpha\sigma_y \quad (3.4)$$

to linear order in α , $(k_1 - k_1^{(0)})$ and $(k_z - k_z^{(0)})$ with m and κ real parameters. The two surfaces with normals \mathbf{n}_+ and \mathbf{n}_- meet in a hinge [see Figure 3.3 (b)]. Equation (3.4) describes a Dirac fermion with a mass of opposite sign on the two surfaces. The hinge therefore forms a domain wall in the Dirac mass, from which a single chiral channel connecting valence and conduction bands arises [113]. As we show in the Appendix, this domain wall either binds a R moving mode with \mathcal{M}_{xy} mirror eigenvalue $i\lambda = i\text{sign}(v_z)$ or a L moving mode with mirror eigenvalue $-i\text{sign}(v_z)$. The equality $n_{\text{sign}(v_z)} = N_{R,\text{sign}(v_z)} + N_{L,-\text{sign}(v_z)}$ follows, which connects the number of hinge modes $N_{L/R,\pm}$ we had introduced before to the mirror-graded numbers of Dirac cones on the (110) surface n_{\pm} . From Equation (3.3) we obtain

$$C_{\mathcal{M}} = (N_{R,+} - N_{R,-} + N_{L,-} - N_{L,+}) \equiv 2n, \quad (3.5)$$

relating the 3D bulk invariant $C_{\mathcal{M}}$ to the number of protected helical hinge pairs n of the HOTI. Notice that by time-reversal symmetry $N_{R,+} - N_{R,-} = N_{L,-} - N_{L,+}$, so that n in Equation (3.5) is integer. ($C_{\mathcal{M}}$ is even as forementioned.)

Note that the above deformation of the surfaces can be extended to nonperturbative angles α , until for example the (100) and (010) surface orientations are reached. The surfaces on either side of the hinge may undergo gap-closing transitions as α is increased, but as we argued at the beginning of the section, surface transitions of this kind may not change the net number of helical hinge states with a given mirror eigenvalue, if they occur in a mirror-symmetric way.

We remark that an equation similar to Equation (3.5) also holds in the absence of time-reversal symmetry for each mirror subspace. Then the Chern number in each mirror subspace is an independent topological invariant, which gives rise to a $\mathbb{Z} \times \mathbb{Z}$ classification on each hinge (as opposed to \mathbb{Z} with time-reversal symmetry). This case corresponds to chiral HOTIs protected by mirror symmetries instead of the $\mathcal{C}_4\mathcal{T}$ symmetry employed in Equation (3.2). Conversely, we show in the Appendix that a helical HOTI protected by \mathcal{C}_4 and \mathcal{T} exists and has a \mathbb{Z}_2 classification.

3.3 Material candidates and experimental setup

We propose that SnTe realizes a helical HOTI. In its cubic rocksalt structure, SnTe is known to be a topological crystalline insulator [8, 9]. This crystal structure has mirror symmetries \mathcal{M}_{xy} [acting as $(x, y, z) \rightarrow (y, x, z)$] as well as its partners under cubic symmetry, $\mathcal{M}_{x\bar{y}}$, \mathcal{M}_{xz} , $\mathcal{M}_{x\bar{z}}$, \mathcal{M}_{yz} , $\mathcal{M}_{y\bar{z}}$. (Further spatial symmetries irrelevant to the discussion are not mentioned.) The bulk electronic structure of SnTe is insulating and topologically characterized by a mirror Chern number $C_{\mathcal{M}} = 2$ with respect to the mirror symmetries on the mirror planes which include the Γ point in momentum space. All other mirror planes have $C_{\mathcal{M}} = 0$. As a result, cubic SnTe has mirror-symmetry protected Dirac cones on specific surfaces. We consider the geometry of Figure 6.1 (b) with open boundary conditions in the x and y direction, and periodic boundary conditions in the z direction. The \mathcal{M}_{xz} , $\mathcal{M}_{x\bar{z}}$ and \mathcal{M}_{yz} , $\mathcal{M}_{y\bar{z}}$ symmetries along with their mirror Chern numbers protect either four Dirac cones at generic surface momenta, or two at the surface Brillouin zone Kramers points on the (100) as well as the (010) surfaces [see Figure 3.4 (b)]. In the case at hand, the former possibility is realized. We now discuss two distortions of the crystal structure that turn SnTe into a HOTI.

(i) At about 98 K, SnTe undergoes a structural distortion into a low-temperature rhombohedral phase via a relative displacement of the two sublattices along the

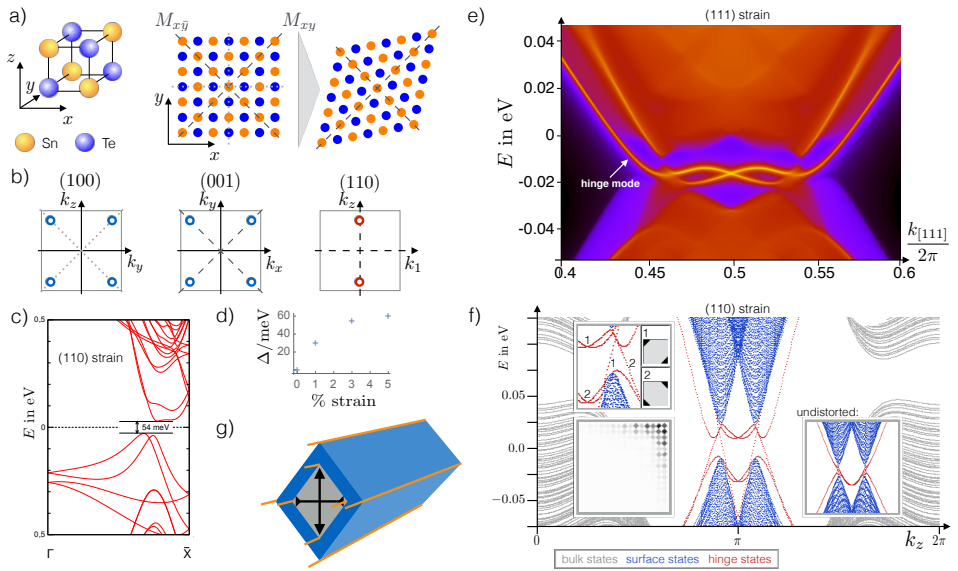


Figure 3.4: Helical HOTI emerging from the topological crystalline insulator SnTe.

(a) Rocksalt lattice structure of SnTe. Uniaxial strain along the (110) direction breaks the mirror symmetries represented by dotted lines, but preserves the ones represented by dashed lines. (b) Circles indicate the location of Dirac cones in the surface Brillouin zone of pristine SnTe for various surface terminations. Those crossed by dotted mirror symmetries are gapped in SnTe with uniaxial strain while the others are retained. The two red Dirac cones are enforced by a mirror Chern number $C_M = 2$, corresponding to one helical pair of hinge modes. k_1 is the momentum along the direction with unit vector $\mathbf{e}_1 = (\mathbf{e}_x - \mathbf{e}_y)/\sqrt{2}$. (c) DFT band structure of a slab of SnTe with open boundary conditions in the (100) direction under 3% strain in the (110) direction. (d) DFT calculation of the gap Δ that develops on the (100) surface of SnTe under (110) uniaxial strain. (e) DFT-based Wannier tight-binding calculation of SnTe with the (111) ferroelectric displacement in a semi-infinite geometry in which the (0̄11) surface and the (1̄01) surface meet at a hinge that is parallel to the (111) direction. A single Kramers pair of hinge states is visible. This distortion breaks all mirror symmetries except those with normal (0̄11), (1̄01), (1̄10), which retain their mirror Chern number 2 for a sufficiently small distortion. The (0̄11) and (1̄01) surfaces considered here are both not invariant under these mirror symmetries, but the hinge formed between them is invariant under the mirror symmetry with normal (1̄10), supporting topological hinge states. (f) Low-energy finite size spectrum of SnTe with uniaxial (110) strain obtained using a tight-binding model (see Appendix) for open boundary conditions in the x and y directions (with $L_x = L_y = 111$ atoms) and periodic boundary conditions in the z direction. States localized in the bulk, on the (100)/(010) surfaces, and on the hinges are color coded. Near $k_z = \pi$ four Kramers pairs of hinge modes, one localized on each hinge, are found. Upper left inset: localization of the gapless modes. Lower left inset: spatial structure of one such mode near a hinge. (Only a small portion of the lattice near the hinge is shown). Right inset: electronic structure of undistorted SnTe in the same geometry, showing two ‘flat band’ hinge modes in addition to the gapless surface Dirac cones. (g) Topological coaxial cable geometry to realize (110) uniaxial displacement. A Si or SiO substrate (gray) is etched to have a rhombohedral cross-section and then coated with SnTe (blue) yielding Kramers pairs of hinge modes (orange).

(111) direction [119, 120, 121]. This breaks the mirror symmetries $\mathcal{M}_{x\bar{z}}$, $\mathcal{M}_{y\bar{z}}$, and $\mathcal{M}_{x\bar{y}}$, but preserves \mathcal{M}_{xz} , \mathcal{M}_{yz} , and \mathcal{M}_{xy} . On the (100) surface in the geometry in Figure 6.1 (b), for instance, the two Dirac cones protected by $\mathcal{M}_{y\bar{z}}$ can thus be gapped out, while the two Dirac cones protected by \mathcal{M}_{yz} remain [and similarly for the (010) surface]. Therefore, the (100) and (010) surfaces remain gapless and the geometry of Figure 6.1 (b) cannot be used to expose the HOTI nature of SnTe with (111) uniaxial displacement. For that reason, we instead consider the $(\bar{1}01)$ and $(0\bar{1}1)$ surfaces, which are not invariant under any mirror symmetry of SnTe with (111) uniaxial displacement. The spectral function focused on the hinge weight of semi-infinite geometry with a single hinge formed between the $(\bar{1}01)$ and $(0\bar{1}1)$ surfaces is shown in Figure 3.4 (e). This tight-binding calculation, based on density functional theory (DFT)-derived Wannier functions (see Appendix A.8), demonstrates the existence of this single Kramers pair of states on the two hinges invariant under \mathcal{M}_{xy} , in line with the prediction of Equation (3.5) for $C_{\mathcal{M}} = 2$.

(ii) If uniaxial strain along the (110) direction is applied to SnTe, \mathcal{M}_{xz} , $\mathcal{M}_{x\bar{z}}$, \mathcal{M}_{yz} , and $\mathcal{M}_{y\bar{z}}$ symmetries are broken, but \mathcal{M}_{xy} and $\mathcal{M}_{x\bar{y}}$ are preserved. This gaps the (100) and (010) surfaces in the geometry in Figure 6.1 (b) completely. We calculated the surface states by using a slab geometry along the (100) direction with DFT. Due to the smallness of the band gap induced by strain, we needed to achieve a negligible interaction between the surface states from both sides of the slab. To reduce the overlap between top and bottom surface states, we considered a slab of 45 layers, 1 nm vacuum thickness and artificially localized the states on one of the surfaces, and adding one layer of hydrogen on one of the surfaces. The evolution of the surface gap size with strain is shown in Figure 3.4 (d) (see Appendix for more details). Figure 3.4 (f) is the spectrum of a tight-binding calculation [9] with (110) strain, demonstrating that there exists one Kramers pair of hinge modes on all four hinges in the geometry of Figure 6.1 (b).

We propose to physically realize the (110) uniaxial strain in SnTe with a *topological coaxial cable* geometry, which would enable the use of its protected hinge states as quasi one-dimensional dissipationless conduction channels [see Figure 3.4 (f)]. Starting point is an insulating nanowire substrate made from Si or SiO, with a slightly rhombohedral cross-section imprinted by anisotropic etching. SnTe is grown in layers on the surfaces by using molecular beam epitaxy, with a thickness of about ten layers. SnTe will experience the uniaxial strain to gap out its surfaces and protect the helical HOTI phase. The hinge states can be studied by scanning tunneling microscopy and transport experiments with contacts applied through electronic-beam lithography. Note that in the process of growth, regions with step edges are likely to form on the surfaces and should be avoided in measurements, as they may

carry their own gapless modes [122]. Alternatively, we propose to use a superconducting substrate to study proximity-induced superconductivity on the helical hinge states.

In addition to the topological crystalline insulator SnTe, we propose weak TIs with nonvanishing mirror Chern number as possible avenues to realize helical HOTIs. We computed the relevant mirror Chern numbers for the weak TIs Bi₂Tel [123], BiSe [124], and BiTe [125], which all turn out to be 2. These materials are therefore dual topological insulators, in the sense that they carry nontrivial weak *and* crystalline topological invariants. Their surface Dirac cones are protected by a nontrivial weak index, i.e., by time reversal together with translation symmetry. To gap them, it is necessary to break at least one of these symmetries, which is possible by inducing magnetic or charge density wave order.

Chapter 4

Experimental realization in elementary bismuth

In this chapter, we present the theoretical and experimental evidence that establishes the electronic band structure of elementary bismuth as that of a higher-order topological insulator.

Various topological aspects of the electronic structure of bismuth have been studied experimentally in the past. This revealed intriguing features such as one-dimensional topological modes localized along step edges on the surface of bismuth [126], conducting hinge channels on bismuth nanowires [127, 71], quasi-one-dimensional metallic states on the bismuth (114) surface [128], and a quantum spin Hall effect in 2D bismuth bilayers [129, 130] and bismuthene on silicon carbide [131]. Here, we show, based on band representations and the theory of topological quantum chemistry [14, 132, 133, 134, 135, 136], that bismuth is in fact a HOTI. This finding provides a unified theoretical origin for all these previous experimental observations. We support our theoretical analysis with experimental data using two complementary techniques: scanning tunneling microscopy/spectroscopy (STM/STS) on surface step edges and Josephson interferometry on bismuth nanowires.

Another 3D material that hosts one-dimensional modes on its surface is the topological crystalline insulator tin telluride. For one, strained tin telluride is proposed to become a HOTI (as explained in Section 3.3). In addition, tin telluride has been experimentally shown to feature one-dimensional flatband modes localized at surface step edges [122]. The latter appear together with the Dirac cone topological surface states and are thus distinct from the hinge modes of a HOTI.

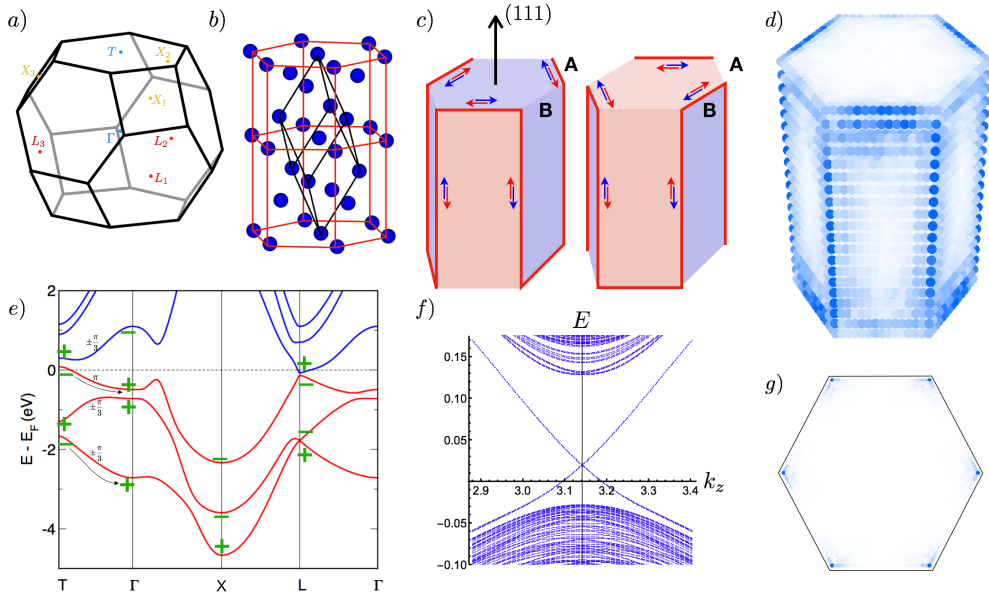


Figure 4.1: Electronic structure of a HOTI with C_3 and I . (a) Brillouin zone with TRS points that are used to evaluate the topological indices in Equation (4.1). (b) Unit cell of the crystal structure of bismuth, which has C_3 and inversion-symmetry. There are six inequivalent sites in the conventional (hexagonal) unit cell, which is shown in red. Black lines delineate the primitive unit cell (tetrahedral), which has only 2 inequivalent atoms. (c) Schematic of the hinge states of a hexagonally-shaped HOTI oriented along the trigonal [111] axis, with C_3 and inversion-symmetry (e.g., bismuth). Note that a prism with triangular rather than hexagonal cross-section would not respect inversion symmetry. All edges of the hexagonal cross-section are along bisectrix axes. Red lines represent a single one-dimensional Kramers pair of gapless protected modes. In the Dirac picture of a HOTI surface, red and blue surfaces correspond to opposite signs of the unique TRS surface mass terms. (d) Localized hinge modes of the minimal tight-binding model of a HOTI with the same topology and symmetries as bismuth, as defined in Appendix B.2. The model is solved on the hexagon geometry described in (c) with open boundary conditions in all directions. Plotted is the sum of the absolute squares of the eigenstates that lie in the bulk and surface gap. Note that while the tight-binding model considered has the same topology as bismuth, it lacks its metallic surface states which are not protected by C_3 and inversion symmetry. (e) Band structure of bismuth with inversion eigenvalues (green) and C_3 eigenvalues on the Γ -T line (black). Since valence bands (red) and conduction bands (blue) are not degenerate anywhere in momentum space, their topological indices, Equation (4.1), are well defined despite the appearance of a small electron and hole pocket. Black arrows indicate the two valence bands contributing to the C_3 -eigenvalue-graded band inversion. (f) Spectrum of the same model solved on a nanowire with hexagonal cross-section and periodic boundary conditions in the trigonal z direction ([111] direction). Only a portion of the spectrum at small momentum deviations from the T point $k_z = \pi$ is shown. Six Kramers pairs of hinge modes traverse the surface and bulk gap. Consult Figure B.2 (c) in Appendix B.2 for a zoomed-out version showing the spectrum for all momenta. (g) Localization of these topologically protected hinge modes in the x-y-plane.

We first develop the theoretical arguments and subsequently present the two types of experimental evidence for topological hinge states in bismuth.

4.1 Topology of \mathcal{I} - and \mathcal{C}_3 -symmetric insulators

Fu and Kane [5] gave a simple topological index for a 3D TI in the presence of inversion symmetry \mathcal{I} : One multiplies the inversion eigenvalues (which are ± 1) of all Kramers pairs of occupied bands at all time-reversal invariant momenta (TRIMs) in the Brillouin zone. If this product is -1 ($+1$), the insulator is topological (trivial). In the topological case, one says the material has a band inversion. Note that when we evaluate this index for bismuth, we obtain $+1$, in accordance with the well known result that the band structure of bismuth is topologically trivial from a first-order perspective [92]. A sample of bismuth thus does not have topologically protected gapless surface states. However, this is not due to bismuth not displaying a band inversion: in fact, we will show that there are two band inversions, the presence of which is not captured by the first-order index, which is only sensitive to the parity of band inversions. We first extend this index to HOTIs with TRS, \mathcal{C}_3 rotation, and inversion symmetry \mathcal{I} . Note that we consider a \mathcal{C}_3 rotational symmetry with axis that is given by the line connecting the TRIMs Γ and T [consult Figure 4.1 (a) for a representation of the Brillouin zone]. For spin-1/2 particles, \mathcal{C}_3 has eigenvalues -1 and $\exp(\pm i\pi/3)$, where a subspace with -1 eigenvalue is closed under TRS, while TRS maps the $\exp(+i\pi/3)$ subspace to the $\exp(-i\pi/3)$ one and vice versa. We can thus define a band inversion separately in the occupied band subspaces of an insulator with \mathcal{C}_3 eigenvalues -1 and $\exp(\pm i\pi/3)$. To do so, observe that of the eight TRIMs, two are invariant under \mathcal{C}_3 (Γ and T), while two groups of three TRIMs transform into each other under \mathcal{C}_3 (call them X_i and L_i , $i = 1, 2, 3$). Denote by $\nu_Y = \prod_{i \in \text{occ}} \xi_{i,Y}$ the product over all inversion eigenvalues $\xi_{i,Y} = \pm 1$ of the occupied bands Kramers pairs at the TRIM $Y \in \{\Gamma, T, X_i, L_i\}$. At Γ and T we further define $\nu_Y^{(\pi)}$ and $\nu_Y^{(\pm\pi/3)}$, where the product is restricted to the Kramers pairs with \mathcal{C}_3 eigenvalues -1 and $\exp(\pm i\pi/3)$, respectively, such that $\nu_Y = \nu_Y^{(\pi)} \nu_Y^{(\pm\pi/3)}$ for $Y = \Gamma, T$. By \mathcal{C}_3 symmetry $\nu_{X_1} = \nu_{X_2} = \nu_{X_3}$ and $\nu_{L_1} = \nu_{L_2} = \nu_{L_3}$, so that the Fu-Kane index is given by $\nu = \nu_\Gamma \nu_T \nu_{X_1} \nu_{L_1}$. Consider a Kramers pair of states at X_1 together with its two degenerate \mathcal{C}_3 partners at X_2 and X_3 . Out of a linear combination of these states, one can construct one Kramers pair with \mathcal{C}_3 eigenvalue -1 , and two Kramers pairs with eigenvalues $\exp(\pm i\pi/3)$. This is shown explicitly in Appendix B.4. When taking the Kramers pair at X_1 together with its degenerate partners at X_2 and X_3 to have negative inversion eigenvalue, these \mathcal{C}_3 symmetric linear combinations also have negative inversion eigenvalue. Thus, a band inversion at X_i as measured by the Fu-Kane formula induces a single band inversion in the -1

subspace, and two (which equals no) band inversions in the $\exp(\pm i\pi/3)$ subspace. The same holds for the L_i points. We conclude that the total band inversion in the occupied subspaces with \mathcal{C}_3 eigenvalues -1 and $\exp(\pm i\pi/3)$ are given by

$$\nu^{(\pi)} = \nu_{\Gamma}^{(\pi)} \nu_T^{(\pi)} \nu_{X_1} \nu_{L_1}, \quad \nu^{(\pm\pi/3)} = \nu_{\Gamma}^{(\pm\pi/3)} \nu_T^{(\pm\pi/3)}, \quad (4.1)$$

respectively. We then distinguish three cases: (i) $\nu^{(\pi)} = \nu^{(\pm\pi/3)} = +1$ for a trivial insulator, (ii) $\nu = \nu^{(\pi)} \nu^{(\pm\pi/3)} = -1$ for a \mathbb{Z}_2 topological insulator, and (iii) $\nu^{(\pi)} = \nu^{(\pm\pi/3)} = -1$ for a HOTI.

Thus far, our considerations apply to all crystals with TRS, \mathcal{C}_3 and \mathcal{I} . We now evaluate the above topological index for elementary bismuth, crystallizing in space group $R\bar{3}m$, No. 166, which possesses these symmetries [see Figure 4.1 (b)]. Even though bismuth is not an insulator, there exists a direct band gap separating valence bands from conduction bands [see Figure 4.1 (e)]. This allows us to evaluate the indices $\nu^{(\pi)}$ and $\nu^{(\pm\pi/3)}$ for the valence bands. We do so with the group characters obtained from first principle calculations (see methods). The result is $\nu^{(\pi)} = \nu^{(\pm\pi/3)} = -1$, which derives from $\nu_T^{(\pi)} = \nu_T^{(\pm\pi/3)} = -1$, i.e., there is a \mathcal{C}_3 -graded double band inversion at the T point. Hence, bismuth is a HOTI according to the topological index defined above (if we neglect the fact that it has a small electron and hole pocket).

As a second approach, we employ the formalism of elementary band representations [14, 132, 133, 134, 135, 136] (EBR) to demonstrate the nontrivial topology. Since there is always an energy separation between valence and conduction bands, we restrict our consideration to the three doubly-degenerate valence bands shown in red in Figure 4.1 (e). In particular, we checked explicitly that the set of all bands at lower energy than these is topologically trivial. At TRIMs the eigenvalues of all symmetry operators have been computed (see methods). Referring to the character tables in the Bilbao Crystallographic Server (BCS) [133], we assign to all the bands their corresponding irreducible representations. The results of the eigenvalue calculations are listed in Appendix B.3. They show that the valence bands can not be decomposed into any linear combination of physical EBRs (pEBR, which are EBRs that respect TRS). It is the main result of Reference [14], that if such a decomposition is not possible, the electronic band structure of bismuth has to be topological and without a description in terms of exponentially localized Wannier states, in contraposition to the conclusion drawn from Fu-Kane's parity criterion [5]. To understand which symmetry protects this topological phase, we are repeating the symmetry eigenvalue calculation with an artificially lowered symmetry. The representative elements of point group $\bar{3}m$ are \mathcal{C}_3 around the z axis (denoted 3 in the space group names), \mathcal{I} (denoted by overbar), two-fold rotational

symmetry about the y axis (denoted 2), and mirror symmetry with respect to the x - z -plane (denoted m). After lowering the space group $R\bar{3}m$ (166) to $R3m$ (160) or $R32$ (155), a similar EBR analysis within the symmetry-reduced space groups shows that the valence bands can be decomposed into pEBRs in this case, indicating that they are topologically trivial. Therefore, neither two-fold rotation nor mirror symmetry protects the nontrivial topology of bismuth. In contrast, as long as \mathcal{I} is preserved, lowering it to space group $R\bar{3}$ (148), the valence bands are still topological in the sense that they can not be decomposed into pEBRs in space group 148. We conclude that the nontrivial topology is protected by \mathcal{I} (in combination with the three-fold rotation). Notice that the rhombohedral lattice always respects the three-fold rotational symmetry. Since we learned from topological quantum chemistry that the bulk bands have no Wannier description, we expect the presence of spectral flow in Bi, and hence protected gapless modes on its boundaries. Since we know the surfaces of bismuth to be non-topological, these gapless boundaries must be hinges. This is compatible with previous works showing that Bi (111) bilayers (possibly on a substrate) host one-dimensional edge channels [129, 130].

Note that when changing the parameters of the tight binding-model of bismuth [137] slightly, it undergoes a transition from a second-order to a first-order topological insulator [138]. However, we confirmed the higher-order character of bismuth that is suggested by the original tight-binding model parameters [137] independently by performing first-principle calculations, as well an analysis in the framework of topological quantum chemistry. In particular, we took into account all occupied bands of bismuth up to its momentum-dependent energy gap. This is important since it has been shown that bands far away from this gap still contribute significantly to measurable effects, such as the unusually large g -factor of holes [139].

4.2 Bulk-boundary correspondence

We present a direct calculation which let us conclude that a TRS system with $\nu^{(\pi)} = \nu^{(\pm\pi/3)} = -1$ has to have hinge modes for terminations of the crystal that globally respect inversion symmetry or further symmetries. We consider a crystal of hexagonal shape [see Figure 4.1 (c)] which preserves C_3 rotational and inversion symmetry. The steps outlined here in words are explicitly demonstrated using a Dirac model in Appendix B.1. We think of the insulator with $\nu^{(\pi)} = \nu^{(\pm\pi/3)} = -1$ as a superposition of two topological insulators, one in each of the independent C_3 subspaces. Consider adiabatically turning off any coupling between these two subspaces, while preserving the bulk gap. The resulting system has two Dirac cones (i.e., a Dirac theory represented by 4×4 matrices) on all surfaces of the

crystal. Next, we seek to gap these surface Dirac cones by weakly coupling the two \mathcal{C}_3 subspaces. We want to do so while preserving the TRS, \mathcal{C}_3 , and \mathcal{I} of the crystal. Of these, TRS is the only constraint that acts locally on a given surface. From the representation theory of the 2D Dirac equation, one finds that for a TRS that squares to -1 , as required for spinful electrons, there exists a unique mass term m that gaps the two Dirac cones in a time-reversal symmetric way. It remains to study how this mass term transforms under \mathcal{C}_3 and \mathcal{I} to determine its relative sign between different surfaces of the crystal. Relative to the kinetic part of the surface Dirac theory, $m \rightarrow -m$ under inversion and $m \rightarrow +m$ under \mathcal{C}_3 (see Section B.1 of the Appendix for details). As a result, the sign of the mass term alternates between adjacent lateral surfaces of the hexagonal crystal [see Figure 4.1 (c)]. Each change of sign in the mass term is a domain wall in the Dirac theory and binds a Kramers pair of modes propagating along it. These are the one-dimensional hinge modes of the HOTI. The sign of the mass term on the top and bottom surface is not universally determined so that both patterns of hinge modes shown in Figure 4.1 (c) are compatible with the bulk topology of $\nu^{(\pi)} = \nu^{(\pm\pi/3)} = -1$ (in a real system, the particular electronic structure determines which pattern has lower energy). Apart from this ambiguity, the argument presented here solely rests on the nontrivial bulk topology and is independent of the exact form of the surface electronic structure, as long as the surface is gapped while preserving the respective symmetries. This constitutes the generalized topological bulk-boundary correspondence characteristic of a HOTI, where the existence of one-dimensional hinge modes directly follows from the 3D bulk topology. The HOTI's bulk-boundary correspondence requires that these hinge modes are locally stable under time-reversal symmetric perturbations that preserve the bulk and surface gaps. From this requirement, we can understand the \mathbb{Z}_2 topological character of the phase: the minimal TRS surface manipulation is the addition of a 2D TI to one surface of the hexagonal nanowire. This would permit hybridizing and gapping out of the pair of hinge modes adjacent to the surface. However, to comply with \mathcal{I} and \mathcal{C}_3 , the same 2D TI has to be added to every surface, thus leaving the Kramers pairs of modes intact at each hinge. We conclude that a single Kramers pair of modes at each hinge is stable under all symmetry-preserving surface perturbations. In fact, such a Kramers pair is locally stable under small perturbations even when the spatial symmetries are broken, e.g., by introducing disorder into the sample, as long a TRS is preserved. The only way to remove it is to annihilate it with another Kramers pair coming from another hinge, which cannot be achieved with just a small perturbation. The higher-order hinge modes of a 3D HOTI are therefore just as stable as the edge modes of a first-order TRS topological insulator in 2D. We further exemplify these results with a tight-binding model, defined in Section B.2 of

the Appendix, whose hinge states are shown in Figure 4.1 (d),(f),(g). Note that our tight-binding model is topologically equivalent to a realistic model [137] of bismuth, however it is easier to interpret in the sense that it does not have metallic bulk and surface states that would obscure the hinge modes in the electronic structure plots we present here. It also has fewer orbitals per unit cell, which makes 3D simulations of large systems feasible.

We now turn to experimental data that support our higher-order bulk-boundary correspondence in bismuth. Even though bismuth is metallic in the bulk and on the surface, only its topological hinge states are protected against scattering by weak disorder as compared to trivial surface states, for example. We expect hinge states between (i) the top surface [which is denoted (111) in the primitive unit vectors] and three of the six lateral surfaces and (ii) between adjacent lateral surfaces. The geometry of the samples was more amenable to study the hinge states of type (i), as we outline below.

4.3 Scanning tunneling microscopy experiment

With a STM, we studied the electronic structure of step edges on the (111) surface of bismuth. Due to the buckled honeycomb structure of the bismuth bilayer along the [111] trigonal direction, STM topographic images of the (111) plane of bismuth show bilayer steps with two different types of bisectrix edges: type A and type B [marked as red and blue lines in Figure 4.2 (a)]. We highlight two structures of triangular and nearly hexagonal shape [Figure 4.2 (a) and (c)]. In particular the step edge in Figure 4.2 (c) can be seen as (the negative of) a one bilayer tall version of the crystals shapes shown in Figure 4.1 (c). We thus expect hinge states at either the type A or the type B edges due to the higher-order topology. (All A type and all B type edges are mutually equivalent due to the C_3 rotational symmetry of the bismuth (111) surface.) Indeed, we observe strongly localized edge states only at type A edges in Figure 4.2 (b) and (d), which display the differential conductance map overlaid on top of the topographic data to illuminate the edge states at the van Hove singularity energy of the bismuth edge states. A previous experimental study [126] showed a one-dimensional van Hove singularity of the edge states ($E = 183$ meV) and quasi-particle interference of the spin-orbit locked edge states. The same study demonstrated the absence of k to $-k$ scattering for these states. These experimental observations and model calculations strongly suggest that the edge states are living in the momentum dependent energy gap of the bismuth (111) surface states [126]. Every other edge of a hexagonal pit exhibits localized edge states and these edge states are discontinued at the corner where

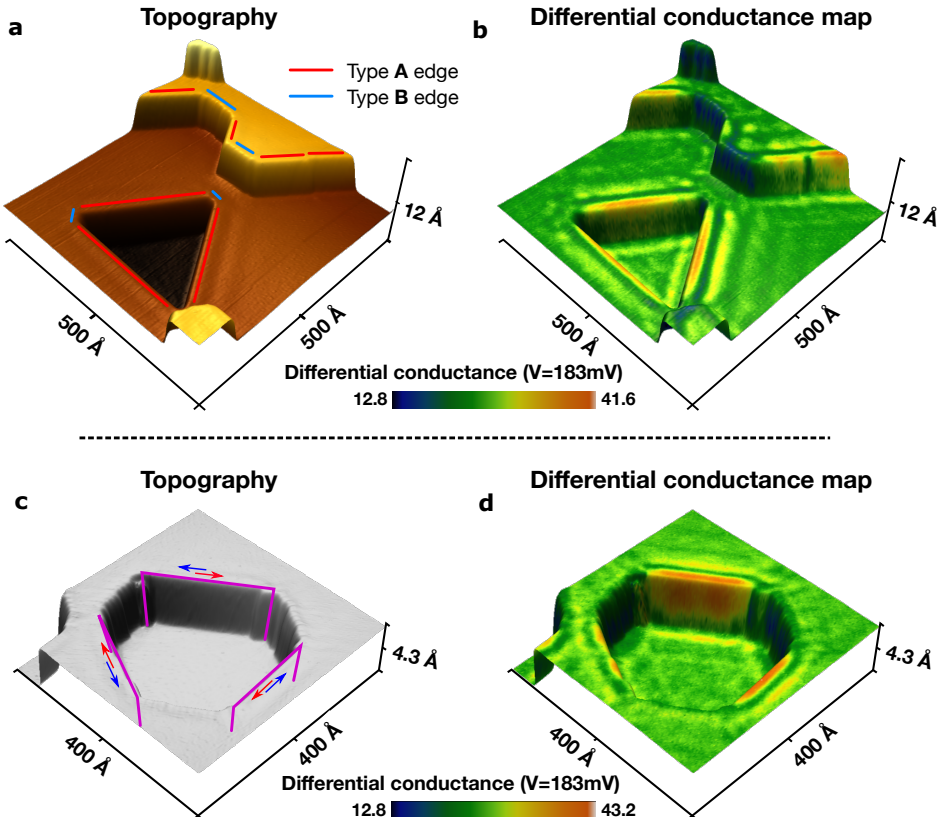


Figure 4.2: Experimental observation of the alternating edge states on a bismuth (111) surface perpendicular to its trigonal axis. (a) 3D rendered topographic image of the bismuth (111) surface. The red (type A) and blue (type B) lines then indicate the types of edge, which are along bisectrix axes. Note that the edges of type B in this particular pit geometry are much shorter than edges of type A, while still large enough to be experimentally accessible. (b) Differential conductance map at the van Hove singularity energy ($V = 183$ meV) of the one-dimensional edge states. In contrast to the type B edges, all the type A edges exhibit localized high conductance. (c) Topographic image of a hexagonal pit on a bismuth (111) surface. The hinge modes are schematically shown as purple lines. Blue and red arrows indicate the flow of the spin-momentum locked hinge modes. (d) Differential conductance map simultaneously acquired with the topographic data from (c), showing high conductance at every other edge of the hexagonal pit.

type A and type B edge meet [Figure 4.2 (c) and (d)]. This feature remarkably reproduces the hinge modes calculated for the hexagonal nanowire as shown in Figure 4.1 (d).

4.4 Transport experiment

We exploited proximity-induced superconductivity to reveal ballistic hinge states along monocrystalline bismuth nanowires [127, 71]. When these (non superconducting) nanowires are connected to superconducting contacts (implementing a superconductor/bismuth nanowire/superconductor or S/Bi/S Josephson junction), a supercurrent runs through them at low temperature. Our experiments unambiguously demonstrate that the supercurrent flows via extremely few narrow one-dimensional channels, rather than via the entire surface or bulk of the nanowire. The experimental indications are the following: i) Periodic oscillations of the critical current through the nanowires caused by a magnetic field, with a period corresponding to one magnetic flux quantum through the wire section perpendicular to the field [127, 71]. Such oscillations indicate interference between two supercurrent-carrying paths located at the nanowire edges [140], since a uniform current density in such a long narrow wire would produce instead a monotonously decaying critical current. ii) The supercurrent flowing through the nanowire persists to extremely high magnetic fields, up to several Teslas in some samples. Since the orbital dephasing due to a magnetic flux through the supercurrent-carrying channel area destroys the induced supercurrent, this indicates that the channels are extremely narrow spatially. iii) Finally, we have recently provided a direct signature of ballistic transport along those one-dimensional channels, by measuring the supercurrent-versus-phase relation (also called current phase relation, or CPR) of the S/Bi/S junction. This was done by inserting the bismuth nanowires into an asymmetric superconducting quantum interference device (SQUID) configuration [141, 71].

Whereas tunneling or diffusive transport give rise to the usual nearly sinusoidal current phase relation of superconductor/normal metal/superconductor Josephson junctions, the sharp sawtooth-shaped current phase relation we found instead, demonstrates that transport occurs ballistically along the wire. The scattering probability p was estimated to be 0.1 along the 1 μm long bismuth wire from the harmonics content of this current phase relation (where the n th harmonic decays like $(1 - p)^{2n}/n$). This leads to a lower bound of the mean free path l_e along these edges equal to 10 μm , much longer than the value $l_e = 0.1 \mu\text{m}$ determined for the surface states. This surprising result is explained by the dominant contribution of the topologically protected hinge states to the supercurrent. Indeed, the

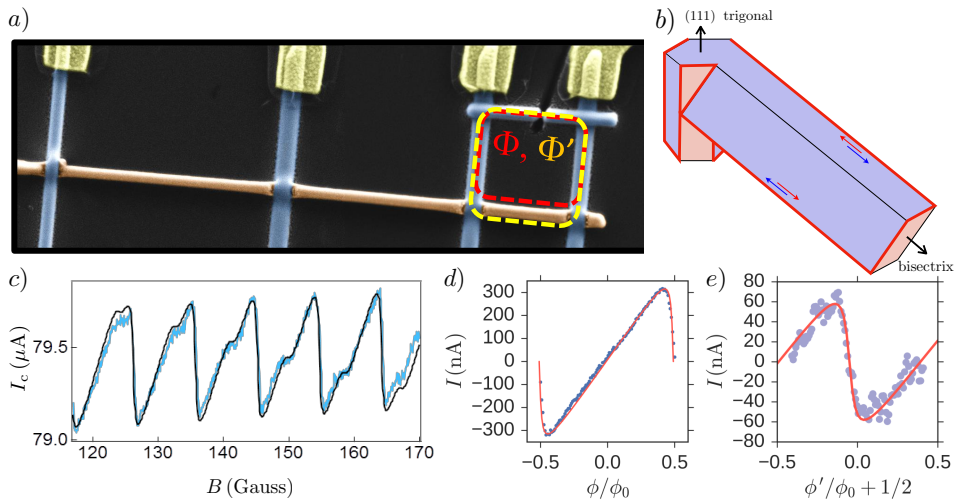


Figure 4.3: Evidence for hinge states in elementary bismuth from Josephson-interference experiments. (a) Single-crystal bismuth nanowire (colored in brown) connected to superconducting electrodes (colored in blue). The $1.4 \mu\text{m}$ long, rightmost section of the wire, in parallel with a superconducting weak link, forms an asymmetric SQUID. (b) Schematic representation of the investigated bismuth nanowire, indicating (red lines) the position of the experimentally identified hinge states in relation to the hinge states determined theoretically in a bismuth sample of hexagonal symmetry oriented along the trigonal [111] axis. (c) The magnetic field dependence of the critical current is modulated by the current phase relation of the bismuth Josephson junction (whose critical current is much lower than the superconducting weak link). It can be decomposed into the sum of two sawtooth waves (d) and (e) of different periods corresponding respectively to the internal and external area of the SQUID Φ and Φ' shown in (a), and thereby, to the two topological hinge modes (the contribution of bulk and surface states is strongly suppressed by disorder).

supercurrent carried by a diffusive channel is $(L/l_e)^2 \approx 100$ times smaller than the supercurrent carried by a ballistic channel (l_e and L are the elastic mean free path and wire length, respectively). The position of the edge states can be deduced from the periodicity of the SQUID oscillations, which is inversely proportional to the area enclosing the flux. In a sample of parallelogrammatic cross-section whose geometry and orientation was precisely determined, we detected a beating of two paths enclosing different fluxes Φ and Φ' [see Figure 4.3 (a)] [71]. This demonstrated that the edge states are located along the two acute edges of the (111) facets. Those edges coincide with the expected hinge states perpendicular to the trigonal [111] axis [see Figure 4.3 (b)]. The contribution of each path was extracted and is shown in Figure 4.3 (d) and (e). The supercurrents carried by the two hinges differ by a factor of four. This can be explained by a difference in the quality of the contact to these hinge states: The top hinges of the wire have been more severely etched than the bottom ones during the deposition of the superconducting electrodes [see Figure 4.3 (a)]. This strong etching reduces the coupling of edge states to the superconducting contacts and the supercurrent is decreased even though the ballistic nature is unaffected.

Comparing Figure 4.3 (d) and Figure 4.1 (c), we note that one of the two hinges on top of the nanowire must be of A type and the other one of B type (the same is true for the bottom two hinges). Our observation of a ballistic channel at one of these hinges at the top, and one at the bottom of the nanowire, is thus in line with the theoretical expectation from the higher-order topology of bismuth.

Chapter 5

Defect and flux response of higher-order topological insulators

In this chapter of the thesis we derive an explicit mapping from the bulk topology of an insulator to the protected midgap bound states it may host when crystal defects and magnetic fluxes are introduced. In particular, we consider dislocations and π -flux tubes that preserve inversion symmetry, the simplest crystalline symmetry that protects higher-order topological insulators. We show that HOTIs can not only be identified via their anomalous hinge states – they also display a unique defect response, in that they host zero-dimensional bound states at the ends of one-dimensional defects such as screw dislocations or flux tubes. This complements and goes beyond the established results for weak topological insulators (WTIs), which are known to host topologically protected one-dimensional gapless modes along one-dimensional screw dislocations [142]. We find that, quite generally, crystal defects are sensitive to weak topological indices (indices reliant on translational symmetry), while magnetic fluxes are sensitive to strong topological indices that survive the breaking of translational symmetry (as long as inversion symmetry \mathcal{I} and all relevant local symmetries such as time-reversal \mathcal{T} are maintained). We conjecture that the presence of Kramers-paired defect bound states exhausts the bulk electromagnetic response of \mathcal{I}, \mathcal{T} -symmetric 3D HOTIs (which represent the most experimentally relevant class of higher-order topological phases, see Chapter 1). Our results also shed new light on the aforementioned screw dislocation bound states in WTIs, as well as on the vortex bound states in Chern insulators and chiral superconductors.

Let us make one important remark about our somewhat lax use of language when speaking of zero-dimensional bound states. Absent any spectral symmetries (which

are rare in realistic non-superconducting crystals), zero-dimensional states can always be energetically pushed out of the bulk gap in a symmetry-preserving fashion, and hybridized with bulk states (thereby losing their exponential localization properties). Instead, and more rigorously, the nontrivial bulk topology expresses itself via a filling anomaly [23, 19, 143, 32, 144]: at a filling that corresponds to an insulating band gap with periodic boundary conditions, the system has to be metallic with open boundary conditions when the relevant symmetries are respected, because the boundary modes are then fractionally filled. This notion does not require a spectral symmetry, which is necessary to pin boundary modes in the middle of a band gap.

5.1 Mapping topology from momentum space to position space

In this section, we provide proofs demonstrating the relationship between the topology of pristine crystals and the electronic states bound to line-like defects and π -flux tubes. We show that crystal defects with integer Burgers vectors [145] and threaded magnetic π -flux can map the topology of lower-dimensional surfaces of the Brillouin zones (BZs) of pristine crystals to surfaces in position space. We show that, under the preservation of specific symmetries, this mapping necessitates the presence of anomalous 0D states bound to the ends of line-like dislocations and flux tubes in 3D higher-order topological insulators.

Specifically, we use general arguments to demonstrate that edge dislocations and flux tubes in d -dimensional crystals can map $(d - 1)$ -D BZ surfaces to $(d - 1)$ -D real-space surfaces, leading in 3D crystals to the presence of 1D and 0D topological defect states. In Section 5.1.1, we prove that generalized edge dislocations in d -D, \mathcal{I} -symmetric crystals map the $(d - 1)$ -D BZ-surface topology of pristine crystals to the topology of $(d - 1)$ -D real-space surfaces between crystal defects, and in Section 5.1.2, we employ similar arguments to analyze the topology of \mathcal{I} -symmetric arrangements of flux tubes in d -D crystals. Finally, in Section 5.1.3, we extend the logic employed in Sections 5.1.1 and 5.1.2 to the experimentally relevant case of 1D screw dislocations in 3D crystals.

We use the many-body (Slater-determinant) ground-states of pristine crystals to determine defect and flux responses. For edge dislocations (Section 5.1.1) and π -flux tubes (Section 5.1.2) in particular, our arguments can be straightforwardly generalized to crystals with arbitrarily large dimensionality d .

We model each dislocation or flux tube as an interface between two thermodynamically large, d -D bulk systems, whose topological indices differ by a combination of $(d - 1)$ -D phases (defined in momentum-space), and then subsequently deduce the presence of $(d - 2)$ -D or $(d - 3)$ -D bound states via the bulk-boundary correspondences of the $(d - 1)$ -D phases. Throughout this section, we assume that any symmetries that enforce the topology of the $(d - 1)$ -D momentum-space subsystems are also preserved by the position-space dislocation or flux-tube geometry itself. Since we assume the crystal without defects to be insulating, any bound states are necessarily localized on the defects and flux tubes (or on their corners and ends), and decay exponentially away from them.

5.1.1 Edge Dislocations in d -D Crystals

Here, we derive the topological relations governing the appearance of bound states arising from the insertion of a set of \mathcal{I} -symmetric edge dislocations into an insulating system with arbitrary dimensionality (d -D). We first focus on an edge dislocation with Burgers vector $\mathbf{B} = \hat{y}$ for clarity, before generalizing to arbitrary Burgers vectors.

Let S be a d -dimensional insulating system defined on a lattice Λ of size $V_S = L_y V_S^\perp$, where L_y is the linear extent in y -direction (we take the lattice spacing to be $a = 1$ along each of the lattice vectors) and V_S^\perp denotes the $(d - 1)$ -dimensional volume spanning the remaining directions. Let S be governed by a gapped single-particle Hamiltonian \mathcal{H} . Making translation symmetry in the y -direction explicit, and leaving translation in the remaining perpendicular directions implicit, we Fourier transform \mathcal{H} to realize a Bloch Hamiltonian $\mathcal{H}(k_y)$ that acts on the degrees of freedom of $(d - 1)$ -dimensional slices (layers or rows) with size V_S^\perp of the lattice. With periodic boundary conditions, and taking L_y to be an even integer without loss of generality, k_y is an element of the discrete Brillouin zone:

$$\text{BZ}_S = \frac{2\pi}{L_y} \left\{ -\left(\frac{L_y}{2} - 1\right), \dots, 0, \dots, \left(\frac{L_y}{2} - 1\right), \frac{L_y}{2} \right\}. \quad (5.1)$$

In the case of N occupied bands, the eigenstates of $\mathcal{H}(k_y)$ are given by:

$$\mathcal{H}(k_y) |u_\alpha(k_y)\rangle = E_\alpha(k_y) |u_\alpha(k_y)\rangle, \quad (5.2)$$

where $\alpha = 1 \dots N$. Reexpressing the eigenstates of $\mathcal{H}(k_y)$ using second-quantization:

$$|u_\alpha(k_y)\rangle = c_\alpha^\dagger(k_y) |0\rangle, \quad (5.3)$$

where the orthonormality of the occupied eigenstates $|u_\alpha(k_y)\rangle$ implies that:

$$\{c_\alpha(k_y), c_\beta^\dagger(k_y)\} = \delta_{\alpha\beta}. \quad (5.4)$$

In this construction, the ground state of S takes the form:

$$|GS_S\rangle = \prod_{k_y} \prod_{\alpha=1}^{\text{BZ}_S} c_\alpha^\dagger(k_y) |0\rangle. \quad (5.5)$$

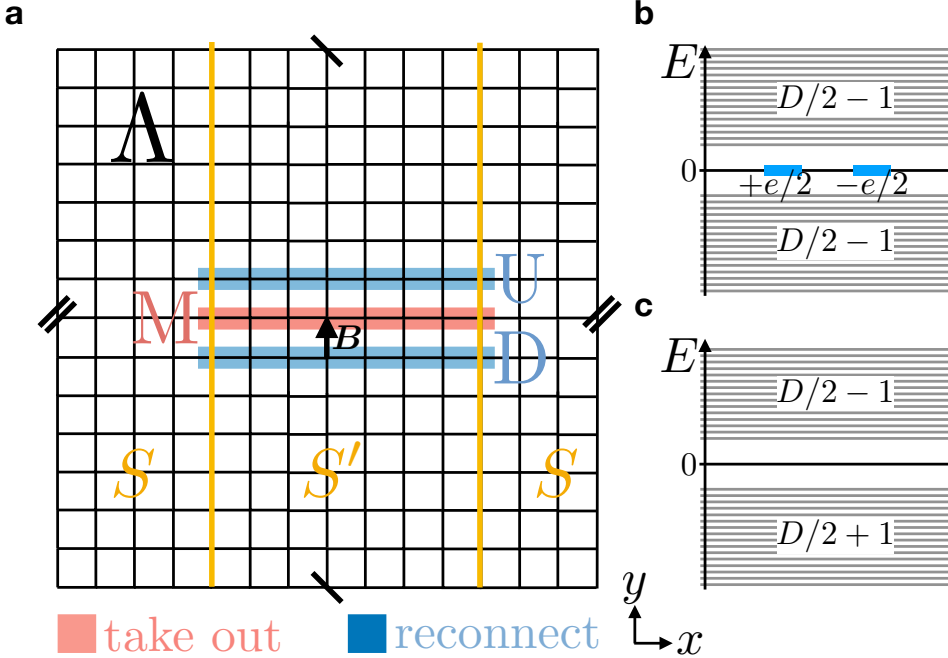


Figure 5.1: (a) To create a pair of edge dislocations with Burgers vectors $\mathbf{B} = \hat{y}$ in a 2D crystal defined on a lattice Λ , we take out the sites belonging to an x -directed line M , and reconnect the sites above, belonging to the line U , with those below, belonging to the line D , as detailed in the text surrounding Equation (5.38). (b) In the spectrum of a 2D \mathcal{I} -symmetric system calculated with open boundary conditions, a pair of dislocations can carry nontrivial topology that is indicated via dislocation bound states pinned to zero energy by a chiral (unitary particle-hole) symmetry Π . In the topologically nontrivial phase, the conductance and valence bands are both missing one state with respect to the same spectrum calculated with periodic boundary conditions. (c) When Π is relaxed, however, the midgap states can be shifted out of the bulk gap. Nevertheless, the nontrivial bulk topology is still present in the system with the pair of dislocations, and is instead more generally indicated via a filling anomaly [19, 143, 32, 144, 146, 147]: specifically, at half filling, there is no gap above the highest occupied state, but there is instead a mismatch in the number of states above and below a large gap at a higher energy (here at $E = 0$).

An edge dislocation with $\mathbf{B} = \hat{y}$ realizes an interface of S with a system S' that has size $V'_S = (L_y - 1)V_S^\perp$, but which otherwise has the same symmetry and topology as S . S' is therefore described by the Bloch Hamiltonian $\mathcal{H}(k'_y)$, where k'_y is instead

an element of the discrete Brillouin zone:

$$BZ_{S'} = \frac{2\pi}{L_y - 1} \left\{ -\left(\frac{L_y}{2} - 1\right), \dots, 0, \dots, \left(\frac{L_y}{2} - 1\right) \right\}. \quad (5.6)$$

The ground state of S' ($|GS_{S'}\rangle$) is formed from the occupied subspaces of $H(k'_y)$ with k'_y being an element of Equation (5.6), such that $|GS_{S'}\rangle$ is given by:

$$|GS_{S'}\rangle = \prod_{k'_y}^{\text{BZ}_{S'}} \prod_{\alpha=1}^N c_\alpha^\dagger(k'_y) |0\rangle. \quad (5.7)$$

Importantly, in Equations (5.6) and (5.7), the $k'_y = \pi$ subspace of the continuum BZ is never sampled over, and thus does not contribute, even though $\text{BZ}_{S'}$ approaches BZ_S as L_y goes to infinity. To restate, as long as L_y is discretely valued, only BZ_S contains $k_y = \pi$.

Comparing Equations (5.1) and (5.6) establishes that there is a mismatch between $|GS_S\rangle$ and $|GS_{S'}\rangle$ that is given by the $(d - 1)$ -D (possibly topological) contribution of $\mathcal{H}(\pi)$ to the ground state of S :

$$|GS_S\rangle \approx \prod_{\alpha=1}^N c_\alpha^\dagger(\pi) |GS_{S'}\rangle, \quad (5.8)$$

where by \approx we mean that the states on either side of the equation are adiabatically related to each other. The $(d - 1)$ -D contribution of $\mathcal{H}(\pi)$ can be trivial or (crystalline or polarization) topological; in the latter case, the edge dislocation acts as a boundary that can host topologically protected states by the bulk-boundary correspondence between S and S' .

To be precise, the ground state of S is adiabatically related to a state given by the (appropriately antisymmetrized) tensor product of the ground state of $\mathcal{H}(k_y = \pi)$ with that of S' . We relate this to the bulk-boundary (domain-wall) correspondence between S and S' by noting that, under the tensor product, which is physically implemented by stacking (*i.e.* superposition), free-fermion topological phases form an additive group [148], which allows us to “subtract” (\ominus) $|GS_{S'}\rangle$ from both sides of the dislocation in Figure 5.1 (a). We then conclude that the ground state of the subsystem of the dislocation is, via this subtraction, adiabatically related to the ground state of $\mathcal{H}(k_y = \pi)$, which is given by:

$$|GS_S\rangle \ominus |GS_{S'}\rangle \approx \prod_{\alpha=1}^N c_\alpha^\dagger(\pi) |0\rangle, \quad (5.9)$$

with respect to the vacuum $|0\rangle$.

The condition for anomalous bound states to be present is that all (unitary and antiunitary) symmetries which protect the topology of $\mathcal{H}(\pi)$ remain enforced by the defect geometry. Importantly, we do not require individual edge dislocations to preserve these symmetries on their own, but we do require the set of dislocations to be arranged in a manner in which the $(d - 1)$ -D surface connecting them does preserve the symmetries enforcing the topology of $\mathcal{H}(k_y)$.

In this thesis, we distinguish between several distinct notions of topological nontriviality. In the language of Topological Quantum Chemistry (TQC) [14, 133, 132, 134], the occupied bands of topological (crystalline) insulators (TIs and TCIs) cannot be represented in terms of maximally localized symmetric Wannier functions [78]. However, the results in this section also apply if the ground state of $\mathcal{H}(k_y = \pi)$ [Equation (5.9)] carries the topology of an obstructed atomic limit (OAL), whose occupied bands *can* be represented in terms of maximally localized Wannier functions, but not on the positions of the underlying atoms [14]. Specifically, if the ground state of $\mathcal{H}(k_y)$ in Equation (5.8) is an OAL, then a dislocation still acts as a boundary for it, and can still host protected (0D) states due to excess charge (or spin) [79, 149, 150, 86, 25, 143, 32]. As shown in recent works [143, 19, 32, 62], fragile TIs (FTIs) also carry the same boundary spin and charge as OALs, and thus our analysis applies to FTIs as well. For simplicity, in this section, we group strong TIs, TCIs, OALs, and FTIs together under the general label “topological,” unless stated otherwise.

In order to generalize to arbitrary Burgers vectors, we phrase the above in coordinate-independent terms. Making the full translational symmetry of \mathcal{H} explicit, we consider its Fourier transform $\mathcal{H}(\mathbf{k})$, where \mathbf{k} is an element of the d -dimensional Brillouin zone. An edge dislocation with Burgers vector (b) forms an interface between two systems S and S' that differ by the ground state of a $(d - 1)$ -dimensional momentum-space subsystem with the Bloch Hamiltonian:

$$\mathcal{H}(\mathbf{k}_\perp), \quad \mathbf{k}_\perp \in \{\mathbf{k} \mid \mathbf{B} \cdot \mathbf{k} = \pi\}. \quad (5.10)$$

5.1.2 π -Flux States in d -D Crystals

Here, we derive the topological relations governing the appearance of bound states arising from the insertion of a set of π -flux tubes into an insulating system with arbitrary dimensionality (d -D). We first focus on the physically relevant cases of two and three dimensions before briefly generalizing to insulators with arbitrarily large dimensionality d .

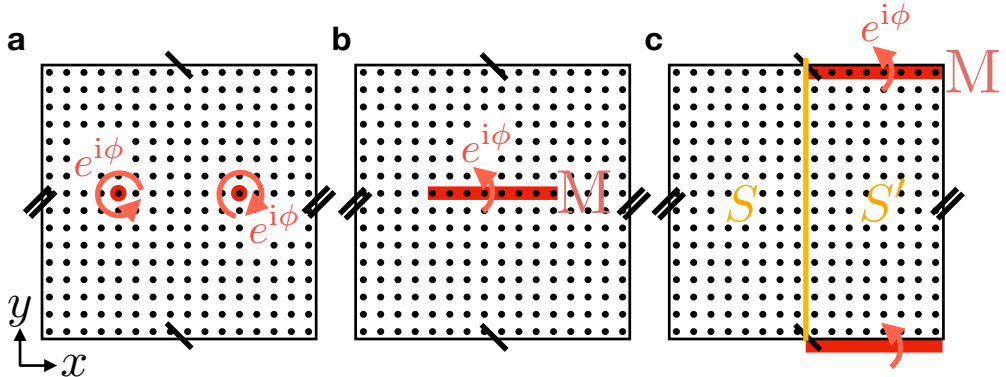


Figure 5.2: (a)–(c) A pair of magnetic $\pm\phi$ -fluxes (flux tubes in 3D) in the (x, y) -plane, shown in (a), can be implemented by multiplying all hoppings across a line (plane) with length L_M in the x -direction connecting the two flux cores (tubes) by $e^{i\phi}$, as shown in (b). This is known as the Peierls substitution [81], and corresponds to a gauge choice for the electromagnetic vector potential. In a system with otherwise periodic boundary conditions, the Peierls substitution in (b) is equivalent to implementing twisted boundary conditions in a part of the system, as shown in (c). The flux cores (tubes) therefore form an interface between the system with standard periodic boundary conditions and the system with twisted boundary conditions [shown in the y -direction in (c)].

A pair of magnetic fluxes (flux tubes) with strength $\pm\phi$ can be introduced in a 2D (3D) system S , containing $L_x L_y$ ($L_x L_y L_z$) lattice sites, by multiplying all hoppings across a line (plane) M of sites in the crystal lattice by a factor of $e^{i\phi}$ in one direction and $e^{-i\phi}$ in the other. This is known as the Peierls substitution [81], and here specifically represents a convenient gauge choice: the only physical (gauge-invariant) requirement is that the hoppings encircling a flux core (tube) in real space accumulate a phase of $e^{\pm i\phi}$. We orient the line (plane) M containing the magnetic phase [red line in Figure 5.2 (b)] along the x -direction in 2D (along the x - and z -directions in 3D), and choose its linear extent to be of half the linear size (here L_M) of our full system [see also Figure 5.2 (a)–(c)]. While our proofs employ this particular straight-line (plane) magnetic gauge, ultimately, the physical observables obtained in both sections (bound charge, spin, or chiral or helical modes) appear at gauge-invariant locations with topologically quantized values (or multiplicities).

As shown in Figure 5.2 (c), in the thermodynamic limit, the flux core (tube) realizes an interface between the original, unmodified system S (with periodic boundary conditions in y -direction), and a system S' with twisted boundary conditions in y -direction (in the straight-line gauge in Figure 5.2). This follows from noting that in S' realized with the gauge in Figure 5.2, there are a total of L_M bonds in the

positive y direction that cross M and carry a rotated hopping phase of $e^{i\phi}$, and that there are L_M bonds in the negative y direction with a hopping phase rotated by $e^{-i\phi}$.

We now individually analyze S and S' in order to deduce the (gauge-invariant) electronic structure of their interface by using the bulk-boundary (domain-wall) correspondence between S and S' . To begin, let S be described by a gapped Bloch Hamiltonian $\mathcal{H}(k_y)$, where we suppress other momentum labels for notational simplicity. Let L_y be even without loss of generality. As in our previous analysis in Section 5.1.1, with periodic boundary conditions, k_y is here an element of the discrete BZ:

$$\text{BZ}_S = \frac{2\pi}{L_y} \left\{ -\left(\frac{L_y}{2} - 1\right), \dots, 0, \dots, \left(\frac{L_y}{2} - 1\right), \frac{L_y}{2} \right\}, \quad (5.11)$$

where for simplicity, we have chosen units in which the lattice spacings $a_{x,y,z} = 1$. In the case of N occupied bands, the occupied eigenstates of $\mathcal{H}(k_y)$ are given by:

$$\mathcal{H}(k_y) |u_\alpha(k_y)\rangle = E_\alpha(k_y) |u_\alpha(k_y)\rangle, \quad (5.12)$$

where $\alpha = 1 \dots N$. Reexpressing the eigenstates of $\mathcal{H}(k_y)$ using second-quantization:

$$|u_\alpha(k_y)\rangle = c_\alpha^\dagger(k_y) |0\rangle, \quad (5.13)$$

where the orthonormality of the occupied eigenstates $|u_\alpha(k_y)\rangle$ implies that:

$$\{c_\alpha(k_y), c_\beta^\dagger(k_y)\} = \delta_{\alpha\beta}. \quad (5.14)$$

In this construction, the ground state of S again takes the form:

$$|\text{GS}_S\rangle = \prod_{k_y} \prod_{\alpha=1}^{\text{BZ}_S} c_\alpha^\dagger(k_y) |0\rangle. \quad (5.15)$$

Conversely, in S' , the twisted boundary conditions that arise from the flux insertion shift all momenta k_y , such that:

$$\text{BZ}_{S'} = \frac{\phi}{L_y} + \text{BZ}_S. \quad (5.16)$$

Specializing to the (\mathcal{T} -invariant) case of $\phi = \pi$ highlighted in this work, Equations (5.11) and (5.16) combine to realize a finite BZ in which all k_y have become shifted by π/L_y :

$$\text{BZ}_{S'} = \frac{2\pi}{L_y} \left\{ -\left(\frac{L_y - 1}{2}\right), \dots, -\frac{1}{2}, \frac{1}{2}, \dots, \left(\frac{L_y - 1}{2}\right) \right\}. \quad (5.17)$$

Crucially, the finite set $BZ_{S'}$ includes neither $k_y = 0$ nor $k_y = \pi$ [Figure 5.3 (a)]. Using Equation (5.17), the corresponding ground state of S' is then given by:

$$|GS'_{S'}\rangle = \prod_{k_y} \prod_{\alpha=1}^{BZ'_S} c_\alpha^\dagger(k_y) |0\rangle. \quad (5.18)$$

As previously in Section 5.1.1, comparing the ground states of S and S' , we find that a flux core (or tube) can host topologically protected boundary states if $|GS_S\rangle$ and $|GS'_{S'}\rangle$ “differ” (\ominus) by a topologically nontrivial phase [as defined in the text surrounding Equation (5.9)].

In this work, we are focused on insulators with spatial inversion symmetry (\mathcal{I}). The operation of \mathcal{I} takes $k_y \rightarrow -k_y$, such that in both 2D and 3D insulators, there are only two \mathcal{I} -invariant values $k_y = 0, \pi$. Crucially, in 1D and 2D, in the presence of only \mathcal{I} symmetry and lattice translation (and optionally \mathcal{T} symmetry), it has been shown in numerous previous works that, excluding the possibilities of nontrivial Chern numbers and particle-hole-symmetric phases, all strong, OAL, and FTI topological (filling-anomaly) indices are \mathbb{Z}_2 valued [79, 150, 77, 115, 108, 110, 62, 19, 32]. Furthermore, in 1D and 2D in the absence of any symmetries besides lattice translation (Class A of the Altland-Zirnbauer classification [151, 47]), the only topologically nontrivial insulating phases with anomalous (intrinsic) boundary states are 2D Chern insulators. Therefore, by reexpressing generic 2D (3D) insulators as (possibly trivial) k_y -indexed pumping cycles of 1D (2D) insulators [152, 153, 154, 77, 1, 5, 114, 25, 23, 19, 143], we conclude that in all 2D (3D) insulators with only \mathcal{I} symmetry [including OALs and FTIs but excluding, for now, the 3D weak Chern insulators (*i.e.* “unfolded” AXIs) in Reference [155]], *only* the Hamiltonians of the $k_y = 0, \pi$ lines (planes) are topologically equivalent to 1D (2D) insulators with topological boundary modes. Therefore, without loss of generality, in 2D and 3D \mathcal{I} -symmetric insulators with threaded π -flux, we conclude that the only possible topologically nontrivial contributions to the difference $|GS_S\rangle \ominus |GS'_{S'}\rangle$ can come from $\mathcal{H}(k_y = 0, \pi)$ [Equations (5.15) and (5.18)]. Specifically, the real-space interface between S and S' in Figure 5.2 (c) carries the summed (superposed) ($d - 1$)-D topologies of $\mathcal{H}(0)$ and $\mathcal{H}(\pi)$. While the location of this interface is gauge-dependent, the location of its boundaries, the flux cores (and tubes), are gauge-independent. Therefore, exploiting that topological phases form an additive group [148], we formally express the ground state of the interface between S and S' as:

$$|GS_S\rangle \ominus |GS'_{S'}\rangle \approx \left[\prod_{\alpha=1}^N c_\alpha^\dagger(0) \otimes \prod_{\alpha=1}^N c_\alpha^\dagger(\pi) \right] |0\rangle, \quad (5.19)$$

with respect to the vacuum $|0\rangle$, and where all products are appropriately antisymmetrized. To summarize, the *boundary* of the interface between S and S' will only exhibit (gauge-invariant) topological (anomalous) boundary modes if $\mathcal{H}(0) \otimes \mathcal{H}(\pi)$ is topologically equivalent to a phase with anomalous boundary modes (*i.e.*, a TI, TCI, or filling-anomalous OAL or FTI).

Unlike previously in Section 5.1.1, Equation (5.19) implies the possibility that $|GS_S\rangle \ominus |GS_{S'}\rangle$ is topologically trivial even though $\mathcal{H}(0, \pi)$ are individually topologically nontrivial. Specifically, if the topology of $\mathcal{H}(0, \pi)$ is diagnosed by a set of indices $(\mathbb{Z}_2)^n$, as is the case for 1D and 2D insulators with only \mathcal{I} (and possibly additionally \mathcal{T}) symmetry and trivial Chern numbers [79, 150, 77, 115, 108, 110, 62, 19, 32], then, if both $\mathcal{H}(0)$ and $\mathcal{H}(\pi)$ have the same \mathbb{Z}_2 topology, $\mathcal{H}(0) \otimes \mathcal{H}(\pi)$ is necessarily topologically trivial. Therefore, with only \mathcal{I} (and optionally \mathcal{T}) symmetry, if the Chern numbers of $\mathcal{H}(0, \pi)$ are zero, then Equation (5.19) implies that $|GS_S\rangle \ominus |GS_{S'}\rangle$ is only topologically nontrivial if $\mathcal{H}(0)$ and $\mathcal{H}(\pi)$ are topologically distinct, which can only occur in a strong topological (insulating) phase in which k_y indexes a nontrivial pumping cycle [152, 154, 153, 1, 5, 114, 25, 23, 19]. We note that if we allow $\mathcal{H}(0, \pi)$ to more generally exhibit \mathbb{Z} - or \mathbb{Z}_n -valued topological indices, such as, respectively, nontrivial (mirror) Chern numbers [156, 152, 155, 92, 157] or particle-hole-asymmetric OAL and FTI indices [143, 144, 146, 147, 32], then the relationship between $|GS_S\rangle \ominus |GS_{S'}\rangle$ and strong bulk topology becomes more subtle, and is beyond the scope of the present work.

Finally, while in this section we have restricted to flux tubes in 2D and 3D insulators, it is straightforward to generalize our arguments to threaded π -flux tubes in insulators with arbitrarily large dimensionality d . Specifically, to generalize the Peierls substitution employed in this section (Figure 5.1) to higher dimensions, we replace the 1D line or 2D plane M with modified hoppings in Figure 5.2 (c) with a $(d - 1)$ -D *hyperplane* with constant y -coordinate. Even if the boundary between S and S' has a dimensionality larger than 2, the analysis employed in this section to derive and analyze Equation (5.19) still applies without further modification [though finer analysis is required if $\mathcal{H}(0, \pi)$ exhibits \mathbb{Z} - or \mathbb{Z}_n -valued ($n > 2$) topological indices].

5.1.3 Screw Dislocations in 3D Crystals

Here, we derive the topological relations governing the appearance of bound states arising from the insertion of a set of screw dislocations into an insulating system. Because the lattice displacements in screw dislocations are more complicated to visualize than those in edge dislocations [145], we restrict consideration in this

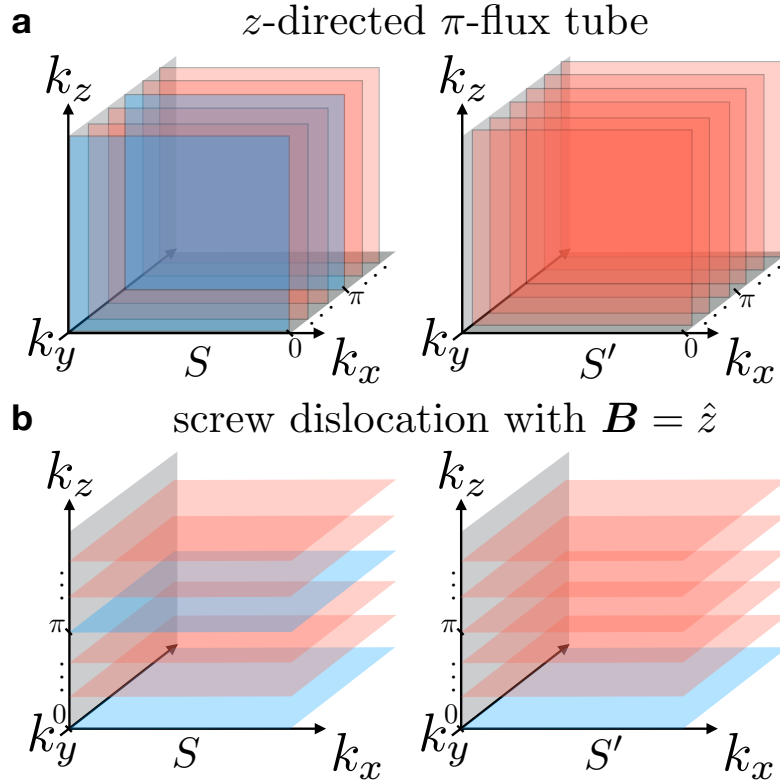


Figure 5.3: 3D Brillouin zones for the systems S and S' as respectively defined in Sections 5.1.2 and 5.1.3 for the cases of (a) a z -directed π -flux tube and (b) a screw dislocation with Burgers vector $\mathbf{B} = \hat{z}$. (a) A z -directed flux tube forms an interface between a pristine system S and, in the gauge in Figure 5.1, a system S' in which all momenta k_y are shifted by π/L_y [Equation (5.16)]. Assuming L_y to be even and S and S' to be \mathcal{I} -symmetric, S contains the (possibly topologically nontrivial) Brillouin zone planes at $k_y = 0, \pi$ (indicated in blue), in addition to planes at intermediate momenta (indicated in red), which are generically equivalent to 2D insulators without edge or corner states (discounting for now the case of weak Chern insulators). In contrast, the discrete BZ of S' [Equation (5.17)] only contains the intermediate values $k_y \neq 0, \pi$. Therefore, an interface between S and S' whose boundary is a π -flux tube will exhibit (given the preservation of bulk symmetries) the (gauge-invariant) boundary modes of the combined (superposed [148]) topologies of the Hamiltonians of the $k_y = 0, \pi$ planes of S [Equation (5.19)]. (b) A screw dislocation with Burgers vector \hat{z} forms an interface between a pristine system S and a system S' in which the momenta k_y are shifted by k_z -dependent amounts k_z/L_y [Equation (5.27)]. Assuming $L_{y,z}$ to be even, S contains the (possibly topologically nontrivial) BZ planes at $k_z = 0, \pi$ (indicated in blue), in addition to planes at intermediate momenta (indicated in red), which are, like those in (a), generically equivalent to 2D insulators without edge or corner states. In contrast to that of S , the discrete BZ of S' only contains the \mathcal{I} -symmetric plane $k_z = 0$, and does not contain $k_z = \pi$ [Equation (5.31)]. Therefore, an interface between S and S' whose boundary is a screw dislocation with an odd-integer Burgers vector will exhibit (given the preservation of bulk symmetries) the (gauge-invariant) boundary modes of the $k_z = \pi$ plane of the pristine insulator S [Equation (5.32)].

section to the more familiar, experimentally relevant case of screw dislocations in 3D insulating crystals. Unlike the edge dislocations analyzed in Section 5.1.1, a screw dislocation corresponds to a dislocation line of displacements that is parallel to its Burgers vector.

We will find it useful to briefly introduce the notion of screw chirality. For a screw dislocation, the direction of net displacement is indicated by a sense vector [145] \mathbf{s} that is parallel to \mathbf{B} . The chirality C of a particular screw dislocation is then indicated by:

$$C = \text{sign}[\mathbf{B} \cdot \mathbf{s}]. \quad (5.20)$$

If the insertion of the screw dislocations preserves an inversion center, then the action of \mathcal{I} exchanges the locations and chiralities of the two screws, in agreement with well-established notion that \mathbf{s} transforms as a vector (\mathcal{I} -odd) and \mathbf{B} transforms as a pseudovector (\mathcal{I} -even), such that C transforms as a pseudoscalar [145].

We therefore consider a pair of $\mathbf{B} = \hat{z}$ screw dislocations, one left- and the other right-handed. To implement a right- (left-) handed screw dislocation with Burgers vector $\mathbf{B} = \hat{z}$, we multiply the lattice hoppings encircling the dislocation in the (x, y) -plane by an accumulated phase of e^{ik_z} (e^{-ik_z}), which originates from the net dislocation translation in the positive (negative) z -direction [145]. This is reminiscent of the Peierls substitution for π -flux tubes [81] previously employed in Section 5.1.2. Specifically, with periodic boundary conditions in z -direction, a pair of screw dislocations is functionally equivalent to modifying the Bloch Hamiltonian $\mathcal{H}(\mathbf{k})$ with a momentum-dependent flux $\phi = k_z$. Therefore, we can model a $\mathbf{B} = \hat{z}$ screw dislocation in a 3D insulator as inhabiting the (linear) boundary of a 2D interface between a system S with periodic boundary conditions in all directions and a system S' with twisted boundary conditions (TBC) in the y -direction for which the twist phase factor is momentum-dependent $e^{\pm ik_z}$ (i.e., the same geometry as the flux tubes in Figure 5.1).

We again individually analyze S and S' in order to deduce the (gauge-invariant) electronic structure of their interface by using the bulk-boundary (domain-wall) correspondence between S and S' . To begin, let S be described by a gapped Bloch Hamiltonian $\mathcal{H}(k_y, k_z)$, where we suppress the momentum k_x for notational simplicity. Let L_y and L_z be even without loss of generality. With periodic boundary conditions, k_y is an element of the discrete BZ:

$$\text{BZ}_{S, k_y} = \frac{2\pi}{L_y} \left\{ -\left(\frac{L_y}{2} - 1\right), \dots, 0, \dots, \left(\frac{L_y}{2} - 1\right), \frac{L_y}{2} \right\}, \quad (5.21)$$

where for simplicity, we have chosen units in which the lattice spacings $a_{x,y,z} = 1$, and where the k_z superscript in Equation (5.21) implies a (here trivial) dependence

of the discretization of k_y on k_z . Unlike previously in Sections 5.1.1 and 5.1.2, k_z is here also an element of a discrete BZ:

$$\text{BZ}_{S,k_z} = \frac{2\pi}{L_z} \left\{ -\left(\frac{L_z}{2} - 1\right), \dots, 0, \dots, \left(\frac{L_z}{2} - 1\right), \frac{L_z}{2} \right\}. \quad (5.22)$$

In the case of N occupied bands, the occupied eigenstates of $\mathcal{H}(k_y, k_z)$ are given by:

$$\mathcal{H}(k_y, k_z) |u_\alpha(k_y, k_z)\rangle = E_\alpha(k_y, k_z) |u_\alpha(k_y, k_z)\rangle, \quad (5.23)$$

where $\alpha = 1 \dots N$. Reexpressing the eigenstates of $\mathcal{H}(k_y, k_z)$ using second-quantization:

$$|u_\alpha(k_y, k_z)\rangle = c_\alpha^\dagger(k_y, k_z) |0\rangle, \quad (5.24)$$

where the orthonormality of the occupied eigenstates $|u_\alpha(k_y, k_z)\rangle$ implies that:

$$\{c_\alpha(k_y, k_z), c_\beta^\dagger(k_y, k_z)\} = \delta_{\alpha\beta}. \quad (5.25)$$

In this construction, the ground state of S takes the form:

$$|\text{GS}_S\rangle = \prod_{k_z}^{\text{BZ}_{S,k_z}} \prod_{k_y}^{\text{BZ}_{S,k_y}} \prod_{\alpha=1}^N c_\alpha^\dagger(k_y, k_z) |0\rangle. \quad (5.26)$$

with respect to the vacuum $|0\rangle$, and where all products are appropriately antisymmetrized.

Conversely, in S' , the twisted boundary conditions that arise from the screw dislocations shift all momenta k_y by a k_z -dependent amount, such that k_y in S' is an element of the discrete BZ:

$$\text{BZ}_{S',k_y}^{k_z} = \frac{k_z}{L_y} + \text{BZ}_{S,k_y}. \quad (5.27)$$

where BZ_{S,k_y} is given in Equation (5.21). However, even though the screw dislocations in this section are z -directed [Figure 5.3 (b)], they *do not* affect the discretization of k_z , such that:

$$\text{BZ}_{S',k_z} = \text{BZ}_{S,k_z}, \quad (5.28)$$

where BZ_{S,k_z} is given in Equation (5.22). The corresponding ground state of S' is then given by:

$$|\text{GS}'_S\rangle = \prod_{k_z}^{\text{BZ}_{S',k_z}} \prod_{k_y}^{\text{BZ}_{S',k_y}^{k_z}} \prod_{\alpha=1}^N c_\alpha^\dagger(k_y, k_z) |0\rangle. \quad (5.29)$$

Crucially, if we restrict to 3D insulators with only \mathcal{I} (and optionally \mathcal{T}) symmetry, Equations (5.27), (5.28), and (5.29) can be reformulated to realize a simple result. Namely, first focusing on the $k_z = \pi$ plane in S' , Equation (5.27) implies that the lines $k_y = 0, \pi$ are absent in the discrete BZ. Therefore, the action of \mathcal{I} (and \mathcal{T}) symmetry no longer takes any of the points in the $k_z = \pi$ plane back to itself, such that in S' , the $k_z = \pi$ plane can no longer exhibit topology enforced by \mathcal{I} or \mathcal{T} . Therefore, when restricted to \mathcal{I} -symmetric insulators, the ground state of S' can be adiabatically deformed from Equation (5.29) to:

$$|GS'_S\rangle = \prod_{\tilde{k}_z} \prod_{\alpha=1}^N c_\alpha^\dagger(\tilde{k}_z) |0\rangle, \quad (5.30)$$

where \tilde{k}_z is now an element of a discrete BZ:

$$\tilde{\mathbb{BZ}}_{S', \tilde{k}_z} = \frac{2\pi}{L_z} \left\{ -\left(\frac{L_z}{2} - \frac{1}{2}\right), \dots, 0, \dots, \left(\frac{L_z}{2} - \frac{1}{2}\right) \right\}. \quad (5.31)$$

that *does not* contain $\tilde{k}_z = \pi$. Specifically, because the topology of a 3D \mathcal{I} - (and optionally \mathcal{T} -) symmetric insulator (that lacks additional rotation and reflection symmetries) is entirely determined by the topologies of the 2D Hamiltonians of the $k_{x,y,z} = 0, \pi$ planes [see the discussion preceding Equation (5.19)], then the ground state of S' can only contain topologically nontrivial contributions from the \mathcal{I} -symmetric Hamiltonian of the $k_z = 0$ ($\tilde{k}_z = 0$) plane.

As previously in Sections 5.1.1 and 5.1.2, we next compare the topology of S and S' . Using the definition of “subtraction” (\ominus) established in the text surrounding Equation (5.9), we find that Equation (5.29) implies that a screw dislocation can host topologically protected boundary states if $|GS_S\rangle$ and $|GS_{S'}\rangle$ “differ” (\ominus) by a topologically nontrivial phase. This can be summarized by stating that the gauge-invariant screw-dislocations represent the boundary of a 2D insulator whose ground state is given by:

$$|GS_S\rangle \ominus |GS_{S'}\rangle = \prod_{\alpha=1}^N c_\alpha^\dagger(k_z = \pi) |0\rangle. \quad (5.32)$$

The screw dislocations therefore bind the 1D or 0D boundary modes of the Hamiltonian of the $k_z = \pi$ plane of S , provided that the dislocation geometry preserves \mathcal{I} symmetry. Generalizing to arbitrarily oriented screw dislocations, we recover Equation (5.10).

5.2 Edge and screw dislocations

In this section, we will present numerical calculations for representative 2D and 3D insulators that confirm the dislocation responses discussed in this chapter of the thesis. First, we will detail the dislocation response of 2D (Section 5.2.1) and 3D (Section 5.2.2) insulators with broken \mathcal{T} symmetry. Then, we will detail analogous calculations demonstrating the dislocation response of \mathcal{T} -symmetric 2D (Section 5.2.3) and 3D (Section 5.2.4) insulators.

5.2.1 2D Point Dislocations in the Absence of \mathcal{T} Symmetry

In this section, we demonstrate the dislocation response of 2D insulators with broken \mathcal{T} symmetry. We begin by comparing the minimal tight-binding model for an inversion- (\mathcal{I} -) symmetric Chern insulator with Chern number $|C| = 1$ (the inversion-symmetric version of the Chern insulator introduced in Section 2.1.1.2) to that of a stack (array) of Su-Schrieffer-Heeger (SSH) chains (introduced in Section 2.1.1.1). Consider the Bloch Hamiltonian:

$$\mathcal{H}(\mathbf{k}) = \sin k_x \sigma_x + \xi \sin k_y \sigma_y + [\alpha \cos k_x + \xi (1 + \beta \cos k_y)] \sigma_z, \quad (5.33)$$

defined on a square lattice, where σ_i , $i = 0, x, y, z$ are Pauli matrices indexing spinless valence s and conduction p orbitals on each site, and $\xi = 0, 1$ and $\alpha, \beta = \pm 1$ are parameters that can be tuned to realize different topological phases. Inversion symmetry (\mathcal{I}) is represented by:

$$\mathcal{I} : \mathcal{H}(\mathbf{k}) \rightarrow \sigma_z \mathcal{H}(-\mathbf{k}) \sigma_z. \quad (5.34)$$

At half-filling there is a single occupied band with the Bloch eigenstates $|u(\mathbf{k})\rangle$. At the four TRIMs $\bar{\mathbf{k}}$ of the 2D Brillouin zone, here defined by $\mathcal{I}\bar{\mathbf{k}} = \bar{\mathbf{k}}$ because \mathcal{T} symmetry is absent [104, 105], we can define the inversion eigenvalue $\lambda_{\bar{\mathbf{k}}}$ of the occupied state $|u(\bar{\mathbf{k}})\rangle$ as:

$$\mathcal{I} |u(\bar{\mathbf{k}})\rangle = \lambda_{\bar{\mathbf{k}}} |u(\bar{\mathbf{k}})\rangle, \quad (5.35)$$

where $\mathcal{I}^2 = 1$ implies that $\lambda_{\bar{\mathbf{k}}} = \pm 1$. For $\alpha = \beta = 0$ and $\xi = 0, 1$, Equation (5.33) is topologically trivial, and its occupied subspace is composed of a single band with inversion eigenvalues $\lambda_{\bar{\mathbf{k}}} = 1$ at all TRIM points.

For $\xi = 1$, $\mathcal{H}(\mathbf{k})$ describes a symmetry-indicated $|C| = 1$ Chern insulator [109, 157, 85, 1, 5, 158] that differs from a trivial (unobstructed) atomic limit by a single sign-change of the inversion eigenvalue of the occupied band at $\bar{\mathbf{k}} = (1 + \alpha, 1 + \beta)\pi/2$. To determine the topology of $\mathcal{H}(\mathbf{k})$, we exploit that the Chern number modulo 2 of

a 2D, \mathcal{T} -broken insulator is indicated by the product of the inversion eigenvalues of the occupied bands [109, 157, 85, 1, 5, 158]. Here, and throughout this chapter, we consider the process of closing a gap and inverting bands to be a *band inversion*, and restrict focus in this and the following section (Section 5.3) to band inversions that exchange the inversion eigenvalues of the valence and conduction bands. We further emphasize that this focus on band inversions, rather than the absolute sign of the inversion eigenvalues, is justified, because most tight-binding models, including our implementation of Equation (5.33), exhibit the same boundary and dislocation bound states under the symmetry redefinition [91]: $\mathcal{I} \rightarrow \mathcal{I}'$ where $\mathcal{I}' = -\sigma_z$.

For $\xi = 0$, $\mathcal{H}(\mathbf{k})$ becomes equivalent to an array of identical x -directed SSH chains indexed by k_y whose polarization (Berry phase) is indicated [85] by the inversion eigenvalues at $k_x = 0, \pi$. More generally, in this thesis, we define a stack or array as an insulating phase whose Bloch Hamiltonian has the same symmetry eigenvalues along a specified momentum-space direction k_i (reciprocal to a real-space direction i), and therefore the same $(d-1)$ -D topological indices in BZ surfaces indexed by k_i . For example, a 3D WTI is equivalent to a stack of 2D TIs [1, 5, 159, 2].

Having established the properties of the Hamiltonian of the pristine system [Equation (5.33)], we now probe the dislocation response. We introduce a pair of 0D dislocations with Burgers vector $\mathbf{B} = \hat{y}$. Through Equation (5.10), we deduce that each dislocation realizes an interface between two insulators S and S' that “differ” by the Hamiltonian of the $k_y = \pi$ plane of Equation (5.33):

$$\mathcal{H}(k_x, \pi) = \sin k_x \sigma_x + [\alpha \cos k_x + \xi(1 - \beta)]\sigma_z. \quad (5.36)$$

Setting, $\alpha = -1$, $\mathcal{H}(k_x, \pi)$ describes an \mathcal{I} -symmetric SSH chain with a trivial (nontrivial) polarization for $\xi = 1$, $\beta = -1$ ($\xi = 1$, $\beta = +1$ and $\xi = 0$) when measured with respect to the valence s orbitals.

For our numerical implementation, we begin with a square lattice Λ of size $|\Lambda| = L^2$ with $L = 16$ and periodic boundary conditions (PBC). We then remove a line of 8 sites to create a pair of dislocations with Burgers vector $\mathbf{B} = \hat{y}$. We note that this is the minimal number of dislocations compatible with (untwisted) PBC: a single point dislocation introduces a fault line in the lattice that has to terminate either at a boundary or at another dislocation.

Next, we analyze the system with two dislocations using the terminology established in Section 5.1.1. We begin by denoting the pristine real-space Hamiltonian corresponding to the model in Equation (5.33) as H . H contains only nearest-neighbor hoppings and has $(2L^2 \times 2L^2) = (512 \times 512)$ elements. Let $H_{a,b}$ be the

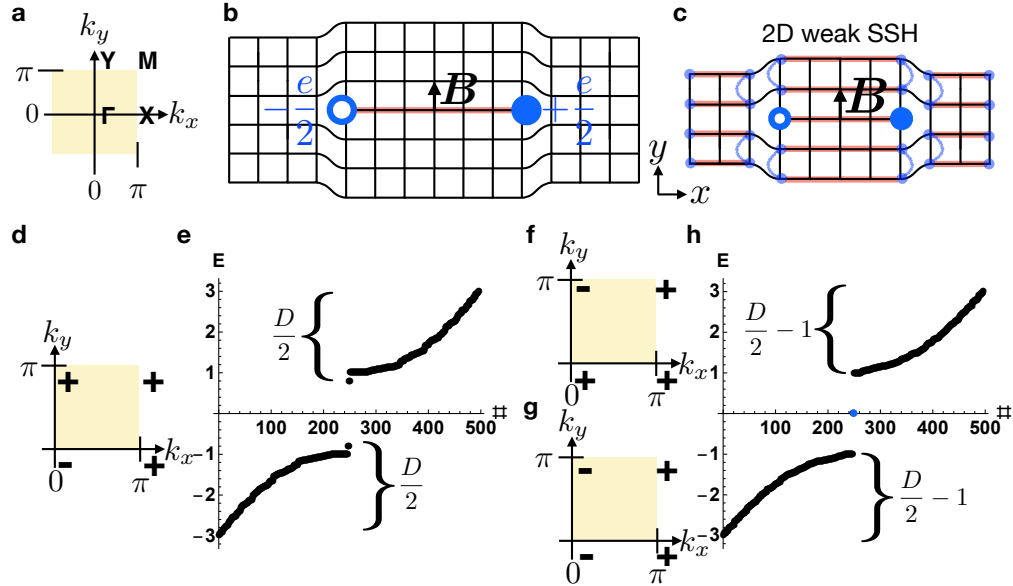


Figure 5.4: 0D dislocation bound states in 2D insulators with inversion (\mathcal{I}) symmetry. (a) The bulk BZ of a 2D rectangular crystal with only \mathcal{I} symmetry. (b) A pair of 0D dislocations with Burgers vector $\mathbf{B} = \hat{y}$ that are related by global \mathcal{I} symmetry and bind anomalous fractional charges. (c) A pair of fractionally charged 0D dislocations can be obtained by coupling an array of 1D x -directed SSH chains along the y -direction; two midgap states, equivalent to the end states of a nontrivial SSH chain, remain bound to the dislocation cores. (d)–(h) Bulk inversion eigenvalues and energy spectra with periodic boundary conditions (PBC) for a pair of dislocations with $\mathbf{B} = \hat{y}$ inserted into 2D insulators whose occupied bands carry the inversion eigenvalues in (d), (f), and (g), respectively. (d),(e) characterize a $|C| = 1$ Chern insulator with band inversion at Γ , (f), (h) characterize a $|C| = 1$ Chern insulator with band inversion at Y , and (g), (h) characterize a weak y -directed array of SSH [79, 150] chains. Anomalous 0D defect states with charge $\pm e/2$ are present in (f) and (g), but not in (d), and are equivalent to the end states of an \mathcal{I} -symmetric, \mathcal{T} -broken SSH chain [79, 150] [Equation (5.36), red line in (b)], and thus persist under the relaxation of particle-hole symmetry in the form of a filling anomaly [100, 160, 161, 19, 143].

components of the $(2|A| \times 2|B|)$ -dimensional submatrix that couples lattice sites taken from the sets A and B . $H_{a,b}$ is the matrix obtained by removing all of the rows from the $(2L^2 \times 2L^2)$ matrix H that do not couple to lattice sites within the set A . Similarly, we remove all of the columns in $H_{a,b}$ that do not couple to the set B . We next introduce the shorthand notation:

$$\sum_{a,b} H_{a,b} |a\rangle \langle b| = \sum_{r \in A} \sum_{r' \in B} \sum_{\mu, \nu \in \{1,2\}} H_{r,r'}^{\mu,\nu} |r, \mu\rangle \langle r', \nu|, \quad (5.37)$$

where $|r, \mu\rangle$ denotes the basis state at position $r \in \Lambda$ with an orbital indexed by μ [the Bloch Hamiltonian (5.33) is a (2×2) matrix in the basis of spinless s and p orbitals].

Using the site labeling U , M , and D established in Figure 5.1 (a), we will now detail how we numerically implement a pair of $\mathbf{B} = \hat{y}$ dislocations. Defining $O = U \cup M \cup D$ and $\bar{O} = \Lambda \setminus O$, we form the expression:

$$H = \sum_{\bar{o}, \bar{o}'} H_{\bar{o}, \bar{o}'} |\bar{o}\rangle \langle \bar{o}'| + \sum_{o, \bar{o}} H_{o, \bar{o}} |o\rangle \langle \bar{o}| + \sum_{\bar{o}, o} H_{\bar{o}, o} |\bar{o}\rangle \langle o| + \sum_{o, o'} H_{o, o'} |o\rangle \langle o'|. \quad (5.38)$$

Noting that H only contains nearest-neighbor hoppings, we then expand Equation (5.38):

$$\begin{aligned} \sum_{o, o'} H_{o, o'} |o\rangle \langle o'| &= \sum_{u, u'} H_{u, u'} |u\rangle \langle u'| \\ &+ \sum_{m, m'} H_{m, m'} |m\rangle \langle m'| + \sum_{d, d'} H_{d, d'} |d\rangle \langle d'| \\ &+ \sum_{u, m} H_{u, m} |u\rangle \langle m| + \sum_{m, u} H_{m, u} |m\rangle \langle u| \\ &+ \sum_{m, d} H_{m, d} |m\rangle \langle d| + \sum_{d, m} H_{d, m} |d\rangle \langle m|. \end{aligned} \quad (5.39)$$

To introduce a pair of dislocations, we form the Hamiltonian \tilde{H} , which is defined on $\tilde{\Lambda} = \Lambda \setminus M$, i.e., the lattice obtained by taking out the set of sites M . Defining $\tilde{O} = U \cup D$ and $\tilde{\bar{O}} = \tilde{\Lambda} \setminus \tilde{O}$, \tilde{H} can be expanded as:

$$\begin{aligned} \tilde{H} &= \sum_{\bar{\tilde{o}}, \bar{\tilde{o}'}} H_{\bar{\tilde{o}}, \bar{\tilde{o}'}} |\bar{\tilde{o}}\rangle \langle \bar{\tilde{o}'}| + \sum_{\bar{o}, \bar{\tilde{o}}} H_{\bar{o}, \bar{\tilde{o}}} |\bar{o}\rangle \langle \bar{\tilde{o}}| \\ &+ \sum_{\bar{\tilde{o}}, \bar{o}} H_{\bar{\tilde{o}}, \bar{o}} |\bar{\tilde{o}}\rangle \langle \bar{o}| + \sum_{\bar{o}, \tilde{o}'} H_{\bar{o}, \tilde{o}'} |\bar{o}\rangle \langle \tilde{o}'|, \end{aligned} \quad (5.40)$$

in which we can further expand:

$$\begin{aligned} \sum_{\tilde{o}, \tilde{o}'} H_{\tilde{o}, \tilde{o}'} |\tilde{o}\rangle \langle \tilde{o}'| &= \sum_{u, u'} H_{u, u'} |u\rangle \langle u'| + \sum_{d, d'} H_{d, d'} |d\rangle \langle d'| \\ &\quad + \sum_{u, d} \tilde{H}_{u, d} |u\rangle \langle d| + \sum_{d, u} \tilde{H}_{d, u} |d\rangle \langle u|. \end{aligned} \quad (5.41)$$

Finally, we conclude that:

$$\tilde{H}_{u, d} = H_{u, m}, \quad \tilde{H}_{d, u} = H_{d, m}, \quad (5.42)$$

such that the matrix elements of \tilde{H} between sites in U and sites in D are given by those of H between U and M . To summarize, Equations (5.38) through (5.42) describe how, in a tight-binding model with nearest-neighbor hoppings and orthogonal lattice vectors, we numerically implement a pair of point dislocations by first removing a line of sites from a pristine lattice, and then subsequently reconnecting the two lines above and below the missing line.

After following the prescription in Equations (5.38) through (5.42), we obtain a Hamiltonian \tilde{H} that contains two $\mathbf{B} = \hat{y}$ point dislocations on the lattice $\tilde{\Lambda}$ and $[2(L^2 - 8) \times 2(L^2 - 8)] = (496 \times 496)$ elements. We will now discuss the electronic structure of \tilde{H} in detail for characteristic values of ξ and β .

5.2.1.1 $\xi = 1, \beta = -1$: Chern insulator with band inversion at Γ

This case corresponds to an inversion-symmetry-indicated $|C| = 1$ Chern insulator [109, 157, 85, 1, 5, 158] driven by a single band inversion at $\mathbf{k} = (0, 0)$ in Equation (5.33). The bulk characterizes a strong topological phase. Because the bands at X , Y , and M are uninverted relative to an atomic insulator with orbitals at the $1a$ position, Equation (5.36) describes a trivial insulator and the dislocations do not bind anomalous charges ($q \bmod e = 0$). In Figure 5.4 (d),(e), we respectively show the inversion eigenvalues of the occupied bands and the dislocation spectrum, which does not exhibit a filling anomaly or midgap dislocation bound states.

5.2.1.2 $\xi = 1, \beta = +1$: Chern insulator with band inversion at Y

This case describes a $|C| = 1$ Chern insulator driven by band inversion at the Y point [109, 157, 85, 1, 5, 158] [Figure 5.4 (a)]. Relative to the initial $1a$ atomic insulator, the band inversion at Y has changed not only the strong index (2D Chern number), but has also induced a transition of the Hamiltonian (5.36) to the non-trivial phase that is characterized by a nonvanishing and quantized polarization [the

inversion eigenvalues of the occupied bands are shown in Figure 5.4 (f), in the non-trivial phase they are of opposite sign at $k_x = 0, \pi$ [85]]. The dislocation response is therefore nontrivial. Correspondingly, in the dislocation spectrum [Figure 5.4 (h)], we observe one midgap localized zero mode per dislocation. The zero modes are protected by the chiral (*i.e.*, unitary particle-hole) symmetry Π , which is defined through the action:

$$\Pi : \mathcal{H}(k_x, \pi) \rightarrow \sigma_y \mathcal{H}(k_x, \pi) \sigma_y, \quad (5.43)$$

such that here, Π is a symmetry of $\mathcal{H}(k_x, \pi)$ if

$$\Pi \mathcal{H}(k_x, \pi) \Pi^{-1} = \sigma_y \mathcal{H}(k_x, \pi) \sigma_y = -\mathcal{H}(k_x, \pi). \quad (5.44)$$

Crucially, if we were to relax Π symmetry, the midgap states could be pushed out of the gap. However, if we preserve \mathcal{I} symmetry while breaking Π , then $e/2$ end charges would still remain bound to the dislocations [162], in a generalization of the conclusions of Goldstone and Wilczek [100, 160, 161].

Equivalently, in the absence of chiral symmetry, we can also identify the nontrivial topology by counting the number of states that are occupied up to a given Fermi level in the gap. Let $\tilde{\mathcal{H}}$ be a $(D \times D)$ matrix [in our numerics, $D = 496$, as explained in the text following Equation (5.42)]. Comparing Figures 5.4 (e) and (h), we observe that they differ by the presence of two midgap states and absence of one state from each of the valence and conduction bands. When chiral symmetry is broken, the energy of the midgap states can be shifted, but only in a manner that preserves \mathcal{I} symmetry, leaving the two states degenerate in the thermodynamic limit. This implies that any gapped Fermi level that encloses either $(D/2 - 1)$ or $(D/2 + 1)$ occupied states indicates a nontrivial topology, whereas a Fermi level enclosing $D/2$ occupied states indicates trivial bulk topology [this is also detailed in Figures 5.1 (b),(c)]. More generally, the presence of anomalous 0D states in arbitrary dimensions can be diagnosed in a similar manner by constructing a 0D system with a boundary that preserves a global point group symmetry and observing an imbalance in the number of states above and below the gap that cannot be resolved without breaking a symmetry (*i.e.*, a filling anomaly) [23, 19, 143, 32, 144, 146, 147].

5.2.1.3 $\xi = 0$: Weak Array of x -Directed SSH Chains

In this case, $\mathcal{H}(\mathbf{k})$ is independent of β , and Equation (5.33) describes a y -directed array of identical x -directed SSH chains. Specifically, the Hamiltonian [Equation (5.33) with $\xi = 0$] is in this case completely independent of k_y . For each SSH chain, the nontrivial polarization is indicated by the difference in the inversion

eigenvalues of the occupied band at $k_x = 0, \pi$ [79, 149, 150, 163, 85, 77, 108]. This case is an example of weak topology, because the Hamiltonian $\mathcal{H}(\mathbf{k})$ can be deformed into a real-space array of decoupled 1D chains without breaking a symmetry or closing the bulk gap. Relative to the initial 1a atomic insulator, $\mathcal{H}(\mathbf{k})$ features band inversions at Γ and Y [the inversion eigenvalues are shown in Figure 5.4 (g)], such that the bulk exhibits a trivial symmetry-indicated Chern number $C \bmod 2 = 0$, and is irrep-equivalent to an OAL from 1a $[(x, y) = (0, 0)]$ to 1c $[(x, y) = (1/2, 0)]$. This implies that even though the bulk is an OAL, the dislocation response is nontrivial (The Hamiltonian (5.36) is again in the nontrivial phase). Correspondingly, in the dislocation spectrum [Figure 5.4 (h)], we observe a filling anomaly.

For the present case of an array of SSH chains, we can also understand the existence of dislocation midgap states intuitively without invoking the more general theory used to derive Equation (5.36). As depicted in Figure 5.4 (c), the dislocations introduce an uncoupled SSH chain into the system whose end states become the dislocation bound states. As long as the “left-over” SSH chain contains an inversion center, its end states also induce a system filling anomaly, consistent with the numerical results shown in Figure 5.4 (h).

5.2.2 3D Screw Dislocations in the Absence of \mathcal{T} Symmetry

In this section, we demonstrate the screw dislocation response of 3D insulators with broken \mathcal{T} symmetry. We begin by comparing the minimal tight-binding model for an axion insulator (AXI), introduced in Section 2.2.4, to that of a weak stack of 2D fragile topological insulators [62, 19] (FTIs), where we retain inversion symmetry in all cases. Consider the Bloch Hamiltonian:

$$\begin{aligned} \mathcal{H}(\mathbf{k}) = & \sin k_x \tau_z \sigma_x + \sin k_y \tau_z \sigma_y + \xi \sin k_z \tau_z \sigma_z \\ & + [\alpha \cos k_x + \beta \cos k_y + \xi (2 + \gamma \cos k_z)] \tau_x \sigma_0 \\ & + \xi \delta (\tau_x \sigma_x + \tau_x \sigma_y + \tau_x \sigma_z), \end{aligned} \quad (5.45)$$

defined on a square lattice. In Equation (5.45), τ_i and σ_i , $i = 0, x, y, z$ are respectively two sets of Pauli matrices indexing sublattice and orbital degrees of freedom, $\xi = 0, 1$ and $\alpha, \beta, \gamma = \pm 1$ are parameters that can be tuned to realize different topological phases, and δ is a small parameter that gaps out the bulk (we will use $\delta = 1/4$ in all calculations). We note that when $\delta = 0$, Equation (5.45) is instead the Hamiltonian of two uncoupled 3D Weyl semimetals. Recall that throughout this thesis, we abbreviate the Kronecker product of Pauli matrices as $\tau_i \otimes \sigma_j \equiv \tau_i \sigma_j$.

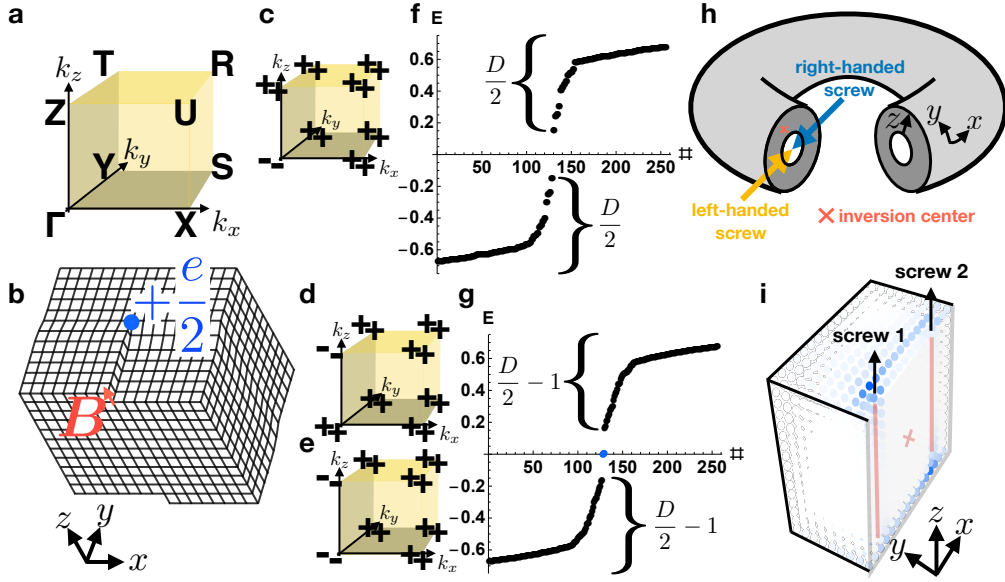


Figure 5.5: 3D screw dislocation bound states in 3D insulators with inversion (\mathcal{I}) symmetry.

(a) The bulk BZ of a 3D rectangular crystal with only \mathcal{I} symmetry. (b) A screw dislocation in this crystal with Burgers vector $B = \hat{z}$ in a geometry with open boundary conditions in all directions. (c)–(g) Bulk inversion eigenvalues and hollow-doughnut-boundary-condition (HDBC) [(h)] energy spectra for the defect in (b) when the crystal with the BZ in (a) is equivalent to (c),(f) an \mathcal{I} -symmetric axion insulator (AXI) [26, 23, 25, 66, 43, 94, 62, 95, 49, 96, 97, 19, 98] with double band inversion at Γ , (d),(g) an AXI with double band inversion at Z , and (e),(g) a weak z -directed stack of \mathcal{I} -symmetric 2D FTIs with $\pm e/2$ corner charges [62, 19]. The HDBC geometry is closely related to the “Corbino doughnut” geometry employed in Reference [5] to characterize 3D TIs; however, here, we thread screw dislocations (and later flux tubes) in a different arrangement than in Reference [5]. In the absence of dislocations, the HDBC geometry does not have any hinges, and so it exhibits the same energy spectrum whether the bulk is topologically equivalent to a trivial insulator or an AXI. In (f),(g), only the 256 lowest-lying states are shown. Anomalous 0D states with charge $\pm e/2$ are present on two of the four dislocation ends in (d) and (e), but not in (c), and are equivalent to the corner states of an \mathcal{I} -symmetric 2D FTI, and thus persist under the relaxation of particle-hole symmetry [62, 19, 143]. (i) Real-space resolved absolute square of the midgap eigenstates shown in (g) for the model in Equation (5.45) on a $16 \times 16 \times 16$ lattice. \mathcal{I} -related bound states appear on two of the four screw dislocation ends. The inversion center in (i) is marked by a red X.

In Equation (5.45), \mathcal{I} symmetry is represented by:

$$\mathcal{I} : \mathcal{H}(\mathbf{k}) \rightarrow \tau_x \sigma_0 \mathcal{H}(-\mathbf{k}) \tau_x \sigma_0. \quad (5.46)$$

At the eight TRIMs $\bar{\mathbf{k}}$ of the 3D Brillouin zone [Figure 5.5 (a)], here defined by $\mathcal{I}\bar{\mathbf{k}} = \bar{\mathbf{k}}$ because \mathcal{T} symmetry is absent [104, 105], we can again compute the inversion eigenvalues $\lambda_{\bar{\mathbf{k}}}^n$, $n = 1, 2$ of the two occupied bands, where $\lambda_{\bar{\mathbf{k}}}^n = \pm 1$.

For $\alpha = \beta = \gamma = 0$ and $\xi = 0, 1$, Equation (5.45) is topologically trivial, and its occupied subspace is composed of two bands with equal inversion eigenvalues $\lambda_{\bar{\mathbf{k}}} = 1$ at all TRIM points. For $\xi = 1$, $\mathcal{H}(\mathbf{k})$ describes a symmetry-indicated axion insulator [66, 43, 49, 96, 97, 19, 98] (AXI) that differs from a trivial (unobstructed) atomic limit by a sign-change of the inversion eigenvalues of the two occupied bands (*i.e.* double band inversion) at $\bar{\mathbf{k}} = (1 + \alpha, 1 + \beta, 1 + \gamma)\pi/2$. For $\xi = 0$, $\mathcal{H}(\mathbf{k})$ describes a weak z -directed stack of identical inversion-symmetry indicated [66, 43, 49, 96, 97, 19, 98] 2D FTIs with $\pm e/2$ corner charges.

Having established the properties of the Hamiltonian of the pristine system [Equation (5.45)], we now probe the dislocation response. In the previous section we discussed 0D states bound to point dislocations in 2D crystals. In 3D, there are point, screw, and mixed [145] (as well as partial [164]) dislocations. In this chapter, we focus on defects with integer Burgers vectors, for which the presence of topological bound states only depends on the direction and length of the Burgers vector and not the details of the dislocation (see Section 5.1). Therefore, in this section, we restrict focus to 3D screw dislocations, with the understanding that our conclusions also apply to edge and mixed dislocations with integer Burgers vectors.

We introduce a pair of 1D screw dislocations with Burgers vector $\mathbf{B} = \hat{z}$ and opposite chiralities [Equation (5.20)] into a system described by Equation (5.45). Through Equation (5.10), we deduce that each screw realizes an interface between two insulators S and S' that “differ” by the Hamiltonian of the $k_z = \pi$ plane of Equation (5.45):

$$\begin{aligned} \mathcal{H}(k_x, k_y, \pi) = & \sin k_x \tau_z \sigma_x + \sin k_y \tau_z \sigma_y \\ & + [\alpha \cos k_x + \beta \cos k_y + \xi(2 - \gamma)] \tau_x \sigma_0 \\ & + \xi \delta (\tau_x \sigma_x + \tau_x \sigma_y + \tau_x \sigma_z). \end{aligned} \quad (5.47)$$

Setting $\alpha = \beta = -1$, $\delta = 1/4$, Equation (5.47) describes an \mathcal{I} -symmetric 2D FTI [62, 19] (trivial insulator) when $\xi = 1$, $\gamma = +1$ ($\xi = 1$, $\gamma = -1$).

To obtain the numerical results presented in Figure 5.5, we begin with a square lattice Λ of size $|\Lambda| = L^2$ with $L = 16$ and PBC to model the (x, y) -plane, while

keeping k_z as a quantum number that labels states by their momentum in the z -direction. We then modify the hoppings across a plane of 8 sites in Λ to create a pair of screw dislocations with Burgers vector $\mathbf{B} = \hat{z}$. We note that this is the minimal number of screw dislocations compatible with (untwisted) PBC.

Next, we analyze the system with two dislocations using the terminology established in Section 5.1.3. We begin by denoting the pristine real-space Hamiltonian corresponding to the Fourier transform of the model in Equation (5.45) within the (x, y) -plane as $H(k_z)$. $H(k_z)$ contains only nearest-neighbor hoppings and has $(4L^2 \times 4L^2) = (1024 \times 1024)$ elements for each value of k_z . As previously in Equation (5.37), $H_{a,b}$ denotes the matrix obtained by removing all of the rows from H that do not couple to lattice sites within the set A and removing all of the columns in H that do not couple to the set B . We next introduce the shorthand notation:

$$\sum_{a,b} H_{a,b}(k_z) |a\rangle \langle b| = \sum_{r \in A} \sum_{r' \in B} \sum_{\mu, \nu \in \{1, 2\}} H_{r,r'}^{\mu,\nu}(k_z) |r, \mu\rangle \langle r', \nu|, \quad (5.48)$$

where $|r, \mu\rangle$ denotes the basis state at position $r \in \Lambda$ with an orbital indexed by μ [the Bloch Hamiltonian (5.45) is a (4×4) matrix, so there are four orbitals].

Using the site labeling U and M established in Figure 5.1 (a), we will now detail how we numerically implement a pair of $\mathbf{B} = \hat{z}$ screw dislocations. Defining $O = U \cup M$ and $\bar{O} = \Lambda \setminus O$, we form the expression:

$$H(k_z) = \sum_{\bar{o}, \bar{o}'} H_{\bar{o}, \bar{o}'}(k_z) |\bar{o}\rangle \langle \bar{o}'| + \sum_{o, \bar{o}} H_{o, \bar{o}}(k_z) |o\rangle \langle \bar{o}| + \sum_{\bar{o}, o} H_{\bar{o}, o}(k_z) |\bar{o}\rangle \langle o| + \sum_{o, o'} H_{o, o'}(k_z) |o\rangle \langle o'|. \quad (5.49)$$

We then expand Equation (5.49):

$$\begin{aligned} \sum_{o, o'} H_{o, o'}(k_z) |o\rangle \langle o'| &= \sum_{u, u'} H_{u, u'}(k_z) |u\rangle \langle u'| + \sum_{m, m'} H_{m, m'}(k_z) |m\rangle \langle m'| \\ &\quad + \sum_{u, m} H_{u, m}(k_z) |u\rangle \langle m| + \sum_{m, u} H_{m, u}(k_z) |m\rangle \langle u|. \end{aligned} \quad (5.50)$$

To introduce a pair of screw dislocations, we form the Hamiltonian $\tilde{H}(k_z)$, which is defined on Λ and labeled by k_z . $\tilde{H}(k_z)$ can be expanded as:

$$\begin{aligned} \tilde{H}(k_z) &= \sum_{\bar{o}, \bar{o}'} H_{\bar{o}, \bar{o}'}(k_z) |\bar{o}\rangle \langle \bar{o}'| + \sum_{o, \bar{o}} H_{o, \bar{o}}(k_z) |o\rangle \langle \bar{o}| \\ &\quad + \sum_{\bar{o}, o} H_{\bar{o}, o}(k_z) |\bar{o}\rangle \langle o| + \sum_{o, o'} \tilde{H}_{o, o'}(k_z) |o\rangle \langle o'|. \end{aligned} \quad (5.51)$$

in which we can further expand:

$$\begin{aligned} \sum_{o,o'} \tilde{H}_{o,o'}(k_z) |o\rangle \langle o'| &= \sum_{u,u'} H_{u,u'}(k_z) |u\rangle \langle u'| + \sum_{m,m'} H_{m,m'}(k_z) |m\rangle \langle m'| \\ &+ \sum_{u,m} e^{-ik_z} H_{u,m}(k_z) |u\rangle \langle m| + \sum_{m,u} e^{ik_z} H_{m,u}(k_z) |m\rangle \langle u|. \end{aligned} \quad (5.52)$$

where the exponential factors $e^{\pm ik_z}$ implement the screw dislocations (we have set the lattice spacing to $a_{x,y,z} = 1$). To summarize, Equations (5.49) through (5.52) describe how, in a tight-binding model with nearest-neighbor hoppings and orthogonal lattice vectors, we numerically implement a pair of screw dislocations by multiplying all hoppings across a line of sites in a pristine lattice by the momentum-dependent phase factor e^{ik_z} in one direction, and e^{-ik_z} in the other. After following this prescription, we obtain a Hamiltonian $\tilde{H}(k_z)$ that contains two $\mathbf{B} = \hat{z}$ screw dislocations [with opposite sense vectors, as described in the text surrounding Equation (5.20)]. We will now discuss the electronic structure of $\tilde{H}(k_z)$ in detail for characteristic values of ξ and γ .

5.2.2.1 $\xi = 1, \gamma = -1$: Axion insulator with double band inversion at Γ

This case corresponds to an inversion-symmetry-indicated AXI driven by a pair of band inversions at $\mathbf{k} = (0, 0, 0)$ in Equation (5.45). In this case, the bulk characterizes a strong topological phase (specifically, an AXI). Because the bands at X, Y, M, Z, U, R , and T are uninverted relative to an atomic insulator with orbitals at the $1a$ position, the defect response Hamiltonian (5.47) is in the topologically trivial phase. The dislocations do not bind anomalous charges ($q \bmod e = 0$). In Figure 5.5 (c),(f), we respectively show the inversion eigenvalues of the occupied bands and the dislocation spectrum, which does not exhibit a filling anomaly or midgap dislocation bound states.

5.2.2.2 $\xi = 1, \gamma = +1$: Axion insulator with double band inversion at Z

This case describes an AXI driven by double band inversion at the Z point [Figure 5.5 (a)]. Relative to the initial trivial atomic insulator, the double band inversion at Z has changed not only the strong AXI index, but has also induced a transition to the regime where the Hamiltonian (5.47) describes a two-dimensional fragile phase with corner filling anomaly [19] [the inversion eigenvalues of the occupied bands are shown in Figure 5.5 (d)]. This implies that the dislocation response is nontrivial. Correspondingly, in the dislocation spectrum [Figure 5.5 (g)], we observe one midgap localized zero mode per dislocation. The zero modes are protected by

the chiral (*i.e.*, unitary particle-hole) symmetry Π , which is defined through the action

$$\Pi : \mathcal{H}(k_x, k_y, \pi) \rightarrow \tau_y \sigma_0 \mathcal{H}(k_x, k_y, \pi) \tau_y \sigma_0, \quad (5.53)$$

such that here, Π is a symmetry of $\mathcal{H}(k_x, k_y, \pi)$ if

$$\Pi \mathcal{H}(k_x, k_y, \pi) \Pi^{-1} = \tau_y \sigma_0 \mathcal{H}(k_x, k_y, \pi) \tau_y \sigma_0 = -\mathcal{H}(k_x, k_y, \pi). \quad (5.54)$$

Crucially, if we were to relax Π symmetry, then the midgap states could be pushed out of the gap. However, if we preserve \mathcal{I} symmetry while breaking Π , then $\pm e/2$ end charges would still remain bound to the dislocations [162], in a generalization of the conclusions of Goldstone and Wilczek [100, 160, 161].

Equivalently, in the absence of chiral symmetry we can also identify the nontrivial topology by counting the number of states that are occupied up to a given Fermi level in the gap[19, 143, 32, 144, 146, 147], as we did previously in Section 5.2.1.2. Let the 3D real-space Hamiltonian corresponding to the system with two screw dislocations be a $(D \times D)$ matrix. Comparing Figures 5.5 (f) and (g), we observe that they differ by the presence of two midgap states and the absence of one state from each of the valence and conduction bands. When chiral symmetry is broken, the energy of the midgap states can be shifted in a manner that preserves \mathcal{I} symmetry, leaving the two states degenerate in the thermodynamic limit. This implies that any gapped Fermi level that encloses either $(D/2 - 1)$ or $(D/2 + 1)$ occupied states indicates a nontrivial topology, whereas a Fermi level enclosing $D/2$ occupied states indicates trivial bulk topology. More generally, the presence of anomalous 0D states in arbitrary dimensions can be diagnosed in a similar manner by constructing a 0D system with a pair of generalized dislocations that preserve a global point group symmetry and observing an imbalance in the number of states above and below the gap that cannot be resolved without breaking a symmetry (*i.e.*, a filling anomaly) [23, 19, 143, 32, 144, 146, 147].

5.2.2.3 $\xi = 0$: Weak FTI stack

In this case, $\mathcal{H}(\mathbf{k})$ is independent of γ , and Equation (5.45) describes a z -directed stack of identical 2D FTI models. Specifically, the Hamiltonian [Equation (5.45) with $\xi = 0$] is in this case completely independent of k_z . This is an example of weak topology, because the Hamiltonian $\mathcal{H}(\mathbf{k})$ can be deformed into a real-space z -directed stack of decoupled 2D FTIs without breaking a symmetry or closing the bulk gap. Relative to the initial trivial atomic insulator, $\mathcal{H}(\mathbf{k})$ features band inversions at Γ and Z [the inversion eigenvalues are shown in Figure 5.5 (e)], such that even though the bulk is an FTI [which is Wannierizable under the addition of trivial

bands], the dislocation response is therefore nontrivial (the Hamiltonian (5.47) is again fragile [19]). Correspondingly, in the dislocation spectrum [Figure 5.5 (g)], we observe a filling anomaly.

For the present case of an array of FTI planes, we can also understand the existence of dislocation midgap states intuitively without invoking the more general theory used to derive Equation (5.47). Specifically, if we were to instead insert a loop of edge dislocations with Burgers vector $\mathbf{B} = \hat{z}$, then we would effectively introduce an uncoupled FTI into the system whose corner states become dislocation end states. As long as the “left-over” FTI contains an inversion center, then its corner states also induce a system filling anomaly, consistent with the numerical results shown in Figure 5.5 (g).

5.2.3 2D Point Dislocations with \mathcal{T} Symmetry

In this section, we demonstrate the dislocation response of 2D insulators with \mathcal{T} symmetry. We begin by comparing the minimal tight-binding model of an inversion- (\mathcal{I} -) symmetric 2D topological insulator (TI, first introduced in Section 2.1.1.3) to that of a stack (array) of \mathcal{I} - and \mathcal{T} -symmetric Su-Schrieffer-Heeger (SSH) chains [79, 149, 150, 77]. Consider the Bloch Hamiltonian:

$$\begin{aligned}\mathcal{H}(\mathbf{k}) = & \sin k_x \tau_0 \sigma_x + \xi \sin k_y \tau_0 \sigma_y \\ & + [\alpha \cos k_x + \xi (1 + \beta \cos k_y)] \tau_z \sigma_z,\end{aligned}\tag{5.55}$$

defined on a square lattice, where $\alpha, \beta = \pm 1$ are parameters that can be tuned to realize different topological phases. Time-reversal and inversion symmetry are represented by:

$$\begin{aligned}\mathcal{T} : \mathcal{H}(\mathbf{k}) & \rightarrow \tau_x \sigma_y \mathcal{H}^*(-\mathbf{k}) \tau_x \sigma_y, \\ \mathcal{I} : \mathcal{H}(\mathbf{k}) & \rightarrow \tau_z \sigma_z \mathcal{H}(-\mathbf{k}) \tau_z \sigma_z.\end{aligned}\tag{5.56}$$

At half-filling there are two occupied bands with the Bloch eigenstates $|u^n(\mathbf{k})\rangle$, $n = 1, 2$. At the four TRIMs of the 2D Brillouin zone shown in Figure 5.4 (a) (*i.e.* the \mathbf{k} points for which $\mathcal{T}\bar{\mathbf{k}} = \bar{\mathbf{k}}$), we can define the inversion eigenvalue $\lambda_{\bar{\mathbf{k}}}$ of the occupied Kramers pair $\{|u^1(\bar{\mathbf{k}})\rangle, |u^2(\bar{\mathbf{k}})\rangle\}$ as:

$$\mathcal{I}|u^1(\bar{\mathbf{k}})\rangle = \lambda_{\bar{\mathbf{k}}} |u^1(\bar{\mathbf{k}})\rangle,\tag{5.57}$$

where $\mathcal{I}^2 = 1$ implies that $\lambda_{\bar{\mathbf{k}}} = \pm 1$. At each TRIM point, states appear in Kramers pairs with the same inversion (\mathcal{I}) eigenvalues, because the eigenvalues of \mathcal{I} are real ($\lambda_{\bar{\mathbf{k}}} = \pm 1$).

For $\alpha = \beta = 0$ and $\xi = 0, 1$, Equation (5.55) is topologically trivial, and its occupied subspace is composed of two bands with the same inversion eigenvalues

$\lambda_{\bar{k}} = 1$ at all TRIM points. For $\xi = 1$, $\mathcal{H}(\mathbf{k})$ describes a symmetry-indicated 2D TI that differs from a trivial (unobstructed) atomic limit by a single sign-change of the inversion eigenvalue of the occupied Kramers pair of bands at $\bar{\mathbf{k}} = (1 + \alpha, 1 + \beta)\pi/2$. Specifically, the \mathbb{Z}_2 TI (Fu-Kane) invariant is indicated by the product of the inversion eigenvalues of the occupied Kramers pairs [5, 158]. For $\xi = 0$, $\mathcal{H}(\mathbf{k})$ becomes equivalent to an array of identical x -directed \mathcal{T} -symmetric SSH chains indexed by k_y whose time-reversal polarization is indicated [79, 149, 150, 163, 85, 77, 108] by the inversion eigenvalues at $k_x = 0, \pi$.

Having established the properties of the Hamiltonian of the pristine system [Equation (5.55)], we now probe the dislocation response. We introduce a pair of 0D dislocations with Burgers vector $\mathbf{B} = \hat{y}$. Through Equation (5.10), we deduce that each dislocation realizes an interface between two insulators S and S' that “differ” by the Hamiltonian of the $k_y = \pi$ plane of Equation (5.55):

$$\mathcal{H}(k_x, \pi) = \sin k_x \tau_0 \sigma_x + [\alpha \cos k_x + \xi(1 - \beta)] \tau_z \sigma_z. \quad (5.58)$$

Setting $\alpha = -1$, $\mathcal{H}(k_x, \pi)$ describes an \mathcal{I} - and \mathcal{T} -symmetric SSH chain with a trivial (nontrivial) time-reversal polarization for $\xi = 1, \beta = -1$ ($\xi = 1, \beta = +1$).

To obtain the numerical results presented in Figure 5.6, we use the same prescription as employed in Section 5.2.1 to obtain a Hamiltonian $\tilde{\mathcal{H}}$ that differs from the pristine 2D Hamiltonian $\mathcal{H}(\mathbf{k})$ by the presence of a pair of point dislocations. With $L = 16$, $\tilde{\mathcal{H}}$ has the dimensions $[4(L^2 - 8) \times 4(L^2 - 8)] = (992 \times 992)$. We will now discuss the electronic structure of $\tilde{\mathcal{H}}$ in detail for characteristic values of ξ and β .

5.2.3.1 $\xi = 1, \beta = -1$: Topological insulator with band inversion at Γ

This case corresponds to an inversion-symmetry indicated TI driven by band inversion at $\mathbf{k} = (0, 0)$ in Equation (5.55). In this case, the bulk characterizes a strong topological phase. Because the bands at X , Y , and M are uninverted relative to an atomic insulator with orbitals at the $1a$ position, the dislocation response is trivial [Equation (5.58) describes a trivial 1D insulator]. In Figure 5.6 (a),(d), we respectively show the inversion eigenvalues of the occupied bands and the dislocation spectrum, which does not exhibit a filling anomaly or midgap dislocation bound states.

5.2.3.2 $\xi = 1, \beta = +1$: Topological insulator with band inversion at Y

This case corresponds to an inversion-symmetry indicated TI driven by band inversion at the Y point [Figure 5.4 (a)]. Relative to the initial $1a$ atomic insulator, the

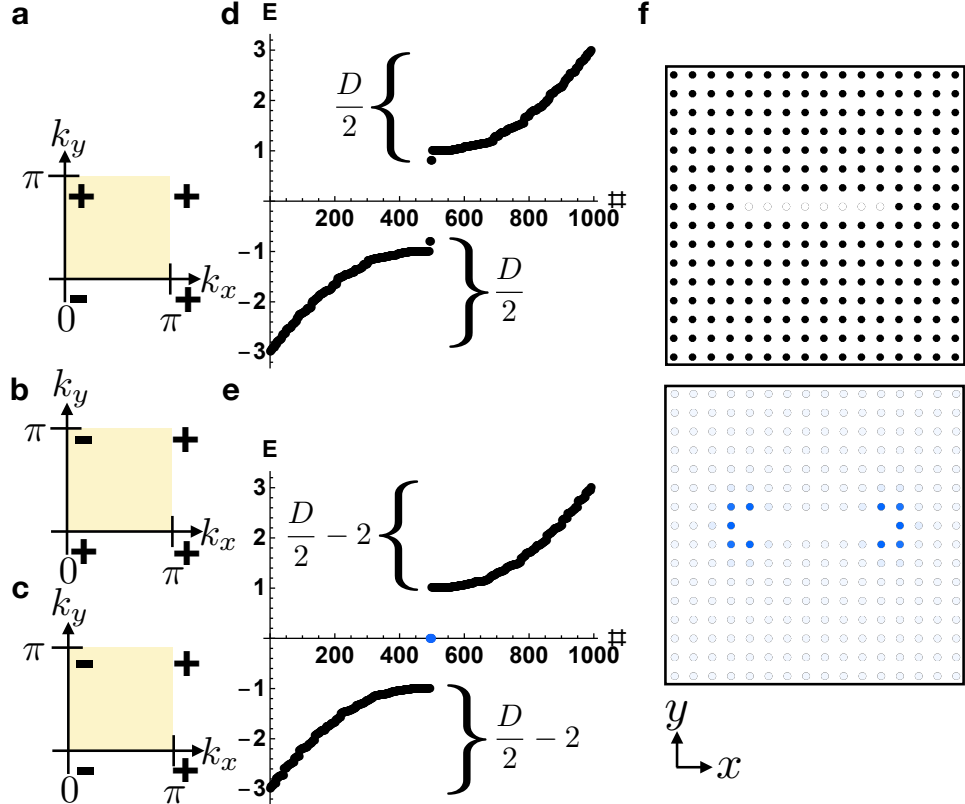


Figure 5.6: 2D point dislocation bound states with inversion (\mathcal{I}) and time-reversal (\mathcal{T}) symmetry. (a)–(e) Bulk inversion eigenvalues and PBC energy spectra for the defect in Figure 5.4 (b) when the bulk is equivalent to (a), (d) a 2D TI with a Kramers pair of band inversions at Γ , (b),(e) a 2D TI with a Kramers pair of band inversions at Y , (c),(e) a weak y -directed array of \mathcal{T} -symmetric SSH chains. Kramers pairs of inversion (inversion) eigenvalues are denoted by a single \pm symbol. Anomalous 0D defect states with chargeless spin are present in (b) and (c), but not in (a), and are equivalent to the end states of an \mathcal{I} - and \mathcal{T} -symmetric SSH chain [79, 149, 150, 77], and thus persist under the relaxation of particle-hole symmetry in the form of a filling anomaly [100, 160, 161, 19, 143, 32, 144, 146, 147]. (f) Real-space geometry with a pair of point dislocations and absolute square of the wavefunction of the midgap states in (e) on a 16×16 lattice. As derived in Equation (5.10), the dislocation response in (a)–(e) is nontrivial when $\mathbf{B} \cdot \mathbf{M}_\nu^{\text{SSH}} \bmod 2\pi = \pi$.

band inversion at Y has changed not only the strong index (the \mathbb{Z}_2 TI invariant), but has also induced a transition of the Hamiltonian 5.58 to the nontrivial phase, which is characterized by a nonvanishing and quantized time-reversal polarization [77] [the inversion eigenvalues of the occupied bands are shown in Figure 5.6 (b)]. This implies that the dislocation response is nontrivial. Correspondingly, in the dislocation spectrum [Figure 5.6 (e)], we observe one midgap Kramers pair of localized zero modes per dislocation. The zero modes are protected by \mathcal{T} -symmetry and the chiral (*i.e.*, unitary particle-hole) symmetry Π , which is defined through the action:

$$\Pi : \mathcal{H}(k_x, \pi) \rightarrow \tau_0 \sigma_y \mathcal{H}(k_x, \pi) \tau_0 \sigma_y, \quad (5.59)$$

such that here, Π is a symmetry of $\mathcal{H}(k_x, \pi)$ if

$$\Pi \mathcal{H}(k_x, \pi) \Pi^{-1} = \tau_0 \sigma_y \mathcal{H}(k_x, \pi) \tau_0 \sigma_y = -\mathcal{H}(k_x, \pi). \quad (5.60)$$

Crucially, if we were to relax Π symmetry, then the midgap states could be pushed out of the gap. However, if we preserve \mathcal{I} symmetry while breaking Π , then chargeless spin would still remain bound to the dislocations, in a generalization of the conclusions of Goldstone and Wilczek [100, 160, 161] and References [165, 166, 167, 168, 162].

5.2.3.3 $\xi = 0$: \mathcal{T} -symmetric weak SSH array

In this case, $\mathcal{H}(\mathbf{k})$ is independent of β , and Equation (5.55) describes a y -directed array of identical x -directed \mathcal{T} -symmetric SSH chains. Specifically, the Hamiltonian [Equation (5.55) with $\xi = 0$] is in this case completely independent of k_y . For each SSH chain, the nontrivial time-reversal polarization is indicated by the difference in the inversion eigenvalues of the occupied bands at $k_x = 0, \pi$ [79, 149, 150, 163, 85, 77, 108]. This case is an example of weak topology, because the Hamiltonian $\mathcal{H}(\mathbf{k})$ can be deformed into a real-space array of decoupled 1D chains without breaking a symmetry or closing the bulk gap. Relative to the initial $1a$ atomic insulator, $\mathcal{H}(\mathbf{k})$ features band inversions at Γ and Y [the inversion eigenvalues are shown in Figure 5.6 (c)], such that the bulk exhibits a trivial symmetry-indicated \mathbb{Z}_2 TI invariant but nontrivial Equation (5.58), and is irrep-equivalent to an OAL from $1a$ [$(x, y) = (0, 0)$] to $1c$ [$((x, y) = (1/2, 0))$]. This implies that even though the bulk is an OAL, the dislocation response is nontrivial. Correspondingly, in the dislocation spectrum [Figure 5.6 (e)], we observe a filling anomaly.

For the present case of an array of SSH chains, we can also understand the existence of dislocation midgap states intuitively without invoking the more general theory used to derive Equation (5.58). The dislocations introduce an uncoupled SSH chain

into the system whose end states become the dislocation bound states. As long as the “left-over” SSH chain is \mathcal{T} -symmetric and contains an inversion center, its end states also induce a system filling anomaly, consistent with the numerical results shown in Figure 5.6 (e).

5.2.4 3D Screw Dislocations with \mathcal{T} Symmetry

In this section, we demonstrate the screw dislocation response of 3D insulators with \mathcal{T} symmetry. We will here focus on higher-order TIs and weak FTIs, which, as we will numerically demonstrate, exhibit 0D dislocation bound states. However, we have also verified that our numerical models exhibit helical modes bound to screw dislocations inserted into insulators with nontrivial weak TI indices, in agreement with the results of References [142, 169, 155, 170, 171, 172]. Specifically, we observe that when the vector of weak indices of a 3D insulator \mathbf{M}_ν satisfies $\mathbf{B} \cdot \mathbf{M}_\nu \bmod 2\pi = \pi$, then the plane spanning the screw dislocations in Equation (5.10) describes a 2D TI with 1D edge states that coincide with the bulk screw dislocation and boundary step edges. For the remainder of this section and chapter, we will restrict focus to 3D insulators for which line-like dislocations bind 0D states.

While in this section we will focus on the topological response of 3D insulators to screw dislocations, we note that we can also consider \mathcal{I} -symmetric internal arrangements of edge dislocations. As shown in Section 5.1, when the Bloch Hamiltonian (5.10) is topologically nontrivial, an edge dislocation loop will bind an anomalous number of 0D states.

We begin by comparing the minimal tight-binding model for a HOTI [26, 23, 25, 66, 43, 94, 62, 95, 49, 96, 97, 19, 98] to that of a stack of 2D \mathcal{T} -symmetric fragile topological insulators [62, 19] (\mathcal{T} -symmetric FTIs), where we retain inversion symmetry for all models. Consider the Bloch Hamiltonian:

$$\begin{aligned}\mathcal{H}(\mathbf{k}) = & \sin k_x \rho_z \tau_z \sigma_x + \sin k_y \rho_z \tau_z \sigma_y + \xi \sin k_z \rho_z \tau_z \sigma_z \\ & + [\alpha \cos k_x + \beta \cos k_y + \xi (2 + \gamma \cos k_z)] \rho_z \tau_x \sigma_0 \\ & + \xi \delta (\rho_y \tau_z \sigma_x + \rho_y \tau_z \sigma_y + \rho_y \tau_z \sigma_z),\end{aligned}\quad (5.61)$$

defined on a square lattice, where ρ_i , τ_i and σ_i , $i = 0, x, y, z$ are three sets of Pauli matrices indexing sublattice and orbital degrees of freedom, respectively, and $\xi = 0, 1$ and $\alpha, \beta, \gamma = \pm 1$ are parameters that can be tuned to realize different topological phases, while δ is a small parameter that gaps out the helical states along dislocations (we will use $\delta = 1/4$ in all calculations, for $\delta = 0$ the Hamiltonian is a model of two uncoupled 3D topological insulators). We abbreviate the Kronecker product by $\rho_i \otimes \tau_j \otimes \sigma_k \equiv \rho_i \tau_j \sigma_k$. Time-reversal (\mathcal{T}) and inversion (\mathcal{I})

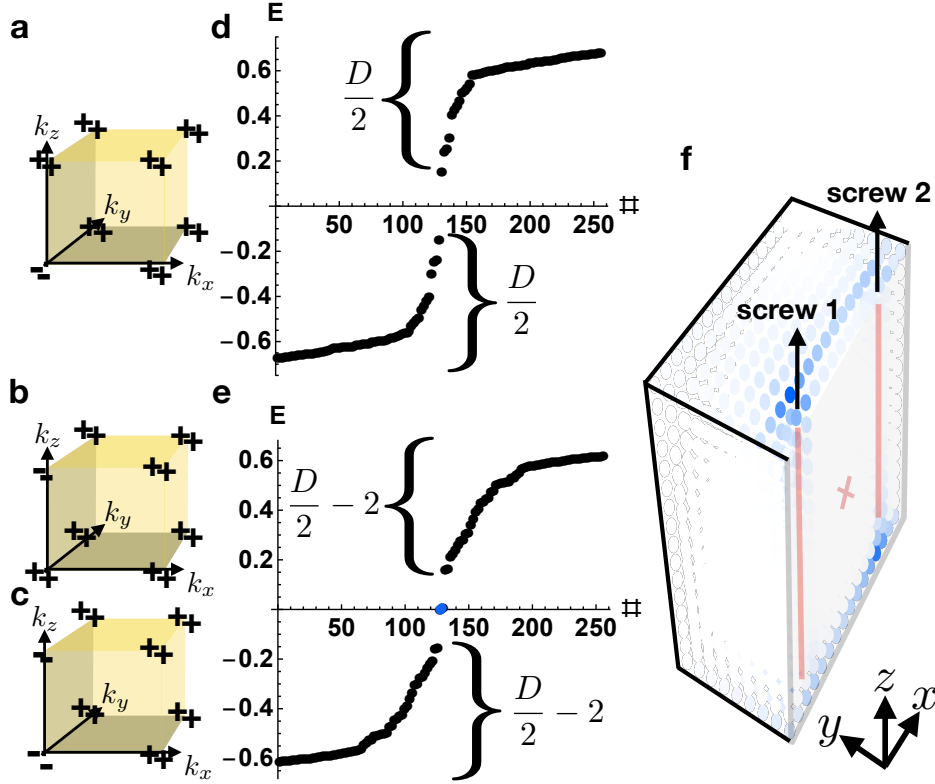


Figure 5.7: 3D screw dislocation bound states with time-reversal (\mathcal{T}) and inversion (\mathcal{I}) symmetry. (a)–(e) Bulk inversion eigenvalues and hollow-doughnut-boundary-condition (HDBC) energy spectra for a pair of screw dislocations [Figure 5.5 (b)] inserted into (a),(d) an \mathcal{I} -symmetric HOTI with double band inversion at Γ , (b),(e) a HOTI with double band inversion at Z , and (c),(e) a weak stack of \mathcal{I} and \mathcal{T} -symmetric 2D FTIs. In (a),(b),(c), Kramers pairs of inversion eigenvalues are denoted with a single \pm symbol. Anomalous 0D states with chargeless spin are present on the dislocation ends in (b) and (c), but not in (a), and are equivalent to the corner states of an \mathcal{I} - and \mathcal{T} -symmetric 2D FTI [62, 19], and thus persist under the relaxation of particle-hole symmetry [62, 19, 143]. In (d),(e), we only show the 256 lowest-lying states. In the presence of an additional chiral symmetry, the two midgap Kramers pairs of dislocation end states in (b) and (c) are pinned to zero energy. In the absence of chiral symmetry, a nontrivial dislocation response can still be diagnosed by observing filling anomaly[19, 143, 32, 144, 146, 147]. (f) Real-space-resolved absolute square of the midgap eigenstates shown in (e) on a $16 \times 16 \times 16$ lattice (cut in half along the transparent grey plane to expose the bound states). \mathcal{I} -related Kramers pairs of bound states appear on two of the four screw dislocation ends. The inversion center in (f) is marked by a red X.

symmetry are respectively represented by:

$$\begin{aligned}\mathcal{T} : \mathcal{H}(\mathbf{k}) &\rightarrow \rho_0 \tau_0 \sigma_y \mathcal{H}^*(-\mathbf{k}) \rho_0 \tau_0 \sigma_y, \\ \mathcal{I} : \mathcal{H}(\mathbf{k}) &\rightarrow \rho_z \tau_x \sigma_0 \mathcal{H}(-\mathbf{k}) \rho_z \tau_x \sigma_0.\end{aligned}\quad (5.62)$$

At the eight TRIM points of the 3D Brillouin zone shown in Figure 5.5 (a), we can again compute the inversion eigenvalues $\lambda_{\bar{\mathbf{k}}}^n$, $n = 1, 2$ of the two occupied Kramers pairs of bands, where $\lambda_{\bar{\mathbf{k}}}^n = \pm 1$. For $\alpha = \beta = \gamma = 0$ and $\xi = 0, 1$, Equation (5.61) is topologically trivial and its occupied subspace is composed of four bands with inversion eigenvalues $\lambda_{\bar{\mathbf{k}}} = 1$ at all TRIM points. For $\xi = 1$, $\mathcal{H}(\mathbf{k})$ describes a symmetry-indicated HOTI [29, 30, 91, 62] driven by a sign-change of the inversion eigenvalues of the two occupied Kramers pairs of bands at $\bar{\mathbf{k}} = (1 + \alpha, 1 + \beta, 1 + \gamma)\pi/2$. For $\xi = 0$, $\mathcal{H}(\mathbf{k})$ becomes equivalent to a z -directed stack of identical \mathcal{I} -symmetry indicated [66, 43, 49, 96, 97, 19, 98] \mathcal{T} -symmetric FTIs indexed by k_z .

Having established the properties of the Hamiltonian of the pristine system [Equation (5.61)], we now probe the dislocation response. We introduce a pair of 1D screw dislocations with Burgers vector $\mathbf{B} = \hat{z}$ and opposite chiralities [Equation (5.20)]. Through Equation (5.10), we deduce that each dislocation realizes an interface between two insulators S and S' that “differ” by the Hamiltonian of the $k_z = \pi$ plane of Equation (5.61):

$$\begin{aligned}\mathcal{H}(k_x, k_y, \pi) = & \sin k_x \rho_0 \tau_z \sigma_x + \sin k_y \rho_0 \tau_z \sigma_y \\ & + [\alpha \cos k_x + \beta \cos k_y + \xi(2 - \gamma)] \rho_z \tau_x \sigma_0 \\ & + \xi \delta (\rho_z \tau_x \sigma_x + \rho_z \tau_x \sigma_y + \rho_z \tau_x \sigma_z).\end{aligned}\quad (5.63)$$

Setting $\alpha = \beta = -1$, $\mathcal{H}(k_x, k_y, \pi)$ describes a 2D trivial insulator (\mathcal{T} -symmetric FTI [62, 19]) for $\xi = 1$, $\gamma = -1$ ($\xi = 1$, $\gamma = +1$, $\delta = 1/4$). We will now discuss the electronic structure of $\tilde{\mathcal{H}}(k_z)$ in detail for characteristic values of ξ and γ (Figure 5.7). To obtain the numerical results presented in Figure 5.7, we use the same prescription as employed in Section 5.2.2 to obtain a Hamiltonian $\tilde{\mathcal{H}}(k_z)$ that differs from a pristine crystal by a pair of screw dislocations.

5.2.4.1 $\xi = 1, \gamma = -1$: Higher-order topological insulator with double band inversion at Γ

This case corresponds to an inversion-symmetry-indicated HOTI driven by two Kramers pairs of band inversions at $\mathbf{k} = (0, 0, 0)$ in Equation (5.61). In this case, the bulk characterizes a strong topological phase. Because the bands at X , Y , M , Z , U , R , and T are uninverted relative to an atomic insulator with orbitals at the

$1a$ position, Equation (5.63) describes a trivial insulator, and so the dislocations do not bind anomalous charges ($q \bmod e = 0$). In Figure 5.7 (a),(d), we respectively show the inversion eigenvalues of the occupied bands and the dislocation spectrum, which does not exhibit a filling anomaly or midgap dislocation bound states.

5.2.4.2 $\xi = 1, \gamma = +1$: Higher-order topological insulator with double band inversion at Z

This case describes a HOTI driven by double band inversion at the Z point [Figure 5.5 (a)]. Relative to a $1a$ trivial (unobstructed) atomic limit, the double band inversion at Z has changed not only the strong \mathbb{Z}_4 HOTI index [29, 30, 91, 62], but has also induced a transition of the Hamiltonian 5.63 to a fragile phase (protected by \mathcal{T} and \mathcal{I} symmetry) with corner filling anomaly [19, 143, 147] [the inversion eigenvalues of the occupied bands are shown in Figure 5.7 (b)]. This implies that the dislocation response is nontrivial. Correspondingly, in the dislocation spectrum [Figure 5.7 (e)], we observe one midgap Kramers pair of localized zero modes per dislocation. The zero modes are protected by the chiral (*i.e.*, unitary particle-hole) symmetry Π , which is defined through the action

$$\Pi : \mathcal{H}(k_x, k_y, \pi) \rightarrow \rho_0 \tau_y \sigma_0 \mathcal{H}(k_x, k_y, \pi) \rho_0 \tau_y \sigma_0. \quad (5.64)$$

such that here, Π is a symmetry of $\mathcal{H}(k_x, k_y, \pi)$ if

$$\Pi \mathcal{H}(k_x, k_y, \pi) \Pi^{-1} = \rho_0 \tau_y \sigma_0 \mathcal{H}(k_x, k_y, \pi) \rho_0 \tau_y \sigma_0 = -\mathcal{H}(k_x, k_y, \pi). \quad (5.65)$$

Crucially, if we were to relax Π symmetry, the midgap states could be pushed out of the gap.

Equivalently, in the absence of chiral symmetry we can also identify the nontrivial topology by counting the number of states that are occupied up to a given Fermi level in the gap[19, 143, 32, 144, 146, 147], just as we did in Section 5.2.3.2. Let the 3D real-space Hamiltonian corresponding to the system with two screw dislocations be a $(D \times D)$ matrix. Comparing Figures 5.7 (d) and (e), we observe that they differ by the presence of two Kramers pairs of midgap states and the absence of two states from each of the valence and conduction bands. When chiral symmetry is broken while preserving \mathcal{I} and \mathcal{T} , then the energy of the midgap states can be shifted, but only in a manner that preserves \mathcal{I} and \mathcal{T} , leaving the four states degenerate in the thermodynamic limit. This implies that any gapped Fermi level that encloses either $(D/2 - 2)$ or $(D/2 + 2)$ occupied states indicates a nontrivial response, whereas a Fermi level enclosing $D/2$ occupied states indicates a trivial screw dislocation response.

5.2.4.3 $\xi = 0$: Weak \mathcal{T} -symmetric FTI stack

In this case, $\mathcal{H}(\mathbf{k})$ is independent of γ , and Equation (5.61) describes a z -directed stack of identical 2D \mathcal{T} -symmetric FTIs. Specifically, the Hamiltonian [Equation (5.61) with $\xi = 0$] is in this case completely independent of k_z . This is an example of weak topology, because the Hamiltonian $\mathcal{H}(\mathbf{k})$ can be deformed into a real-space stack of decoupled 2D \mathcal{T} -symmetric FTIs without breaking a symmetry or closing the bulk gap. Relative to the initial trivial atomic insulator, $\mathcal{H}(\mathbf{k})$ features double band inversions at Γ and Z [the inversion eigenvalues are shown in Figure 5.7 (c)], such that Equation (5.63) again describes a fragile insulator. This implies that even though the bulk is Wannierizable (after the addition of trivial bands), the dislocation response is nontrivial. Correspondingly, in the dislocation spectrum [Figure 5.7 (e)], we observe a filling anomaly.

For the present case of an array of FTI planes, we can also understand the existence of dislocation midgap states intuitively without invoking the more general theory used to derive Equation (5.63). Specifically, if we were to instead insert a loop of edge dislocations with Burgers vector $\mathbf{B} = \hat{z}$, then we would effectively introduce an uncoupled \mathcal{T} -symmetric FTI into the system whose corner states become dislocation end states. As long as the “left-over” FTI plane contains an inversion center, then its corner states will also induce a system filling anomaly, consistent with the numerical results shown in Figure 5.7 (e).

5.3 Magnetic fluxes and flux tubes

5.3.1 2D Fluxes in the Absence of \mathcal{T} Symmetry

In this section, we demonstrate the π -flux response of \mathcal{I} -symmetric 2D insulators with broken \mathcal{T} symmetry [169, 155, 170, 165, 166, 167, 168, 173]. We begin by considering a pristine 2D insulator described by the Bloch Hamiltonian $\mathcal{H}(\mathbf{k})$ in Equation (5.33) of Section 5.2.1. We then numerically introduce a pair of π -fluxes related by a bulk \mathcal{I} center as discussed in Section 5.1.2.

To obtain the numerical results presented in Figure 5.8, we begin with a square lattice Λ of size $|\Lambda| = L^2$ with $L = 16$ and PBC to model the (x, y) -plane. We then modify the hoppings across a line of 8 sites in Λ to create a pair of π -fluxes. This is the minimal number of fluxes compatible with (untwisted) PBC. We define H and $H_{A,B}|A\rangle\langle B|$ using the same notation employed in Section 5.2.1. Using the site labeling U and M established in Figure 5.1 (a), we will now detail how we numerically implement a pair of π -fluxes.

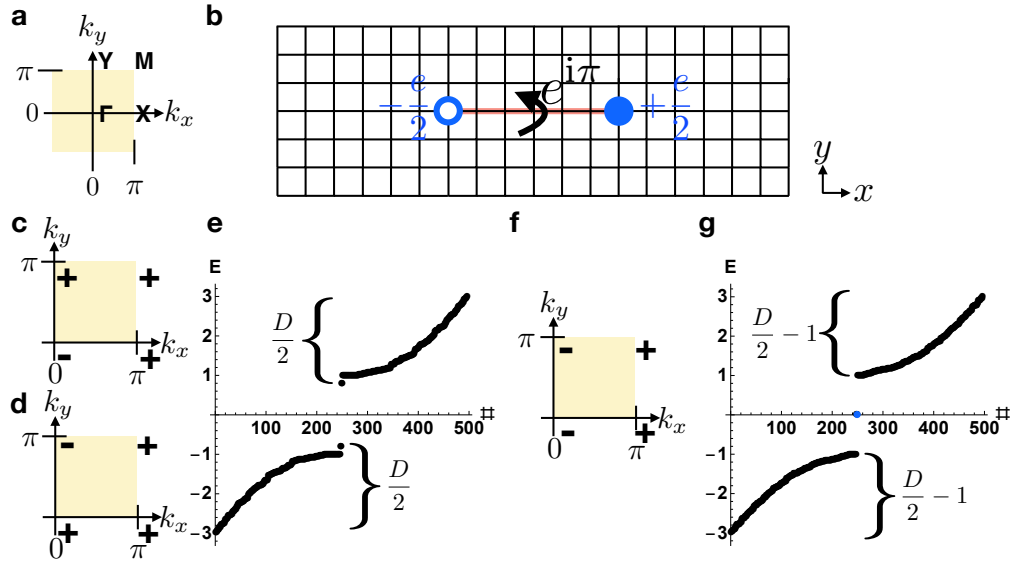


Figure 5.8: 2D π -flux bound states with inversion symmetry. (a) The bulk BZ of a 2D rectangular crystal with only I symmetry. (b) We implement a pair of 0D π -fluxes related by I by multiplying all of the hoppings along the red line of sites by $e^{i\pi}$ in the positive y -direction, and by multiplying all of the hoppings along the same line by $e^{-i\pi}$ in the negative y -direction. (c)–(g) Bulk inversion eigenvalues and PBC energy spectra for the flux in (b) when the crystal with the with BZ in (a) is equivalent to (c),(g) a $|C|=1$ Chern insulator with band inversion at Γ , (d),(g) a $|C|=1$ Chern insulator with band inversion at Y , and (f),(e) a weak y -directed array of SSH [79, 150] chains. Anomalous 0D flux states with charge $\pm e/2$ are present in (c) and (d), but not in (f), and are equivalent to the end states of an I -symmetric, T -broken SSH chain [79, 150] [Equation (5.36), red line in (b)], and thus persist under the relaxation of particle-hole symmetry [100, 160, 161, 19, 143].

Defining $S = U \cup M$ and $\bar{S} = \Lambda \setminus S$, we form the expression:

$$H = H_{\Lambda,\Lambda}|\Lambda\rangle\langle\Lambda| = H_{\bar{S},\bar{S}}|\bar{S}\rangle\langle\bar{S}| + H_{S,\bar{S}}|S\rangle\langle\bar{S}| + H_{\bar{S},S}|\bar{S}\rangle\langle S| + H_{S,S}|S\rangle\langle S|. \quad (5.66)$$

We then expand Equation (5.66):

$$H_{S,S}|S\rangle\langle S| = H_{U,U}|U\rangle\langle U| + H_{M,M}|M\rangle\langle M| + H_{U,M}|U\rangle\langle M| + H_{M,U}|M\rangle\langle U|. \quad (5.67)$$

To introduce a pair of π -fluxes, we form the Hamiltonian \tilde{H} , which is defined on Λ , and can be expanded as:

$$\tilde{H} = \tilde{H}_{\Lambda,\Lambda}|\Lambda\rangle\langle\Lambda| = H_{\bar{S},\bar{S}}|\bar{S}\rangle\langle\bar{S}| + H_{S,\bar{S}}|S\rangle\langle\bar{S}| + H_{\bar{S},S}|\bar{S}\rangle\langle S| + \tilde{H}_{S,S}|S\rangle\langle S|, \quad (5.68)$$

in which we can further expand:

$$\tilde{H}_{S,S}|S\rangle\langle S| = H_{U,U}|U\rangle\langle U| + H_{M,M}|M\rangle\langle M| + e^{-i\pi}H_{U,M}|U\rangle\langle M| + e^{i\pi}H_{M,U}|M\rangle\langle U|, \quad (5.69)$$

where the exponential factors $e^{\pm i\pi}$ implement the π -fluxes. To summarize, Equations 5.66 through 5.69 describe how, in a tight-binding model with nearest-neighbor hoppings and orthogonal lattice vectors, we numerically implement a pair of π -fluxes by multiplying all of the hoppings across a line of sites in a pristine lattice by the phase factors $e^{\pm i\pi}$.

We will now discuss the electronic structure of \tilde{H} in detail for characteristic values of ξ and β , setting $\alpha = -1$ for all of the cases discussed in this section.

5.3.1.1 $\xi = 1, \beta = -1$: Chern insulator with band inversion at Γ

In this case, we consider the system response to a pair of π -fluxes spatially separated in the x direction. As shown in Section 5.1.2, the π -flux response is given in this case by the summed topologies of the $k_y = 0, \pi$ lines in the 2D BZ of $\mathcal{H}(\mathbf{k})$ (which can be summarized as the bulk Chern number $C \bmod 2$). In the pristine insulating bulk, the $k_y = 0$ ($k_y = \pi$) line characterizes a nontrivial (trivial) SSH chain, and the bulk correspondingly exhibits an inversion-symmetry-indicated Chern number [114] $|C| = 1$. We observe a single midgap state at each π -flux core, which can be pinned to zero energy by the chiral symmetry in Equation (5.43) or diagnosed via a filling anomaly [19, 143, 32, 144, 146, 147]. The bulk inversion eigenvalues and the flux spectrum are respectively shown in Figure 5.8 (c),(g).

5.3.1.2 $\xi = 1, \beta = +1$: Chern insulator with band inversion at Γ

As in the previous case of a $|C| = 1$ Chern insulator driven by band inversion at Γ , because the summed topology of the $k_y = 0, \pi$ lines in the 2D BZ of $\mathcal{H}(\mathbf{k})$ is again nontrivial (and, equivalently, because the bulk Chern number is odd), we observe a nontrivial flux response. This underlines the fact that, in contrast to the dislocation response, the π -flux response of 2D and 3D insulators only depends on the strong topological index (Section 5.1.2), and in particular does not depend on where bands are inverted. The bulk inversion eigenvalues and the flux spectrum are respectively shown in Figure 5.8 (d),(g).

5.3.1.3 $\xi = 0$: Weak SSH array

The bulk inversion eigenvalues and the flux spectrum are shown in Figure 5.8 (f),(e). Because the bulk carries a trivial Chern number, the π -flux response is trivial.

5.3.2 3D Flux Tubes in the Absence of \mathcal{T} Symmetry

In this section, we demonstrate the π -flux response of \mathcal{I} -symmetric 3D insulators with broken \mathcal{T} symmetry [169, 155, 170, 165, 166, 167, 168, 173]. We begin by considering a pristine 3D insulator described by the Bloch Hamiltonian $\mathcal{H}(\mathbf{k})$ in Equation (5.45) of Section 5.2.2. We then numerically introduce a pair of π -flux tubes related by a bulk \mathcal{I} center as discussed in Section 5.1.2. Each tube corresponds to a π -flux in each real-space plane indexed by z , or equivalently, at each momentum k_z . As in Section 5.2.2, we set $\alpha = \beta = -1$ in Equation (5.45). In our numerics, the flux tubes are implemented by following the procedure employed for the 2D insulators in Section 5.3.1 in each z -indexed, real-space plane of the 3D insulators examined in this section.

We will now discuss the electronic structure of the Hamiltonian with two π -flux tubes $\tilde{\mathcal{H}}(k_z)$ in detail for representative values of ξ and γ . The numerical results are summarized in Figure 5.9.

5.3.2.1 $\xi = 1, \gamma = -1$: Axion insulator with double band inversion at Γ

In this case, we consider the system response to a pair of z -directed π -flux tubes that are spatially separated in the x direction. As shown in Section 5.1.2, the π -flux response is given in this case by the summed topologies of the $k_y = 0, \pi$ planes in the 3D BZ of $\mathcal{H}(\mathbf{k})$ (which can be summarized by the value of the strong AXI index [19]). In the pristine insulating bulk, the $k_y = 0$ ($k_y = \pi$) plane characterizes an \mathcal{I} -symmetric 2D FTI (trivial insulator), and the bulk correspondingly exhibits an

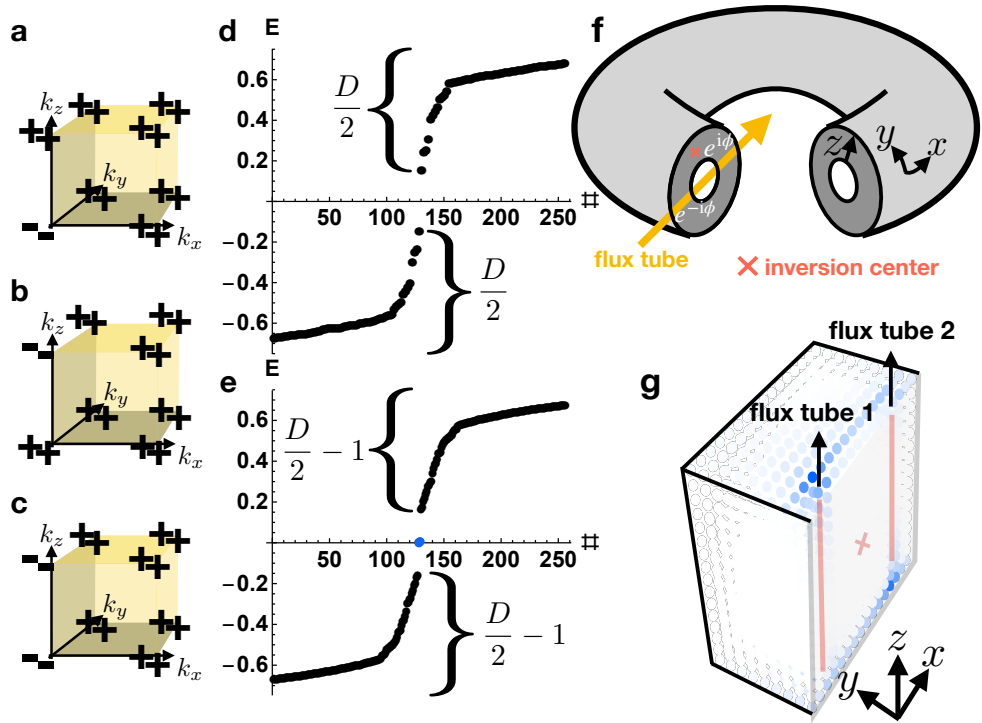


Figure 5.9: 3D flux tube bound states with inversion symmetry. (a)–(e) Bulk inversion eigenvalues and HDBC energy spectra for the flux in Figure 5.8 (b), extended along the z -direction, when the crystal with the BZ in Figure 5.5 (a) is equivalent to (a),(e) an \mathcal{I} -symmetric axion insulator (AXI) [26, 23, 25, 66, 43, 94, 62, 95, 49, 96, 97, 19, 98] with double band inversion at Γ , (b),(e) an AXI with double band inversion at Z , (c),(d) a weak stack of \mathcal{I} -symmetric 2D FTIs with $\pm e/2$ corner charges [62, 19]. Only the 256 lowest-lying states are shown in (d),(e). Anomalous 0D states with charge $\pm e/2$ are present on \mathcal{I} -related flux tube ends in (a) and (b), but not in (c), and are equivalent to the corner states of an \mathcal{I} -symmetric, T -broken 2D FTI [62, 19], and thus persist under the relaxation of particle-hole symmetry [62, 19, 143]. This is consistent with the conclusions of Section 5.1.2, in which it was determined that only topological phases with nontrivial strong indices exhibit a nontrivial π -flux response. (f) Hollow doughnut boundary conditions (HDBC) used to obtain the flux tube end states. Crucially, the HDBC geometry does not have any hinges, such that, absent π -flux tubes, trivial insulators and AXIs exhibit the same gapped energy spectra. (g) Absolute square of the wavefunction of the midgap states in (e) on a $16 \times 16 \times 16$ lattice (cut in half along the transparent grey plane to expose the bound states on two of the four flux tube ends). The inversion center in (g) is marked by a red X. In (g), the wavefunction exhibits some residual localization on all four flux tube ends. However, there is no symmetry that relates the two flux tube ends on each surface (as opposed to flux tube ends on opposing tubes and surfaces, which are here related by bulk \mathcal{I}). Therefore, in the thermodynamic limit and in the presence of symmetry-allowed terms that break all artificial mirror reflection symmetries [62, 18], we expect the two anomalous midgap states to more strongly localize on only two of the four tube ends.

inversion-symmetry-indicated nontrivial AXI index [26, 23, 25, 66, 43, 94, 62, 95, 49, 96, 97, 19, 98]. We observe a single midgap state on two of four flux tube ends, which can be pinned to zero energy by the chiral symmetry in Equation (5.53) or diagnosed via a filling anomaly [19, 143, 32, 144, 146, 147]. The bulk inversion eigenvalues and the flux spectrum are respectively shown in Figure 5.9 (a),(e).

5.3.2.2 $\xi = 1, \gamma = +1$: Axion insulator with double band inversion at Γ

As in the previous case of an AXI driven by double band inversion at Γ , because the summed topology of the $k_y = 0, \pi$ planes in the 3D BZ of $\mathcal{H}(\mathbf{k})$ is again nontrivial (and, equivalently, because the bulk strong AXI index is nontrivial), we observe a nontrivial flux response. This further underlines the fact that, in contrast to the dislocation response, the π -flux response of 2D and 3D insulators only depends on the strong topological index (Section 5.1.2), and in particular does not depend on where bands are inverted. The bulk inversion eigenvalues and the flux spectrum are respectively shown in Figure 5.9 (b),(e).

5.3.2.3 $\xi = 0$: Weak FTI stack

The bulk inversion eigenvalues and the flux spectrum are respectively shown in Figure 5.9 (c),(d). Because the bulk carries a trivial strong (AXI) index, then the π -flux response is trivial.

5.3.3 2D Fluxes with \mathcal{T} Symmetry

In this section, we demonstrate the π -flux response of \mathcal{I} - and \mathcal{T} -symmetric 2D insulators [169, 155, 170, 165, 166, 167, 168, 173]. We begin by considering a pristine 2D insulator described by the Bloch Hamiltonian $\mathcal{H}(\mathbf{k})$ in Equation (5.55) of Section 5.2.3. We then numerically introduce a pair of π -fluxes related by a bulk \mathcal{I} center as discussed in Section 5.1.2 (Figure 5.10). To obtain the numerical results presented in Figure 5.10, we use the same prescription as employed in Section 5.3.1 to create a pair of π -fluxes. We will now discuss the electronic structure of the resulting model $\tilde{\mathcal{H}}$ in detail for $\alpha = -1$ and for representative values of ξ and β .

5.3.3.1 $\xi = 1, \beta = -1$: Topological insulator with band inversion at Γ

In this case, we consider the system response to a pair of π -fluxes spatially separated in the x direction. As shown in Section 5.1.2, the π -flux response is given in this case by the summed topologies of the $k_y = 0, \pi$ lines in the 2D BZ of $\mathcal{H}(\mathbf{k})$ (which can be summarized as the bulk \mathbb{Z}_2 invariant [110, 115, 108]). In the pristine

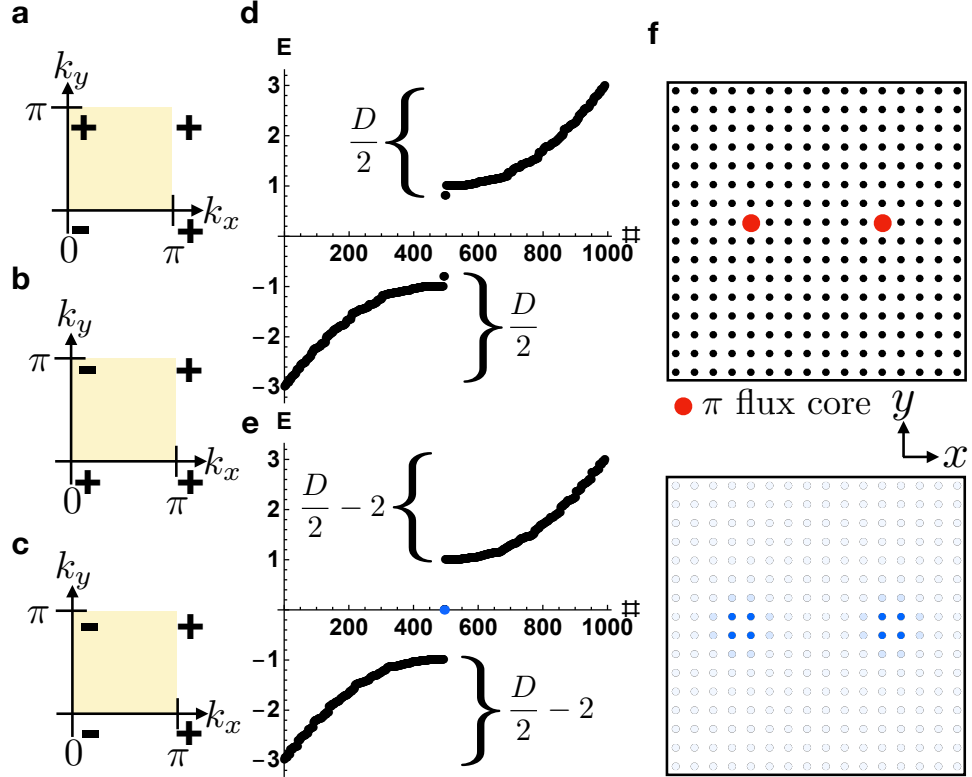


Figure 5.10: 2D π -flux bound states with time-reversal and inversion symmetry. (a)–(e) Bulk inversion eigenvalues and PBC energy spectra for the flux in Figure 5.8 (b) when the crystal with the BZ given by Figure 5.8 (a) is equivalent to (a),(e) a 2D TI driven by band inversion at Γ , (b),(e) a 2D TI driven by band inversion at Y , and (c),(d) a weak y -directed array of T -symmetric SSH [79, 150, 149, 77] chains. In (a)–(c), we denote Kramers pairs of inversion eigenvalues with a single \pm sign. Anomalous 0D flux states with chargeless spin [165, 166, 167, 168] are present in (a) and (b), but not in (c), and are equivalent to the end states of an I - and T -symmetric SSH chain [79, 150, 149, 77]. With chiral symmetry, the two midgap Kramers pairs that are present in (a) and (b) are pinned to zero energy. In the absence of chiral symmetry, a nontrivial π -flux response can still be diagnosed by observing a filling anomaly[19, 143, 32, 144, 146, 147]. (f) Real-space geometry with a pair of π -flux tubes and absolute square of the wavefunction of the midgap states in (e) on a 16×16 lattice.

insulating bulk, the $k_y = 0$ ($k_y = \pi$) line characterizes a nontrivial (trivial) \mathcal{T} -symmetric SSH chain, and the bulk correspondingly exhibits an inversion-symmetry-indicated nontrivial 2D TI \mathbb{Z}_2 Fu-Kane index [1, 5]. We observe a Kramers pair of midgap states at each π -flux core, which can be pinned to zero energy by the chiral symmetry in Equation (5.59) or diagnosed via a filling anomaly [19, 143, 32, 144, 146, 147]. The bulk inversion eigenvalues and the flux spectrum are respectively shown in Figure 5.10 (a),(e).

5.3.3.2 $\xi = 1, \beta = +1$: Topological insulator with band inversion at Γ

As in the previous case of a 2D TI driven by band inversion at Γ , because the summed topology of the $k_y = 0, \pi$ lines in the 2D BZ of $\mathcal{H}(\mathbf{k})$ is again nontrivial (and, equivalently, because the bulk 2D TI index is nontrivial), we observe a nontrivial flux response. This further underlines the fact that, in contrast to the dislocation response, the π -flux response of 2D and 3D insulators only depends on the strong topological index (Section 5.1.2), and in particular does not depend on where bands are inverted. The bulk inversion eigenvalues and the flux spectrum are respectively shown in Figure 5.10 (b),(e).

5.3.3.3 $\xi = 0$: Weak \mathcal{T} -symmetric SSH array

The bulk inversion eigenvalues and the flux spectrum are respectively shown in Figure 5.10 (c),(d). Because the bulk carries a trivial 2D TI index, the π -flux response is trivial.

5.3.4 3D Flux Tubes with \mathcal{T} Symmetry

In this section, we demonstrate the π -flux response of 3D insulators with \mathcal{I} and \mathcal{T} symmetry [169, 155, 170, 165, 166, 167, 168, 173]. We begin by considering a pristine 3D insulator described by the Bloch Hamiltonian $\mathcal{H}(\mathbf{k})$ in Equation (5.61) of Section 5.2.4. We then numerically introduce a pair of π -flux tubes related by a bulk \mathcal{I} center as detailed in Section 5.3.2. As in Section 5.2.4, we set $\alpha = \beta = -1$ in Equation (5.61). We will now discuss the electronic structure of the Hamiltonian with two π -flux tubes $\tilde{\mathcal{H}}(k_z)$ in detail for representative values of ξ and γ . The numerical results are summarized in Figure 5.11.

5.3.4.1 $\xi = 1, \gamma = -1$: Higher-order topological insulator with double band inversion at Γ

In this case, we consider the system response to a pair of z -directed π -flux tubes that are spatially separated in the x direction. As shown in Section 5.1.2, the

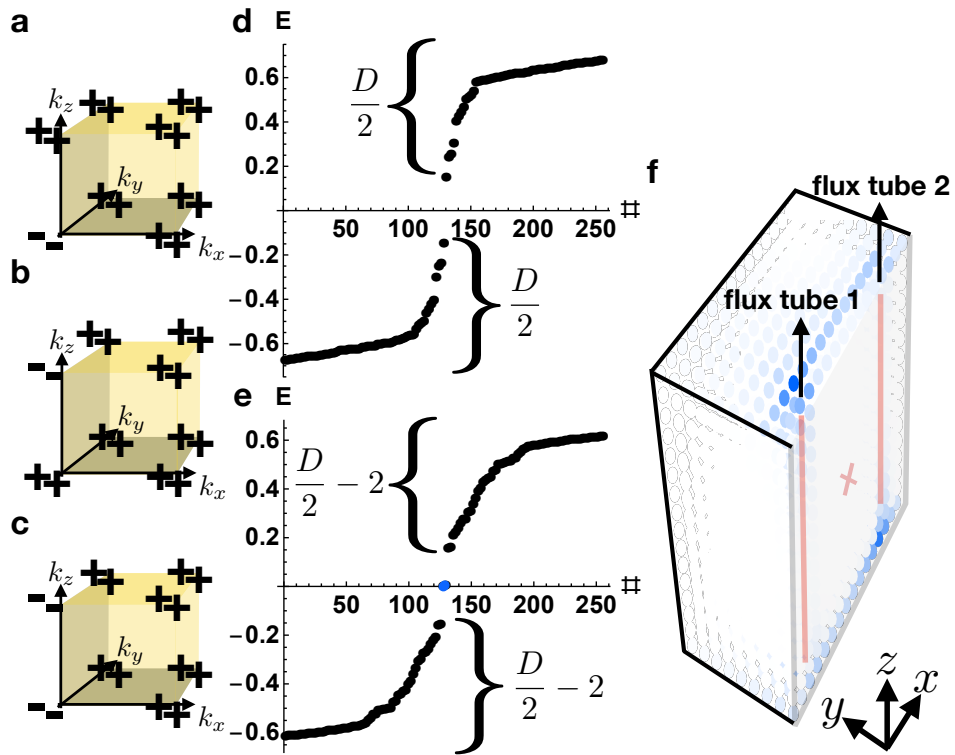


Figure 5.11: 3D flux tube bound states with time-reversal and inversion symmetry. (a)–(e) Bulk inversion eigenvalues and HDBC energy spectra for the flux in Figure 5.8 (b), extended along the z -direction, when the crystal with the BZ shown in Figure 5.5 (a) is equivalent to (a),(e) an \mathcal{I} -symmetric HOTI driven by double band inversion at Γ , (b),(e) a HOTI with double band inversion at Z , and (c),(d) a weak stack of \mathcal{I} and \mathcal{T} -symmetric symmetric 2D FTIs [62] with corner midgap Kramers pairs. In (a)–(c), we denote Kramers pairs of inversion eigenvalues with a single \pm sign. Only the 256 lowest-lying states are shown in (d),(e). Anomalous 0D states with chargeless spin [165, 166, 167, 168] are present on \mathcal{I} -related flux tube ends in (a) and (b), but not in (c), and are equivalent to the corner states of an \mathcal{I} - and \mathcal{T} -symmetric 2D FTI [62, 19], and thus persist under the relaxation of particle-hole symmetry [62, 19, 143]. This is consistent with the conclusions of Section 5.1.2, in which it was determined that only topological phases with nontrivial strong indices exhibit a nontrivial π -flux response. With chiral symmetry, the two midgap Kramers pairs that are present in (a) and (b) are pinned to zero energy. In the absence of chiral symmetry, the π -flux tube response can still be diagnosed as topologically nontrivial by observing a filling anomaly[19, 143, 32, 144, 146, 147]. (f) Absolute square of the midgap states in (e) on a $16 \times 16 \times 16$ lattice (cut in half along the transparent grey plane to expose the bound states on two of the four flux tube ends). The inversion center in (f) is marked by a red X. In (f), the wavefunction exhibits some residual localization on all four flux tube ends. However, there is no symmetry that relates the two flux tube ends on each surface (as opposed to flux tube ends on opposing tubes and surfaces, which are here related by bulk \mathcal{I}). Therefore, in the thermodynamic limit and in the presence of symmetry-allowed terms that break all artificial mirror reflection symmetries [62, 18], we expect the two anomalous Kramers pairs of midgap states to more strongly localize on only two of the four tube ends.

π -flux response is given in this case by the summed topologies of the $k_y = 0, \pi$ planes in the 3D BZ of $\mathcal{H}(\mathbf{k})$ (which can be summarized by the value of the strong \mathbb{Z}_4 HOTI index [19, 62]). In the pristine insulating bulk, the $k_y = 0$ ($k_y = \pi$) plane characterizes an \mathcal{I} - and \mathcal{T} -symmetric 2D FTI (trivial insulator), and the bulk correspondingly exhibits an inversion-symmetry-indicated nontrivial \mathbb{Z}_4 HOTI index [29, 30, 91, 62]. We observe a Kramers pair of midgap states on two of four flux tube ends, which can be pinned to zero energy by the chiral symmetry in Equation (5.64) or diagnosed via a filling anomaly [19, 143, 32, 144, 146, 147]. The bulk inversion eigenvalues and the flux spectrum are respectively shown in Figure 5.11 (a),(e).

5.3.4.2 $\xi = 1, \gamma = +1$: Higher-order topological insulator with double band inversion at \mathcal{Z}

As in the previous case of a HOTI driven by double band inversion at Γ , because the summed topology of the $k_y = 0, \pi$ planes in the 3D BZ of $\mathcal{H}(\mathbf{k})$ is again nontrivial (and, equivalently, because the bulk is a symmetry-indicated HOTI [19, 62]), we observe a nontrivial flux response. This further underlines the fact that, in contrast to the dislocation response, the π -flux response of 2D and 3D insulators only depends on the strong topological index (Section 5.1.2), and in particular does not depend on where bands are inverted. The bulk inversion eigenvalues and the flux spectrum are respectively shown in Figure 5.11 (b),(e).

5.3.4.3 $\xi = 0$: Weak \mathcal{T} -symmetric FTI stack

The bulk inversion eigenvalues and the flux spectrum are respectively shown in Figure 5.11 (c),(d). Because the bulk carries trivial strong TI and HOTI indices, then the π -flux response is trivial.

Part III

Extensions

Chapter 6

Higher-order topology in classical electric circuits

In this chapter, we extend the notion of higher-order topology to the theory of classical electric circuits (RLC circuits), which allows us to arrive at a tabletop experimental realization of protected midgap corner states in two dimensions.

The Berry phase provides a powerful language to describe the topological character of band structures and single-particle systems [174, 163] (recall that Section 2.2.1 introduced the Wilson loop as a non-abelian generalization of the Berry phase). Manifestly, it allows to treat fermionic and bosonic quantum systems on the same footing. Furthermore, the Berry phase concept is not tied to Hilbert space, but applies to the connectivity of any given coordinate space, and as such accounts for classical degrees of freedom as well [175]. It is thus intuitive that, with the discovery of various topological quantum states of matter such as quantum Hall [106] and quantum spin Hall effect [176], classical systems with similar phenomenology could also be identified. This was initiated in the context of photonics [177, 178], and subsequently transferred to other fields such as mechanics [179, 180], acoustics [181], electronics [182, 183], and other fields. Even though spectra and eigenstates of the single particle problem, including edge modes, might look similar or even identical, it is the fundamental degrees of freedom which pose the central distinction between quantum systems and their designed classical analogues. First, quantization phenomena deriving from topological invariants usually necessitate the non-commutativity of phase space and as such are often reserved to quantum systems. Second, internal symmetries pivotal to the protection of a topological phase might not carry over to classical systems as the degrees of freedom are changed from fermionic to bosonic. For instance, this applies to time-reversal symmetry

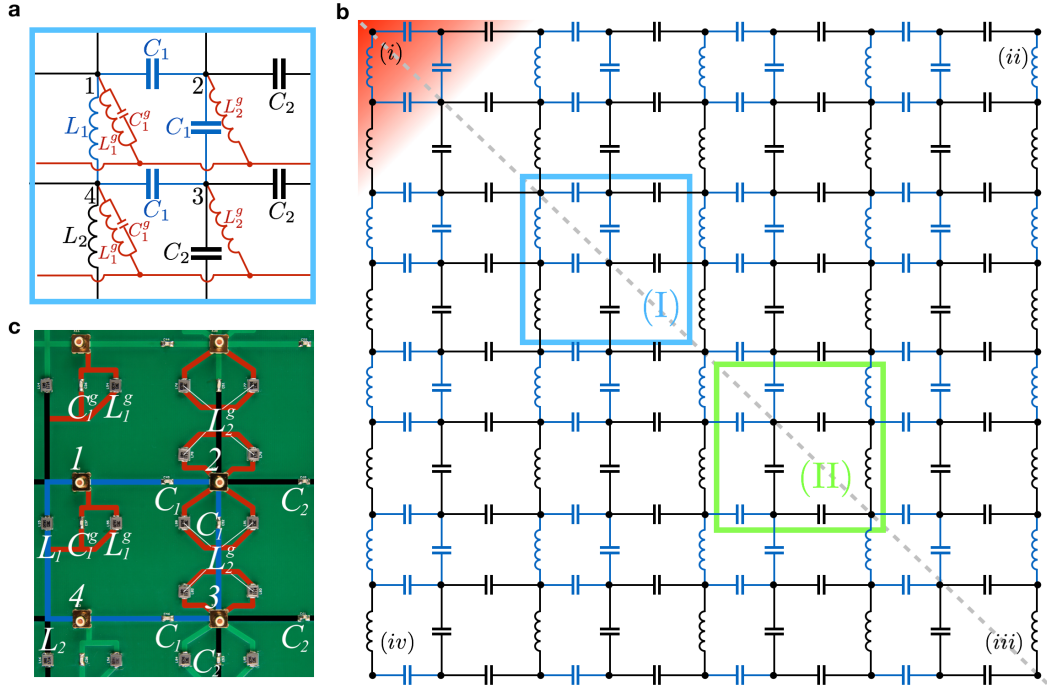


Figure 6.1: Electrical circuit exhibiting a topological corner state with nodes of the circuit indicated by black dots. (a) Unit cell of the circuit. Blue and black circuit elements correspond to weak and strong bonds in a tight-binding or mechanical analogue of the circuit. Red circuit elements connect to the ground. All capacitor-inductor pairs have the same resonance frequency $\omega_0 = 1/\sqrt{L_1 C_1} = 1/\sqrt{L_2 C_2} = 1/\sqrt{L_1^g C_1^g}$. (b) Layout of the full circuit which has been realized experimentally. The corners (i) and (iii) are invariant under the mirror symmetry that leaves the dashed grey line invariant. They are compatible with the bulk unit cell choices (I) and (II), respectively, which correspond to an interchange of strong and weak bonds. As a consequence we expect a topological bound state at corner (i) but not at corner (iii). (c) Unit cell of the experimentally realized circuit.

\mathcal{T} as the protecting symmetry of the quantum spin Hall effect, where the half integer spin of electrons implies Kramer's degeneracy due to $\mathcal{T}^2 = -1$ in the quantum case, while it does not in the classical case $\mathcal{T}^2 = 1$. Whereas the classical counterpropagating edge modes might still be detectable, there is no particular topological protection left, rendering the classical system much more vulnerable to perturbations [184].

From this perspective, at least two directions appear as most promising to develop classical topological band structure models that are universally stable beyond fine-tuning. The first is the realization of classical analogues to topological semimetals [185, 186, 187, 188, 189, 190], where the extensive edge mode degeneracy suggests unambiguous persistent spectral edge features also in the presence of small perturbations. The second is to focus on topologically insulating quantum electronic states where either no protecting symmetries are needed such as for the quantum Hall effect [177], or where the protecting symmetries obey the same algebraic relations in the classical and quantum mechanical case.

Electric quadrupole insulators [86] fall in the latter category. While the quantum case is most suitably constructed from the viewpoint of quantized multipole moments of an electronic crystal, the complementary protecting symmetry perspective is most intuitive for the classical system design. The symmetry group that protects the quantization of the quadrupole moment includes two non-commuting reflection symmetries \mathcal{M}_x and \mathcal{M}_y as well as a C_4 rotation symmetry. In particular, they obey $\mathcal{M}_{x,y}^2 = 1$, and as such directly carry over to the classical degrees of freedom. In analogy to the relation between the quantization of bulk dipole moment (which is quantized to half-integer values by inversion symmetry) and the appearance of protected end states in the topological Su-Schrieffer-Heeger model, an additional spectral symmetry, the chiral symmetry, is needed to pin the topological boundary modes in the middle of the bulk energy gap. All these symmetries are realized in the microscopic model given in Reference [86]. Hence, the only task is to implement the hopping model given by a four site unit cell and real, but sign-changing hybridization elements. Due to recent progress in implementing waveguide elements that invert the sign of hybridization [191], the complexity of this model could recently be captured by a photonic cavity lattice structure [192]. We turn to topoelectrical circuits to realize the quadrupole insulators in a classical environment.

6.1 Linear circuit theory and topology

We consider non-dissipative linear electric circuits, i.e., circuits made of capacitors and inductors. Labeling the nodes of a circuit by $a = 1, 2, \dots$, the response of the

circuit at frequency ω is given by Kirchhoff's law

$$I_a(\omega) = \sum_{b=1,2,\dots} J_{ab}(\omega) V_b(\omega) \quad (6.1)$$

that relates the voltages V_a to the currents I_a via the grounded circuit Laplacian

$$J_{ab}(\omega) = i\omega C_{ab} - \frac{i}{\omega} W_{ab}. \quad (6.2)$$

Here, the off-diagonal components of the matrix C contain the capacitance C_{ab} between nodes $a \neq b$, while its diagonal component is given by the total node capacitance

$$C_{aa} = -C_{a0} - \sum_{b=1,2,\dots} C_{ab} \quad (6.3)$$

including the capacitance C_{a0} between node a and the ground. Similarly, the off-diagonal components of the matrix W contain the inverse inductivity $W_{ab} = L_{ab}^{-1}$ between nodes $a \neq b$, while its diagonal components are given by the total node inductivity

$$W_{aa} = -L_{a0}^{-1} - \sum_{b=1,2,\dots} L_{ab}^{-1} \quad (6.4)$$

including the inductivity L_{a0} between node a and the ground.

At fixed frequency ω , $J_{ab}(\omega)$ determines the linear response of the circuit in that the impedance Z_{ab} between two nodes a and b is given by

$$Z_{ab}(\omega) = G_{aa}(\omega) + G_{bb}(\omega) - G_{ab}(\omega) - G_{ba}(\omega), \quad (6.5)$$

where $G(\omega) = J^{-1}(\omega)$ is the circuit Green's function. The impedance is thus dominated by the smallest eigenvalues $j_n(\omega)$ of $J(\omega)$ at this given frequency, provided that the sites a and b are in the support of the corresponding eigenfunctions.

In turn, frequencies ω for which an exact zero eigenvalue $j_n(\omega) = 0$ exists correspond to eigenmodes of the circuit. They are determined by the equations of motion satisfied by the electric potential $\phi_a(t)$ at node a

$$\sum_{b=1,2,\dots} C_{ab} \frac{d^2}{dt^2} \phi_b(t) + \sum_{b=1,2,\dots} W_{ab} \phi_b(t) = 0. \quad (6.6)$$

The spectrum ω^2 of eigenmodes of the circuit is thus given by the spectrum of the dynamical matrix

$$D = C^{-1/2} W C^{-1/2}, \quad (6.7)$$

with matrix multiplication implied.

We now explain why topological properties can be defined for the matrices $J(\omega)$ and D that describe the physics of the circuit. In order to define topological properties of a physical system, the notions of *locality* and *adiabaticity* (enabled by spectral gaps) are of central importance. Locality naturally arises when we consider circuits in which the nodes a are arranged in a (in the case at hand two-dimensional) lattice. This also allows to define spatial symmetry transformations. Adiabaticity in turn follows from the spectral continuity of $J(\omega)$ as a function of ω , that is, if a specific frequency ω_0 lies in a gap in the spectrum of D , the spectrum of $J(\omega_0)$ also has a gap around zero eigenvalues. Furthermore, a spectrally isolated eigenvalue (which may be a topological bound state) of D at frequency ω_0 is in correspondence with a spectrally isolated zero mode of $J(\omega_0)$.

Due to these relations between $J(\omega)$ and D , protected boundary modes of a circuit can arise from the topological properties of either matrix. In this work, we choose to build a two-dimensional circuit for which the topology of $J(\omega_0)$ at a specific frequency ω_0 protects corner modes. The topological protection of spectrally isolated zero modes always requires a spectral (chiral or particle-hole) symmetry that relates eigenvalues of equal magnitude and opposite sign. Spectrally and locally isolated eigenstates of this symmetry, if present, are protected in that they are pinned to the eigenvalue zero. As an eigenstate of $J(\omega)$, such a state naturally dominates the linear response of the circuit.

6.2 Electric circuit with corner states

To realize a quadrupole insulator with topologically protected corner states, the system should have two *anticommuting* mirror symmetries, as well as a C_4 rotation symmetry in the bulk. The fundamental mirror symmetries in classical systems *commute*. To build a classical analogue of a electric quadrupole insulator, we thus devise a circuit that has an *emergent* pair of anticommuting mirror symmetries M_x and M_y for modes near a specific frequency ω_0 . This means that $J(\omega_0)$ commutes exactly with M_x and M_y and the eigenspaces of D are approximately invariant under M_x and M_y for frequencies near ω_0 .

We first discuss the bulk properties of a periodically repeating circuit unit cell, depicted in Figure 6.1, before considering boundary modes. The circuit unit cell contains four sites denoted by pairs $(i, j) \in \{(0, 0), (0, 1), (1, 0), (1, 1)\}$. We use two pairs of capacitors and inductors (C_1, L_1) and (C_2, L_2) which have the same resonance frequency $\omega_0 = 1/\sqrt{L_1 C_1} = 1/\sqrt{L_2 C_2}$ to couple these sites. The latter equality is automatically satisfied if we set $C_2 = \lambda C_1$, $L_2 = L_1/\lambda$ for some real positive parameter λ . Sites 1 and 4 are connected to the ground via an LC circuit

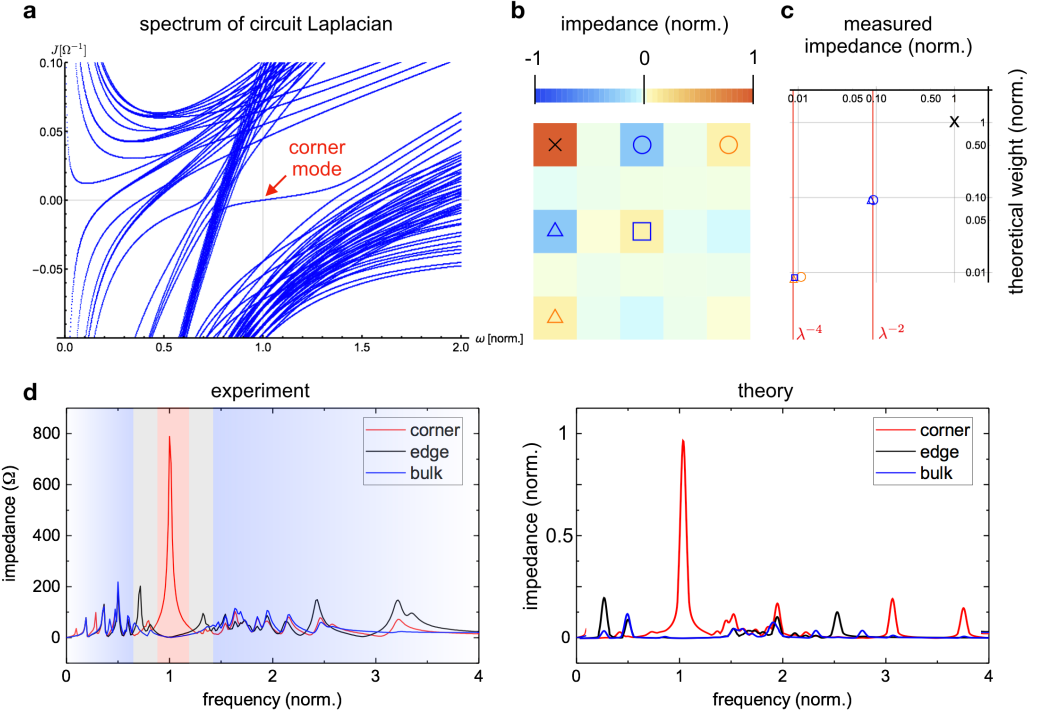


Figure 6.2: Comparison of experimental and theoretical results for the circuit spectrum and corner mode. (a) Theoretical spectrum of the circuit Laplacian $J(\omega)$ as a function of the driving frequency. All frequency scales are normalized to the resonance frequency ω_0 . An isolated mode crossing the gap, which corresponds to a zero energy eigenvalue of $J(\omega)$ at $\omega = \omega_0$ is clearly visible. It corresponds to the topological corner mode. The calculation includes a random disorder of 1% for all capacitors and 2% for all inductors. (b) Theoretical weight distribution of the eigenstate of $J(\omega_0)$ that corresponds to the corner mode [Equation (6.9)], where only the circuit nodes near the corner are shown. (c) Comparison between the experimental corner mode impedance at $\omega = \omega_0$, measured between nearest neighbor nodes along the horizontal and vertical edges, and along the diagonal, and the theoretically computed weight of the corner mode eigenstate. Both decay with the decay constant $\lambda = 3.3$ set by the ratio of alternating capacitors/inductors. (d) Frequency scan (normalized with respect to ω_0) of the impedance between two nearest-neighbor sites at the corner, at the edge, and in the bulk. Both the experimental and theoretical curves show the corner state resonance isolated in the gap of bulk and edge states.

with $C_1^g = C_1$ and $L_1^g = L_1$ such that it has the same resonance frequency ω_0 . Sites 2 and 3 are connected to the ground via an inductivity $L_2^g = L_1/[2(1 + \lambda)]$. In this setup, the circuit is parametrized by the parameters ω_0 and λ .

We now describe the circuit with periodic boundary conditions in momentum space. The Fourier components of the matrix $J_\lambda(\omega)$, denoted by $\tilde{J}_\lambda(\omega, \mathbf{k})$, are 4×4 matrices that satisfy

$$\begin{aligned}\mathcal{M}_x \tilde{J}_\lambda(\omega_0, k_x, k_y) \mathcal{M}_x^{-1} &= \tilde{J}_\lambda(\omega_0, -k_x, k_y), \\ \mathcal{M}_y \tilde{J}_\lambda(\omega_0, k_x, k_y) \mathcal{M}_y^{-1} &= \tilde{J}_\lambda(\omega_0, k_x, -k_y), \\ \mathcal{C}_4 \tilde{J}_\lambda(\omega_0, k_x, k_y) \mathcal{C}_4^{-1} &= \tilde{J}_\lambda(\omega_0, k_y, -k_x),\end{aligned}\quad (6.8)$$

where $\mathcal{M}_x = \sigma_1 \tau_3$, $\mathcal{M}_y = \sigma_1 \tau_1$, and $2\mathcal{C}_4 = (\sigma_1 + i\sigma_2)\tau_0 + (\sigma_1 - i\sigma_2)(i\tau_2)$ are the representations of the symmetries satisfying $\mathcal{M}_x \mathcal{M}_y = -\mathcal{M}_y \mathcal{M}_x$ and $\mathcal{C}_4 \mathcal{M}_x \mathcal{C}_4^{-1} = \mathcal{M}_y$. Here, σ_μ and τ_μ , $\mu = 0, 1, 2, 3$ are the 2×2 identity matrix and the three Pauli matrices acting on the i and j sublattice index, respectively. Note that the circuit is then also invariant under the combined symmetries $\mathcal{M}_{x\bar{y}} = \mathcal{C}_4 \mathcal{M}_x$ and $\mathcal{M}_{xy} = \mathcal{C}_4 \mathcal{M}_y$ that map $(x, y) \rightarrow (-y, -x)$ and $(x, y) \rightarrow (y, x)$, respectively. In addition, $\tilde{J}_\lambda(\omega_0, \mathbf{k})$ has a chiral symmetry $\mathcal{C} = \sigma_3 \tau_0$, which by $\mathcal{C} \tilde{J}_\lambda(\omega_0, \mathbf{k}) \mathcal{C}^{-1} = -\tilde{J}_\lambda(\omega_0, \mathbf{k})$ implies a spectral symmetry. Up to an overall factor of i , the circuit Laplacian $\tilde{J}_\lambda(\omega_0, \mathbf{k})$ takes exactly the same form as the Bloch Hamiltonian matrix of the quadrupole insulator introduced in Reference [86] (see Appendix C.1). For $\lambda \neq 1$ the spectrum of $\tilde{J}(\omega_0, \mathbf{k})$ is gapped, and the gapless point $\lambda = 1$ corresponds to a topological phase transition between a quadrupole circuit for $\lambda > 1$ and a trivial circuit for $\lambda < 1$.

We now turn to a circuit with open boundary conditions to realize topologically protected corner modes. In general, two criteria must be met to realize a topological bulk-boundary correspondence. First, the symmetries which protect the topological character may not be broken by the boundary. Second, the system termination must be compatible with the choice of bulk unit cell for which a topological invariant has been defined, i.e., the boundary should not cut through unit cells. We demonstrate all of these properties on a single circuit by choosing different boundary terminations as follows. In order for the open system to obey the chiral symmetry \mathcal{C} , the diagonal elements of $J(\omega)$ need to vanish at ω_0 . This holds for all bulk sites by the construction of the model. Imposing this symmetry also for edge and corner sites in an open geometry fixes the circuit elements (capacitor and or inductor) that connect each site to the ground. (See Appendix C.5 for the specific grounding at the edge termination that was used for the open circuit.)

With this condition imposed on the boundary sites, we terminate the upper left edge of the circuit in a way compatible with the choice of bulk unit cell denoted as (I) in

Figure 6.1 (c). The lower right circuit termination is chosen to be compatible with the unit cell denoted as (II) in Figure 6.1 (c). This edge termination preserves the mirror symmetry $\mathcal{M}_{x\bar{y}} = \mathcal{C}_4 \mathcal{M}_x$ and breaks all other spatial symmetries mentioned above. Topological corner modes could thus potentially be protected at the upper left and the lower right corner, which are invariant under $\mathcal{M}_{x\bar{y}}$, but not at the other two corners. However, the bulk circuit Laplacians which correspond to the two choices of unit cell (I) and (II) satisfy $\tilde{\mathcal{J}}_\lambda^{(II)}(\omega_0, \mathbf{k}) = \lambda \tilde{\mathcal{J}}_{1/\lambda}^{(I)}(\omega_0, \mathbf{k})$ for an appropriate labeling of unit cell sites. Recalling that the topological phase transition occurs at $\lambda = 1$, this implies that when $\tilde{\mathcal{J}}^{(I)}(\omega_0, \mathbf{k})$ is in a topological phase, $\tilde{\mathcal{J}}^{(II)}(\omega_0, \mathbf{k})$ is trivial and vice versa. As a result, our choice of boundary termination renders one corner topologically non-trivial (the upper left one for $\lambda > 1$) and the opposite corner trivial.

We thus expect that for $\lambda > 1$ and at eigenfrequency ω_0 , the circuit depicted in Figure 6.1 (c) supports a localized topological corner state at the upper left corner, and none at the lower right or any other corner. We further note that the corner mode should be an exact eigenstate of the $\mathcal{M}_{x\bar{y}}$ symmetry. We will now present impedance measurements that support this expectation.

6.3 Experimental circuit realization

For the experimental realization of topological corner modes a circuit board with 4.5×4.5 unit cells was designed. The line spacing on the board was chosen such that spurious inductive coupling between the circuit elements was below our measurement resolution. All impedance measurements were performed with a HP 4194 A Impedance/Gain-Phase Analyzer in a full differential configuration. In order to achieve a clearly resolvable corner state resonance on the superimposed resistive background of the bulk states, i.e., the combined impedance contribution of our RLC circuit, which is of the order of a few hundreds of milli-ohm at the resonance, the values of the circuit elements were chosen for the resonance frequency to be at 2.8 MHz. The ratio λ between the capacitors/inductors was set to 3.3, so that the spatially decaying corner state resonance could be observed over 3 unit cells in each spatial direction.

Figure 6.2 compares the experimental data with the theoretical predictions, finding excellent agreement between the two. It demonstrates the existence of a spectrally and spatially localized topological corner state. In Figure 6.2 (a) the frequency-dependent spectrum of the circuit Laplacian shows the isolated corner mode and illustrates the connection between a (bulk and edge) spectral gap of $J(\omega)$ at fixed frequency ω and a gap in the spectrum of the dynamical matrix D , which corre-

sponds to a range of frequencies without zero modes of $J(\omega)$. In Figure 6.2 (b) and (c) the corner mode at $\omega = \omega_0$ is mapped out with single-site resolution. The exponential decay of the measured impedance is in excellent correspondence with the theoretical expectation

$$\phi_c(x, y) = (-\lambda)^{-(x+y)} \phi_c(0, 0), \quad (6.9)$$

where $\lambda = C_2/C_1$ according to Figure 6.1 and $x, y \in \mathbb{N}$ label the absolute distance from the upper left edge in both spatial directions in units of the circuit lattice constant. The experimental demonstration that the corner mode is indeed spectrally isolated, and as such not deriving from a bulk or edge effect, is shown in Figure 6.2 (d) via a comparison between measurement and simulation. The theoretical impedance corner peak is normalized to unity, while the corresponding impedance corner peak in the actual measurement reaches 800Ω .

6.4 Physical interpretation of corner modes

Along the x and y direction, the circuit corresponds to a collection of connected pairs of linear circuits with alternating capacitors and inductors, respectively. With the appropriate boundary conditions discussed previously, electric charge on the capacitors forms “dimerized”, isolated oscillators as described in Reference [190, 193]. Note that the capacitances alternate between C_1 and C_2 with $C_1 < C_2$, constituting in each direction a one-dimensional Su-Schrieffer-Heeger (SSH) model. Such models possess well-known eigenmodes, i.e. potential and current profiles where every second node exhibits no current and accordingly no potential difference [190], which occurs here since a fixed amount of charge Q between each pair of capacitors give rise to a potential difference $V_1 > V_2$, since $Q = V_1 C_1 = V_2 C_2$. With appropriate boundary conditions, we can thus infer the existence of a boundary mode of anti-phase currents that is decaying exponentially by a factor of $1/\lambda = C_1/C_2$ per unit cell.

A novel feature of our measured corner mode is that this mode is *not* the result of edge polarization, i.e., even though the Laplacian eigenstate of the corner mode [Equation (6.9)] suggests a similar form in x and y direction, it cannot be arrived at by combining SSH models along the different edges. This hints at topological *quadrupole* polarization in the given circuit, as opposed to dipole polarization in the SSH case. It is instructive to decompose the given circuit in terms of pairs of vertical and horizontal SSH-type circuit chains, where we see both SSH chains built by capacitors as well as their dual form built by inductors in each unit cell string along the x or y axis. The alternating *L*-type and *C*-type SSH chains within the

unit cell then are arranged such that their edge charge polarizations cancel. To see this concretely, we turn to frequency space, where a voltage difference equals Q/C across a capacitor C , but takes the form $L\ddot{Q} \rightarrow -\omega^2 L Q$ across an inductor L . By identifying $1/C \equiv -\omega^2 L$, we notice that the L-type dual chain possesses effective "negative couplings" in the Laplacian compared to the C-type chain. For $\omega \rightarrow \omega_0$ this then gives the same absolute but sign-reversed effective coupling, and the dipolar SSH-type polarization cancels out in each unit cell. Physically, the sign difference between the effective couplings of capacitors and inductors results from their opposite quarter-period phase shifts, which add up to a sign reversal.

Chapter 7

Fractional corner charges in two-dimensional systems

In this chapter of the thesis, we explore higher-order topological insulators in two spatial dimensions. Naively, these would feature corner-localized zero-dimensional midgap states in finite geometries. However, absent spectral symmetries such as particle-hole or chiral symmetry, all corner states can be collectively pushed out of the bulk energy gap by symmetry preserving potential terms. In contrast, first-order phases in two dimensions do not share this problem, as their one-dimensional edge states undergo a spectral flow that connects valence with conductance bands.

In order to arrive at a meaningful notion of higher-order topology in two dimensions, it becomes therefore necessary to exchange corner states for filling anomalies, as was already discussed in Chapter 5 (for an explicit example, see Section 5.2.1.2): A paradigmatic example are one-dimensional (1D) lattices with inversion symmetry, as represented by the Su-Schrieffer-Heeger model. There exist two atomic limits, with Wannier centers at inequivalent high-symmetry positions in the unit cell. One of them, with Wannier center at the unit cell boundary (potentially realized in polyacetylene), is an obstructed atomic limit (OAL), and leads to half charges at the end of an open chain [194, 162, 195].

The physical consequences of filling anomalies are fractional charges that accumulate at sample boundaries. Crystal symmetries can impose quantization constraints on charge fractionalization, as explored in Reference [32]. Here, we extend the charge fractionalization picture of two-dimensional higher-order topological phases to the physically relevant case of time-reversal symmetric crystals with significant spin-orbit coupling. We focus on 2D OALs, whose charge fractionalization can be

intuitively understood by thinking of boundary terminations as means of cutting through the integer-charged Wannier functions.

In addition to the general classification of corner charges in spinful 2D crystals, we discuss buckled bilayers of Bi, As, and Sb as a family of 2D materials that can realize OALs and corner charges. Based on density functional theory (DFT) calculations, we provide a phase diagram as a function of buckling strength (which may be controlled with a suitable substrate), identifying strong topological insulator (TI) phases and 2D OALs. One of the OALs supports corner charges, while the other one does not.

The chapter is structured as follows. In Section 7.1 we define the precise meaning of corner charge for our work as well as the role of the sample termination. In Section 7.2, we show how OALs can be identified by bulk invariants. Finally, in Section 7.3 the material candidates are discussed.

7.1 Charge quantization in time-reversal symmetric insulators

The 2D phases we are interested in support no 1D gapless boundaries. The bulk gap may be populated by boundary-localized midgap states, but those cannot be stabilized by TRS or crystalline symmetries. In this section, we will show that it is nevertheless often possible to diagnose a phase as an OAL in 2D via its corner charge fractionalization. We establish that this property remains invariant even when all midgap states are pushed out of the bulk gap and arbitrary symmetry-preserving boundary manipulations are allowed [25, 196, 90, 18, 32].

7.1.1 Quantization of the corner charge

We consider 2D spinful insulating systems with TRS T (class AII in the Altland-Zirnbauer classification, $T^2 = -1$) and the spatial symmetries corresponding to a symmetry group \mathcal{G} . We exclude first-order topological insulators so that the models we are studying are generically gapped even in a geometry with open boundary conditions. Additionally, we exclude insulators with bulk (TRS) polarization because those have edge-induced filling anomalies that scale with edge length and therefore result in metallic edges that preclude the existence of stable localized corner charges[32].

We assume a tight-binding description of the system of interest. Denote by a_1 and a_2 the translation vectors corresponding to the decomposition of the \mathcal{G} -symmetric

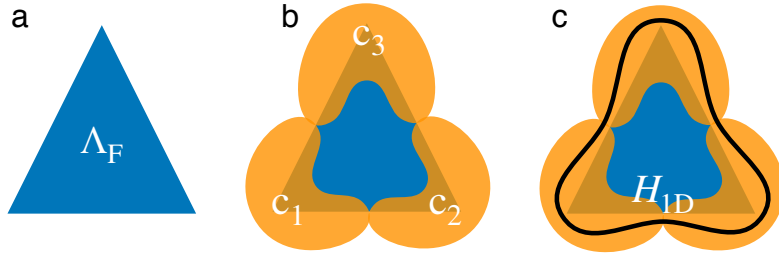


Figure 7.1: Corner charge fractionalization due to C_3 rotational symmetry. (a) The finite system Λ_F on which H_F is defined. (b) The boundary regions $c_1, c_2, c_3 \in C$. Due to the C_3 symmetry in G_F , we have that $Q_{c_1} = Q_{c_2} = Q_{c_3}$. Together with $Q_{c_1} + Q_{c_2} + Q_{c_3} \in 2\mathbb{Z}$, this implies a corner charge fractionalization in even multiples of $1/3$. (c) A 1D edge addition, modeled by the Hamiltonian H_{1D} . We prove in section 7.1.2 that the corner charges Q_{c_i} are only changed by even integers.

lattice Λ into n -site unit cells $S = \{\mathbf{r}_1, \dots, \mathbf{r}_n\}$, where \mathbf{r}_i denotes the position of site i in the unit cell as measured from the unit cell origin $\mathbf{r}_1 \equiv 0$. (Note that here and in the following, we only treat unit cells that are mapped to themselves under all available point-group symmetries, and do not cut through atomic sites. By these properties, a finite-size termination which does not cut through unit cells becomes possible.) We have

$$\Lambda = \bigcup_{x,y \in \mathbb{Z}} \bigcup_{\mathbf{r} \in S} (x\mathbf{a}_1 + y\mathbf{a}_2 + \mathbf{r}). \quad (7.1)$$

We are considering tight-binding Hamiltonians of the form

$$H = \sum_{\mathbf{v}, \mathbf{w} \in \Lambda} \sum_{\mu, \nu} h_{\mathbf{v}\mu, \mathbf{w}\nu} c_{\mathbf{v}\mu}^\dagger c_{\mathbf{w}\nu}, \quad (7.2)$$

where μ, ν run over orbital degrees of freedom defined at each lattice site and $c_{\mathbf{v}\mu}^\dagger$ creates an electron in orbital μ at lattice site \mathbf{v} . Hermiticity of H as well as the symmetry requirements posed by T and the symmetry group \mathcal{G} imply relations among the Hamiltonian elements $h_{\mathbf{v}\mu, \mathbf{w}\nu}$ which we implicitly assume to be fulfilled here and in the following.

Given a unit cell decomposition of Λ in terms of S , we define a *trivial atomic limit* by a Hamiltonian that is adiabatically deformable into one for which the implication

$$\mathbf{v} \in \bigcup_{\mathbf{r} \in S} (x\mathbf{a}_1 + y\mathbf{a}_2 + \mathbf{r}) \not\ni \mathbf{w} \Rightarrow h_{\mathbf{v}\mu, \mathbf{w}\nu} = 0 \quad (7.3)$$

holds for all choices of x and y , that is, there are no couplings between different unit cells.

To calculate corner charges we consider a finite system of $|F|$ unit cells, via restricting H to a subset $\Lambda_F \in \Lambda$ (thereby obtaining H_F), which is given by

$$\Lambda_F = \bigcup_{x,y \in F} \bigcup_{r \in S} (x\mathbf{a}_1 + y\mathbf{a}_2 + \mathbf{r}). \quad (7.4)$$

We choose Λ_F so as to retain all point group symmetries contained in \mathcal{G} , a subgroup we denote by \mathcal{G}_F (it does not contain translations or nonsymmorphic symmetries). Then we consider a subset $C \subset \Lambda_F$ comprised of a minimal (but larger than 1) number of disjoint boundary regions that form an orbit under \mathcal{G}_F and contain an integer number of unit cells each. We choose C to cover all boundaries of Λ_F . A particular boundary region $c \subset C$ has charge

$$Q_c = \sum_{v \in c} \sum_{\mu} \sum_{n \in \text{occ}} |\langle v\mu | n \rangle|^2, \quad (7.5)$$

where $|n\rangle$ denotes an eigenstate of H_F that is taken out of the occupied subspace occ bounded by E_{Fermi} and we have $|v\mu\rangle = c_{v\mu}^\dagger |0\rangle$ where $|0\rangle$ denotes the electronic vacuum. Since we only consider regions c that are related to each other by elements of \mathcal{G}_F , they have necessarily the same charge. Now, note that the charge of the full system is an even integer (given by $|\text{occ}|$), as is the charge of the complement of C , as long as we choose the regions in C large enough so as to ensure that the eigenstates localized in the complement are pure bulk-like in character and unaffected by the presence of a boundary. This is always possible when the linear extent by which C penetrates the bulk is much larger than the correlation length set by the bulk gap. We may then view the states contributing to the charge of the complement of C as states of a complete system of reduced size that has periodic boundary conditions and even integer charge. We thus deduce that Q_c is quantized in even integer multiples of $1/q$, where $q = |C|$ denotes the number of elements in C . See Figures 7.1 (a) and (b) for an example with threefold rotational symmetry.

We call Q_c the corner charge since, in a pristine OAL, its fractional part derives from exponentially localized Wannier orbitals that are “cut through” by corners in the boundary of the system [90, 197, 32]: The Wannier orbitals in OALs are localized at maximal Wyckoff positions in the unit cell, and have shapes that respect the little group of their Wyckoff position. When a Wyckoff position lies on the boundary of the unit cell, the latter cuts through the respective Wannier orbital. The corner charge Q_c can then be calculated conveniently and is equal to the volume that all occupied Wannier functions integrate to in c (where a single Wannier function is normalized to unit volume).

Note that Wannier orbitals which are cut through by edges instead of corners contribute to the TRS polarization [77, 32, 198] and thereby correspond to a charge that scales linearly with the extent of the boundary. The corner charge, on the other hand, stays constant as the thermodynamic limit is taken. It is thus well defined only in absence of TRS polarization.

Importantly, not all OALs have a fractional corner charge in all finite geometries. For example, as we will see for the $1a$ OAL discussed in section 7.3, sometimes there are no symmetry-preserving terminations that cut through Wannier functions (if only entire unit cells are retained), even though the latter are not centered at the atomic positions of the crystal.

Any trivial atomic limit has $Q_c \in 2\mathbb{Z}$ for any such choice of boundary region: when different unit cells are not coupled to each other, the charge in each unit cell has to be equal to the total charge of the occupied subspace of $H_{F=\{(0,0)\}}$, which is necessarily an even integer. We may then define *corner charge fractionalization* as occurring in systems for which $Q_c \bmod 2$ is equal to non-zero even integer multiples of $1/q$ (odd integer multiples are forbidden by TRS). Note that in this work we assume all systems with nontrivial corner charge to be given by OALs, which have a representation in terms of exponentially localized Wannier functions [78, 14]. However, the corner charge formulas we supply in section 7.2.3 apply equally well to fragile phases [15, 16, 18, 19, 20, 21, 22]. These can always be adiabatically continued into OALs when other OALs are added. For a calculation of the corner charge in spinful materials, such a “trivialization” of a fragile phase becomes necessary only in the symmetry class that has \mathcal{C}_4 rotational symmetry as its sole crystalline component, since this symmetry does not by itself allow for explicit corner charge formulas in terms of the elementary topological invariants we consider.

The classification of corner charge fractionalization in class All and symmetry group \mathcal{G} is given by the set of inequivalent $Q_c \bmod 2$ that cannot be changed without breaking \mathcal{G}_F or closing the bulk gap. We present the classification for all layer groups \mathcal{G} in section D.2 of the Appendix.

7.1.2 Robustness of the corner charge

We now discuss to what extent symmetry-preserving edge manipulations can change the corner charge Q_c defined in Equation (7.5). We treat an edge manipulation as the introduction of an additional 1D system along the circumference of the finite 2D sample, and ask how the corner charges of the combined system, defined on the appropriately augmented Hilbert space, can differ from those of the original 2D model. Since charges are additive it is enough to determine the possible charges

of the 1D system. In the following, we take Q to be the total charge of the 1D addition. It is even due to the requirement that we may only add complete and non-anomalous gapped 1D systems with TRS. We then use the remaining crystalline symmetries to derive further constraints on the charges Q_c that the 1D system contributes to a boundary region c .

We note that the point group symmetries in 2D that \mathcal{G}_F can contain are mirror and n -fold rotational symmetries, where $n \in \{2, 3, 4, 6\}$. We first discuss the latter case of \mathcal{C}_n rotational symmetries. For spinful systems with TRS, we have $(\mathcal{C}_n)^n = -1$. Let H_{1D} denote a general 1D TRS gapped Hamiltonian defined on a Hilbert space of L lattice sites (with L/n an integer), possibly augmented by orbital degrees of freedom [see also Figure 7.1 (c)]. A \mathcal{C}_n rotational symmetry

$$\mathcal{C}_n H_{1D} \mathcal{C}_n^\dagger = H_{1D}, \quad (7.6)$$

implies that we can choose the order of regions $c_i \in C$ (which in combination cover all of the L sites of the 1D system) such that in real space the symmetry effects $c_i \rightarrow c_{i+1 \bmod n}$, that is, a translation by L/n sites. Now, due to $(\mathcal{C}_n)^n = -1$, rotations are equivalent to translations around a 1D circle that encloses a π -flux. Let t be the operator for translations by a single site, i.e., it shifts site $r \in \{1, \dots, L\}$ of the 1D lattice to site $r + 1 \bmod L$. It is not a symmetry of H_{1D} , however, we can obtain a t -symmetric Hamiltonian (on a ring enclosing a π -flux) by adding up L/n copies of H_{1D} that are subsequently shifted by one lattice site, to arrive at

$$H_{1D}^{\text{TRN}} = H_{1D} \oplus t H_{1D} t^\dagger \oplus \dots \oplus t^{L/n-1} H_{1D} (t^\dagger)^{L/n-1}, \quad (7.7)$$

which acts on an L/n -fold enlarged Hilbert space. The occupied subspace of H_{1D}^{TRN} has a total charge of QL/n and enjoys a translational symmetry that corresponds to L repeated unit cells, with twisted boundary conditions so as to accommodate the π -flux. It is gapped and has TRS just as H_{1D} , and its charge thus necessarily corresponds to an even integer number of filled Bloch bands, which each hold L states. We conclude that its charge per unit cell Q/n is an even integer. Returning our attention to H_{1D} , since all boundaries c carry the same charge, this is exactly the corner charge $Q_c = Q/n$. Thus in the case of \mathcal{C}_n -symmetries there is no 1D addition that can trivialize the fractional corner charges of a 2D OAL.

Next, we turn to mirror symmetries, which for spinful systems satisfy $\mathcal{M}^2 = -1$. In the case of two reflections, say \mathcal{M}_x and \mathcal{M}_y , we also have a two-fold rotation symmetry $\mathcal{C}_2 = \mathcal{M}_x \mathcal{M}_y$, which by the argument above allows us to conclude that all corner charges Q_c contributed by any gapped and TRS 1D addition are necessarily even (note that the minimal nontrivial boundary decomposition has $q = 2$). When there is only a single mirror symmetry, we cannot argue along these lines, since

it does not act on the 1D real space as a translation. In fact, it “translates” different sites along the 1D chain by different amounts. Hence, here the symmetry constraint on Q_c is the same as that for the 2D bulk, namely that $Q_{c_i} \in \mathbb{Z}$, $i = 1, 2$, (compare this to the $Q_{c_i} \in 2\mathbb{Z}$ we obtain for \mathcal{C}_2 symmetry) and a fractional charge of $1 \bmod 2$ can be trivialized.

Finally, we note that in the case where we have \mathcal{C}_3 symmetry as well as 3D inversion symmetry \mathcal{I} (which is the same as $\mathcal{C}_2\mathcal{M}_z$ symmetry), we can define an effective $1/6$ translation by $t_{1/6} = \mathcal{I}\mathcal{C}_3^2$ which allows to argue that patches c of size $1/6$ of the linear extent of the full 1D system have even integer charge. This is important for the robustness of the $Q_c = 1/6$ corner charges of this symmetry class.

Since any finite-size geometry breaks the remaining non-symmorphic symmetries a system might have, we do not need to consider their effect on charge fractionalization. We conclude that quantized corner charges can be changed by 1D edge manipulations only in the case of a single mirror symmetry.

7.2 Identification of two-dimensional obstructed atomic limits

In this section we give a prescription for obtaining the corner charge of the occupied subspace of a bulk model represented by a Bloch Hamiltonian $\mathcal{H}(\mathbf{k})$ [the Fourier transform of the translationally invariant tight-binding model given in Equation (7.2)], assuming that its occupied subspace realizes an OAL. We take a Wannier center point of view: in particular, we define an OAL by the way it is built up from exponentially localized and symmetric Wannier functions[78, 14].

As shown in section 7.1.2, mirror symmetries can protect fractional corner charges only when they are combined to yield a twofold rotational symmetry. The protecting symmetries we consider are therefore \mathcal{C}_n rotations, with or without an additional 3D inversion symmetry \mathcal{I} . The inclusion of \mathcal{I} symmetry allows us to extend our discussion to the experimentally relevant case of 2D honeycomb monolayers with nonzero buckling, and our classification (given in the Appendix) to the 80 layer groups instead of the 17 wallpaper groups. We note that inversion effectively replaces \mathcal{C}_2 in its role of enforcing a $Q_c = 0, 1 \bmod 2$ quantization of the corner charge, but due to $\mathcal{I}^2 = +1$ [whereas $(\mathcal{C}_2)^2 = -1$] allows for symmetry indicator invariants. Furthermore, in the case of \mathcal{C}_4 symmetry, we find that we require an additional inversion symmetry in order to be able to read off the corner charge from the available topological invariants. Inversion symmetry is however, unlike \mathcal{C}_4 , not necessary for the topological robustness of the corner charge.

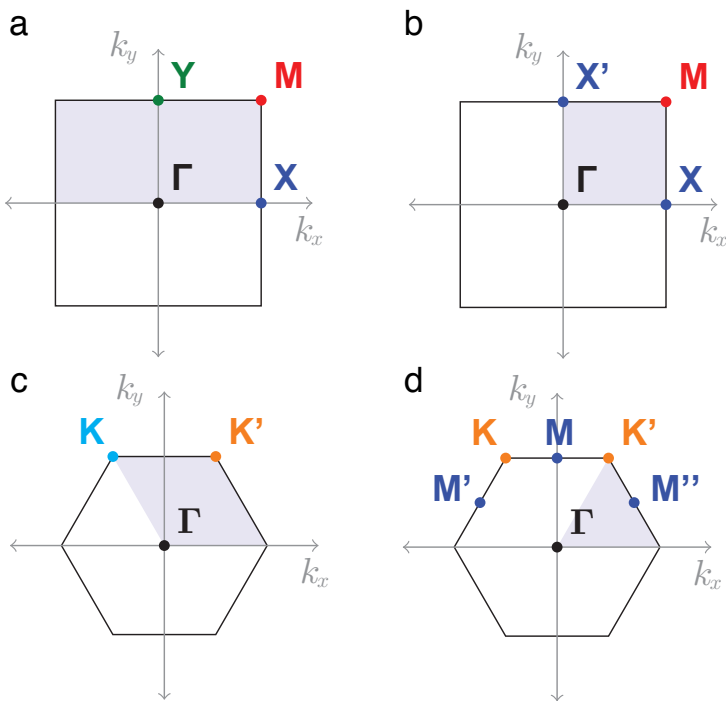


Figure 7.2: Brillouin zones of crystals with \mathcal{C}_2 , \mathcal{C}_4 , \mathcal{C}_3 , and \mathcal{C}_6 symmetries and their rotation invariant points. In \mathcal{C}_2 -symmetric systems there are three 2-fold high-symmetry points (HSPs): \mathbf{X} , \mathbf{Y} , and \mathbf{M} . In \mathcal{C}_4 -symmetric systems there are two 2-fold HSPs: \mathbf{X} and \mathbf{X}' , and one 4-fold HSP: \mathbf{M} . In \mathcal{C}_3 -symmetric systems there are only two 3-fold HSPs: \mathbf{K} and \mathbf{K}' . Finally, in \mathcal{C}_6 -symmetric systems there are three 2-fold HSPs: \mathbf{M} , \mathbf{M}' , and \mathbf{M}'' , as well as two 3-fold HSPs: \mathbf{K} and \mathbf{K}' .

We first establish which topological invariants can be defined for each point group in 7.2.1. We then go on to calculate these indices for the elementary band representations of each symmetry class in 7.2.2. Finally, in 7.2.3 we present formulas that allow for a determination of the corner charge in all symmetry classes except for the one that as its only crystalline component has \mathcal{C}_4 rotational symmetry.

A list of all possible corner charges for the various layer groups is given in Table D.1 of the Appendix. The remaining symmetry operations a layer group may contain in addition to the ones listed in section 7.2.3 are either irrelevant for finite-size corner terminations since they involve translations (as in the case of non-symmorphic symmetries), or merely impose constraints for the shape of the finite-size termination, without affecting the corner charge quantization itself (such as mirror symmetries).

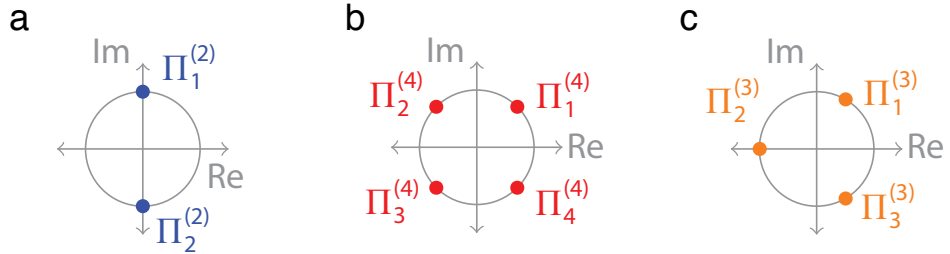


Figure 7.3: Sets of allowed eigenvalues for spinful rotational symmetries. (a) C_2 symmetry. (b) C_4 symmetry. (c) C_3 symmetry. The possible eigenvalues of C_6 symmetry are not shown, since they do not allow for the definition of symmetry indicators (there is at most one C_6 -symmetric point in any two-dimensional Brillouin zone).

7.2.1 Bulk topological indices

To identify different EBRs, we employ a combination of symmetry indicator [158, 157, 199, 200, 201, 29, 14, 91, 30, 32] and Wilson loop [202, 203, 204, 163, 199, 85, 201, 16] topological invariants. We already introduced both kinds of invariants in Section 2.2, however, to be explicit and for the sake of pedagogy, we here review them again in the context of two-dimensional spinful crystals. They can be evaluated from the Bloch Hamiltonian $\mathcal{H}(\mathbf{k})$ and so do not require a real-space calculation to be performed. The main ingredient for both kinds of invariants is the bundle of occupied Bloch states $|u_m(\mathbf{k})\rangle$, $m = 1 \dots N$. [\mathbf{k} is an element of the first Brillouin zone (BZ) of the crystal.] Note that in this chapter, we work in a convention where the Bloch Hamiltonian satisfies $\mathcal{H}(\mathbf{k}) = \mathcal{H}(\mathbf{k} + \mathbf{G})$ for \mathbf{G} a reciprocal lattice vector, it is therefore possible to choose a perfectly periodic gauge for its eigenstates.

Given a unitary crystal symmetry \mathcal{S} that is realized on the Bloch Hamiltonian as $\mathcal{S}\mathcal{H}(\mathbf{k})\mathcal{S}^\dagger = \mathcal{H}(S\mathbf{k})$ and acts on the momenta as $\mathbf{k} \rightarrow S\mathbf{k}$, we can calculate its corresponding symmetry indicator topological invariants from the eigenvalues of the matrices

$$S_{mn} = \langle u_m(\bar{\mathbf{k}}) | \mathcal{S} | u_n(\bar{\mathbf{k}}) \rangle, \quad (7.8)$$

where m, n run over the occupied subspace only and $\bar{\mathbf{k}} = S\mathbf{k}$ are high-symmetry points (HSPs) of the Brillouin zone that are left invariant by the symmetry \mathcal{S} (see also Figure 7.2). An n -fold symmetry acting on spinful fermions satisfies $\mathcal{S}^n = \pm 1$ (positive sign for 3D inversion, negative sign for 2D mirror and rotational symmetries), this, together with TRS, imposes constraints on the possible eigenvalues of S_{mn} and allows for the definition of topological invariants that capture the different symmetry representations of the occupied bands across the BZ. A trivial OAL, being deformable to a momentum-independent Hamiltonian, will have the same

representation across HSPs that are invariant under the same symmetry and hence will have trivial symmetry indicator invariants. Nonzero symmetry indicator invariants, on the other hand, indicate that the bands adopt different representations of the symmetry across the BZ and correspond to nontrivial OALs.

In this chapter, we use a slightly different definition for the Wilson loop, which is equivalent to the one of Section 2.1 as long as a gauge is chosen where the Bloch Hamiltonian satisfies $\mathcal{H}(\mathbf{k}) = \mathcal{H}(\mathbf{k} + \mathbf{G})$ for a reciprocal lattice vector \mathbf{G} . The advantage of the definition used in this chapter is that it simplifies the proofs we will give to establish how crystal symmetries quantize the topological invariants derived from Wilson loops. Specifically, in this chapter, we define the Wilson loop (along a closed, non-contractible path γ in the BZ that starts and ends at the momentum \mathbf{k}^*) as

$$W_\gamma = \prod_k^\gamma P(\mathbf{k}), \quad (7.9)$$

where $P(\mathbf{k}) = \sum_{m \in \text{occ}} |u_m(\mathbf{k})\rangle \langle u_m(\mathbf{k})|$ is the projector onto the subspace of filled bands at momentum \mathbf{k} . The product is path-ordered along γ . This Wilson loop operator satisfies $W_\gamma W_\gamma^\dagger = P(\mathbf{k}^*)$ and so, since any projector satisfies $[P(\mathbf{k})]^2 = P(\mathbf{k})$, its eigenvalues are either zero or of the form $e^{i\theta_\alpha^\gamma}$, $\alpha = 1 \dots N$. In the following, we refer to the set of $\{\theta_\alpha^\gamma\}_{\alpha=1\dots N}$ as the Wilson loop spectrum, suppressing the zero eigenvalues (thereby making it the same as the spectrum of the type of Wilson loop considered in previous chapters).

The anti-unitary TRS \mathcal{T} acts on the Bloch Hamiltonian as $\mathcal{T}\mathcal{H}(\mathbf{k})\mathcal{T}^{-1} = \mathcal{H}(-\mathbf{k})$. For the projectors this implies $\mathcal{T}P(\mathbf{k})\mathcal{T}^{-1} = P(-\mathbf{k})$. When γ is mapped onto itself by TRS, and its starting point satisfies $\mathbf{k}^* = -\mathbf{k}^*$ up to a reciprocal lattice vector, we then have

$$\mathcal{T}W_\gamma\mathcal{T}^\dagger = \prod_k^\gamma P(-\mathbf{k}) = W_\gamma^\dagger. \quad (7.10)$$

Due to \mathcal{T} being anti-unitary and $\mathcal{T}^2 = -1$, this implies a Kramers degeneracy of the Wilson loop spectrum, i.e., every θ_α^γ is (at least) two-fold degenerate when γ is mapped onto itself by time reversal. Compare also the discussion in Section 2.1.1.3.

Now, if there is a crystal symmetry \mathcal{S} that reverses the direction of γ and leaves the starting point invariant so that $\mathbf{k}^* = \mathcal{S}\mathbf{k}^*$ up to a reciprocal lattice vector, we have

$$\mathcal{S}W_\gamma\mathcal{S}^\dagger = \prod_k^\gamma [\mathcal{S}P(\mathbf{k})\mathcal{S}^\dagger] = W_\gamma^\dagger. \quad (7.11)$$

Since \mathcal{S} is unitary, the Wilson loop is unitarily equivalent to its complex conjugate and so its eigenvalues come in complex conjugated pairs. This implies a symmetry of the Wilson loop spectrum around $\theta = 0$, for every θ_α^γ there is a corresponding $-\theta_\alpha^\gamma \bmod 2\pi$.

We may furthermore employ nested Wilson loops (see also Section 2.2.1 and Appendix A.5.2). Let $W_i(k_j)$, $i \neq j$, denote the Wilson loop along the noncontractible loop $\gamma : (k_i = 0, k_j) \rightarrow (k_i = 2\pi, k_j)$, where (k_i, k_j) labels a point in the two-dimensional BZ in some basis (chosen such that $k_{i,j} = 0$ and $k_{i,j} = 2\pi$ are related by reciprocal lattice vectors). Consider the Wilson loop Hamiltonian $H_{W_i}(k_j)$, defined by

$$[e^{iH_{W_i}(k_j)}]_{mn} = \langle u_m(k_i = 0, k_j) | W_i(k_j) | u_n(k_i = 0, k_j) \rangle. \quad (7.12)$$

Equations (7.10) and (7.11) then imply

$$\begin{aligned} \mathcal{T}_{k_j} H_{W_i}(k_j) \mathcal{T}_{k_j}^\dagger &= H_{W_i}(-k_j), \\ \mathcal{S}_{k_j} H_{W_i}(k_j) \mathcal{S}_{k_j}^\dagger &= -H_{W_i}(Sk_j), \end{aligned} \quad (7.13)$$

where we defined

$$\begin{aligned} (\mathcal{T}_{k_j})_{mn} &= \langle u_m(-k_j) | \mathcal{T} | u_n(k_j) \rangle, \\ (\mathcal{S}_{k_j})_{mn} &= \langle u_m(Sk_j) | \mathcal{S} | u_n(k_j) \rangle. \end{aligned} \quad (7.14)$$

We see that \mathcal{T} implies a TRS of the Wilson loop Hamiltonian, whereas \mathcal{S} implies a particle-hole symmetry. These properties are needed for the definition of quantized topological invariants of the *nested Wilson loop*: We define W_i^b as the Wilson loop calculated from a gapped set eigenstates b of $H_{W_i}(k_j)$ along a closed, non-contractible path $k_j : 0 \rightarrow 2\pi$ in the reduced BZ.

We differentiate between three kinds of nested Wilson loops that differ by the choice of the set of eigenstates b : 1) The nested loop W_i^0 , which is calculated from the two bands in the spectrum of $H_{W_i}(k_j)$ that at $k_j = 0, \pi$ have a degeneracy pinned to the Wilson eigenvalue 0 [note that any such degeneracy at $k_j = 0$ implies one at $k_j = \pi$ and vice versa due to the absence of Wannier center flow in (obstructed) atomic limits]. 2) The nested Wilson loop W_i^λ , calculated for the upper or lower half of the bands in the spectrum of $H_{W_i}(k_j)$ that are *not* pinned at $k_j = 0, \pi$ to a Wilson eigenvalue 0, π (that is, half of the freely dangling Wilson bands, which by the particle hole symmetry come in pairs). 3) The nested loop W_i^π , which is calculated from the two bands in the spectrum of $H_{W_i}(k_j)$ that at $k_j = 0, \pi$ have a degeneracy pinned to the Wilson eigenvalue π .

The nested Wilson loops of type (1) and (3) cannot be trivialized by transformations that preserve \mathcal{S} and \mathcal{T} and are adiabatic with respect to the bulk gap. The

reason is that the invariants calculated from these loops are equal to the partial polarizations of Wilson bands pinned to eigenvalues 0 or π by \mathcal{S} at the transverse momenta $k_j = 0, \pi$. Wilson gap closings that preserve the energy gap can only occur in pairs (due to \mathcal{S}) at intermediate transverse momenta $k_j, -k_j$. It is rigorously shown in Appendix A of Reference [205] that these gap closings together always contribute integer multiples of 2π to the nested partial polarization, and therefore cannot trivialize Wilson loops of type (1) and (3). In this work, we do not consider invariants derived from Wilson loops of type (2).

We will now list the topological invariants that can be defined for a given point group. We find that often the inclusion of \mathcal{I} symmetry allows for the replacement of Wilson-loop invariants by symmetry indicator invariants.

Note that in the following, and as motivated at the beginning of section 7.1.1, we explicitly exclude invariants that characterize topological insulators because they are necessarily gapless along the edges in a 2D geometry with open boundary conditions, and so do not allow for stable quantized corner charges. In addition to removing some invariants from our analysis altogether, this imposes constraints on Wilson loops.

We emphasize that our list of invariants may not be exhaustive. As noted in Reference [16], it is in general difficult to identify all possibly nontrivial Wilson loop invariants. In this work we only treat “straight” (nested) Wilson loops, which (given a starting point) go around one of the two inequivalent noncontractible loops of the Brillouin zone torus.

7.2.1.1 \mathcal{C}_2 symmetry

Symmetry indicator invariants: The BZ has four HSPs, see also Figure 7.2 (a). All the points are invariant under \mathcal{C}_2 . Thus, they all have \mathcal{C}_2 eigenvalues $+i, -i$ [see Figure 7.3 (a)]. However, since all the HSPs are also TRIMs, the eigenvalues have to come in complex-conjugate pairs, leading to a single available 2D irreducible representation. Therefore, the \mathcal{C}_2 eigenvalues on their own do not afford a topological distinction and there are no symmetry indicator invariants.

Wilson-loop invariants: For every closed high-symmetry line γ (which connects two HSPs) of the 2D BZ that is left invariant by \mathcal{C}_2 , we can define a Wilson loop that is TRS and \mathcal{C}_2 symmetric. Due to Equations (7.10) and (7.11) the parities of the numbers of $\theta_\alpha^\gamma = 0$ and $\theta_\alpha^\gamma = \pi$ eigenvalues in its spectrum cannot be changed under adiabatic deformations of $\mathcal{H}(\mathbf{k})$: adiabatic perturbations of the Hamiltonian at most move particle-hole related Kramers pairs of eigenvalues in and out of 0 and π , this does not change the total parity.

A topological invariant of W_γ with spectrum $\{\theta_\alpha^\gamma\}_{\alpha=1\dots N}$ is therefore given by

$$\nu_\gamma = -\frac{i}{\pi} \log \left(\prod_{\alpha=1,3,\dots,N-1} e^{i\theta_\alpha^\gamma} \right) \mod 2, \quad (7.15)$$

where the product is taken over only one eigenvalue of each Wilson loop Kramers pair. We call $\nu_\gamma = 0$ trivial and $\nu_\gamma = 1$ nontrivial. This invariant is equivalent to the TRS polarization [198] and counts the parity number of Wilson loop pairs of eigenvalues equal to π . We also define

$$\mu_\gamma = -\frac{i}{\pi} \log \left(\prod_{\alpha=1,3,\dots,N-1} e^{i(\pi-\theta_\alpha^\gamma)} \right) \mod 2, \quad (7.16)$$

which counts the number of Wilson loop pairs of eigenvalues equal to 0. The invariants ν_γ and μ_γ are not independent when the total number of bands is fixed. They obey

$$\mu_\gamma = \nu_\gamma + \frac{N}{2} \mod 2. \quad (7.17)$$

Therefore, we drop μ_γ as it provides redundant topological information. In the following, we will consider Wilson loops that go through high-symmetry points in the 2D BZ. We denote by ν_{AB} the loop that goes from point A to point B and then back to A via the shortest non-contractible loop around the BZ torus.

There are in total four TRIMs and three topologically inequivalent straight and C_2 -symmetric Wilson loops. This can be seen by noting that, holding one of the four C_2 -symmetric momenta fixed as a starting point, there are two incontractible loops around the Brillouin zone torus (which necessarily go through one other C_2 -symmetric momentum). Keeping in mind that path-reversed Wilson loops are not independent [as per Equation (7.11)], this naively yields the set of Wilson loop invariants $\{\nu_{\Gamma X}, \nu_{\Gamma Y}, \nu_{X M}, \nu_{Y M}\}$. We note however that the path denoted by $\mathbf{Y}\Gamma - \Gamma\mathbf{X} - \mathbf{X}\mathbf{M}$ is topologically equivalent to the path denoted by $\mathbf{Y}\mathbf{M}$ and so we have

$$\nu_{YM} = \nu_{\Gamma Y} \nu_{\Gamma X} \nu_{XM}. \quad (7.18)$$

The remaining invariants are further constrained due to the requirement that the \mathbb{Z}_2 TI invariant Δ_{TI} vanishes: we have that

$$\begin{aligned} \Delta_{TI} &= \nu_{\Gamma X} + \nu_{YM} \mod 2 \\ &= \nu_{\Gamma Y} + \nu_{XM} \mod 2. \end{aligned} \quad (7.19)$$

We are left with two Wilson loop invariants.

Similarly, we may define the quantized invariants $\nu_{x,y}^{0,\pi}$ and $\mu_{x,y}^{0,\pi}$ from the nested Wilson loops $W_{x,y}^{0,\pi}$, since these are calculated for particle-hole symmetric sets of bands [62, 19] [in contrast to $W_{x,y}^\lambda$, which does not satisfy Equation (7.13)]: the anti-commutativity with the Wilson loop Hamiltonian that distinguishes particle-hole symmetry from a reflection symmetry is irrelevant from the point of view of the nested Wilson loop, as long as the latter is defined via a projector onto a particle-hole symmetric set of bands. We may therefore define $\nu_{x,y}^{0,\pi}$ and $\mu_{x,y}^{0,\pi}$ just as in Equations (7.15) and (7.16), where θ_α^γ this time refers to the spectrum of the nested Wilson loop. As before, we drop the μ invariants since they are not independent when the number of occupied Wilson bands is held fixed. Taking into account the constraints [205]

$$\begin{aligned}\nu_x^0 + \nu_x^\pi \mod 2 &= \nu_{\Gamma Y}, \\ \nu_y^0 + \nu_y^\pi \mod 2 &= \nu_{\Gamma X}, \\ \nu_x^\pi &= \nu_y^\pi,\end{aligned}\tag{7.20}$$

reduces the number of independent invariants to three. The third equation can be seen in the following way: ν_x^π is nonzero if and only if the occupied subspace hosts an odd number of Wannier Kramers pairs whose centers are shifted by $1/2$ in both x and y direction (taking the lattice constant to be 1) with respect to the center of the unit cell, i.e., if there is an odd number of Kramers pairs at Wyckoff position $1b$ of the crystal (see also Table 7.2). This Wyckoff position stays unchanged when exchanging x and y , we therefore obtain that ν_x^π is nonzero if and only if ν_y^π is nonzero. Note that the corresponding statement does not hold for ν_x^0 and ν_y^0 , since these indicate Wannier Kramers pairs at the $1c$ and $1d$ Wyckoff positions, respectively.

We therefore choose the classification to be given by

$$\chi^{(2)} = \{\nu_{\Gamma X}, \nu_{\Gamma Y}, \nu_x^\pi\}.\tag{7.21}$$

With inversion symmetry: $\mathcal{C}_2 + \mathcal{I}$ symmetry is equivalent to \mathcal{I} symmetry for all our purposes. Inversion symmetry allows us to replace the \mathbb{Z}_2 valued Wilson-loop invariants by $2\mathbb{Z}$ -valued symmetry indicators. The BZ has the \mathcal{I} -invariant points Γ , X , Y and M , which support the six inversion eigenvalue invariants

$$\begin{aligned}[X_i^\mathcal{I}] &= \#X_i^\mathcal{I} - \#\Gamma_i^\mathcal{I}, \\ [Y_i^\mathcal{I}] &= \#Y_i^\mathcal{I} - \#\Gamma_i^\mathcal{I}, \\ [M_i^\mathcal{I}] &= \#M_i^\mathcal{I} - \#\Gamma_i^\mathcal{I},\end{aligned}\tag{7.22}$$

where $\#X_i^{\mathcal{I}}$ ($\#\Gamma_i^{\mathcal{I}}$) is the number of occupied states with inversion eigenvalue $X_i^{\mathcal{I}}$ ($\Gamma_i^{\mathcal{I}}$), and $X_{i=1,2}^{\mathcal{I}}, \Gamma_{i=1,2}^{\mathcal{I}} = \{1, -1\}$, and similarly for \mathbf{Y} and \mathbf{M} . Due to the fixed number of occupied bands, we have the constraints

$$\begin{aligned}[X_1^{\mathcal{I}}] + [X_2^{\mathcal{I}}] &= 0, \\ [Y_1^{\mathcal{I}}] + [Y_2^{\mathcal{I}}] &= 0, \\ [M_1^{\mathcal{I}}] + [M_2^{\mathcal{I}}] &= 0.\end{aligned}\tag{7.23}$$

The three remaining invariants completely fix [85] the Wilson loops in Equation (7.21). Due to TRS they are necessarily even integers. We retain the classification

$$\chi_{\mathcal{I}}^{(2)} = \{[X_2^{\mathcal{I}}], [Y_2^{\mathcal{I}}], [M_2^{\mathcal{I}}]\}.\tag{7.24}$$

7.2.1.2 \mathcal{C}_3 symmetry

Symmetry indicator invariants: The BZ only has the \mathcal{C}_3 -invariant points \mathbf{K} and \mathbf{K}' , see also Figure 7.2 (c). Now, we discuss the invariants that compare the representations at the \mathbf{K} (\mathbf{K}') and Γ points of the BZ,

$$[K_i^{(3)}] = \#K_i^{(3)} - \#\Gamma_i^{(3)},\tag{7.25}$$

where $K_{i=1,2,3}^{(3)}, \Gamma_{i=1,2,3}^{(3)} = \{e^{i\pi/3}, -1, e^{-i\pi/3}\}$, and similarly for \mathbf{K}' [see Figure 7.3 (c)]. Unlike \mathbf{M} , the HSP \mathbf{K} is *not* a TRIM. Instead, TRS relates \mathbf{K} and \mathbf{K}' . TRS imposes the constraints,

$$\begin{aligned}[K_1^{(3)}] &= [K_3'^{(3)}], \\ [K_2^{(3)}] &= [K_2'^{(3)}], \\ [K_3^{(3)}] &= [K_1'^{(3)}].\end{aligned}\tag{7.26}$$

The six invariants are subject to the constraints (7.26) along with

$$\begin{aligned}[K_1^{(3)}] + [K_2^{(3)}] + [K_3^{(3)}] &= 0, \\ [K_1'^{(3)}] + [K_2'^{(3)}] + [K_3'^{(3)}] &= 0.\end{aligned}\tag{7.27}$$

due to the constant number of occupied states across the BZ. The symmetry-indicated part of the classification is given by the two invariants

$$\chi^{(3)} = \{[K_1^{(3)}], [K_2^{(3)}]\}.\tag{7.28}$$

Wilson-loop invariants: There are no Wilson loop invariants in this class due to the lack of a twofold symmetry.

With inversion symmetry: Inversion symmetry implies $[K_i^{(3)}] = [K'_i]^{(3)}$, $i = 1, 2, 3$. We therefore drop $[K_1^{(3)}]$ from the list of independent invariants. The BZ has the \mathcal{I} -invariant points \mathbf{M} , \mathbf{M}' and \mathbf{M}'' , which support the invariants

$$[M_i^{\mathcal{I}}] = \#M_i^{\mathcal{I}} - \#\Gamma_i^{\mathcal{I}}, \quad (7.29)$$

where $M_{i=1,2}^{\mathcal{I}}$, $\Gamma_{i=1,2}^{\mathcal{I}} = \{1, -1\}$, and similarly for \mathbf{M}' and \mathbf{M}'' . TRS implies that the states belonging to a Kramers pair have equal inversion eigenvalue. \mathcal{C}_3 imposes the constraints

$$\begin{aligned} [M_1^{\mathcal{I}}] &= [M_1'^{\mathcal{I}}] = [M_1''^{\mathcal{I}}], \\ [M_2^{\mathcal{I}}] &= [M_2'^{\mathcal{I}}] = [M_2''^{\mathcal{I}}]. \end{aligned} \quad (7.30)$$

In addition we have

$$[M_1^{\mathcal{I}}] + [M_2^{\mathcal{I}}] = 0. \quad (7.31)$$

We retain $[M_2^{\mathcal{I}}]$ as the invariant that determines the classification, in addition to the \mathcal{C}_3 invariant $[K_2^{(3)}]$:

$$\chi_{\mathcal{I}}^{(3)} = \{[M_2^{\mathcal{I}}], [K_2^{(3)}]\}. \quad (7.32)$$

7.2.1.3 \mathcal{C}_4 symmetry

Symmetry indicator invariants: The BZ has four HSPs [Figure 7.2 (b)]. Two of them are invariant under \mathcal{C}_2 and give rise to trivial indicators due to time reversal symmetry. We can then only build indices that compare the \mathcal{C}_4 symmetry representations at \mathbf{M} with those at Γ as follows:

$$[M_i^{(4)}] = \#M_i^{(4)} - \#\Gamma_i^{(4)}, \quad i \in \{1, 2, 3, 4\}, \quad (7.33)$$

where the eigenvalues are taken from the set

$$M_{i=1,2,3,4}^{(4)}, \Gamma_{i=1,2,3,4}^{(4)} = \{e^{i\pi/4}, e^{i3\pi/4}, e^{-i3\pi/4}, e^{-i\pi/4}\}, \quad (7.34)$$

respectively [see Figure 7.3 (b)]. Since all the HSPs are also TRIMs, the rotation eigenvalues have to come in complex-conjugate pairs. Therefore, we have the constraints on the invariants

$$\begin{aligned} [M_1^{(4)}] &= [M_4^{(4)}], \\ [M_2^{(4)}] &= [M_3^{(4)}]. \end{aligned} \quad (7.35)$$

Since the number of occupied states is constant across the BZ, we have that $\sum_i \#M_i^{(4)} = \sum_i \#\Gamma_i^{(4)}$, or

$$[M_1^{(4)}] + [M_2^{(4)}] + [M_3^{(4)}] + [M_4^{(4)}] = 0. \quad (7.36)$$

With the constraints in (7.35) and (7.36), we eliminate the redundant invariants $[M_2^{(4)}]$, $[M_3^{(4)}]$, and $[M_4^{(4)}]$. Thus, the classification due to \mathcal{C}_4 symmetry has only one symmetry-indicator invariant, $[M_1^{(4)}]$.

Wilson-loop invariants: \mathcal{C}_4 symmetry implies having \mathcal{C}_2 symmetry as well and so we can immediately take over the Wilson loops given in Equation (7.21) as possible invariants, where due to \mathcal{C}_4 we have $\nu_{\Gamma X} = \nu_{\Gamma Y}$.

We conclude that the classification is given by

$$\chi^{(4)} = \left\{ \nu_{\Gamma X}, \nu_X^\pi, [M_1^{(4)}] \right\}. \quad (7.37)$$

With inversion symmetry: The invariants given in Equation (7.24) (together with the \mathcal{C}_4 constraint $[X_2^{\mathcal{I}}] = [Y_2^{\mathcal{I}}]$) allow us to replace $\nu_{\Gamma X}, \nu_{\Gamma M}$. We conclude that the classification with inversion symmetry is given by

$$\chi_{\mathcal{I}}^{(4)} = \left\{ [X_2^{\mathcal{I}}], [M_2^{\mathcal{I}}], [M_1^{(4)}] \right\}. \quad (7.38)$$

7.2.1.4 \mathcal{C}_6 symmetry

Symmetry indicator invariants: In a \mathcal{C}_6 -symmetric BZ, there are two inequivalent HSPs, \mathbf{M} , which is invariant under \mathcal{C}_2 , and \mathbf{K} , which is invariant under \mathcal{C}_3 [Figure 7.2 (d)]. All other points are related by rotations, and thus provide redundant representations for the purpose of classification. Furthermore, \mathbf{M} is both a HSP and a TRIM. Thus, from the analysis of the previous classifications, no invariants can be derived from its representations. Now, we discuss the invariants that compare the representations at the \mathbf{K} and Γ points of the BZ,

$$[K_i^{(3)}] = \#K_i^{(3)} - \#\Gamma_i^{(3)}, \quad (7.39)$$

where $K_{i=1,2,3}^{(3)}$, $\Gamma_{i=1,2,3}^{(3)} = \{e^{i\pi/3}, -1, e^{-i\pi/3}\}$. Unlike \mathbf{M} , the HSP \mathbf{K} is *not* a TRIM. Instead, TRS relates \mathbf{K} and \mathbf{K}' . TRS imposes the constraints,

$$\begin{aligned} [K_1^{(3)}] &= [K_3^{(3)}], \\ [K_2^{(3)}] &= [K_2^{(3)}], \\ [K_3^{(3)}] &= [K_1^{(3)}]. \end{aligned} \quad (7.40)$$

But the representations at \mathbf{K} and \mathbf{K}' are the same due to \mathcal{C}_6 symmetry,

$$\begin{aligned} [K_1^{(3)}] &= [K_1'^{(3)}], \\ [K_2^{(3)}] &= [K_2'^{(3)}], \\ [K_3^{(3)}] &= [K_3'^{(3)}]. \end{aligned} \quad (7.41)$$

The last two sets of constraints leave us with only two non-redundant invariants, $[K_1^{(3)}]$ and $[K_2^{(3)}]$. However, due to the constant number of occupied states, we have $\sum_i \#K_i^{(3)} = \sum_i \#\Gamma_i^{(3)}$ or $2[K_1^{(3)}] + [K_2^{(3)}] = 0$, which makes one of these invariants redundant too. We choose the symmetry-indicated part of the classification to be given by $[K_2^{(3)}]$.

Wilson-loop invariants: \mathcal{C}_6 symmetry implies having \mathcal{C}_2 symmetry as well and so we can define $\mu_{\Gamma M}$ as an invariant due to Equation (7.16). We choose $\mu_{\Gamma M}$ here instead of $\nu_{\Gamma M}$ since it directly indicates Wannier centers at the 3c Wyckoff position (see Figure 7.4 (d) and Table 7.5) of the hexagonal unit cell. We do not consider nested Wilson loops in this symmetry class because the corner charge can be completely determined without them. In conclusion, we have

$$\chi^{(6)} = \{\mu_{\Gamma M}, [K_2^{(3)}]\}. \quad (7.42)$$

With inversion symmetry: The BZ has the \mathcal{I} -invariant points \mathbf{M} , \mathbf{M}' and \mathbf{M}'' , which support the invariants

$$[M_i^{\mathcal{I}}] = \#M_i^{\mathcal{I}} - \#\Gamma_i^{\mathcal{I}}, \quad (7.43)$$

where $M_{i=1,2}^{\mathcal{I}}$, $\Gamma_{i=1,2}^{\mathcal{I}} = \{1, -1\}$, and similarly for \mathbf{M}' and \mathbf{M}'' . TRS implies that the states belonging to a Kramers pair have equal inversion eigenvalue. \mathcal{C}_6 imposes the constraints

$$\begin{aligned} [M_1^{\mathcal{I}}] &= [M_1'^{\mathcal{I}}] = [M_1''^{\mathcal{I}}], \\ [M_2^{\mathcal{I}}] &= [M_2'^{\mathcal{I}}] = [M_2''^{\mathcal{I}}]. \end{aligned} \quad (7.44)$$

In addition we have

$$[M_1^{\mathcal{I}}] + [M_2^{\mathcal{I}}] = 0. \quad (7.45)$$

We retain $[M_2^{\mathcal{I}}]$ as the invariant that determines the classification. Due to \mathcal{C}_6 symmetry[32] and TRS, $[M_2^{\mathcal{I}}] \in 4\mathbb{Z}$. We conclude that

$$\chi_{\mathcal{I}}^{(6)} = \{[M_2^{\mathcal{I}}], [K_2^{(3)}]\}. \quad (7.46)$$

\mathcal{S}	without \mathcal{I}	with \mathcal{I}
\mathcal{I}	none	$[X_2^{\mathcal{I}}], [Y_2^{\mathcal{I}}], [M_2^{\mathcal{I}}]$
\mathcal{C}_2	$\nu_{\Gamma X}, \nu_{\Gamma Y}, \nu_x^\pi$	$[X_2^{\mathcal{I}}], [Y_2^{\mathcal{I}}], [M_2^{\mathcal{I}}]$
\mathcal{C}_3	$[K_1^{(3)}], [K_2^{(3)}]$	$[M_2^{\mathcal{I}}], [K_2^{(3)}]$
\mathcal{C}_4	$\nu_{\Gamma X}, \nu_x^\pi, [M_1^{(4)}]$	$[X_2^{\mathcal{I}}], [M_2^{\mathcal{I}}], [M_1^{(4)}]$
\mathcal{C}_6	$\mu_{\Gamma M}, [K_2^{(3)}]$	$[M_2^{\mathcal{I}}], [K_2^{(3)}]$

Table 7.1: Summary of Wilson loop and symmetry indicator invariants.

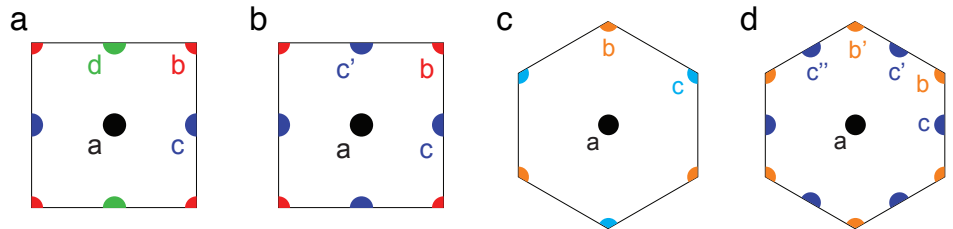


Figure 7.4: Maximal Wyckoff positions for unit cells with rotational symmetry. (a) \mathcal{C}_2 symmetry. (b) \mathcal{C}_4 symmetry. (c) \mathcal{C}_3 symmetry. (d) \mathcal{C}_6 symmetry or $\mathcal{C}_3 + \mathcal{I}$ symmetry. Boundary charges arise when the Wyckoff positions which Wannier centers are located at are cut through by the crystal termination.

7.2.1.5 Summary

We summarize our findings in Table 7.1.

7.2.2 Decomposition into EBRs

Tables 7.2-7.5 list the EBRs [199, 201, 14, 136, 134, 16, 206, 207] supported by systems with \mathcal{C}_n rotational symmetry, together with their invariants and corner charges. The minimal block sizes correspond to the multiplicities of the respective Wyckoff positions (multiplied by two to account for spin). If multiple choices for the site-symmetry group [14] representation at a Wyckoff position W are available, we denote the representation with eigenvalues $e^{i\alpha}$ as $W|_\alpha$.

7.2.3 Formulas for corner charges

In this section, we provide explicit formulas for the corner charge in terms of the topological invariants as evaluated on the entire occupied subspace of a given model. For systems with \mathcal{I} , \mathcal{C}_3 , and $\mathcal{C}_3 + \mathcal{I}$ symmetry, we can uniquely identify the spinless limit of a given spinful model. In this case we can employ the results of Reference [32]. In the remaining cases we deduce the formulas from the EBR tables

\mathcal{C}_2	$\nu_{\Gamma X}$	$\nu_{\Gamma Y}$	ν_x^π	Q_c
1a	0	0	0	0
1b	1	1	1	1
1c	1	0	0	0
1d	0	1	0	0

Table 7.2: EBRs with \mathcal{C}_2 symmetry induced from the maximal Wyckoff positions listed in the first column [see Figure 7.4 (a)], and their invariants. All atomic limits can be decomposed into EBRs formed by single Kramers pairs.

\mathcal{C}_4	$\nu_{\Gamma X}$	ν_x^π	$[M_1^{(4)}]$	Q_c
1a	0	0	0	0
$1b _{\pm \frac{\pi}{4}}$	1	1	-1	1/2
$1b _{\pm \frac{3\pi}{4}}$	1	1	1	1/2
2c	1	0	0	0
$1b _{\pm \frac{\pi}{4}} \oplus 1b _{\pm \frac{3\pi}{4}}$	0	0	0	1

Table 7.3: EBRs with \mathcal{C}_4 symmetry induced from the maximal Wyckoff positions listed in the first column [see Figure 7.4 (b)], and their invariants. All atomic limits can be decomposed into EBRs formed by at most two Kramers pairs. Importantly, the (non-elementary) band representation $1b|_{\pm \frac{\pi}{4}} \oplus 1b|_{\pm \frac{3\pi}{4}}$ has trivial \mathcal{C}_4 invariants but nonzero corner charge. In systems with \mathcal{C}_4 as the sole crystalline symmetry, this obstructs a determination of the corner charge in terms of topological invariants.

\mathcal{C}_3	$[K_1^{(3)}]$	$[K_2^{(3)}]$	Q_c
1a	0	0	0
$1b _\pi$	0	-2	2/3
$1b _{\pm \frac{\pi}{3}}$	0	1	2/3
$1c _\pi$	2	-2	0
$1c _{\pm \frac{\pi}{3}}$	-1	1	0

Table 7.4: EBRs with \mathcal{C}_3 symmetry induced from the maximal Wyckoff positions listed in the first column [see Figure 7.4 (c)], and their invariants. All atomic limits can be decomposed into EBRs formed by single Kramers pairs.

\mathcal{C}_6	$\mu_{\Gamma M}$	$[K_2^{(3)}]$	Q_c
1a	0	0	0
$2b _\pi$	0	-4	$4/3$
$2b _{\pm \frac{\pi}{3}}$	0	2	$4/3$
3c	1	0	1

Table 7.5: EBRs with \mathcal{C}_6 symmetry induced from the maximal Wyckoff positions listed in the first column [see Figure 7.4 (d)], and their invariants. All atomic limits can be decomposed into EBRs formed by at most three Kramers pairs.

given in section 7.2.2. Importantly, all corner charges appearing in these formulas as well as in the EBR tables apply only to crystal terminations where Λ_F in Equation (7.4) has corners at the intersection of 1D edges that are obtained from translating unit cells with crystal lattice vectors [32], but not necessarily primitive ones.

As noted before, in the case where we only have \mathcal{C}_4 symmetry at our disposal, no corner charge formula can be constructed from our invariants. We leave the investigation of this symmetry class to future work.

7.2.3.1 \mathcal{I} symmetry

Inversion symmetry becomes equal to \mathcal{C}_2 symmetry in the spinless case. This means that, using inversion eigenvalues, we can uniquely read off the \mathcal{C}_2 eigenvalues of the spinless version of any model at hand, and may then use the formula presented in Reference [32] for spinless \mathcal{C}_2 symmetry to infer the corner charge of our model. Note that the doubling of the corner charge, which comes with going from spinless to spinful and imposing TRS, is automatically taken into account by the fact that the inversion eigenvalues are equal for Kramers partners. We therefore obtain

$$Q_c = \frac{1}{4} ([X_2^{\mathcal{I}}] + [Y_2^{\mathcal{I}}] - [M_2^{\mathcal{I}}]) \mod 2. \quad (7.47)$$

A nonzero value implies two equal fractional corner charges at \mathcal{I} -related sectors with $Q_c = 1$.

7.2.3.2 \mathcal{C}_2 symmetry

Comparing with Table 7.2, we have

$$Q_c = \nu_x^\pi, \quad (7.48)$$

where, if $H_{W_x}(k_y = 0, \pi)$ does not have pinned bands at eigenvalue π , we declare $\nu_x^\pi = 0$. We note that ν_x^π is \mathbb{Z}_2 valued, in accordance with the fact that two Wannier Kramers pairs at $1b$ are trivial in that they can be removed from $1b$ and moved around the unit cell in a \mathcal{C}_2 symmetric fashion. A nonzero value of $Q_c = 1$ implies two equal fractional corner charges at \mathcal{C}_2 -related sectors.

7.2.3.3 \mathcal{C}_3 symmetry

As shown in Appendix D.1, there is a one-to-one mapping between the \mathcal{C}_3 eigenvalues of the spinless and spinful cases. It implies that

$$Q_c = \frac{2}{3} \left([K_1^{(3)}] + [K_2^{(3)}] \right) \mod 2. \quad (7.49)$$

A nonzero value implies three equal fractional corner charges at \mathcal{C}_3 -related corners, with possibilities $Q_c = \frac{2}{3}$ or $Q_c = \frac{4}{3}$.

7.2.3.4 $\mathcal{C}_3 + \mathcal{I}$ symmetry

The one-to-one mapping of \mathcal{C}_3 eigenvalues from Appendix D.1, as well the observation that inversion symmetry becomes the same as \mathcal{C}_2 symmetry in the spinless case, yields

$$Q_c = -\frac{1}{4}[M_2^{\mathcal{I}}] - \frac{1}{3}[K_2^{(3)}] \mod 2. \quad (7.50)$$

A nonzero value implies six equal fractional corner charges at $\mathcal{C}_3, \mathcal{I}$ -related corners, with possibilities $Q_c = \frac{1}{3}$, $Q_c = \frac{2}{3}$, $Q_c = 1$, $Q_c = \frac{4}{3}$, or $Q_c = \frac{5}{3}$.

7.2.3.5 \mathcal{C}_6 symmetry

Comparing with Table 7.5, we have

$$Q_c = \mu_{\Gamma M} - \frac{1}{3}[K_2^{(3)}] \mod 2, \quad (7.51)$$

where $\mu_{\Gamma M}$ denotes the parity of the number of $W_{\Gamma M}$ zero eigenvalue pairs. A nonzero value implies six equal fractional corner charges at \mathcal{C}_6 -related corners, with possibilities $Q_c = \frac{1}{3}$, $Q_c = \frac{2}{3}$, $Q_c = 1$, $Q_c = \frac{4}{3}$, or $Q_c = \frac{5}{3}$.

7.2.3.6 Summary

We summarize our findings in Table 7.6.

\mathcal{S}	Q_c
\mathcal{I}	$\frac{1}{4}([X_2^{\mathcal{I}}] + [Y_2^{\mathcal{I}}] - [M_2^{\mathcal{I}}])$
\mathcal{C}_2	ν_x^π
\mathcal{C}_3	$\frac{2}{3}([K_1^{(3)}] + [K_2^{(3)}])$
$\mathcal{C}_3 + \mathcal{I}$	$-\frac{1}{4}[M_2^{\mathcal{I}}] - \frac{1}{3}[K_2^{(3)}]$
\mathcal{C}_6	$\mu_{\Gamma M} - \frac{1}{3}[K_2^{(3)}]$

Table 7.6: Summary of corner charge formulas.

7.3 Material candidates with corner charge fractionalization

We propose the group-V buckled honeycomb monolayers of elemental antimony (Sb) and arsenic (As) as material realizations of protected fractional corner charges. Theoretical studies suggest that antimonene and arsenene can serve as an excellent platform for electronics due to high band gap tunability and mechanical stability [208, 209, 210, 211]. Moreover, these 2D materials, as well as atomically thin bismuth monolayers (called bismuthene), deposited on a SiC substrate, are promising candidates for a realization of the quantum spin Hall states at room temperature [129, 212, 213]. Only recently, several experimental reports have demonstrated a successful fabrication of a monolayer structure of antimony [214, 215, 216] and arsenic [217].

Free-standing monolayers with nonzero buckling d_z have a three-fold rotational symmetry \mathcal{C}_3 as well as inversion \mathcal{I} symmetry [consult Figure 7.5 (d)]. (In practice, we consider weak substrate coupling so that the inversion symmetry is approximately retained.) Applying strain leads to a decreasing d_z parameter up to a fully flat structure with six-fold symmetry. In Figure 7.5 (a),(b),(c), we present the band gap evolution of Bi, Sb and As as a function of tensile strain, which is modeled by a modification to the in-plane lattice parameter (larger strain corresponds to a longer in-plane distance between atoms). First, we note the qualitative similarity of the phase diagrams for all three investigated materials. At $d_z = 0$ (which corresponds to a large strain around $\sim 25\%$), there is an additional mirror symmetry \mathcal{M}_z , and all structures are in an topological crystalline insulating (TCI) phase, protected by a mirror Chern number, which we verified by Wilson loop calculations (not shown here). This phase does not have exponentially localized Wannier functions that respect all symmetries of the model. Small buckling breaks the mirror symmetry and the materials then realize an OAL with localized Wannier orbitals centered at the center of the hexagons in the honeycomb lattice (Wyckoff position 1a of the crys-

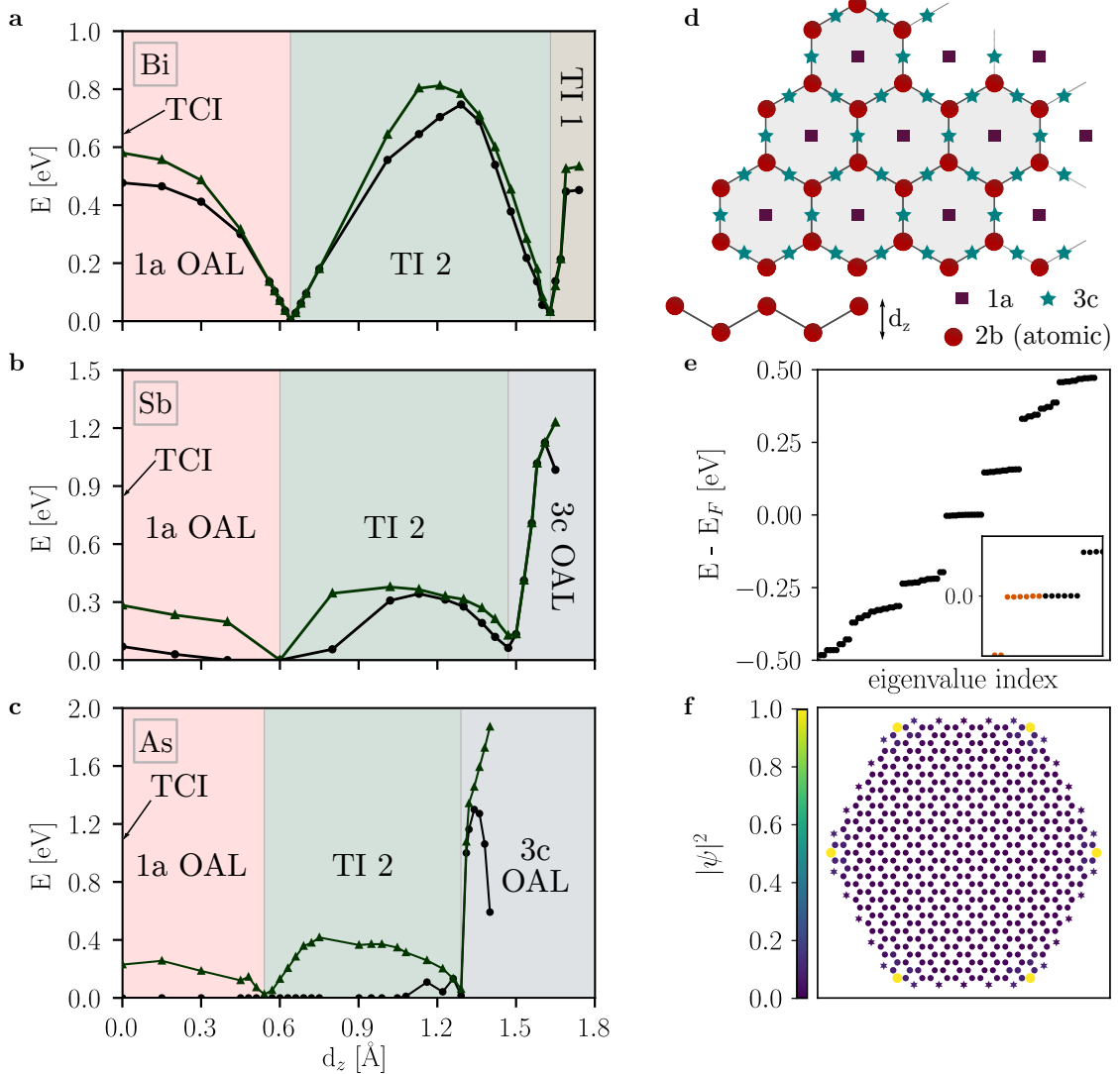


Figure 7.5: Energy gap as a function of the buckling parameter d_z for (a) bismuth, (b) antimony and (c) arsenic monolayers. The black line (circles) indicates the indirect gap, while the green line (triangles) indicates the direct gap. Top and side views of the lattice structure are illustrated in (d), together with the Wyckoff positions of the space group 164. (e) Low-energy spectrum of a finite armchair-terminated flake of the 3c OAL. The inset presents the energies around the Fermi level, with filled states in orange. (f) The electronic densities of the corner states with color scale proportional to the normalized square modulus $|\psi_i|^2$ of the eigenstates (normalized with respect to the largest $|\psi_i|^2$). The tellurium atoms used for edge passivation are shown as stars.

tal). Upon further decreasing strain, a transition to a \mathbb{Z}_2 topological insulator (TI) is observed via a band gap closing around $d_z = 0.6 \text{ \AA}$. To confirm this topological phase transition, we compute the \mathbb{Z}_2 topological index Δ_{TI} given by the product of the inversion eigenvalues of the occupied bands at the time-reversal invariant momenta in the BZ [5], and obtain $\Delta_{\text{TI}} = 1$. As strain decreases further, another band gap closing occurs. Here, the Bi monolayer reenters a TI phase (with different symmetry indicator invariants as shown in Table 7.7), as confirmed by the \mathbb{Z}_2 index remaining nontrivial. In contrast, the almost fully buckled Sb and As monolayers enter once again in an OAL phase, this time with bands induced from the Wyckoff positions $3c$ [which is located on the bonds of the hexagon, see Figure 7.4 (d)]. Hence, our results reveal more details on the previously investigated strain-induced topological phase transitions in these materials [218, 219, 220].

Let us consider the systems with open boundary conditions. To establish the presence of corner charges, we perform open flake calculations for distinct OALs using the localized basis DFT method SIESTA [221]. In Figure 7.5 (e),(f), we show results for a fully buckled antimony flake as a representative of the $3c$ OAL. The most direct indicator of fractional corner charges are corner-localized midgap states. If present, they are expected to appear close to the Fermi level. However, they are not necessarily well-separated from the bulk or edge modes. Therefore, we passivate the structure with tellurium atoms [marked with stars in Figure 7.5 (f)] in order to remove spurious dangling edge states from the bulk gap. The energy spectrum [see Figure 7.5 (e)] then exhibits 12 exactly degenerate corner states at the Fermi level, with only half of them filled. We thus obtain a fractional corner charge of $Q_c = 1 \bmod 2$ per corner, realizing a filling anomaly, as at the given filling it is not an insulating state that satisfies both charge neutrality and the crystalline symmetries [32].

We confirm this corner charge using the topological indices developed in section 7.2.1. In Table 7.7, we evaluate the symmetry indicators for all discussed phases. We may then compute the corner charge of the $3c$ OAL on a hexagonal flake using Equation (7.50). The relevant unit cell is the hexagonal cell, shown in Figure 7.4 (d), which contains three primitive unit cells of the honeycomb lattice [space group 164 ($P\bar{3}m1$)]. The symmetry indicators in Table 7.7 are given for the primitive unit cell. To obtain the corresponding indicators for the hexagonal cell, we note that an enlargement of the unit cell results in a BZ folding, where the K and K' points are mapped onto Γ , while the M , M' and M'' points are left unchanged. Referring to Table 7.7, this implies $\chi_{\mathcal{I}}^{(3)} = (4, 0)$ for the hexagonal cell, from which we obtain $Q_c = 1 \bmod 2$ by Equation (7.50). This is in agreement with the numerical results presented in Figure 7.5 (e),(f).

Correspondingly, in the case of the 1a OAL, we obtain $\chi_{\mathcal{I}}^{(3)} = (0, 0)$ for the hexagonal cell (the primitive cell cannot be used to build a C_3 -symmetric finite geometry). We conclude that there are no fractional charges. This is a case in point: although the 1a atomic limit is obstructed, in the sense that the electrons are localized away from the atomic sites, which are located at the 2b Wyckoff position of the crystal, there are no protected corner charges. (There may however be such charges in C_3 -symmetric geometries that are terminated by cutting through unit cells. We do not consider these geometries here, mainly because there is no bulk-boundary correspondence in this case, and the actual corner charge is dependent on how the boundary unit cells are cut.)

phase	$\#\Gamma_2^{\mathcal{I}}$	$\#M_2^{\mathcal{I}}$	$\#\Gamma_2^{(3)}$	$\#K_2^{(3)}$	$\chi_{\mathcal{I}}^{(3)}$	Δ_{TI}
TI 1	4	6	0	4	(2, 4)	1
TI 2	4	6	2	4	(2, 2)	1
3c OAL	2	6	2	4	(4, 2)	0
1a OAL	4	4	2	4	(0, 2)	0

Table 7.7: Topological invariants and symmetry indicators $\chi_{\mathcal{I}}^{(3)} = ([M_2^{\mathcal{I}}], [K_2^{(3)}])$ corresponding to different regions in the phase diagrams. The symmetry indicators were calculated using the primitive 2-site unit cell of the honeycomb lattice. The indices $\chi_{\mathcal{I}}^{(3)}$ allow for a more refined classification even of the strong TIs. We find that the 3c and 1a OALs differ in their inversion indicator $[M_2^{\mathcal{I}}]$ and thus, as explained in the main text, inversion-symmetric flakes built from their hexagonal unit cells differ by a protected corner charge equal to $1 \bmod 2$.

Chapter 8

Position-space perspective on topological superconductors

In the previous Chapter 7, and also in Chapter 5, we saw how a position-space, Wannier function-based perspective can aid the understanding of crystalline topological phases in one and two dimensions, where it gives an intuitive picture of charge accumulation and zero-dimensional edge states.

More generally, within the framework of Topological Quantum Chemistry [14], a position-space approach has led to a classification and materials prediction program for topological insulators. In this approach, topology is defined in terms of an obstruction to finding a gauge in which the Wannier functions are exponentially localized and preserve all of the symmetries of the system. In this sense, the obstructed atomic limit phases we discussed in Chapter 7 of this thesis are not true topological insulators, because they can be trivialized by adding unoccupied atomic sites at the Wannier centers in the unit cell, thereby removing the obstruction.

The fundamental bridge between momentum space topology and real space structure is the equivalence of Wilson loop spectra and Wannier centers, as derived in Section 2.1.1 [87, 88, 89]. In the present chapter, we ask whether it is possible to extend this fruitful correspondence to superconductors, whose ground states are a condensate of pairs of electrons. Topological superconductors (TSCs) have a gapped bulk spectrum and exotic edge excitations that are their own anti-particles (so called Majorana modes) [222, 223, 224, 225, 226]. TSCs provide a candidate hardware platform for fault-tolerant quantum computation [227].

The mean-field description of superconductors is formally equivalent to the band theory of non-interacting electrons. However, the ground state of a superconductor

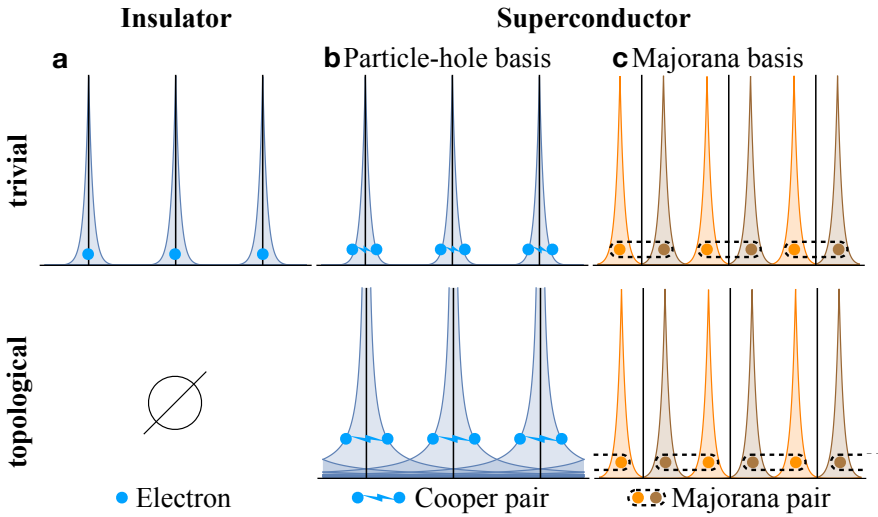


Figure 8.1: Position-space picture of insulators and superconductors in 1D lattices, with atomic sites indicated by vertical lines. (a) The ground state of an insulator as a product over Wannier states. All 1D electronic band structures (absent symmetries) can be realized by exponentially localized Wannier functions. In contrast to superconductors, there are therefore no topological insulators in 1D (topologically insulating phases first appear in 2D, a prime example being the Chern insulator). (b) The fixed-particle number component of the superconducting ground state as a product of Cooper pair states with wavefunctions decaying exponentially in the trivial phase and polynomially in the topological phase. (c) The ground state as a product over Majorana Wannier functions with quantized Majorana charge. In the trivial phase, these can be paired up to give back the original electrons and holes localized at the atomic sites. In the topological phase, Majoranas from different atomic sites are paired up, leaving behind unpaired Majorana zero modes at the boundaries.

involves pairing of electrons and is therefore qualitatively different from the Slater-determinant ground state of an insulator. This fact leads to striking differences between TSCs and TIs. In particular, we show that topology in superconductors can be phrased in terms of an obstruction to finding a gauge in which electron pairs are tightly (exponentially) bound. While such an obstruction was discussed for a model of a two-dimensional (2D) p -wave superconductor [222, 228], we generalize it to arbitrary systems in arbitrary dimension. Furthermore, expressing the ground state in a basis of Majorana fermions, we find that the total spectral weight on the two Majorana degrees of freedom corresponding to each electron is split evenly, allowing us to introduce the concept of a quantized Majorana polarization. We exemplify these concepts in a simple one-dimensional (1D) single-band model. Our results are partially summarized in Figure 8.1.

8.1 p -wave superconductor in particle-hole basis

We consider a 1D p -wave TSC, which could be realized by a nanowire with a single conduction band that is brought in proximity with an s -wave (trivial) superconductor [229, 230]. Within mean-field theory, the nanowire is described by the Hamiltonian

$$H = \sum_k \Psi_k^\dagger \mathcal{H}_k \Psi_k, \quad (8.1)$$

where we have introduced the Nambu spinor $\Psi_k = (c_k, c_{-k}^\dagger)/\sqrt{2}$ and the Bogoliubov–de-Gennes (BdG) Hamiltonian

$$\mathcal{H}_k = \begin{pmatrix} \epsilon_k & \Delta_k \\ \bar{\Delta}_k & -\epsilon_{-k} \end{pmatrix}, \quad (8.2)$$

with μ the chemical potential and $\Delta_k = -\Delta_{-k}$ due to Fermi statistics (the bar denotes complex conjugation). The operator c_k^\dagger creates an electron at momentum $k \in \{1, \dots, N\}2\pi/N$, and N is the number of sites (periodic boundary conditions are assumed). For $|\mu| < 2|t|$, Equation (8.1) is in the topological phase, which hosts a single Majorana zero mode at each end of the nanowire, while for $|\mu| > 2|t|$ the system is in the trivial phase. We refer to the convention in Equation (8.2) as the particle-hole basis. In contrast to insulators, the mean-field description of superconductors allows for the additional freedom of choosing a basis in Nambu space; this freedom is important for our position-space interpretation. We can diagonalize this Hamiltonian by introducing Bogoliubov quasiparticle operators

$$\begin{pmatrix} \alpha_k \\ \alpha_{-k}^\dagger \end{pmatrix} = \begin{pmatrix} u_k & -v_k \\ -\bar{v}_{-k} & \bar{u}_{-k} \end{pmatrix} \begin{pmatrix} c_k \\ c_{-k}^\dagger \end{pmatrix} \equiv D_k \begin{pmatrix} c_k \\ c_{-k}^\dagger \end{pmatrix}, \quad (8.3)$$

where the matrix D_k is unitary, with

$$\begin{aligned} u_k \bar{u}_k + v_k \bar{v}_k &= u_k \bar{u}_k + v_{-k} \bar{v}_{-k} = 1, \\ u_k v_{-k} + v_k u_{-k} &= \bar{u}_k v_k + v_{-k} \bar{u}_{-k} = 0. \end{aligned} \quad (8.4)$$

For $|\mu| \neq 2|t|$ the spectrum is gapped and H has the ground state

$$\begin{aligned} |\Omega\rangle &= \frac{1}{\mathcal{N}} \exp \left(\sum_k \frac{v_k}{u_k} c_k^\dagger c_{-k}^\dagger \right) |0\rangle, \\ &= \frac{1}{\mathcal{N}} \exp \left(\sum_{xy} g_{xy} c_x^\dagger c_y^\dagger \right) |0\rangle, \\ g_{xy} &= \frac{1}{N} \sum_k e^{ik(x-y)} \frac{v_k}{u_k}, \end{aligned} \quad (8.5)$$

where $|0\rangle$ is the fermionic vacuum, $(-\nu_{-k}, u_{-k})$ is the negative-energy eigenvector of the BdG Hamiltonian \mathcal{H}_k , and \mathcal{N} is a normalization factor. In the second line, we introduced the Fourier-transformed operators

$$c_r^\dagger = \frac{1}{N} \sum_k e^{-ikr} c_k^\dagger, \quad r = 1 \dots N, \quad (8.6)$$

that create a particle at site r of the nanowire. We emphasize that the possibility of representing the ground state in the form of Equation (8.5), reminiscent of a coherent state of Cooper pairs $c_k^\dagger c_{-k}^\dagger$, singles out the particle-hole basis, since it crucially relies on the anticommutation relations $\{c_p, c_q^\dagger\} = \delta_{pq}$, $\{c_p, c_q\} = \{c_p^\dagger, c_q^\dagger\} = 0$ of electronic creation and annihilation operators. Furthermore, extracting from Equation (8.5) the contribution to the N -particle state $|\Omega_N\rangle$, we obtain the amplitudes

$$\langle r_1 \dots r_N | \Omega_N \rangle \propto A [g_{r_1 r_2} g_{r_3 r_4} \dots g_{r_{N-1} r_N}], \quad (8.7)$$

where $A[\cdot]$ denotes an antisymmetrization over all positions $r_1 \dots r_N$. Invoking the Paley–Wiener theorem allows to determine the large-separation dependence of g_{xy} on general grounds. In fact, g_{xy} will fall off exponentially as $|x - y| \rightarrow \infty$ if the momentum space function v_k/u_k is analytic [231, 232]. On the other hand, if v_k/u_k diverges at some k , g_{xy} will at most fall off polynomially with separation.

We now relate the analytical properties of v_k/u_k to the topological characterization of the superconducting phase. We assume no further symmetries other than particle-hole symmetry (PHS), which is intrinsic to all superconductors in the mean-field description, and in the particle-hole basis reads

$$\mathcal{P} \mathcal{H}_k \mathcal{P}^\dagger = -\mathcal{H}_{-k}, \quad \mathcal{P} = \begin{pmatrix} 0 & \mathbb{1} \\ \mathbb{1} & 0 \end{pmatrix} K. \quad (8.8)$$

PHS quantizes the Berry phase topological invariant

$$\begin{aligned} \gamma &= i \int dk (\bar{u}_k \partial_k u_k + \bar{v}_k \partial_k v_k) \mod 2\pi \\ &= \frac{i}{2} \int dk \text{Tr} [D_k^\dagger \partial_k D_k] \mod 2\pi \\ &= \int_0^\pi dk \partial_k \lambda_k \mod 2\pi = (\lambda_\pi - \lambda_0) \mod 2\pi, \end{aligned} \quad (8.9)$$

where we wrote $\det D_k = e^{-i\lambda_k}$ and used that PHS implies $\lambda_{-k} = -\lambda_k \mod 2\pi$, and hence, $\lambda_0, \lambda_\pi = 0, \pi$. For γ to assume values $0, \pi$, we take the BdG functions u_k and v_k to be periodic functions in momentum space. This property, together with Equation (8.6), corresponds to a convention where all atomic orbitals are located

at the origin of the unit cell in position space. The physical atomic positions are irrelevant for the salient features of our analysis, as we do not consider crystalline symmetries. Our results can be straightforwardly generalized to arbitrary atomic positions, see Appendix E.2.

Now, if $\gamma = 0$, we can adiabatically deform the system to one in which only u_k is nonzero and constant. Its inverse is then always well defined, and the ground state in position space, as expressed via g_{xy} , is a coherent superposition of exponentially-closely bound Cooper pairs. We next show that if $\gamma = \pi$, there are necessarily divergences in v_k/u_k , leading to a polynomial decay of g_{xy} . The proof proceeds by contradiction. Without loss of generality, we take $\gamma = \pi$ to be realized by $\lambda_0 = 0, \lambda_\pi = \pi$, implying $\det D_0 = 1$ and $\det D_\pi = -1$. Let us assume that u_k is nonzero throughout momentum space. It therefore has a well-defined inverse, and we may reexpress $\det D_k$ as

$$\begin{aligned} \det D_k &= u_k \bar{u}_{-k} \left(\frac{u_k \bar{u}_{-k} - v_k \bar{v}_{-k}}{u_k \bar{u}_{-k}} \right) \\ &= u_k \bar{u}_{-k} \left(1 - \frac{v_k \bar{v}_{-k}}{u_k \bar{u}_{-k}} \right) \\ &= \frac{u_k}{u_{-k}} = 1 \text{ at } k = 0, \pi, \end{aligned} \tag{8.10}$$

where we used the constraints in Equation (8.4). This result is, however, in contradiction to our earlier assertion that $\det D_\pi = -1$. We conclude that either u_0 or u_π are zero in systems with $\gamma = \pi$. This result carries over to an arbitrary number of bands [233].

Thus, just as for the two-dimensional p -wave superconductor [222, 228], the long-distance behavior of the Cooper pair wavefunction is indicative of the topological character of the phase: In the trivial phase, there is strong pairing and the wavefunction decays exponentially with separation, while in the topological case, there is weak pairing and the wavefunction decays only polynomially. This *pairing obstruction* is in close correspondence to the position-space picture of insulating topological phases, where symmetric and maximally localized electronic Wannier functions decay exponentially in trivial insulators and polynomially in TIs [234, 153, 14]. In contrast to insulators, the particle-hole symmetry inherent to superconductivity allows for topological phases already in one dimension.

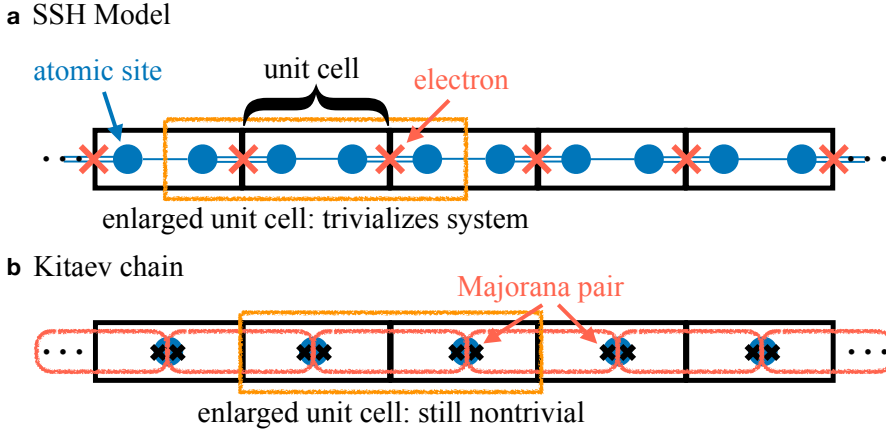


Figure 8.2: Comparison of 1D topological insulators and superconductors. (a) In the Su-Schrieffer-Heeger (SSH) model [79], spatial inversion symmetry is required to pin electrons to the unit cell edges, leading to midgap states in an open geometry. However, it is possible to choose an inversion-symmetric enlarged unit cell that has no end states. (b) In the Kitaev chain [227], Majorana modes are paired across unit cells, leaving behind unpaired Majorana zero modes in an open geometry. Since unit cells may not cut through atomic sites, any enlarged unit cell shows the same topological behavior.

8.2 p -wave superconductor in Majorana basis

We introduce the Majorana modes $a_k = c_k + c_{-k}^\dagger$, $b_k = (c_k - c_{-k}^\dagger)/i$, and the Majorana BdG Bloch functions $v_k^M = (v_k - u_k)/\sqrt{2}$ and $u_k^M = i(v_k + u_k)/\sqrt{2}$. Let a_r, b_r be the Fourier transforms of the Majorana modes [using the same convention as in Equation (8.6)]. We can then reexpress the ground state in Equation (8.5) in terms of Majorana Wannier functions $W_{R\alpha}^M(r)$, $\alpha = a, b$, which we define by

$$|\Omega\rangle = \frac{1}{N} \prod_R \left(\sum_r W_{Ra}^M(r) a_r + W_{Rb}^M(r) b_r \right) |0\rangle, \quad (8.11)$$

$$\begin{pmatrix} W_{Ra}^M(r) \\ W_{Rb}^M(r) \end{pmatrix} = \frac{1}{N} \sum_k e^{-ik(R-r)} \begin{pmatrix} -v_k^M \\ u_k^M \end{pmatrix}.$$

As for any 1D system [78], the Wannier functions $W_{R\alpha}^M(r)$ can be exponentially localized. In the unit cell, they are centered around the position

$$x_o = \sum_{r,\alpha} \overline{W}_{0\alpha}^M(r) r W_{0\alpha}^M(r) \bmod 1. \quad (8.12)$$

(The subscript o stands for the occupied subspace spanned by the Majorana Wannier functions, corresponding to the negative-energy eigenspace of the BdG Hamiltonian.) Particle-hole symmetry implies that $x_o = x_e$, where x_e denotes the center

of Wannier functions built from the empty Majorana bands. At the same time, the Wannier centers for all bands (which form a complete basis for the Hilbert space) are always exponentially localized on the lattice sites. We therefore have $x_0 + x_e \bmod 1 = 0$. We conclude that $x_0 = 0, 1/2$ is quantized and provides a topological invariant characterizing the many-body ground state. In fact, we know from the general theory of maximally localized Wannier functions [78] that $x_0 = \gamma/2\pi = 0, 1/2$, where γ is defined similar to Equation (8.9):

$$\gamma = i \int dk (\bar{u}_k^M \partial_k u_k^M + \bar{v}_k^M \partial_k v_k^M) \bmod 2\pi \quad (8.13)$$

(the two definitions are equivalent). Therefore, the Wannier states in Equation (8.11), which are labelled by the position R of the unit cell they belong to, can be adiabatically continued back to the original delta-localized Majorana basis states at position R , created by the bare operators a_R and b_R , if and only if the Berry phase vanishes: These original basis states have Wannier functions $W_{R\alpha}^M(r) = \delta_{R,r}\delta_{\alpha,1}$ or $W_{R\alpha}^M(r) = \delta_{R,r}\delta_{\alpha,2}$, both of which correspond to $x_0 = 0$. This property implies a Majorana pairing obstruction: It is impossible to adiabatically connect the topological superconducting ground state to a collection of physical (i.e., deriving from the atomic positions) electrons or holes. On the other hand, in a trivial superconductor it is possible to turn off superconductivity without closing the gap between positive and negative-energy quasiparticle states.

We next show that the Majorana representation is set apart from other basis decompositions of Equation (8.1) in that it allows for a meaningful generalization of polarization to superconductors. Taking the trace of the Majorana version of the constraint in Equation (8.4), we find that

$$\begin{aligned} \sum_k \bar{v}_k^M v_k^M &= \frac{N}{2} = \sum_k \bar{u}_{-k}^M u_{-k}^M, \\ \sum_r \bar{W}_{0\alpha}^M(r) W_{0\alpha}^M(r) &= \frac{1}{N} \sum_k \left(\begin{pmatrix} \bar{v}_k^M & v_k^M \\ \bar{u}_k^M & u_k^M \end{pmatrix} \right)_\alpha = \frac{1}{2}. \end{aligned} \quad (8.14)$$

This implies that the total spectral weight carried by Majoranas of a or b type is always equal, a property that is not realized in other bases: In the particle-hole basis, for example, the total spectral weight carried by holes is zero in the case of a band insulator. The total Wannier function support within a unit cell therefore splits into equal contributions of Majoranas of a and b type. This result carries over to an arbitrary number of bands [233].

We therefore introduce a quantized *Majorana charge*, nominally equal to $1/2$, and a corresponding Majorana polarization that is computed via Equation (8.12), or alternatively via the Berry phase in Equation (8.13). Figure 8.2 shows how Majorana

dimension	g_{xy} decay	$W_{R\alpha}^M(r)$ decay	phase label
1D	exponential	exponential	trivial
	polynomial	exponential	p -wave TSC
2D	exponential	exponential	trivial
	polynomial	polynomial	chiral TSC
	polynomial	exponential	2nd order TSC
3D	exponential	exponential	trivial
	polynomial	polynomial	2nd order TSC
	polynomial	exponential	3rd order TSC

Table 8.1: Overview of topological superconductors without time-reversal symmetry. The 1D p -wave TSC hosts zero-dimensional Majorana end states. The 2D chiral TSC can be obtained from it via a Thouless pump, which naturally explains why its Wannier functions cannot be exponentially localized. Another possibility in 2D is the 2nd order TSC with Majorana corner states. In 3D, the only Wannier obstructed superconductor absent time-reversal symmetry is the 2nd order TSC with 1D Majorana hinge states similar to the edge states of the 2D p -wave TSC.

polarization, unlike electronic polarization, survives translational symmetry breaking. We can now draw a direct connection to the anomalous end states of a 1D superconductor in the topological regime, where the nonzero Majorana polarization of 1/2 results in a single Majorana mode localized at the end of an open geometry. Due to particle-hole symmetry, this mode is necessarily a zero-energy state.

Note that our concept of Majorana polarization differs from that of Reference [235]. In particular, the latter work introduced a continuous and local quantity that captures the Majorana character of a given state in Nambu space, similar to how spin polarization captures local spin alignment. The Majorana polarization defined here, on the other hand, is a quantized and global bulk property, and guarantees the presence of Majorana end states.

8.3 Chiral superconductor and generalization to higher dimensions

The two-dimensional p -wave superconductor [222, 228] can be obtained from a Thouless pump of bulk Majorana fermions. Such a superconductor is characterized by a nonzero Chern number of the occupied BdG eigenstates. We interpret this Chern number as a flow of the Majorana separation from the atomic sites, Equation (8.12), with a transversal momentum coordinate. Consider a two-dimensional

BdG Hamiltonian \mathcal{H}_k . Particle-hole symmetry implies $\mathcal{P}\mathcal{H}_k\mathcal{P}^\dagger = -\mathcal{H}_{-\mathbf{k}}$, with \mathcal{P} defined in Equation (8.8). Writing $\mathbf{k} = (k_x, k_y)$, there are two special values of $k_y = 0, \pi$, at which $\mathcal{H}_{(k_x, k_y=0,\pi)} \equiv \mathcal{H}_{k_x}^{0,\pi}$ can be interpreted as the BdG Hamiltonian of a 1D superconductor. In the Majorana basis, we introduce hybrid Wannier functions that are indexed by k_y , affording a k_y -dependent Majorana polarization

$$x_o^{k_y} = \sum_{r,\alpha} \overline{W}_{0\alpha}^M(k_y, r_x) r_x W_{0\alpha}^M(k_y, r_x) \mod 1. \quad (8.15)$$

We note again that we are working in a convention where the atomic positions are all at $\mathbf{r}_i = (0, 0)$. Crucially, due to the action of particle-hole symmetry, the related Berry phase is only quantized for $k_y = 0, \pi$, namely $x_o^{0,\pi} = \gamma^{0,\pi}/2\pi = 0, 1/2$, where γ^{k_y} is evaluated along 1D momentum space slices of constant k_y . The Berry phase winding as a function of k_y is related to the Chern number

$$C = \frac{1}{2\pi} \int dk_y \partial_{k_y} \gamma^{k_y} = \int dk_y \partial_{k_y} x_o^{k_y}. \quad (8.16)$$

We conclude that in a 2D $p_x + ip_y$ superconductor with $C = 1$, the Majorana polarization $x_o^{k_y}$ continuously evolves from 0 to 1 $\equiv 0$ as k_y undergoes a noncontractible cycle. Importantly, this implies that it is impossible to exponentially localize the Majorana Wannier functions $W_{0\alpha}^M(k_y, r_x)$ also in the y -direction, as they are not smooth functions of k_y .

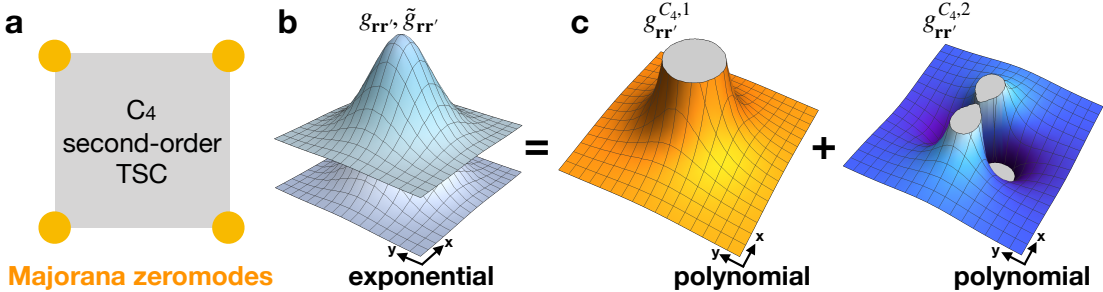


Figure 8.3: Real-space structure of a \mathcal{C}_4 -symmetric second-order topological superconductor. (a) Majorana corner modes in a square-shaped sample geometry. (b) Naively, the two ground state Cooper pair wavefunctions [generalizations of Equation (8.5)] $g_{rr'}$ and $\tilde{g}_{rr'}$ decay exponentially with electron separation. (c) When chosen as eigenfunctions of \mathcal{C}_4 symmetry, the Cooper pair wavefunctions of each \mathcal{C}_4 subsector, $g_{rr'}^{\mathcal{C}_4,1}$ and $g_{rr'}^{\mathcal{C}_4,2}$, necessarily decay polynomially as a consequence of the nontrivial second-order topology.

We therefore find that a topological 2D p -wave superconductor admits neither an exponentially decaying Cooper pair function g_{xy} , nor exponentially decaying Majorana Wannier functions $W_{R\alpha}^M(\mathbf{r})$. A natural question is then if there exists a 2D

superconductor with a polynomially decaying Cooper pair function but exponentially decaying Majorana Wannier functions. This “Majorana obstructed atomic limit” phase is naturally realized by the recently discovered higher-order TSCs, which feature Majorana zero modes localized at the corners of samples terminated in both x and y directions [24, 43, 236, 237]. Our results imply that these phases are “stronger” than their insulating counterparts, in that they cannot be trivialized by the introduction of uncharged ancillas [238].

In particular, our results shed new light on second-order topological superconductors protected by \mathcal{C}_4 rotation symmetry and spinful time-reversal. These host four Kramers pairs of Majorana zero-energy states at the corners of a square-shaped sample, and otherwise have a gapped bulk and gapped edge spectrum. Analyzing their topological properties from a real-space perspective is particularly interesting, as all symmetry indicators and (nested) Wilson loop topological indices are trivial [32, 239]. Nevertheless, second-order TSCs can be identified by the decay behavior of their Cooper pair wavefunctions. We show in Appendix E.3 that the Cooper pairs *in individual \mathcal{C}_4 eigenvalue subspaces* are subject to a pairing obstruction. See Figure 8.3 for an illustration.

Chapter 9

Toy models for interacting higher-order topological phases

In this last Chapter of the thesis, we will switch gears and explore how one can construct interacting symmetry-protected topological (SPT) phases of bosons which share the phenomenology of higher-order topological insulators. Note that while non-interacting fermionic systems may have topologically nontrivial ground states, the same is not true for non-interacting bosonic systems whose ground state is a trivial Bose-Einstein condensate [240]. Therefore, for bosons we necessarily need interactions to stabilize a topological phase. We first give a lightning introduction to SPT phases via a very simple model in 1D. A topologically nontrivial SPT state is defined as the gapped ground state of a Hamiltonian, for which there exists no adiabatic interpolation to an atomic limit Hamiltonian without breaking the protecting symmetries or losing the locality of the Hamiltonian along the interpolation [241].

9.1 One-dimensional first-order model with local symmetry

Consider a chain of N spin-1/2 degrees of freedom with Hamiltonian

$$H = - \sum_{i=2}^{N-1} A_i, \quad A_i = \sigma_{i-1}^z \sigma_i^x \sigma_{i+1}^z, \quad (9.1)$$

which describes a system with open boundary conditions. All the A_i commute with each other and can therefore be simultaneously diagonalized.

The Hamiltonian H respects a time-reversal \mathbb{Z}_2^T symmetry $[\mathcal{T}, H] = 0$ represented by the operator

$$\mathcal{T} = K \prod_i \sigma_i^x. \quad (9.2)$$

Note that $\mathcal{T}^2 = +1$.

We now consider a set of operators

$$\Sigma^x = \sigma_1^x \sigma_2^z, \quad \Sigma^y = \sigma_1^y \sigma_2^z, \quad \Sigma^z = \sigma_1^z, \quad (9.3)$$

which act locally on the left end of the chain and furnish a Pauli algebra. A similar set of operators can be defined for the other end of the chain.

Since $[\mathcal{T}, \Sigma^a]_+ = 0$, where $[\cdot, \cdot]_+$ denotes the anti-commutator, these end operators cannot be added as a perturbation to the Hamiltonian without breaking the \mathbb{Z}_2^T symmetry. However, they commute with all the A_i in H . This algebra can only be realized on a space with minimum dimension 2, imposing a twofold degeneracy on the eigenstates of H for each end of the chain. This degeneracy can be interpreted as one gapless spin-1/2 degree of freedom at each end of the chain. Note that a unitary version of \mathcal{T} would commute with Σ^y rather than anti-commute and therefore not protect these edge degrees of freedom.

9.2 Two-dimensional second-order model with crystalline symmetry

We can set up a very similar construction in 2D to arrive at a SPT model with gapless corner modes. Note however that we know from the classification of SPTs by group cohomology [241] that while in 1D the \mathbb{Z}_2^T symmetry from before indeed protects a \mathbb{Z}_2 topological classification, in 2D there is no corresponding nontrivial phase. As was the case for non-interacting fermions, we therefore have to turn to spatial symmetries to protect corner states. Other than that, the construction is very similar to the 1D case.

Consider a square lattice of spin-1/2 degrees of freedom, again with Hamiltonian

$$H = - \sum_i A_i, \quad A_i = \sigma_i^x \prod_{j_i \in N(i)} \sigma_{j_i}^z, \quad (9.4)$$

where the set $N(i)$ stands for the four next-to-nearest neighbor sites of site i , which are located along the xy and $x\bar{y}$ diagonals [see Figure 9.1(a)]. Again, verify that all A_i commute with each other and thus can be simultaneously diagonalized. We will

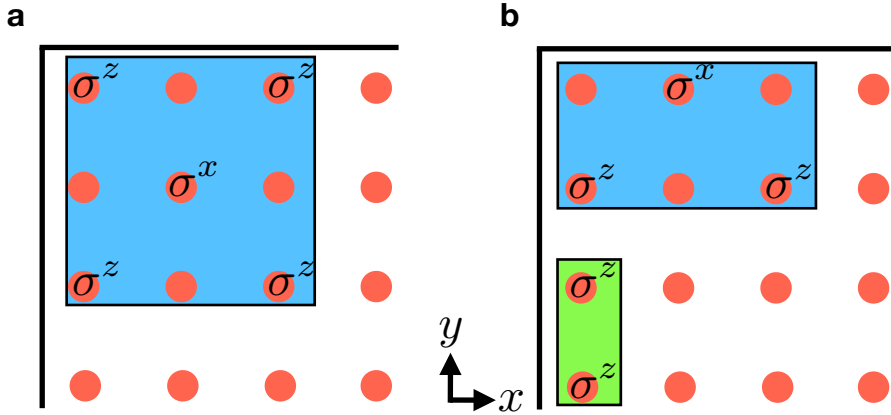


Figure 9.1: Local operators of a higher-order SPT Hamiltonian with protected corner modes. Each site carries a spin-1/2 degree of freedom acted upon by the Pauli matrices σ^i , $i = 0, x, y, z$. (a) The bulk Hamiltonian consists of the sum over all sites of tensor products of σ_x acting on a given site with σ_z on all four adjoining sites along the two diagonals. (b) Two possible edge Hamiltonian elements which naively would both satisfy the symmetry $\mathcal{M}_{xy}\mathcal{T}$ when repeated over all edge sites. However, the ground state corresponding to the operator in green spontaneously breaks the symmetry and the operator is thus forbidden. Therefore, we may only terminate the edge with the operator in blue, leading to a two-fold degeneracy in the resulting ground state for each corner.

be interested in open boundary conditions, in which case the sum over i runs only over the interior sites of the lattice, i.e., not the sites on the edges or corners.

Trivially, the model has the same symmetry as given by Equation (9.2). However, we need to enrich it with a spatial transformation in order for it to protect topological features. We choose $\mathcal{T} = K \prod_i \sigma_i^x$ as before and define

$$\mathcal{M}_{x\bar{y}} : (x, y) \rightarrow (-y, -x). \quad (9.5)$$

The model is then invariant under the symmetry $\mathcal{M}_{x\bar{y}}\mathcal{T}$. We will now show that this symmetry protects a pair of corner states along the $x\bar{y}$ diagonal. In order to also protect states at the other pair of corners we would have to perform the same analysis and require $\mathcal{M}_{xy}\mathcal{T}$ or \mathcal{C}_4^z symmetry in addition.

Indeed, at each corner along the $x\bar{y}$ diagonal, we have a Pauli algebra generated by

$$\Sigma^x = \sigma_c^x \sigma_{j_c}^z, \quad \Sigma^y = \sigma_c^y \sigma_{j_c}^z, \quad \Sigma^z = \sigma_c^z, \quad (9.6)$$

where c denotes the corner site and j_c denotes the site which is the next-to-nearest neighbor of the corner along the diagonal. Crucially, there is a single next-to-nearest neighbor site for each corner, while in the bulk there are four next-to-nearest neighbors along the diagonals.

Since $[\mathcal{M}_{x\bar{y}}\mathcal{T}, \Sigma^a]_+ = 0$, these corner terms Σ^x , Σ^y , and Σ^z cannot be added as a perturbation to the Hamiltonian without breaking the symmetry. However, they commute with all the A_i in H , again imposing a two-fold degeneracy on the eigenstates of H for each corner. We therefore have one gapless spin-1/2 degree of freedom at each corner lying along the diagonal corresponding to the respective mirror symmetry we require to hold.

Unlike in the 1D case, this is not the end of the story. We have merely shown that each corner provides a two-fold degeneracy, but what about the edge degrees of freedom? In order to arrive at a higher-order phase, we need to gap them out. A natural way to do this is to include in the Hamiltonian not only the A_i terms with four next-to-nearest neighbors, but also the corresponding edge terms which only have two next-to-nearest neighbors. This is in fact symmetry-allowed for all the edge sites except the corners. The terms are sketched in Figure 9.1(b).

We may however also just put an Ising model on the edge by adding the Hamiltonian

$$H_{\text{edge}} = - \sum_{i \in E} \sigma_i^z \sigma_{N_E(i)}^z, \quad (9.7)$$

where E denotes the set of all boundary sites, including the corners [see Figure 9.1(b)], and $N_E(i)$ denotes one of the two nearest-neighbor sites of i on the edge chosen according to an arbitrary but globally fixed edge orientation. Hamiltonian (9.7) contains as many terms as there are edge and corner sites combined. The bulk Hamiltonian contains as many terms as there are bulk sites. We want to find a ground state that has simultaneously eigenvalue +1 with respect to all these commuting operators. At first sight, because there are as many terms as sites, these constraints fix the ground state completely. However, this is not true. The product of all terms in Hamiltonian (9.7) is the identity, because each site is acted upon by two σ^z operators in this product. This means we have globally one less constraint than sites. This degeneracy corresponds to two magnetized ground states of the Ising model that is formed by the gapped edge. Luckily, either of these magnetized ground states of the quantum Ising model in 1D necessarily breaks the $\mathcal{M}_{x\bar{y}}$ symmetry (remember that we are, as always in these notes, working at zero temperature). This spontaneous symmetry breaking preempts the definition of our topological case and renders the edge termination defined in Equation (9.7) not permissible.

Part IV

Conclusions and outlook

We here review the achievements of, and challenges posed by, each chapter of the thesis, before concluding with a general outlook on future developments in the study of topological phases of matter.

In Chapter 3, we introduced 3D higher-order topological insulators that have gapped surfaces, but gapless hinge modes, as intrinsically 3D topological phases of matter. Both time-reversal symmetry breaking and time-reversal symmetric systems were explored, which support hinge states akin to those of the integer quantum Hall effect and 2D time-reversal symmetric TIs, respectively. The former may be realized in magnetically ordered topological insulators; we propose the naturally occurring rhombohedral or a uniaxially distorted phase of SnTe as a material realization for the latter. Despite their global topological characterization based on spatial symmetries, the hinge states are as robust against local perturbations as quantum (spin) Hall edge modes. The concepts introduced here can be extended to define novel topological superconductors with chiral and helical Majorana modes at their hinges and may further be transferred to strongly interacting, possibly topologically ordered, states of matter and to mechanical [242], electrical [243], and photonic analogues of Bloch Hamiltonians.

The bismuth-antimony alloy, $\text{Bi}_{1-x}\text{Sb}_x$, was the first material realization of a 3D topological insulator [5, 3]. The composition x was used to interpolate between bismuth, without band inversion, and the band inverted antimony. In Chapter 4, we demonstrated theoretically that the allegedly trivial end of this interpolation, bismuth, has in fact a 3D topological band structure as well. It is a higher-order topological insulator with helical hinge states. We presented two complementary pieces of experimental evidence supporting this result, using scanning tunneling microscopy and Josephson-interferometry measurements.

The type of hinge states discussed in Chapters 3 and 4 may be used for lossless electronic transport due to their local protection from backscattering by time-reversal symmetric disorder. Further applications include spintronics, due to their spin-momentum locking, and – when proximitized with superconductivity – topological quantum computation. For the latter, a bismuth nanowire with hexagonal cross-section may provide a particularly convenient way of building a hexon – a group of six Majorana states, one at each hinge. Hexons have been proposed as building blocks for a measurement-only quantum computer [244].

In Chapter 5, we explored the crystal defect and magnetic flux response of topological crystalline phases with inversion symmetry. The presence of zero-dimensional end states bound to flux tubes in a higher-order topological insulator, but not in a trivial insulator, provides the first example of a response effect that distinguishes

the gapped surfaces of higher-order topological and trivial insulators. Specifically, when cut into a hingeless slab geometry, both higher-order topological and trivial insulators exhibit fully gapped spectra. However, when we pierce each of the two insulators with a π -flux that preserves an inversion center, the higher-order topological insulator exhibits a filling anomaly, whereas the trivial insulator does not.

The defect end states proposed in Chapter 5 should be observable through scanning tunneling microscopy probes of the corners of edge dislocations and the surface terminations of screw dislocations and flux tubes (solenoids) in 3D higher-order topological insulators. As evidenced by the robust inversion- and rotation-protected hinge states observed in bismuth crystals (Chapter 4), the global crystal symmetries required to protect defect end states can be preserved in real materials. This, along with the recent theoretical identification of higher-order topological phases in materials beyond bismuth, including MoTe_2 and WTe_2 [62], $\alpha\text{-Bi}_4\text{Br}_4$ [74], and the $\text{Ba}_3\text{Cd}_2\text{As}_4$ family [65], as well as the recent establishment of vast databases of topological materials [69, 70, 75, 245] (see also the survey of HOTI materials in Chapter 1) indicates particular promise for future experimental investigations of flux and defect end states.

In Chapter 6, we considered a classical analog of a higher-order topological phase, inspired by the recently very fruitfully exploited equivalence of the physics of electronic band structures and coupled oscillators of any kind. A fundamental difference between classical topological systems (e.g., of mechanical degrees of freedom, electrical circuits, photonic metamaterials) and topological insulators built from fermions is that consequences of topology in the former are found in the excitations, while in the latter case – thanks to the Fermi sea brought about by the Pauli principle – it is the ground state which is nontrivial. For example, a fermionic electric quantum quadrupole insulator has a quantized bulk quadrupole moment that is in principle measurable – characteristic of its zero temperature ground state. (A more canonical example is the bulk Hall conductivity of an integer quantum Hall effect.) In contrast, topological boundary modes are in principle as accessible for measurements in classical as in fermionic quantum systems, since they correspond to spectrally isolated excitations. For this reason, we focused on the boundary characteristics of the topological circuit in Chapter 6. Nevertheless, venues for bulk measurements of the topological characteristics of classical systems have been suggested in photonic systems [246].

We showed in Chapter 7 that the nontrivial bulk topology of two-dimensional higher-order topological phases – mostly realized by obstructed atomic limits – can be revealed via charge fractionalization at boundaries. This represents the

simplest mechanism for a topological bulk-boundary correspondence protected by crystalline symmetries. We presented theory and material candidates for charge fractionalization at corners in 2D systems with significant spin-orbit coupling, thus providing a broader picture than the one presented in previous treatments of this phenomenon [90, 197, 32]. Diagnosing spinful OALs with time-reversal symmetry in 2D was particularly challenging because the irreducible representations of the occupied bands at high-symmetry points in momentum space are usually two-dimensional, yielding trivial C_2 symmetry indicator invariants. Symmetry indicators are therefore insufficient to identify the Wannier centers in C_2 , C_4 , and C_6 symmetric insulators. To overcome this difficulty, we considered Wilson loop and nested Wilson loop invariants, which could better resolve the positions of the Wannier centers. Wilson loops, however, are essentially one dimensional objects that extract projections of the 2D positions of the Wannier centers along particular directions. Nested Wilson loops are a best-effort attempt to localize the Wannier centers in 2D, but cannot always be interpreted literally due to the possible non-commutation of Wilson loops along different directions. In the presence of crystalline symmetries, Wilson and nested Wilson loops have eigenvalues with quantized phases, which clearly distinguish different OALs in C_2 and C_6 symmetric insulators, but are insufficient for insulators which only have C_4 symmetry. An interesting challenge for future work is finding a formula for the corner charge in C_4 -symmetric systems.

Chapter 8 examined the position-space structure of topological superconductors, motivated by the success of position-space reformulations of (higher-order) topological insulators, which have previously led to highly instructive notions such as that of the obstructed atomic limit (explored in Chapter 7). The mean-field description of superconductors is uncannily similar to the Bloch description of non-interacting electrons, enabling a remarkable amount of concept transfer and cross-fertilization between the descriptions of topological superconductors and insulators. However, it is often not clear what becomes of the physical interpretation of the mathematical quantities involved. An example is the Berry phase, which captures the electric polarization of an insulator, something that is evidently not well defined for superconductors. Employing a position-space picture phrased in terms of Cooper pairs and Majorana excitations, the results presented in Chapter 8 give physical meaning to the Berry phase in the superconducting context via the notion of pairing obstruction and Majorana polarization. A natural next step is the inclusion of time-reversal and crystalline symmetries into our framework, which will allow for a systematic treatment of topological crystalline superconductors, and enable a position-space based classification via their Cooper pair and Majorana Wannier functions akin to that of Topological Quantum Chemistry. Another area of potential future work is

to use our formalism to understand the peculiarities of number-conserving models of topological superconductors [247, 248, 249].

Finally, in Chapter 9, we demonstrated how one can construct an interacting bosonic version of a 2D higher-order topological phase protected by mirror symmetries, where protection means that the symmetry may not be broken either explicitly or spontaneously in order for gapless corner modes to be present. A natural future direction is the investigation of similar interacting bosonic models for 3D higher-order topological phases with hinge states.

Having reviewed the contents of the thesis, as well as the questions they raise, we now conclude with an outlook on the study of topological phases of matter in general. It can be said with some confidence that by now our understanding of the possible topological band structures of non-interacting electrons can be considered in many ways complete. Remaining open questions are for instance the diagnosis of band structures for which the known topological invariants fail (such as the C_4 -symmetric obstructed atomic limit discussed in Chapter 7), or a full classification of topological band structures in all 230 space groups. Nevertheless, the last few years have seen dramatic progress with regards to the characterization of topological band structures, and it seems reasonable to expect that our current picture will not be subject to qualitative modifications.

However, the notion of the order of a topological phase with respect to its boundary excitations, which we developed in this thesis, is more general than any particular realization, be it electronic band structures (Chapters 1–5, 7) or classical analog devices (Chapter 6). The concept applies equally well to topological superconductors (Chapter 8) and can be straightforwardly generalized to strongly correlated systems (Chapter 9). The latter class of systems provides a seemingly endless trove of emergent phenomena that expose the consequences of quantum mechanics in ways that are well beyond what the microscopic laws of nature would naively seem to allow for. We therefore expect that, in addition to finding practical applications of topological materials, the study of interacting topological phases of matter will take center stage in the future development of condensed matter physics.

Part V

Appendices

Appendix A

More on higher-order topological insulators

This is the appendix for Chapter 3.

A.1 Chiral higher-order TI tight-binding model

We consider a model on a simple cubic lattice spanned by the basis vectors e_i , $i = x, y, z$, with two orbitals $d_{x^2-y^2}$ (denoted $\alpha = 0$ below), and $f_{z(x^2-y^2)}$ ($\alpha = 1$) on each site, which is populated by spin 1/2 electrons. It is defined by the tight-binding Hamiltonian

$$\begin{aligned} H_c = & \frac{M}{2} \sum_{\mathbf{r}, \alpha} (-1)^\alpha c_{\mathbf{r}, \alpha}^\dagger c_{\mathbf{r}, \alpha} \\ & + \frac{t}{2} \sum_{\mathbf{r}, \alpha} \sum_{i=x,y,z} (-1)^\alpha c_{\mathbf{r}+e_i, \alpha}^\dagger c_{\mathbf{r}, \alpha} \\ & + \frac{\Delta_1}{2} \sum_{\mathbf{r}, \alpha} \sum_{i=x,y,z} c_{\mathbf{r}+e_i, \alpha+1}^\dagger \sigma_i c_{\mathbf{r}, \alpha} \\ & - \frac{\Delta_2}{2i} \sum_{\mathbf{r}, \alpha} \sum_{i=x,y,z} (-1)^\alpha n_i c_{\mathbf{r}+e_i, \alpha+1}^\dagger c_{\mathbf{r}, \alpha} + \text{h.c.}, \end{aligned} \quad (\text{A.1})$$

where α is defined modulo 2, $\mathbf{n} = (1, -1, 0)$, and $c_{\mathbf{r}, \alpha}^\dagger = (c_{\mathbf{r}, \alpha, \uparrow}^\dagger, c_{\mathbf{r}, \alpha, \downarrow}^\dagger)$ creates a spinor in orbital α at lattice site \mathbf{r} . We denote by σ_0 and σ_i , $i = x, y, z$, respectively, the 2×2 identity matrix and the three Pauli matrices acting on the spin 1/2 degree of freedom.

A.2 Chern-Simons topological invariant

A.2.1 Quantization from electromagnetic response

We first argue that the topological invariant for chiral HOTIs, the Chern-Simons (CS) form, is quantized for systems with $\mathcal{C}_4^z\mathcal{T}$ symmetry to evaluate to either 0 or π , just as in the case of \mathcal{T} symmetry alone (see also the discussion in Section 2.2.4). The CS form is given by

$$\theta = \frac{1}{4\pi} \int d^3k \epsilon_{abc} \text{tr} \left[A_a \partial_b A_c + i \frac{2}{3} A_a A_b A_c \right], \quad (\text{A.2})$$

written in terms of the non-Abelian Berry gauge field $A_{a;n,n'} = -i \langle u_n | \partial_a | u_{n'} \rangle$, where $|u_n\rangle$ are the Bloch eigenstates of the chiral HOTI Hamiltonian and the indices n, n' run over its filled bands.

To derive the quantization from the electromagnetic response, we consider the effective action quantifying the response to an external electromagnetic $U(1)$ field A_μ of a system with non-vanishing θ . The effective action is given by a contribution to the path integral in the form of the axion term

$$\exp \left[i \frac{\theta}{8\pi^2} \int d^3x dt \epsilon_{\mu\nu\sigma\tau} \partial_\mu A_\nu \partial_\sigma A_\tau \right]. \quad (\text{A.3})$$

Observe that

$$\frac{i}{8\pi^2} \int d^3x dt \epsilon_{\mu\nu\sigma\tau} \partial_\mu A_\nu \partial_\sigma A_\tau \quad (\text{A.4})$$

changes sign under a $\mathcal{C}_4^z\mathcal{T}$ transformation due to the anti-unitary nature of \mathcal{T} which takes $i \rightarrow -i$ (the axion term is otherwise rotationally invariant and therefore unaffected by \mathcal{C}_4^z). Furthermore, Equation (A.4) is a topological invariant, the second Chern number, which is quantized to integer values. Thus, for the theory to be invariant under \mathcal{T} or $\mathcal{C}_4^z\mathcal{T}$, $\theta = 0, \pi \bmod 2\pi$ is required. We conclude that θ serves as a topological invariant in $\mathcal{C}_4^z\mathcal{T}$ symmetric TIs, exactly as in \mathcal{T} symmetric ones. An alternative, more explicit proof can be found in the Supplementary Information of Reference [26].

A.2.2 Evaluation of the Chern-Simons invariant

Here, we calculate θ explicitly for the chiral HOTI model from Equation (3.1) in the main text, which in its topological phase is given by the representative parameter

choice $M = 2$,

$$\begin{aligned}\mathcal{H}_c(\mathbf{k}) = & \left(2 + \sum_i \cos k_i\right) \tau_z \sigma_0 + \sum_i \sin k_i \tau_y \sigma_i \\ & + \Delta_2 (\cos k_x - \cos k_y) \tau_x \sigma_0,\end{aligned}\quad (\text{A.5})$$

containing a \mathcal{T} breaking term proportional to Δ_2 . This Hamiltonian has a band inversion at $\mathbf{k}_0 = (\pi, \pi, \pi)$. Expanding around this point with $\mathbf{k} = \mathbf{k}_0 + \tilde{\mathbf{k}}$, we obtain

$$\mathcal{H}_c(\tilde{\mathbf{k}}) = -\tau_z \sigma_0 + \sum_i \tilde{k}_i \tau_y \sigma_i. \quad (\text{A.6})$$

We choose a gauge in which the normalized eigentstates of the two occupied bands are (to first order in $\tilde{\mathbf{k}}$)

$$\begin{aligned}u_1(\tilde{\mathbf{k}}) = & \frac{1}{f(\tilde{\mathbf{k}})} \left\{ \tilde{k}_x - i\tilde{k}_y, -\tilde{k}_z, 0, 0 \right\}, \\ u_2(\tilde{\mathbf{k}}) = & \frac{1}{f(\tilde{\mathbf{k}})} \left\{ +\tilde{k}_z, \tilde{k}_x + i\tilde{k}_y, 0, 0 \right\},\end{aligned}\quad (\text{A.7})$$

where we have defined the normalization $f(\tilde{\mathbf{k}}) = |\tilde{\mathbf{k}}|$. Note that for $\tilde{k}_z = 0$, we have $\frac{\tilde{k}_x - i\tilde{k}_y}{f(\tilde{\mathbf{k}})} = \frac{\tilde{k}_x - i\tilde{k}_y}{\sqrt{\tilde{k}_x^2 + \tilde{k}_y^2}}$. This expression, which occurs in both eigenstates, is multi-valued at $\tilde{\mathbf{k}} = 0$ [for instance, in the limit $(\tilde{k}_x \rightarrow 0, \tilde{k}_y = 0)$ it evaluates to 1, while for $(\tilde{k}_y \rightarrow 0, \tilde{k}_x = 0)$ it evaluates to i]. On the other hand, for an expansion around the other $\mathcal{C}_4^z \mathcal{T}$ invariant momenta $\mathbf{k}_0 \in \{(0, 0, 0), (\pi, \pi, 0), (0, 0, \pi)\}$, we obtain $f(\tilde{\mathbf{k}}) = \sqrt{4 + 3\tilde{\mathbf{k}}^2}$ and the eigenstates are well defined in the vicinity of these points.

Note that Equation (A.2) can be written as the integral of a total derivative which vanishes on the Brillouin zone torus (which has no boundary) as long as all functions are single-valued. Therefore, contributions to the CS form can be thought of as arising from points in momentum space where Bloch states in a given gauge are multi-valued. The resulting form of the Berry gauge field near $\mathbf{k}_0 = (\pi, \pi, \pi)$, expanded in the basis of Pauli matrices, is given by

$$\mathcal{A}(\tilde{\mathbf{k}}) = \frac{1}{|\tilde{\mathbf{k}}|^2} \tilde{\mathbf{k}} \wedge \begin{pmatrix} -\sigma_x \\ \sigma_y \\ \sigma_z \end{pmatrix} + \mathcal{O}(1), \quad (\text{A.8})$$

in which we recognize the gauge field of an $SU(2)$ monopole. As a result of this monopole, the CS form evaluates to $\theta = \pi$ independent of Δ_2 , i.e., even if \mathcal{T} symmetry is broken as long as $\mathcal{C}_4^z \mathcal{T}$ symmetry is preserved.

A.3 Topological characterization of chiral higher-order topological insulators with inversion symmetry

Note that the Hamiltonian given in Equation (3.1) in the main text is invariant under the combination of time-reversal and inversion symmetry \mathcal{IT} , with representations $\mathcal{I} = \tau_z \sigma_0$ and $\mathcal{T} = \tau_0 \sigma_y K$. This symmetry, which forces the bands to be two-fold degenerate at all \mathbf{k} , is not essential for the topological phase of the model, and may be broken by adding a perturbation $\delta \tau_x \sigma_0$ to the Hamiltonian, with δ a small real parameter. However, when \mathcal{IT} symmetry holds, we may formulate a topological index that simplifies the topological characterization.

To achieve this, the unitary symmetry $\mathcal{C}_4\mathcal{I}$ with matrix representation $S_{mn}(\mathbf{k}) = \langle u_m(\mathbf{k}) | \mathcal{C}_4\mathcal{I} | u_n(\mathbf{k}) \rangle$, where $|u_n(\mathbf{k})\rangle$ span the filled subspace, can be used in the same way inversion symmetry is used in Reference [5]. We can study the eigenvalues of $S(\mathbf{k})$ at the four high symmetry points

$$\mathbf{k} \in \mathcal{I}_{\mathcal{C}_4^z\mathcal{T}} = \{(0, 0, 0), (\pi, \pi, 0), (0, 0, \pi), (\pi, \pi, \pi)\}. \quad (\text{A.9})$$

Since $(\mathcal{C}_4\mathcal{I})^4 = -1$, the eigenvalues of $S(\mathbf{k})$ are the fourth roots of -1 . Due to $[\mathcal{C}_4\mathcal{I}, \mathcal{IT}] = 0$, and \mathcal{IT} being anti-unitary, they have to come in complex-conjugated pairs $\{\xi_k e^{i\pi/4}, \xi_k e^{-i\pi/4}\}$ with $\xi_k = +1$ or $\xi_k = -1$. The symmetry action of $\mathcal{C}_4\mathcal{I}$ on the filled subspace at a high symmetry point $\mathbf{k} \in \mathcal{I}_{\mathcal{C}_4^z\mathcal{T}}$ is then characterized by the set $\xi_{n,k}$, $n = 1, \dots, N/2$, where N is the number of filled bands.

We may therefore define the topological invariant in the presence of \mathcal{IT} symmetry as

$$(-1)^{\nu_c} = \prod_{n=1}^{N/2} \prod_{\mathbf{k} \in \mathcal{I}_{\mathcal{C}_4^z\mathcal{T}}} \xi_{n,k}, \quad (\text{A.10})$$

which resembles the Fu-Kane formula for inversion-symmetric TIs [1]. This invariant is well defined for the following reason: by the bulk-boundary correspondence of chiral HOTIs, when breaking \mathcal{T} but preserving $\mathcal{C}_4^z\mathcal{T}$, the band inversion which in the first-order TI case led to gapless surfaces now induces gapless channels along the hinges separating the x and y surfaces. To detect this phase transition, Fu and Kane have used a product over the inversion \mathcal{I} eigenvalues at the time-reversal invariant momenta, which should be -1 in the nontrivial case. Here, we do not have \mathcal{I} symmetry, but only $\mathcal{C}_4^z\mathcal{I}$, which we may however use in the very same way, as indicated in Equation (A.10). We prove this formula by adiabatically interpolating to the unperturbed case (with \mathcal{T} , \mathcal{C}_4^z , and \mathcal{I} symmetry), which can be done without a

bulk gap closing. In this situation, both the Fu-Kane formula and Equation (A.10) evaluate to the same result, i.e., the eigenvalues of $\mathcal{C}_4^z\mathcal{I}$ show the same inversion as those of \mathcal{I} for the following reason: the \mathcal{C}_4^z eigenvalues of the occupied bands at $(k_x, k_y) = (0, 0)$ and $(k_x, k_y) = (\pi, \pi)$ are well-defined for all k_z and—since the system is insulating—are independent of k_z . Thus, each Kramers pair of \mathcal{C}_4^z eigenvalues enters twice in the product in Equation (A.10), once at $k_z = 0$ and once at $k_z = \pi$. Thus, any possible inversion in the \mathcal{C}_4^z eigenvalues is rendered trivial by the product in Equation (A.10), and only the band inversions of \mathcal{I} enter. In particular, only the band inversions at the $\mathbf{k} \in \mathcal{I}_{\mathcal{C}_4^z\mathcal{T}}$ enter, as for all other points, \mathcal{C}_4 symmetry makes inversion eigenvalues come in pairs [e.g., $(0, \pi, 0)$ and $(\pi, 0, 0)$ have the same inversion eigenvalues].

More explicitly, if we denote by $\chi_{n,k}$ the inversion eigenvalues of band pair n at the time-reversal invariant momenta $\mathcal{I}_{\mathcal{T}}$, the following identity holds for a \mathcal{C}_4^z and \mathcal{T} invariant system:

$$\begin{aligned} \prod_n \prod_{\mathbf{k} \in \mathcal{I}_{\mathcal{T}}} \chi_{n,k} &= \prod_n \chi_{n,(0,0,0)} \chi_{n,(\pi,\pi,0)} \chi_{n,(0,0,\pi)} \chi_{n,(\pi,\pi,\pi)} \\ &= \prod_n \xi_{n,(0,0,0)}^2 \xi_{n,(\pi,\pi,0)}^2 \chi_{n,(0,0,0)} \chi_{n,(\pi,\pi,0)} \chi_{n,(0,0,\pi)} \chi_{n,(\pi,\pi,\pi)} \\ &= \prod_n (\xi_{n,(0,0,0)} \chi_{n,(0,0,0)}) (\xi_{n,(\pi,\pi,0)} \chi_{n,(\pi,\pi,0)}) (\xi_{n,(0,0,\pi)} \chi_{n,(0,0,\pi)}) (\xi_{n,(\pi,\pi,\pi)} \chi_{n,(\pi,\pi,\pi)}). \end{aligned} \quad (\text{A.11})$$

We used that $\xi_{n,k}^2 = 1$, $\prod_n \xi_{n,(0,0,0)} = \prod_n \xi_{n,(0,0,\pi)}$ and $\prod_n \xi_{n,(\pi,\pi,0)} = \prod_n \xi_{n,(\pi,\pi,\pi)}$ as well as $\prod_n \chi_{n,(\pi,0,k_z)} = \prod_n \chi_{n,(0,\pi,k_z)}$ for $k_z = 0, \pi$. The left-hand side of Equation (A.11) is exactly the Fu-Kane band inversion formula and the right-hand side is Equation (A.10). Since the right-hand side is also well-defined if only $\mathcal{C}_4^z\mathcal{T}$ is a symmetry, but not \mathcal{C}_4 and \mathcal{T} alone, and the two cases are connected without gap closing, it constitutes a well-defined invariant for this case. In the case of the model given by Equation (3.1) in the main text, there is a single inversion $\xi_{\mathbf{k}} = -1$ at $\mathbf{k} = (\pi, \pi, \pi)$ or $\mathbf{k} = (0, 0, 0)$ for $1 < M < 3$ or $-1 > M > -3$, respectively, confirming $\nu_c = -1$ in these parameter regimes.

A.4 Degeneracies in the chiral higher-order topological insulator bulk and Wilson loop spectra

Here we discuss the degeneracies in the chiral HOTI bulk and Wilson loop spectra enforced by $\mathcal{C}_4^z\mathcal{T}$. At the four $\mathcal{C}_4^z\mathcal{T}$ invariant momenta \mathbf{k} taken from $\mathcal{I}_{\mathcal{C}_4^z\mathcal{T}} =$

$\{(0, 0, 0), (\pi, \pi, 0), (0, 0, \pi), (\pi, \pi, \pi)\}$ the relation $(\mathcal{C}_4^z \mathcal{T})^4 = -1$ enforces a Kramers-like degeneracy: if we assume $\mathcal{C}_4^z \mathcal{T} |\psi\rangle = e^{i\alpha} |\psi\rangle$ for an energy eigenstate $|\psi\rangle$ at the high-symmetry points, applying $(\mathcal{C}_4^z \mathcal{T})^3$ from the left on this equation leads to the contradiction $|\psi\rangle = -|\psi\rangle$, hence a doublet must exist.

We now show that a similar degeneracy is induced in the band structure of the Wilson loop $W^z(k_x, k_y)$ (see Section 2.2.1) at the $\mathcal{C}_4^z \mathcal{T}$ invariant momenta $(k_x, k_y) = (0, 0)$ and $(k_x, k_y) = (\pi, \pi)$.

In general, $\mathcal{C}_4^z \mathcal{T}$ invariance implies

$$\mathcal{C}_4^z \mathcal{T} |u_n(\mathbf{k})\rangle = B_{nm}(\mathbf{k}) |u_m(D_{\mathcal{C}_4^z \mathcal{T}} \mathbf{k})\rangle, \quad (\text{A.12})$$

where $B_{nm}(\mathbf{k}) = \langle u_m(D_{\mathcal{C}_4^z \mathcal{T}} \mathbf{k}) | \mathcal{C}_4^z \mathcal{T} | u_n(\mathbf{k}) \rangle$ is the unitary sewing matrix that connects states at \mathbf{k} with those at $D_{\mathcal{C}_4^z \mathcal{T}} \mathbf{k}$ which have the same energy. Summation over repeated indices is implied here as well as below.

Since the filled subspace at all two-dimensional momenta (k_x, k_y) is invariant under $\mathcal{C}_4^z \mathcal{T}$, all projectors $P(\mathbf{k})$ that enter $W^z(k_x, k_y)$ commute with $\mathcal{C}_4^z \mathcal{T}$. Therefore, at the $\mathcal{C}_4^z \mathcal{T}$ -invariant momenta $(k_x, k_y) \in \{(0, 0), (\pi, \pi)\}$, $W^z(k_x, k_y)$ transforms under $\mathcal{C}_4^z \mathcal{T}$ as

$$W_{mn}^z(k_x, k_y) = B_{mi}(k_z = 0) [[W^z(k_x, k_y)]^{-1}]_{ij}^* [B^{-1}(k_z = 0)]_{jn}. \quad (\text{A.13})$$

When writing $W^z(k_x, k_y) = e^{i\mathcal{H}_W(k_x, k_y)}$, Equation (A.13) implies that $\mathcal{H}_W(k_x, k_y) = [B(\mathbf{k})K]\mathcal{H}_W(k_x, k_y)[B(\mathbf{k})K]^{-1}$, i.e., $B(\mathbf{k})K$ is an anti-unitary symmetry. Due to the relation $[B(\mathbf{k})K]^4 = -1$ for each \mathbf{k} [which can be derived by writing out $B_{mn}(\mathbf{k})$ as the matrix elements of $\mathcal{C}_4^z \mathcal{T}$ in the filled subspace], the eigenvalues of \mathcal{H}_W are degenerate for the $\mathcal{C}_4^z \mathcal{T}$ -invariant values of (k_x, k_y) by the same argument as above.

A.5 Nested boundary spectra: entanglement spectrum and Brillouin zone Wilson loop

In this section we study the boundary degrees of freedom of HOTIs. We focus on the chiral case as exemplified by $\mathcal{H}_c(\mathbf{k})$ given in Equation (3.1) of the main text. The most direct way to determine the boundary spectrum is to perform a *slab calculation*, where open instead of periodic boundary conditions are imposed in one direction (chosen to be x here). The slab Hamiltonian $\mathcal{H}_{\text{slab}}(k_y, k_z)$ has one less good momentum quantum number and its spectrum is gapless if the system

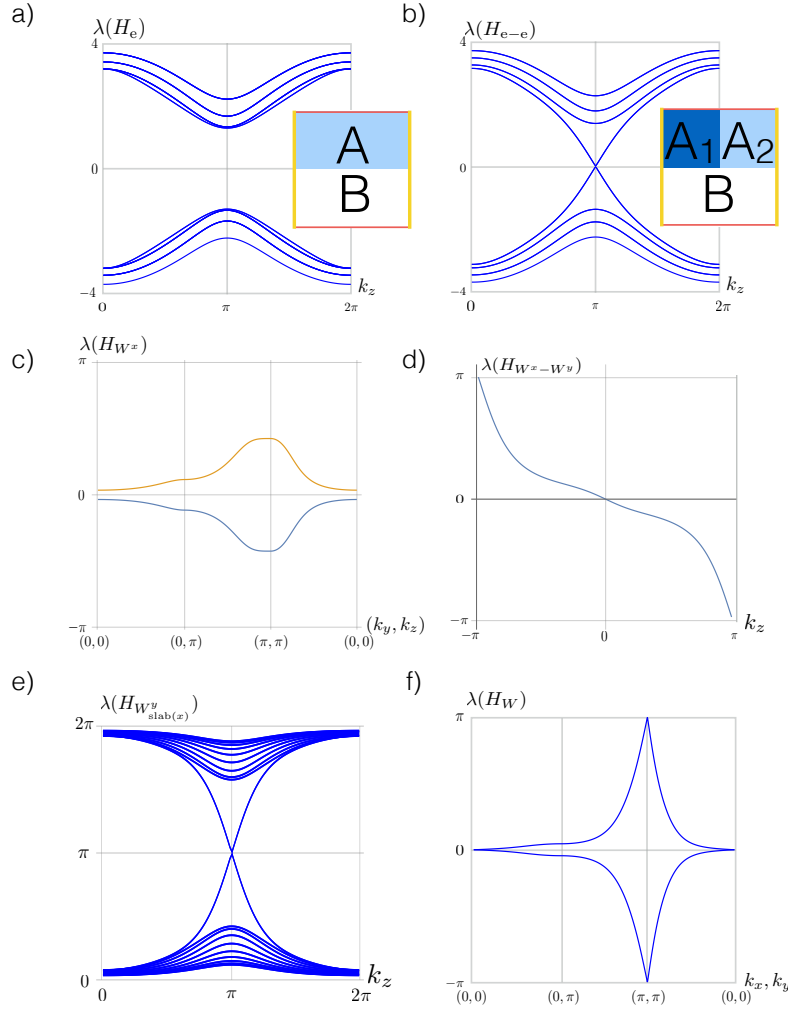


Figure A.1: Nested entanglement and Wilson loop spectra for the second-order 3D chiral TI model defined in Equation (3.1) in the main text with $M/t = 2$ and $\Delta_1/t = \Delta_2/t = 1$. (a) Gapped Entanglement spectrum of $H_e(k_y, k_z)$ for a bipartitioning of the system in the x - y -plane as shown in the inset. (b) Nested entanglement spectrum obtained from the ground state of the entanglement Hamiltonian $H_e(k_y, k_z)$ itself by further tracing out the subsystem A_2 . The chiral gapless modes, localized at the hinges of region A_1 reflect the presence of chiral hinge modes. (c) Eigenvalues of the Wilson loop Hamiltonian $H_W(k_y, k_z)$ in x -direction. The spectrum is gapped for all (k_y, k_z) , in accordance with the gapped surface spectrum of a second-order 3D TI. (d) Higher-order Berry phase spectrum defined by diagonalizing the nested, second-order Wilson loop Hamiltonian in the ‘‘filled’’ subspace of the gapped first-order Wilson loop Hamiltonian $H_W(k_y, k_z)$ along the k_y -direction, obtaining a Wilson-of-Wilson loop Hamiltonian that only depends on k_z . The nontrivial winding along k_z is in one-to-one correspondence with gapless hinge-excitations in the geometry of Figure 6.1 (a). (e) The same nontrivial winding can be obtained when computing the Wilson loop spectrum of the slab Hamiltonian of model (3.1). Being the Wilson loop of a slab, the number of bands is proportional to the linear system size (the thickness of the slab). (f) Non-nested z -direction Wilson loop spectrum.

is a first-order TI. In the following we employ two alternative approaches that allow us to infer information about the (topological) boundary spectrum of a bulk gapped Hamiltonian $\mathcal{H}(\mathbf{k})$ and hence about the topological bulk-boundary correspondence.

A.5.1 Nested entanglement spectrum

The single-particle *entanglement spectrum* [116] is the spectrum of the logarithm of the reduced density matrix ρ_A of a system that is obtained by subdividing the single-particle Hilbert space into two parts A and B and tracing out the degrees of freedom of B

$$\rho_A = \text{Tr}_B |\Psi\rangle\langle\Psi| \equiv \frac{1}{Z_e} e^{-\mathcal{H}_e}, \quad (\text{A.14})$$

where $|\Psi\rangle$ is the gapped many-body ground state of $\mathcal{H}(\mathbf{k})$. The last equality then defines the entanglement Hamiltonian \mathcal{H}_e , with normalization $Z_e = \text{Tr } e^{-\mathcal{H}_e}$. Here we are interested in a real-space cut separating regions A and B such that all lattice sites \mathbf{r} with $x > 0$ are in A , and B is the complement of A . In this case, k_y and k_z are good quantum numbers which label the blocks of \mathcal{H}_e as $\mathcal{H}_e(k_y, k_z)$. The entanglement spectrum [the spectrum of $\mathcal{H}_e(k_y, k_z)$] of a topological state has been shown to be in direct correspondence with the spectrum of the physical slab Hamiltonian for open boundary conditions in the x -direction [118]. In fact, for the model given in Equation (3.1) of the main text it is fully gapped [see Figure A.1 (a)].

To determine the presence of hinge modes for HOTIs, we introduce the *nested entanglement spectrum*. Consider a further subdivision of region A into parts A_1 and A_2 [right inset of Figure A.1 (b)]. Let $|\Psi_e\rangle$ be the gapped many-body ground state of $\mathcal{H}_e(k_y, k_z)$, where we consider half-filling. Note that half-filling here itself defines a subspace within the filled energy bands. In fact, the half-filled single particle entanglement spectrum bands physically correspond to the many-body ground state of the density matrix with half of the particles in region A and half of the particles in region B . The nested entanglement Hamiltonian $\mathcal{H}_{e-e}(k_z)$ on A_1 is then defined by

$$\text{Tr}_{A_2} |\Psi_e\rangle\langle\Psi_e| \equiv \frac{1}{Z_{e-e}} e^{-\mathcal{H}_{e-e}}. \quad (\text{A.15})$$

It has one less good momentum quantum number and is in correspondence with the spectrum of the slab with open boundary conditions in two directions, that is, with the spectrum of the physical system in the presence of a surface termination featuring hinges. The nested entanglement spectrum in Figure A.1 (b) shows the

gapless chiral hinge modes of \mathcal{H}_{e-e} (one located at each of the four hinges of region A_1).

A.5.2 Nested Wilson loop

Recall that the *Wilson loop* (along the k_x direction, for example) is an operator on the filled band subspace of $\mathcal{H}(\mathbf{k})$ defined as

$$W_{mn}^x(k_y, k_z) = \langle u_m(2\pi, k_y, k_z) | \prod_{k_x}^{2\pi \leftarrow 0} P(\mathbf{k}) | u_n(0, k_y, k_z) \rangle, \quad (\text{A.16})$$

where $|u_m(\mathbf{k})\rangle$ are the Bloch eigenstates of the Hamiltonian $\mathcal{H}(\mathbf{k})$, the indices m, n run over its filled bands, $P(\mathbf{k}) = |u_m(\mathbf{k})\rangle \langle u_m(\mathbf{k})|$ is the projector on the subspace of filled bands at momentum \mathbf{k} , and summation over repeated indices is implied here as well as below. The spectrum of $W^x(k_y, k_z)$ shares its topological features (such as protected boundary modes) with the physical slab Hamiltonian for open boundary conditions in the x -direction [84, 85]. Being a unitary operator, $W^x(k_y, k_z)$ can be written as $W^x(k_y, k_z) = e^{i\mathcal{H}_W(k_y, k_z)}$, where $\mathcal{H}_W(k_y, k_z)$ is a Hermitian operator called the Wilson loop Hamiltonian [86]. We observe from direct numerical computation for the chiral HOTI defined in Equation (3.1) that the spectrum of $W^x(k_y, k_z)$ is fully gapped, reflecting the gapped nature of the surface [see Figure A.1 (c)]. In fact, $\mathcal{H}_W(k_y, k_z)$ can be seen as a Hamiltonian for a 2D insulator. Explicit computation reveals that the half-filled subspace carries a nontrivial Chern number $C = \pm 1$.

We can now compute the Wilson loop spectrum of the Wilson loop Hamiltonian $\mathcal{H}_W(k_y, k_z)$, following the concept of nested Wilson loops introduced in Reference [86]. To do this, we first diagonalize the gapped Hamiltonian $\mathcal{H}_W(k_y, k_z)$ and evaluate a y -directed Wilson loop in its filled subspace. As a result, we obtain an effective one-dimensional system with good momentum quantum number k_z that shows the gapless, symmetry protected spectral flow of a Chern insulator [see Figure A.1 (d)].

Finally, Figure A.1 (f) exemplifies the non-trivial \mathbb{Z}_2 winding in the spectrum of the first-order (so non-nested) Wilson loop operator $W^z(k_x, k_y)$. The gapless spectrum of the Wilson loop $W^z(k_x, k_y)$ is also in correspondence with the gapless nature of the (001) surface of the model mentioned above. The connectivity of the Wilson loop bands between the the $\mathcal{C}_4^z\mathcal{T}$ -enforced Kramers pairs at momenta $(k_x, k_y) \in \{(0, 0), (\pi, \pi)\}$ is a \mathbb{Z}_2 topological invariant [84, 85]. In contrast to 3D TIs with \mathcal{T} symmetry, the Wilson loop spectrum has no Kramers degeneracies at momenta $(k_x, k_y) \in \{(0, \pi), (\pi, 0)\}$.

A.6 Bulk-surface-hinge correspondence for the helical higher-order TI

A.6.1 Constraints on mirror eigenvalues of domain wall modes in two-dimensional systems

In this subsection we discuss constraints on domain wall modes in strictly two-dimensional systems, that are imposed by mirror symmetry. Consider a two-dimensional system with a mirror symmetry that maps one half of the system (A) to the other (B). For concreteness, let us consider a spinful system with mirror eigenvalues $\pm i$, while noting that the proof also applies to spinless systems with mirror eigenvalues ± 1 . Let the system be insulating in either half and consider a situation, where along the line that is left invariant under the mirror symmetry, gapless bound states may propagate [see Figure A.2 (a)]. We will denote the mirror invariant line as *domain wall* and the two edges, which are mapped into each other by the mirror symmetry, as the *boundary* of the system. *We want to show that necessarily the number of right-movers (R) along the domain wall with mirror eigenvalues $+i$ equals the number of right-movers with mirror eigenvalue $-i$.* The same is true for the left-movers (L). Domain wall modes as shown in Figure A.2 (b) are then disallowed, where green and blue arrows denote mirror eigenvalues $+i$ and $-i$, respectively. These statements hold independent of whether or not the system is time-reversal symmetric. If present, time-reversal symmetry simply enforces the additional constraint that the number of right-movers with mirror eigenvalue $\pm i$ equals the number of left-movers with mirror eigenvalue $\mp i$.

We will first give a simple intuitive argument and then a more detailed technical proof. For concreteness, let the mirror symmetry M_x send $(x, y) \rightarrow (-x, y)$. Furthermore, let the system be translationally invariant with periodic boundary conditions along the y direction for simplicity [see Figure A.2 (a)]. All eigenstates of the mirror symmetric system, independent of their localization, can be labeled by mirror eigenvalues $\pm i$. We consider the spectrum in the $+i$ subspace and of the $-i$ subspace separately. Suppose now, we have one R mode with eigenvalue $+i$ at the domain wall, represented by the green arrow in Figure A.2 (c). As k_y is advanced by 2π , this chiral mode connects the valence and conduction band of the two-dimensional bulk, as shown in Figure A.2 (d). However, the total number of bands below the bulk gap has to be equal at $k_y = 0$ and $k_y = 2\pi$ for the spectrum to be periodic. This implies that there is one antichiral L mode (2) with the same mirror eigenvalue $+i$ in the system. Since by assumption this mode is not localized at the domain wall and the bulk is gapped, it needs to be localized at the system

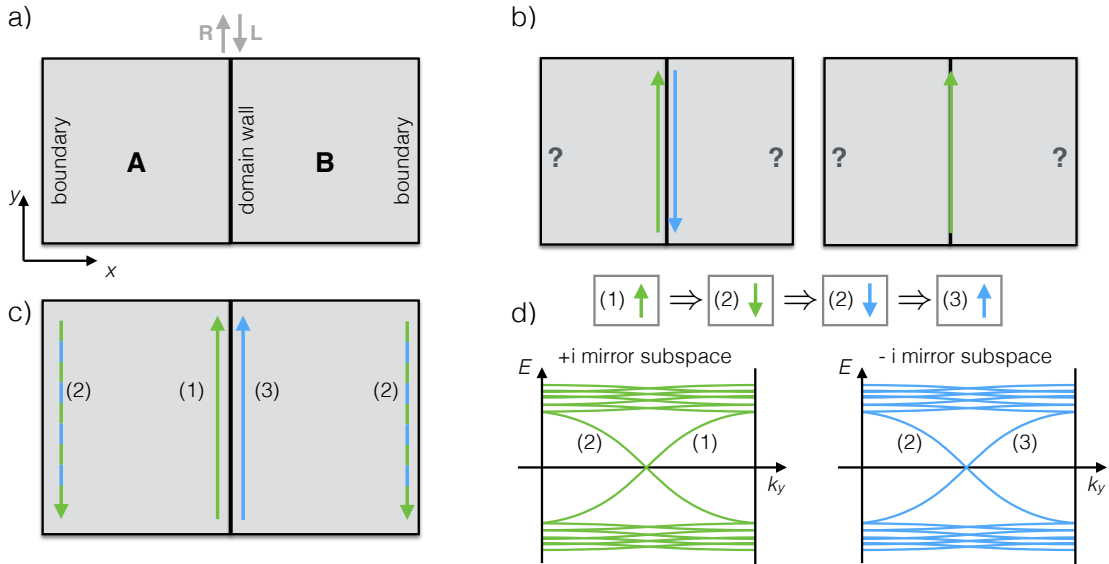


Figure A.2: (a) Domain wall geometry considered for the proof that there is no excess of mirror eigenvalue $+i$ chiral states moving chirally in definite direction along the domain wall. (b) These two configurations and any superposition thereof are not allowed in strictly two-dimensional systems. Green and blue arrows stand for modes with mirror eigenvalue $+i$ and $-i$, respectively. (c) The minimal allowed configuration with domain wall modes. (d) Logical chain of implications why the existence of mode (1) implies the existence of mode (3). Each implication is explained in the text. The first and third implication follow from the spectral continuity of the system as a function of k_y when periodic boundary conditions are imposed in the y direction: the number of bands of a given mirror eigenvalue below the Fermi level cannot change as k_y is advanced by 2π . Hence chiral modes at the domain wall must be compensated by antichiral modes at the boundary.

boundary. To be an eigenstate of mirror symmetry, it needs to be localized on both boundaries at the same time. However, since we cannot place ‘half’ of a mode on each boundary, there must be another gapless L mode (2), which is also localized on both boundaries and also a mirror eigenstate. Since we have already completed the band structure of the $+i$ mirror subspace with one R and one L gapless mode, this second L boundary mode must have $-i$ mirror eigenvalue. (Appropriate equal amplitude superpositions of the L modes with $+i$ and $-i$ mirror eigenvalues will give the L modes fully localized on only one side of the boundary.) By the argument of spectral continuity, the $-i$ mirror subspace cannot support a single L mode either. Rather, we conclude that there exists also a R mode (3) with mirror eigenvalue $-i$. We cannot split this mode up to be localized on both sides on the boundary (without also introducing an additional $+i$ R mode). Hence, the R mode (3) must be localized at the domain wall. Thus, via the chain of implications shown in Figure A.2 (d), we have argued that the existence of exactly one R mode at the domain wall with $+i$ mirror eigenvalue implies the existence of exactly one R mode at the domain wall with $-i$ mirror eigenvalue. This line of arguments carries over to any integer number of modes.

Let us now turn to a more technical elaboration on one aspect of the above argument: we want to show that each mode that is localized on the system boundary (not at the domain wall) with a specific mirror eigenvalue has a degenerate partner with the opposite mirror eigenvalue that is also localized at the boundary.

Boundary-localized modes with definite mirror eigenvalue (i.e., mirror eigenstates) have to have equal weight on both boundaries. Their nature can be understood as follows: boundary modes have support, up to exponentially small corrections, only near the two boundaries. Denote such an eigenstate of mirror eigenvalue $+i$ by

$$\psi_+(k_y) = [\psi_A(k_y), \psi_B(k_y)]^\top, \quad (\text{A.17})$$

where $\psi_A(k_y)$ [$\psi_B(k_y)$] is the part of the wave function that lives in the single particle Hilbert space of part A [B] of the system at given k_y . The mirror symmetry exchanges A and B and therefore has a representation of the form

$$M_x = i \begin{pmatrix} 0 & m_x \\ m_x^{-1} & 0 \end{pmatrix} \quad (\text{A.18})$$

with m_x unitary in order for M_x to be unitary.

Further, $\psi_+(k_y)$ is eigenstate of the Bloch Hamiltonian of the system

$$\mathcal{H}(k_y) = \begin{pmatrix} \mathcal{H}_{AA}(k_y) & \mathcal{H}_{AB}(k_y) \\ \mathcal{H}_{AB}(k_y)^\dagger & \mathcal{H}_{BB}(k_y) \end{pmatrix}. \quad (\text{A.19})$$

Here, $\mathcal{H}_{AB}(k_y)$ are terms in the Hamiltonian that couple parts A and B , i.e., local terms near the domain wall. Due to the localization properties of the boundary mode,

$$\mathcal{H}_{AB}(k_y)\psi_B(k_y), \quad \mathcal{H}_{AB}(k_y)^\dagger\psi_A(k_y), \quad (\text{A.20})$$

are exponentially small in the width of the system over the correlation length in the bulk of either part, compared to $\mathcal{H}_{BB}(k_y)\psi_B(k_y)$ and $\mathcal{H}_{AA}(k_y)\psi_A(k_y)$. As a consequence, $\psi_+(k_y)$ is (up to these exponential corrections) also an eigenstate of

$$\tilde{\mathcal{H}}(k_y) = \begin{pmatrix} \mathcal{H}_{AA}(k_y) & 0 \\ 0 & \mathcal{H}_{BB}(k_y) \end{pmatrix}. \quad (\text{A.21})$$

This in turn implies that $\psi_A(k_y)$ is an eigenstate of $\mathcal{H}_{AA}(k_y)$ and $\psi_B(k_y)$ is an eigenstate of $\mathcal{H}_{BB}(k_y)$, both with the same eigenvalue. Notice also that the mirror symmetry M_x in Equation (A.18) commutes with both $\mathcal{H}(k_y)$ and $\tilde{\mathcal{H}}(k_y)$.

Now, $\psi_+(k_y)$ is by assumption a mirror eigenstate with eigenvalue $+i$, i.e.,

$$\psi_A(k_y) = m_x \psi_B(k_y). \quad (\text{A.22})$$

Then, the state

$$\psi_-(k_y) = [\psi_A(k_y), -\psi_B(k_y)]^T, \quad (\text{A.23})$$

is an eigenstate of M_x with mirror eigenvalue $-i$ because

$$M_x \psi_-(k_y) = - \begin{pmatrix} m_x \psi_B(k_y) \\ -m_x^{-1} \psi_A(k_y) \end{pmatrix} = -\psi_-(k_y). \quad (\text{A.24})$$

Furthermore, by the above arguments $\psi_-(k_y)$ is an eigenstate of $\tilde{\mathcal{H}}(k_y)$ and thus also of $\mathcal{H}(k_y)$, with the same energy and chirality (R/L) as $\psi_+(k_y)$.

We have thus shown that for any mirror eigenstate localized at the system boundaries and of definite chirality R/L that has mirror eigenvalue $+i$ we can construct a degenerate state with the same chirality, but the opposite mirror eigenvalue. Then also the domain wall has to bind an equal number of chiral modes with mirror eigenvalue $+i$ and $-i$ that propagate in the R direction, for example. We denote this number by N_R . The same is true for the L direction, with an equal number of N_L modes in each mirror subspace. In a time-reversal breaking system, these two numbers N_R and N_L can in general differ and their difference is the Hall conductivity (in units of e^2/h) on the A side of the system, which differs by a minus sign from the Hall conductivity on the B side.

If in addition we consider a time-reversal symmetric system, the Hall conductivities have to vanish, and the number of $-i$ R modes equals the number of $+i$ L modes at

the domain wall. Thus, $N_L = N_R$, i.e., the number of R modes equals the number of L modes in the $+i$ sector. However, counter-propagating modes in a given sector can be gapped pairwise by local perturbations at the domain wall. Thus, all potentially existing modes in the $+i$ sector can generically gap. The same holds for the $-i$ sector. We conclude that the domain wall in a mirror and time-reversal symmetric two-dimensional system does not host any protected modes.

A.6.2 Correspondence between C_M and hinge modes

Here, we show that a non-vanishing mirror Chern number C_M pertaining to the mirror symmetry \mathcal{M}_{xy} implies the presence of $C_M/2$ Kramers pairs of hinge modes in a geometry terminated by the (100) and (010) surfaces.

We begin with a Hamiltonian that models the combination of $\mathcal{H}_{D,+}$ and $\mathcal{H}_{D,-}$ (which are defined in Equation (3.4) in the main text) on the surfaces with normals \mathbf{n}_+ and \mathbf{n}_- , respectively, which meet at a hinge as depicted in Figure 3.3 (c) in the main text. Denote by k_1 the in-plane momentum of the (110) surface that is perpendicular to k_z . The hinge is then modeled as a domain wall in the mass term $m(x_1)$, with x_1 the position conjugate to k_1 . We consider the effective Dirac Hamiltonian

$$\mathcal{H}(k_1, k_z) = v_1 k_1 \sigma_z + v_z k_z \sigma_x + m(x_1) \sigma_y, \quad (\text{A.25})$$

where we have chosen $k_1^{(0)} = k_z^{(0)} = 0$ as an expansion point. Since we want to find topologically protected hinge modes, we can choose $m(x_1) = \bar{m} \tanh(x_1/\lambda)$, as a smooth interpolation to represent the domain wall. Solving for a zero-energy state at $k_z = 0$, we find two solutions,

$$|\pm\rangle = f_{\pm}(x_1)(1, \pm 1)^T, \quad f_{\pm}(x_1) = \mathcal{N} [\cosh(x)]^{\mp \bar{m}\lambda/v_1}, \quad (\text{A.26})$$

where \mathcal{N} is a normalization constant. The solutions $|\pm\rangle$ have eigenvalues $\pm i$, respectively, under the mirror symmetry $\mathcal{M}_{xy} = i\sigma_x$ that sends $x_1 \rightarrow -x_1$. For a given solution to be normalizable, we require $\pm \frac{\bar{m}\lambda}{v_1} > 0$. Thus, for either choice of the sign of $\frac{\bar{m}\lambda}{v_1}$, exactly one solution is normalizable. To determine the chiral dispersion of the solution, we reinstate k_z and consider the energy shift to first order

$$\Delta E_{\pm} = \langle \pm | v_z k_z \sigma_x | \pm \rangle = \pm v_z k_z. \quad (\text{A.27})$$

From this we deduce that the domain wall either binds a R moving mode with mirror eigenvalue $i \text{sign}(v_z)$, or an L moving mode with mirror eigenvalue $-i \text{sign}(v_z)$, as claimed in the main text.

A.7 SnTe as a higher-order topological insulator

A.7.1 Tight-binding model with (110) strain

We consider a modification of a model describing the topological crystalline insulator [8] SnTe [9, 12]. SnTe forms a rocksalt lattice structure on top of which we consider a distortion due to uniaxial stress [see Figure 3.4 (a)] along the (110) direction modeled by a crystal field splitting parameter Δ . For pristine SnTe, we have $\Delta = 0$. Strained SnTe with $\Delta \neq 0$ has lower octahedral symmetry. The Hamiltonian

$$\begin{aligned} H_h = & m \sum_j (-1)^j \sum_{\mathbf{r}, s} \mathbf{c}_{j,s,\mathbf{r}}^\dagger \cdot \mathbf{c}_{j,s,\mathbf{r}} \\ & + \sum_{j,j'} t_{jj'} \sum_{(\mathbf{r}, \mathbf{r}'), s} \mathbf{c}_{j,s,\mathbf{r}}^\dagger \cdot \mathbf{d}_{\mathbf{r}, \mathbf{r}'} \mathbf{d}_{\mathbf{r}, \mathbf{r}'} \cdot \mathbf{c}_{j,s',\mathbf{r}'} + \text{h.c.} \\ & + i\lambda \sum_j \sum_{\mathbf{r}, s, s'} \mathbf{c}_{j,s,\mathbf{r}}^\dagger \times \mathbf{c}_{j,s',\mathbf{r}} \cdot \boldsymbol{\sigma}_{ss'} \\ & + \Delta \sum_j \sum_{\mathbf{r}, s} \left(c_{j,s,\mathbf{r}, p_x}^\dagger c_{j,s,\mathbf{r}, p_y} + c_{j,s,\mathbf{r}, p_y}^\dagger c_{j,s,\mathbf{r}, p_x} \right) \end{aligned} \quad (\text{A.28})$$

acts on the degrees of freedom on a rocksalt lattice structure [see Figure 3.4 (a)], of which Sn atoms ($j = 1$) and Te atoms ($j = 2$) each form one sublattice. The operators $c_{j,s,\mathbf{r}, p_i}^\dagger$, $i = x, y, z$, create an electron at lattice site \mathbf{r} , sublattice j , with spin $s = \uparrow, \downarrow$ in one of the three p orbitals p_x, p_y, p_z , and are combined into the spinor $\mathbf{c}_{j,s,\mathbf{r}}^\dagger = (c_{j,s,\mathbf{r}, p_x}^\dagger, c_{j,s,\mathbf{r}, p_y}^\dagger, c_{j,s,\mathbf{r}, p_z}^\dagger)$. The summation $(\mathbf{r}, \mathbf{r}')$ includes both nearest and next-nearest neighbor hopping and $\mathbf{d}_{\mathbf{r}, \mathbf{r}'}$ is the unit vector in the direction of the hopping process. We choose the parameters [250] $m = 1.65$ for the staggered sublattice potential, $t_{12} = t_{21} = 0.9$, $t_{11} = -t_{22} = 0.5$, for the nearest and next-nearest neighbor hopping amplitude, and $\lambda = 0.7$ for the strength of spin-orbit coupling. To disentangle the hinge electronic structure obtained with $\Delta = -0.4$, we furthermore apply an on-site chemical potential $|\mu_{\text{hinge}}| = 0.2$, which is nonvanishing only on the hinge sites, and has positive sign on the pair of sites invariant under the \mathcal{M}_{xy} mirror symmetry, and negative sign on the pair invariant under $\mathcal{M}_{x\bar{y}}$. This creates a difference in value between the xy hinge state eigenenergies and the $x\bar{y}$ hinge state eigenenergies.

In order to write down the corresponding Bloch Hamiltonian, we choose the lattice spacing $a = 1$ and define $m_{\text{Sn}} = -m_{\text{Te}} = 1.65$ to automatically incorporate the staggered sublattice potential. We also introduce the orbital angular momentum

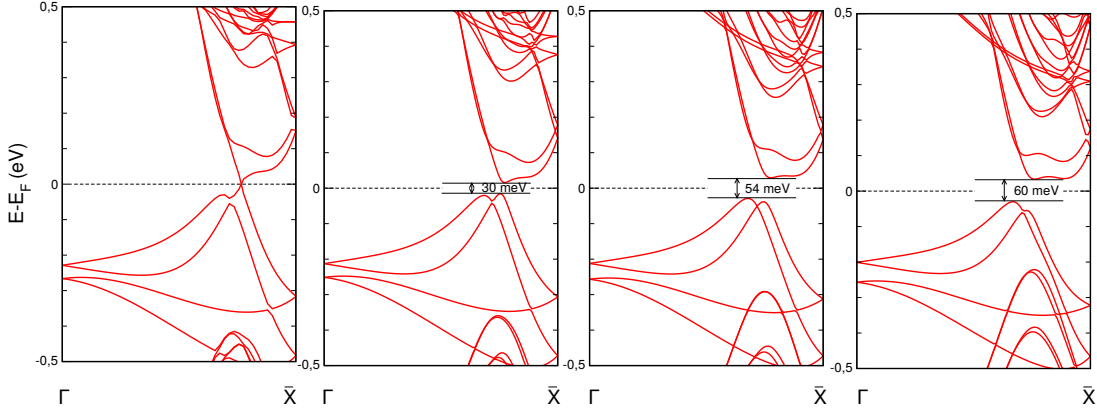


Figure A.3: Band structure of the surface Dirac cones of the topological crystalline insulator SnTe calculated in a slab geometry, from left to right: undistorted cubic phase with gapless Dirac cones, with 1%, 3%, and 5% strain along the (110) direction. The strain breaks the mirror symmetry that protects the Dirac cones and hence can open a gap.

operators

$$L_x = i \begin{pmatrix} 0 & 0 & 0 \\ 0 & 0 & -1 \\ 0 & 1 & 0 \end{pmatrix}, \quad L_y = i \begin{pmatrix} 0 & 0 & 1 \\ 0 & 0 & 0 \\ -1 & 0 & 0 \end{pmatrix}, \quad (A.29)$$

$$L_z = i \begin{pmatrix} 0 & -1 & 0 \\ 1 & 0 & 0 \\ 0 & 0 & 0 \end{pmatrix},$$

as well as the hopping matrices $T_i = \mathbf{d}_i \otimes \mathbf{d}_i$, $i \in \{x, y, z, xy, x\bar{y}, xz, x\bar{z}, yz, y\bar{z}\}$, where

$$\begin{aligned} \mathbf{d}_x &= (1, 0, 0), & \mathbf{d}_y &= (0, 1, 0), & \mathbf{d}_z &= (0, 0, 1), \\ \mathbf{d}_{xy} &= (1, 1, 0)/2, & \mathbf{d}_{x\bar{y}} &= (1, -1, 0)/2, \\ \mathbf{d}_{xz} &= (1, 0, 1)/2, & \mathbf{d}_{x\bar{z}} &= (1, 0, -1)/2, \\ \mathbf{d}_{yz} &= (0, 1, 1)/2, & \mathbf{d}_{y\bar{z}} &= (0, 1, -1)/2. \end{aligned} \quad (A.30)$$

The on-site Hamiltonian is then given by

$$\mathcal{H}_j^{\text{os}} = m_j + \lambda \sum_{\alpha=1}^3 L_\alpha \otimes \sigma_\alpha, \quad j \in \{\text{Sn, Te}\}, \quad (A.31)$$

and the \mathbf{k} -independent part of the full Hamiltonian reads

$$\mathcal{H}_0 = \begin{pmatrix} \mathcal{H}_{\text{Sn}}^{\text{os}} & t_{12} T_x^\dagger \\ t_{21} T_x & \mathcal{H}_{\text{Te}}^{\text{os}} \end{pmatrix}. \quad (A.32)$$

We may then set up the hopping matrices ($j \in \{1, 2\}$)

$$\begin{aligned}\mathcal{H}_{jj}^{xy}(\mathbf{k}) &= t_{jj} (e^{ik_x} T_{xy} + e^{i(k_z - k_y)} T_{x\bar{y}}), \\ \mathcal{H}_{jj}^{xz}(\mathbf{k}) &= t_{jj} (e^{ik_z} T_{xz} + e^{i(k_x - k_y)} T_{x\bar{z}}), \\ \mathcal{H}_{jj}^{yz}(\mathbf{k}) &= t_{jj} (e^{ik_y} T_{yz} + e^{i(k_x - k_z)} T_{y\bar{z}}), \\ \mathcal{H}_{12}^{xy}(\mathbf{k}) &= t_{12} (e^{i(k_x + k_z - k_y)} T_x + e^{ik_x} T_y), \\ \mathcal{H}_{21}^{xy}(\mathbf{k}) &= t_{21} e^{i(k_y - k_z)} T_y, \\ \mathcal{H}_{12}^z(\mathbf{k}) &= t_{12} e^{i(k_z)} T_z, \\ \mathcal{H}_{21}^z(\mathbf{k}) &= t_{21} e^{i(k_y - k_x)} T_z,\end{aligned}\tag{A.33}$$

in order to define

$$\mathcal{H}_1(\mathbf{k}) = \begin{pmatrix} \mathcal{H}_{11}^{xy}(\mathbf{k}) + \mathcal{H}_{11}^{xz}(\mathbf{k}) + \mathcal{H}_{11}^{yz}(\mathbf{k}) & \mathcal{H}_{12}^{xy}(\mathbf{k}) + \mathcal{H}_{12}^z(\mathbf{k}) \\ \mathcal{H}_{21}^{xy}(\mathbf{k}) + \mathcal{H}_{21}^z(\mathbf{k}) & \mathcal{H}_{22}^{xy}(\mathbf{k}) + \mathcal{H}_{22}^{xz}(\mathbf{k}) + \mathcal{H}_{22}^{yz}(\mathbf{k}) \end{pmatrix}. \tag{A.34}$$

The full Bloch Hamiltonian is then given by

$$\mathcal{H}(\mathbf{k}) = \mathcal{H}_0 + \mathcal{H}_1(\mathbf{k}) + \mathcal{H}_1(\mathbf{k})^\dagger. \tag{A.35}$$

Diagonalizing the Hamiltonian in the geometry described above with $\Delta \neq 0$ reveals a fully gapped electronic structure, except at the hinges [see Figure 3.4 (c)], where one Kramers pair of gapless modes is localized at each hinge. It is worth noting that there are ‘flat-band’ hinge states connecting the k_z projections of the surface Dirac cones already for $\Delta = 0$ [see inset of Figure 3.4 (c)], reminiscent of the ‘flat-band’ states at the zig-zag edge of graphene and states bound to the surface step edges of topological crystalline insulators [122]. With these ‘flat-band’ states, undistorted SnTe may be viewed as a higher-order topological semimetal.

A.8 First-principle calculations

We employed density functional theory (DFT) as implemented in the Vienna Ab Initio Simulation Package (VASP) [251, 252, 253, 254]. The exchange correlation term is described according to the Perdew-Burke-Ernzerhof (PBE) prescription together with projected augmented-wave pseudopotentials [255, 256]. For the autoconsistent calculations we used a $12 \times 12 \times 12$ \mathbf{k} -points mesh for the bulk and $7 \times 7 \times 1$ for the slab calculations.

For the electronic structure of SnTe with (110) distortion, the kinetic energy cut off was set to 400 eV. We calculated the surface states by using a slab geometry along the (100) direction. Due to the smallness of the band gap induced by strain, we needed to achieve a negligible interaction between the surface states from both sides of the slab (to avoid a spurious gap opened by the creation of bonding and anti-bonding states from the top and bottom surface states). To reduce the overlap between top and bottom surface states, we considered a slab of 45 layers, 1 nm vacuum thickness and artificially localized the states on one of the surfaces. The latter was done by adding one layer of hydrogen to one of the surfaces.

To obtain the electronic structure of bulk SnTe with (111) ferroelectric distortion, the cutoff energy for wave-function expansion was set to 500 eV. We use the parameter λ introduced in Reference [120] to parameterize a path linearly connecting the cubic structure (space group $Fm\bar{3}m$) to the rhombohedral structure (space group $R\bar{3}m$). Our calculations are focused on the $\lambda = 0.1$ structure. Then, to obtain the hinge electronic structure, we first constructed the maximally-localized Wannier functions (WFs) from the bulk ab-initio calculations. These WFs were used in a Green's function calculation for a system finite in a direction, semi-infinite in b direction and periodic in c direction (a , b , c are the conventional lattice vectors in space group $R\bar{3}m$). The hinge state spectrum is obtain by projecting on the atoms at the corner, which preserve the mirror symmetry \mathcal{M}_{xy} .

A.8.1 Surface gaps from DFT

Figure A.3 shows the evolution of the surface Dirac cones under uniaxial strain along the (110) direction. 1% strain is sufficient to open a gap of 30 meV which might be enough to detect hinge states in this gap. All four cones on the (100) and (010) surfaces are symmetry-equivalent with respect to this strain direction. For this reason it is sufficient to study one of them.

Appendix B

More on bismuth

This is the appendix for Chapter 4.

B.1 Bulk-boundary correspondence

In this section, we derive the bulk-surface-hinge correspondence for a HOTI with TRS, \mathcal{C}_3 rotation, and \mathcal{I} . To that end, we consider a Dirac model representation of a HOTI based on the Bernevig-Hughes-Zhang (BHZ) model for 3D topological insulators [110]. Our model corresponds to a continuum limit of the tight-binding model considered in the next section (when expanded around the T point in the Brillouin zone) and shares all relevant topological features with elementary bismuth. It has eight bands and is written in the orbital basis $\{|p_- \uparrow\rangle, |d_- \downarrow\rangle, |p_+ \downarrow\rangle, |d_+ \uparrow\rangle, |p_+ \uparrow\rangle, |d_+ \downarrow\rangle, |p_- \downarrow\rangle, |d_- \uparrow\rangle\}$, where $p_\pm = p_x \pm ip_y$ and $d_\pm = d_{xy} \pm id_{x^2-y^2}$. We are interested in preserving \mathcal{C}_3 rotation symmetry around the z axis (our spin quantization axis). It is represented as

$$\mathcal{C}_3^z = e^{-i\frac{2\pi}{3}s}, \quad s = \text{diag} \left(\frac{1}{2}, \frac{5}{2}, -\frac{1}{2}, -\frac{5}{2}, \frac{3}{2}, \frac{3}{2}, -\frac{3}{2}, -\frac{3}{2} \right). \quad (\text{B.1})$$

Inversion and TRS are represented by $\mathcal{I} = \sigma_0 \otimes \sigma_0 \otimes \sigma_3$ (since p and d orbitals have opposite inversion eigenvalues) and $\mathcal{T} = \sigma_0 \otimes \sigma_2 \otimes \sigma_0 K$, where K denotes complex conjugation, σ_0 the 2×2 identity matrix, and $\sigma_1, \sigma_2, \sigma_3$ the three Pauli matrices. Here, the tensor product is defined such that $\text{diag}(\sigma_3 \otimes \sigma_0 \otimes \sigma_0) = (1, 1, 1, 1, -1, -1, -1, -1)$.

The Hamiltonian for two \mathcal{C}_3 eigenspaces which are (as of yet) not connected is given by

$$H(\mathbf{k}) = H_1(\mathbf{k}) \oplus H_3(\mathbf{k}), \quad (\text{B.2})$$

where \mathbf{k} is measured from the T point in the BZ, and the blocks are defined as

$$H_j(\mathbf{k}) = \begin{pmatrix} M(\mathbf{k}) & A_j k_+^j & 0 & \tilde{A} k_z \\ A_j k_-^j & -M(\mathbf{k}) & \tilde{A} k_z & 0 \\ 0 & \tilde{A} k_z & M(\mathbf{k}) & -A_j k_-^j \\ \tilde{A} k_z & 0 & -A_j k_+^j & -M(\mathbf{k}) \end{pmatrix}, \quad (\text{B.3})$$

for $j = 1, 3$. Here $k_{\pm} = k_x \pm i k_y$ and $M(\mathbf{k}) = M_0 - M_1 \mathbf{k}^2$. M_0 , M_1 and \tilde{A} are free parameters, which we choose to be equal in both \mathcal{C}_3 eigenspaces for simplicity. For the same reason, we only consider the case $A_1 = A_3 \equiv A$ in this section. We also make the choice $\text{diag}(1, -1, 1, -1)$ for the matrix multiplying the function $M(\mathbf{k})$ without loss of generality. In $H_1(\mathbf{k})$ we recognize the BHZ model. To motivate this ansatz, consider for example the matrix element

$$\langle p_- \uparrow | H(\mathbf{k}) | d_- \downarrow \rangle = \langle p_- \uparrow | (\mathcal{C}_3^z)^{-1} H(\mathcal{C}_3^z \mathbf{k}) \mathcal{C}_3^z | d_- \downarrow \rangle = e^{-i\frac{4\pi}{3}} \langle p_- \uparrow | H(\mathcal{C}_3^z \mathbf{k}) | d_- \downarrow \rangle, \quad (\text{B.4})$$

where \mathcal{C}_3 symmetry requires that (to lowest order) it has to be proportional to either k_+ , which satisfies $\mathcal{C}_3 k_+ = e^{-i\frac{2\pi}{3}} k_+$, or k_-^2 , which satisfies $\mathcal{C}_3 k_-^2 = e^{i\frac{4\pi}{3}} k_-^2$, i.e., \mathcal{C}_3^z -symmetry requires this matrix element to be proportional to k_+^n with $n = 1 \pmod{3}$. Since p (d) orbitals are odd (even) under inversion, we are restricted to odd powers of k by inversion symmetry, therefore only k_+ is admissible. Likewise, this off-diagonal coupling has to be modified to k_+^3 in $H_3(\mathbf{k})$ due to inversion symmetry and the specific representation of \mathcal{C}_3 in Equation (B.1).

Each Hamiltonian block has a band inversion at $\mathbf{k} = 0$ and thus the full model represents a HOTI as we showed in the main text. In the case of bismuth, were the band inversion happens at the T point, \mathbf{k} should be understood as the momentum measured from that point. When discussing the bulk-boundary correspondence we will introduce couplings between the two blocks $H_1(\mathbf{k})$ and $H_3(\mathbf{k})$.

To analytically solve for the hinge modes, we consider Hamiltonian (B.2) on a cylinder of radius r_0 with the cylinder axis parallel to z . Each of the independent blocks of Hamiltonian (B.2) is a 3D TI and should thus support one Dirac cone on the surface. We will first solve for these Dirac states and then gap them out via mutual coupling. We will show that for this coupling term to comply with the symmetry requirements it has to have zeros along six lines on the cylinder surface that run parallel to z and correspond to the hinge states. Note that while the geometry that we chose is a cylinder with continuous rotational symmetry, the Hamiltonian (B.2) has only \mathcal{C}_6 rotational symmetry. First, we only solve for the states that form the degeneracy point of the surface Dirac electrons, i.e., those with vanishing transversal momentum on the surface. We thus set $k_z = 0$ and

replace $k_+ \rightarrow -ie^{i\phi}\partial_\rho$, where $r \equiv r_0 + \rho$ is the radial coordinate of the cylinder, and ϕ the angular coordinate. A domain wall between the topologically nontrivial sample and the vacuum is realized by setting $M_0 \rightarrow M_0(\rho) = \bar{M} \operatorname{sgn} \rho$. We can set $M_1 = 0$ for the purpose of solving for surface states. The Hamiltonian $H = H_1 \oplus H_3$ is then composed of

$$H_j = \begin{pmatrix} h_j & 0 \\ 0 & h_j^* \end{pmatrix}, \quad h_j = \begin{pmatrix} \bar{M} \operatorname{sgn} \rho & A(-i)^j e^{ij\phi} \partial_\rho^j \\ A(-i)^j e^{-ij\phi} \partial_\rho^j & -\bar{M} \operatorname{sgn} \rho \end{pmatrix}. \quad (\text{B.5})$$

Each H_j has two normalizable zero-energy solutions,

$$|v_j\rangle = a_j \begin{pmatrix} 1 \\ i^j e^{-ij\phi} \operatorname{sgn} \frac{\bar{M}}{A} \\ 0 \\ 0 \end{pmatrix}, \quad |w_j\rangle = a_j \begin{pmatrix} 0 \\ 0 \\ 1 \\ (-i)^j e^{ij\phi} \operatorname{sgn} \frac{\bar{M}}{A} \end{pmatrix}, \quad (\text{B.6})$$

with $a_j \equiv e^{-|\frac{\bar{M}}{A}|^{\frac{1}{j}} |\rho|}$. In combination, H has four normalizable zero-energy solutions. When reintroducing k_z and the surface (angular) momentum conjugate to ϕ , these zero-energy states disperse as a pair of surface Dirac cones, as is expected from having a strong topological insulator in each of the two \mathcal{C}_3 subspaces. However, we can gap out these two Dirac cones by introducing a coupling between them without breaking TRS. Requiring in addition \mathcal{C}_3 and \mathcal{I} to be preserved then imposes constraints on the real space dependence of a possible mass term $M_s(\phi)$ on the surface of the cylinder.

Let us first focus on the local constraints on such a mass term. In order to gap out the surface Dirac cones, M_s should anticommute with all the surface kinetic terms that multiply the two transverse momenta on the surface. Further, M_s should couple different \mathcal{C}_3 subspaces, i.e., it must be proportional to $\sigma_i \otimes \sigma_\mu \otimes \sigma_\nu$ with $i = 1, 2$ when written in the original basis of Hamiltonian (B.2). Any other choice of $i = 0, 3$ would not couple the two distinct time-reversal symmetric \mathcal{C}_3 subspaces. M_s should also be TRS. Finally, M_s should anticommute with the bulk mass term involving M in Equation (B.2), which is proportional to $\sigma_0 \otimes \sigma_0 \otimes \sigma_3$. Otherwise it represents a competing mass and results in a gapless region near the surface.

Taking all the local restrictions into account, we find that the only allowed surface mass term is of the form

$$M_s(\phi) = m(\phi) \sigma_2 \otimes \sigma_0 \otimes \sigma_2 + \tilde{m}(\phi) \sigma_2 \otimes \sigma_3 \otimes \sigma_1, \quad (\text{B.7})$$

where we discarded a possible ρ -dependence that is unaffected by the above restrictions. We now impose \mathcal{C}_3 symmetry. It transforms the matrices in Equation (B.7) as

$$\begin{aligned}\mathcal{C}_3^z(\sigma_2 \otimes \sigma_0 \otimes \sigma_2)(\mathcal{C}_3^z)^{-1} &= \cos \frac{2\pi}{3} \sigma_2 \otimes \sigma_0 \otimes \sigma_2 - \sin \frac{2\pi}{3} \sigma_2 \otimes \sigma_3 \otimes \sigma_1, \\ \mathcal{C}_3^z(\sigma_2 \otimes \sigma_3 \otimes \sigma_1)(\mathcal{C}_3^z)^{-1} &= \cos \frac{2\pi}{3} \sigma_2 \otimes \sigma_3 \otimes \sigma_1 + \sin \frac{2\pi}{3} \sigma_2 \otimes \sigma_0 \otimes \sigma_2.\end{aligned}\quad (\text{B.8})$$

In addition, both matrices in Equation (B.7) anticommute with inversion. To maintain \mathcal{C}_3 symmetry, we require

$$\mathcal{C}_3^z M_s(\phi)(\mathcal{C}_3^z)^{-1} = M_s \left(\phi + \frac{2\pi}{3} \right). \quad (\text{B.9})$$

This means that to lowest order the allowed harmonics of the coefficients $m(\phi)$ and $\tilde{m}(\phi)$ in ϕ that are compatible with \mathcal{C}_3^z and \mathcal{I} symmetry are given by

$$\begin{aligned}m(\phi) &= m'' \sin(\phi) + m' \cos(\phi), \\ \tilde{m}(\phi) &= -m' \sin(\phi) + m'' \cos(\phi),\end{aligned}\quad (\text{B.10})$$

with arbitrary real coefficients m' and m'' . Without loss of generality we may choose $m'' = 0$ (which amounts to fixing an origin for ϕ so that $\phi = 0$ corresponds to the x -direction). We can now project the corresponding mass term in the basis of surface Dirac states,

$$\begin{aligned}\langle v_1 | M_s(\phi) | v_3 \rangle &\propto -e^{-i4\phi}(e^{i6\phi} - 1), \\ \langle w_1 | M_s(\phi) | w_3 \rangle &\propto e^{-i2\phi}(e^{i6\phi} - 1),\end{aligned}\quad (\text{B.11})$$

with all matrix elements not related to these by hermiticity vanishing. Importantly, the mass projected into the surface states vanishes at exactly six equally spaced angles due to the prefactor $(e^{i6\phi} - 1)$. Expanding around, for instance, $\phi = 0$, we have $\langle v_1 | M_s(\phi) | v_3 \rangle = \langle w_1 | M_s(\phi) | w_3 \rangle \sim \phi$. Thus, the surface mass has a domain wall located at $\phi = 0$ at which it changes sign. By \mathcal{C}_3 together with \mathcal{I} the same is true at all ϕ of the form $\phi = \frac{2\pi}{3}n$, $n = 0, \dots, 5$. Since a domain wall in the mass of a pair of 2D TRS Dirac fermions binds a Kramers pair of gapless modes, the model represented by $H(\mathbf{k})$ has a helical pair of gapless modes at each of the hinges in a hexagonal real-space geometry that preserves \mathcal{C}_3 and \mathcal{I} , while the surfaces are gapped. This constitutes the second-order bulk-boundary correspondence of the HOTI.

Instead of considering a mass in real space, we can also gap out the surface Dirac cones due to the Hamiltonian in Equation (B.2) by adding a momentum-dependent

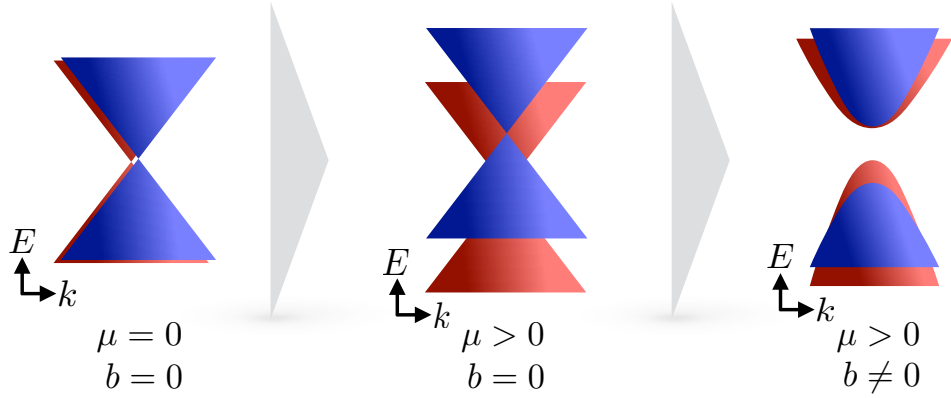


Figure B.1: Effect of the surface mass term in Equation (B.13) on the two Dirac cones on the (001) surface of the continuum model given by Equation (B.2). Since initially both cones are centered at the projection of the bulk BZ T point onto the surface BZ, which is invariant under C_3 symmetry, they cannot be directly gapped out due to their different C_3 eigenvalues. However, after a relative shift in energy effected by a finite μ in Equation (B.13), we can gap out the resulting nodal line.

mass term to the bulk theory. The corresponding bulk Hamiltonian reads

$$H_1(\mathbf{k}) \oplus H_3(\mathbf{k}) + \begin{pmatrix} 0 & H_{M_\rho}(\mathbf{k}) \\ H_{M_\rho}(\mathbf{k})^\dagger & 0 \end{pmatrix}, \quad H_{M_\rho}(\mathbf{k}) = \begin{pmatrix} -\bar{a} k_+^2 & 0 & 0 & 0 \\ 0 & -ak_-^2 & 0 & 0 \\ 0 & 0 & ak_-^2 & 0 \\ 0 & 0 & 0 & \bar{a} k_+^2 \end{pmatrix}, \quad (\text{B.12})$$

where a is a complex number that, when non-vanishing, gaps out the surface Dirac cones in the cylindrical geometry described above almost everywhere, leaving behind six propagating hinge modes compatible with C_3 and \mathcal{I} symmetry.

Finally, we discuss the case of open boundary conditions in the z -direction. In several other HOTIs protected by a rotational symmetry, surfaces with normal parallel to the rotation axis are gapless [26, 31]. In contrast, for the case at hand the z -surface can be gapped. A subtlety arises from the fact that the two Dirac cones on this surface cannot be gapped by a straightforward Dirac mass term, because of a mismatch in rotation eigenvalue in the two subspaces with C_3 eigenvalues -1 and $\exp(\pm i\pi/3)$. However, a combination of a relative energy shift between the two subspaces and a mass term that vanishes at the Dirac node can induce a gap [257] (see Figure B.1). The correspondingly perturbed Hamiltonian

reads

$$H_1(\mathbf{k}) \oplus H_3(\mathbf{k}) + \begin{pmatrix} \mu \sigma_0 \otimes \sigma_0 & H_{M_z}(\mathbf{k}) \\ H_{M_z}(\mathbf{k})^\dagger & -\mu \sigma_0 \otimes \sigma_0 \end{pmatrix},$$

with $H_{M_z}(\mathbf{k}) = \begin{pmatrix} 0 & 0 & 0 & -ibk_- \\ 0 & 0 & i \bar{b}k_+ & 0 \\ 0 & -i \bar{b}k_+ & 0 & 0 \\ ibk_- & 0 & 0 & 0 \end{pmatrix}$, (B.13)

where b is another complex number. Therefore, the full HOTI bulk Dirac theory, where all surfaces are gapped in the open geometry of a hexagonal prism, and only hinge modes remain, reads

$$H_D(\mathbf{k}) = H_1(\mathbf{k}) \oplus H_3(\mathbf{k}) + \begin{pmatrix} \mu & H_{M_\rho}(\mathbf{k}) + H_{M_z}(\mathbf{k}) \\ H_{M_\rho}(\mathbf{k})^\dagger + H_{M_z}(\mathbf{k})^\dagger & -\mu \end{pmatrix}. \quad (\text{B.14})$$

B.2 Tight-binding model

In addition to the Dirac model, we also provide a tight-binding model for a HOTI. It is defined on the simple hexagonal lattice spanned by the lattice vectors $\mathbf{a}_1 = (1, 0, 0)$, $\mathbf{a}_2 = (-1/2, \sqrt{3}/2, 0)$, and $\mathbf{a}_3 = (0, 0, 1)$, see Figure B.2 (a) for the lattice structure. At each site of the lattice we place a p_x , a p_y , a d_{xy} , and a $d_{x^2-y^2}$ orbital, each of which has two spin states. This gives eight local fermionic degrees of freedom per unit cell. Note that this does not correspond to the case of bismuth, which has 16 relevant inequivalent local fermionic degrees of freedom per primitive unit cell and 48 degrees of freedom in the conventional unit cell [137]. However, our tight-binding model has the very same bulk topology as bismuth, which we obtained from DFT calculations and topological quantum chemistry, and which furthermore agrees with the bulk topology of the realistic tight-binding model [137]. As we want to probe the topological features of bismuth, it is therefore sufficient to study the simpler model used here as long as this condition of topological equivalence is

met. The model is defined via the eight-band Bloch Hamiltonian

$$\begin{aligned}
H_{\text{TB}}(\mathbf{k}) &= \begin{pmatrix} H_{\text{TB},\text{I}}(\mathbf{k}) + \epsilon & \delta M_{\text{TB}}(\mathbf{k}) \\ \delta M_{\text{TB}}(\mathbf{k})^\dagger & H_{\text{TB},\text{II}}(\mathbf{k}) - \epsilon \end{pmatrix}, \\
H_{\text{TB},\text{I}}(\mathbf{k}) &= \Gamma_1 \left\{ m_{\text{I}} (1 + \cos \mathbf{k} \cdot \mathbf{a}_3) - t_{\text{I}} [\cos \mathbf{k} \cdot \mathbf{a}_1 + \cos \mathbf{k} \cdot \mathbf{a}_2 + \cos \mathbf{k} \cdot (\mathbf{a}_1 + \mathbf{a}_2)] \right\} \\
&\quad + \lambda_{\text{I}} [\Gamma_2 \sin \mathbf{k} \cdot \mathbf{a}_1 + \Gamma_{2,1}^{\text{I},\text{I}} \sin \mathbf{k} \cdot \mathbf{a}_2 - \Gamma_{2,2}^{\text{I},\text{I}} \sin \mathbf{k} \cdot (\mathbf{a}_1 + \mathbf{a}_2) + \Gamma_3 \sin \mathbf{k} \cdot \mathbf{a}_3], \\
H_{\text{TB},\text{II}}(\mathbf{k}) &= \Gamma_1 \left\{ m_{\text{II}} (1 + \cos \mathbf{k} \cdot \mathbf{a}_3) - t_{\text{II}} [\cos \mathbf{k} \cdot \mathbf{a}_1 + \cos \mathbf{k} \cdot \mathbf{a}_2 + \cos \mathbf{k} \cdot (\mathbf{a}_1 + \mathbf{a}_2)] \right\} \\
&\quad + \lambda_{\text{II}} [\Gamma_2 \sin \mathbf{k} \cdot \mathbf{a}_1 + \Gamma_{2,1}^{\text{II},\text{II}} \sin \mathbf{k} \cdot \mathbf{a}_2 - \Gamma_{2,2}^{\text{II},\text{II}} \sin \mathbf{k} \cdot (\mathbf{a}_1 + \mathbf{a}_2) + \Gamma_3 \sin \mathbf{k} \cdot \mathbf{a}_3] \\
&\quad + \Gamma_4 \gamma_{\text{II}} [\sin \mathbf{k} \cdot (\mathbf{a}_1 + 2\mathbf{a}_2) + \sin \mathbf{k} \cdot (\mathbf{a}_1 - \mathbf{a}_2) - \sin \mathbf{k} \cdot (2\mathbf{a}_1 + \mathbf{a}_2)], \\
M_{\text{TB}}(\mathbf{k}) &= \Gamma_2 [\sin \mathbf{k} \cdot \mathbf{a}_1 + \sin \mathbf{k} \cdot (2\mathbf{a}_1 + \mathbf{a}_2)] + \Gamma_{2,1}^{\text{I},\text{II}} [\sin \mathbf{k} \cdot \mathbf{a}_2 + \sin \mathbf{k} \cdot (\mathbf{a}_2 - \mathbf{a}_1)] \\
&\quad - \Gamma_{2,2}^{\text{I},\text{II}} [\sin \mathbf{k} \cdot (\mathbf{a}_1 + \mathbf{a}_2) + \sin \mathbf{k} \cdot (\mathbf{a}_1 + 2\mathbf{a}_2)] \\
&\quad - i\Gamma_5 [\cos \mathbf{k} \cdot \mathbf{a}_1 + \cos \mathbf{k} \cdot (2\mathbf{a}_1 + \mathbf{a}_2)] \\
&\quad - i\Gamma_{5,1}^{\text{I},\text{II}} [\cos \mathbf{k} \cdot \mathbf{a}_2 + \cos \mathbf{k} \cdot (\mathbf{a}_2 - \mathbf{a}_1)] \\
&\quad - i\Gamma_{5,2}^{\text{I},\text{II}} [\cos \mathbf{k} \cdot (\mathbf{a}_1 + \mathbf{a}_2) + \cos \mathbf{k} \cdot (\mathbf{a}_1 + 2\mathbf{a}_2)],
\end{aligned} \tag{B.15}$$

where $\Gamma_1 = \sigma_3 \otimes \sigma_0$, $\Gamma_2 = \sigma_1 \otimes \sigma_1$, $\Gamma_3 = \sigma_2 \otimes \sigma_0$, $\Gamma_4 = \sigma_1 \otimes \sigma_2$, $\Gamma_5 = \sigma_3 \otimes \sigma_1$, and

$$\Gamma_{\mu,\nu}^{i,j} = (C_{3,i}^z)^\nu \Gamma_\mu (C_{3,j}^z)^{-\nu}. \tag{B.16}$$

Here, $\mu \in \{1, \dots, 5\}$, $i, j \in \{\text{I}, \text{II}\}$, $\nu \in \{1, 2\}$, $C_{3,\text{I}}^z = \sigma_0 \otimes e^{i\frac{\pi}{3}\sigma_3}$ and $C_{3,\text{II}}^z = -\sigma_0 \otimes \sigma_0$ so that the full threefold rotation symmetry is given by $\mathcal{C}_3^z = C_{3,\text{I}}^z \oplus C_{3,\text{II}}^z$. Terms involving Γ_1 and Γ_3 implement intra and inter-orbital hopping, respectively, whereas the other terms correspond to various forms of spin-orbit coupling. All \mathbf{k} -dependencies involving \mathbf{a}_1 and its \mathcal{C}_3^z rotations \mathbf{a}_2 , $-(\mathbf{a}_1 + \mathbf{a}_2)$ correspond to nearest-neighbor couplings, while terms involving $(\mathbf{a}_1 + 2\mathbf{a}_2)$ and its \mathcal{C}_3^z rotations $-(2\mathbf{a}_1 + \mathbf{a}_2)$, $(\mathbf{a}_1 - \mathbf{a}_2)$ correspond to next-nearest neighbor couplings. To enhance readability we have simplified the expressions such that the arguments of trigonometric functions come with positive sign.

The Hamiltonian consists of two 3D topological insulators, given by $H_{\text{TB},\text{I}}$ and $H_{\text{TB},\text{II}}$, which are coupled together via the mass matrix M_{TB} . In the parameter regime $1 < |m_i| < 3$ for $i = \text{I}, \text{II}$, there is a single band inversion in the spectrum of $H_{\text{TB},i}$ at T and the respective Hamiltonian is in the topologically insulating phase. Outside of these two regimes, the full model given by H_{TB} is topologically trivial. In contrast, in the parameter regime where $1 < |m_i| < 3$ holds only for a single i , the full Hamiltonian represents a first-order topological insulator (assuming always that δ is small enough so as not to close the bulk gap), with a single Dirac cone on all surface terminations. Finally, in the regime where $1 < |m_i| < 3$ holds for all i , H_{TB} is trivial from a first order perspective, since it has an even number of

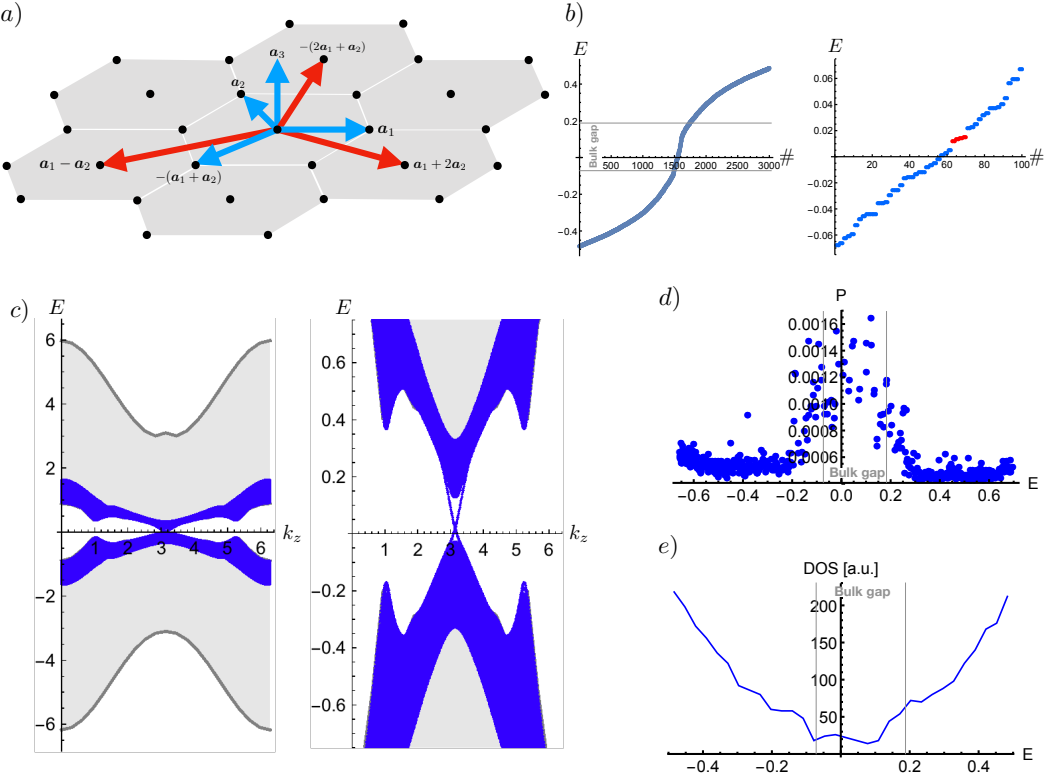


Figure B.2: Tight-binding model for a HOTI with C_3 and \mathcal{I} . (a) 2D slice of the hexagonal crystal lattice. Nearest-neighbor and next-nearest-neighbor hoppings are indicated by blue and red arrows, respectively. (b) Spectrum of the Hamiltonian given in Equation (B.15) on a hexagonal geometry with open boundary conditions in all three directions. 3000 eigenstates are shown. Right panel: A closer view of 100 in-gap eigenstates. The sum of the real-space weights of the states in red is plotted in Figure 4.1 (d) in the main text. (c) k_z -resolved spectrum of the tight-binding model with hexagonal cross-section and periodic boundary conditions in z -direction. The 1000 lowest lying eigenstates are shown in blue, the bulk spectrum in gray. The right panel represents a close-up on the low-energy part. The in-gap states at $k_z = \pi$ are twelve-fold degenerate, corresponding to six helical Kramers pairs of hinge modes. Consult Figure 4.1 (f) in the main text for a further zoomed-in version. (d) Participation ratios of the 1000 eigenstates pertaining to the eigenvalues at $k_z = \pi$ in (c). For an eigenstate $|\Psi\rangle$ with elements $\Psi_i = \langle i|\Psi\rangle$, $i = 1, \dots, N$ (where N is the dimension of the full single-particle Hilbert space including lattice and on-site degrees of freedom), the participation ratio is defined as $P = \sum_i |\Psi_i|^4$. It is small for bulk states and large for edge and corner states. (e) Density of states (DOS) corresponding to the spectrum in (b). The one-dimensional hinge states have an approximately constant DOS and are visible around zero energy.

band inversions, and indeed, for any small finite δ , the two surface Dirac cones gap out. However, it is a HOTI, since $H_{\text{TB},\text{I}}$ and $H_{\text{TB},\text{II}}$ belong to different C_3^z subspaces.

In all calculations we choose $m_{\text{I}} = m_{\text{II}} = 2$, $t_{\text{I}} = t_{\text{II}} = 1$, $\lambda_{\text{I}} = 0.3$, $\lambda_{\text{II}} = \gamma_{\text{II}} = 1$, $\epsilon = 0.1$, and $\delta = 0.3$ to be deep in the HOTI phase. The particular values of these parameters are chosen so that the surface gaps of the tight-binding model in an open geometry are maximized in the HOTI phase. See Figure B.2 (b) for the spectrum of the system in a hexagonal geometry cut out from a $30 \times 30 \times 20$ cuboid.

The HOTI Dirac theory presented in Section B.1, as given by $H_{\text{D}}(\mathbf{k})$ in Equation (B.14), is unitarily equivalent to an expansion of the present tight-binding model $H_{\text{TB}}(\mathbf{k})$ about the T point in the BZ. The expansion is to linear order in k_z , to third order in k_x , k_y for the terms resulting in the kinetic parts $H_1(\mathbf{k})$ and $H_3(\mathbf{k})$ and to second order in k_x , k_y for the terms resulting in the mass-term. This expansion relates the parameters entering the two models as follows

$$\begin{aligned} M_0 &= -3t_{\text{I}} = -3t_{\text{II}}, & M_1 &= \frac{1}{4}M_0, \\ \tilde{A} &= \lambda_{\text{I}} = \lambda_{\text{II}} = -3\sqrt{3}\gamma_{\text{II}}, & A_1 &= \frac{3}{2}\tilde{A}, & A_3 &= -\frac{1}{8}\tilde{A} \\ a &= \frac{3}{32} \left(5i - 3\sqrt{3} \right) \delta, & b &= \frac{3}{8} \left(5 + \sqrt{3}i \right) \delta, & \mu &= \epsilon. \end{aligned} \quad (\text{B.17})$$

For this choice of parameters and to the orders prescribed above we then have that

$$UH_{\text{TB}}(\mathbf{k})U^\dagger \approx H_{\text{D}}(\mathbf{k}),$$

$$U = \begin{pmatrix} -e^{i\frac{\pi}{4}} & 0 & 0 & 0 & 0 & 0 & 0 & 0 \\ 0 & 0 & 0 & -ie^{-i\frac{\pi}{4}} & 0 & 0 & 0 & 0 \\ 0 & ie^{i\frac{\pi}{4}} & 0 & 0 & 0 & 0 & 0 & 0 \\ 0 & 0 & e^{-i\frac{\pi}{4}} & 0 & 0 & 0 & 0 & 0 \\ 0 & 0 & 0 & 0 & 0 & -e^{i\frac{\pi}{4}} & 0 & 0 \\ 0 & 0 & 0 & 0 & 0 & 0 & -ie^{-i\frac{\pi}{4}} & 0 \\ 0 & 0 & 0 & 0 & ie^{i\frac{\pi}{4}} & 0 & 0 & 0 \\ 0 & 0 & 0 & 0 & 0 & 0 & 0 & e^{-i\frac{\pi}{4}} \end{pmatrix}, \quad UU^\dagger = \mathbb{1}. \quad (\text{B.18})$$

B.3 Irreducible representations for bismuth

Our goal is to tell if the three valence bands highlighted in red in Figure 4.1 (e) in the main text can be expressed as any linear combination of pEBRs. The bismuth atoms are located at the Wyckoff position $6c$, which is a high-symmetry line that induces composite EBRs instead of pEBRs in momentum space. However, the site-symmetry group of $6c$ is a subgroup of the maximal Wyckoff positions $3a$ and $3b$, which induce pEBRs. We thus consider the pEBRs induced from the Wyckoff positions $3a$ and $3b$ listed in Table B.1 as an example. One can observe that, in order to have a pEBR, the number of occurrences of little group irreducible representations (irreps) at the different high symmetry points are not independent of one another. For instance, the pEBR $\bar{\Gamma}_{4+5}^{3a} \uparrow G$ contributes the irreps $\bar{X}_3\bar{X}_4$ to the valence bands at the X point and the irreps $\bar{\Gamma}_4\bar{\Gamma}_5$ at the Γ point. The pEBR $\bar{\Gamma}_8^{3a} \uparrow G$ also contributes the irreps $\bar{X}_3\bar{X}_4$ to the valence bands at the X point and the irrep $\bar{\Gamma}_8$ at the Γ point. From these considerations, we can deduce that the number of occurrences of $\bar{X}_3\bar{X}_4$ among all valence bands at the X point needs to equal the number of occurrences of $\bar{\Gamma}_4\bar{\Gamma}_5$ and $\bar{\Gamma}_8$ at the Γ point. We compare this constraint to the irreps computed for bismuth and listed in Table B.2 and realize that it is not met: we find $\bar{X}_3\bar{X}_4$ once, but $\bar{\Gamma}_4\bar{\Gamma}_5$ and $\bar{\Gamma}_8$ together appear three times.

The same analysis has been applied to all pEBRs in the space group, taking into account all Wyckoff positions. The constraints arising in this general case are substantially more complex than in the above example and have been analyzed with a computer algorithm. (The full information about high-symmetry momentum points can be found in the BCS). We find also in this general case that no linear combination of pEBRs matches the irreps in the valence bands of bismuth. Therefore, bismuth must have nontrivial topology, in connection with a bulk band structure that is not expressible in terms of exponentially localized Wannier functions. Note in addition that the \mathbb{Z}_4 inversion index [30, 91] evaluates to $\kappa_1 = 2$ for bismuth, underlining its non-trivial topology from another point of view.

B.4 Effect of a band inversion at the X points

We will show here that, as claimed in the main text, adding a C_3 symmetric triplet of negative inversion eigenvalue Kramers pairs to the occupied bands at X_1 , X_2 and X_3 corresponds to the addition of a single such Kramers pair in the $e^{i\pi}$ eigenvalue subspace of C_3 , and the addition of two in the $\exp(\pm i\pi/3)$ subspace.

	X	Γ	L	T
$3a$				
$\bar{\Gamma}_{4+5}^{3a} \uparrow G$	$\bar{X}_3\bar{X}_4$	$\bar{\Gamma}_4\bar{\Gamma}_5$	$\bar{L}_3\bar{L}_4$	$\bar{T}_4\bar{T}_5$
$\bar{\Gamma}_{6+7}^{3a} \uparrow G$	$\bar{X}_5\bar{X}_6$	$\bar{\Gamma}_6\bar{\Gamma}_7$	$\bar{L}_5\bar{L}_6$	$\bar{T}_6\bar{T}_7$
$\bar{\Gamma}_8^{3a} \uparrow G$	$\bar{X}_3\bar{X}_4$	$\bar{\Gamma}_8$	$\bar{L}_3\bar{L}_4$	\bar{T}_8
$\bar{\Gamma}_9^{3a} \uparrow G$	$\bar{X}_5\bar{X}_6$	$\bar{\Gamma}_9$	$\bar{L}_5\bar{L}_6$	\bar{T}_9
$3b$				
$\bar{\Gamma}_{4+5}^{3b} \uparrow G$	$\bar{X}_3\bar{X}_4$	$\bar{\Gamma}_4\bar{\Gamma}_5$	$\bar{L}_5\bar{L}_6$	$\bar{T}_6\bar{T}_7$
$\bar{\Gamma}_{6+7}^{3b} \uparrow G$	$\bar{X}_5\bar{X}_6$	$\bar{\Gamma}_6\bar{\Gamma}_7$	$\bar{L}_3\bar{L}_4$	$\bar{T}_4\bar{T}_5$
$\bar{\Gamma}_8^{3b} \uparrow G$	$\bar{X}_3\bar{X}_4$	$\bar{\Gamma}_8$	$\bar{L}_5\bar{L}_6$	\bar{T}_9
$\bar{\Gamma}_9^{3b} \uparrow G$	$\bar{X}_5\bar{X}_6$	$\bar{\Gamma}_9$	$\bar{L}_3\bar{L}_4$	\bar{T}_8

Table B.1: pEBRs of space group 166 with TRS. The notation $\bar{\Gamma}_j^{3a/b} \uparrow G$ stands for the induction of the site-symmetry group $\bar{\Gamma}_j^{3a/b}$ in the space group G , which subduces a pEBR.

	3 doubly-degenerate valence bands
X	$\bar{X}_3\bar{X}_4; \bar{X}_5\bar{X}_6; \bar{X}_5\bar{X}_6$
Γ	$\bar{\Gamma}_8; \bar{\Gamma}_8; \bar{\Gamma}_4\bar{\Gamma}_5$
L	$\bar{L}_3\bar{L}_4; \bar{L}_5\bar{L}_6; \bar{L}_5\bar{L}_6$
T	$\bar{T}_9; \bar{T}_8; \bar{T}_6\bar{T}_7$

Table B.2: The computed little-group irreps for bismuth are presented as follows.

Let the added Kramers pair at X_1 be denoted by the eigenstates $|u_{X_1}^k\rangle$, $k = 1, 2$, where $|u_{X_1}^2\rangle = T|u_{X_1}^1\rangle$ and T is the representation of the anti-unitary time-reversal operator. Take \mathcal{C}_3 to be the representation matrix of threefold rotation. Since in a spinful system $\mathcal{C}_3^3 = -1$, we can always choose the gauge

$$\mathcal{C}_3 \begin{pmatrix} |u_{X_1}^1\rangle \\ |u_{X_2}^1\rangle \\ |u_{X_3}^1\rangle \end{pmatrix} = e^{i\pi/3} \begin{pmatrix} 0 & 1 & 0 \\ 0 & 0 & 1 \\ 1 & 0 & 0 \end{pmatrix} \begin{pmatrix} |u_{X_1}^k\rangle \\ |u_{X_2}^k\rangle \\ |u_{X_3}^k\rangle \end{pmatrix}. \quad (\text{B.19})$$

This means that we can find eigenvectors

$$\begin{aligned} |u_\pi^k\rangle &= e^{i2\pi/3} |u_{X_1}^k\rangle + e^{-i2\pi/3} |u_{X_2}^k\rangle + |u_{X_3}^k\rangle, \\ |u_{+\pi/3}^k\rangle &= |u_{X_1}^k\rangle + |u_{X_2}^k\rangle + |u_{X_3}^k\rangle, \\ |u_{-\pi/3}^k\rangle &= e^{-i2\pi/3} |u_{X_1}^k\rangle + e^{i2\pi/3} |u_{X_2}^k\rangle + |u_{X_3}^k\rangle. \end{aligned} \quad (\text{B.20})$$

with eigenvalues -1 , $e^{i\pi/3}$, and $e^{-i\pi/3}$, respectively. This means that when the added Kramers pairs are odd under inversion symmetry, the time-reversal invariant

subspaces with \mathcal{C}_3 eigenvalues -1 and $e^{\pm i\pi/3}$ are augmented by one and two such Kramers pairs, respectively. Being a \mathbb{Z}_2 quantity, only $\nu^{(\pi)}$ is affected by the inversion eigenvalues at the X points. The same argument holds for the L points.

B.5 First-principle calculations

We employed density functional theory (DFT) as implemented in the Vienna Ab Initio Simulation Package (VASP) [251, 252, 253, 254]. The exchange correlation term is described according to the Perdew-Burke-Ernzerhof (PBE) prescription together with projected augmented-wave pseudopotentials [255, 256] and the spin-orbit interaction included. For the self-consistent calculations we used a $12 \times 12 \times 12$ k -points mesh for the bulk band structure calculations. The eigenvalues of the symmetry transformations were deduced from the matrix representations of the respective symmetry operation calculated using the Bloch eigenstates from VASP.

B.6 STM experiment

Bismuth crystals were cleaved at room temperature in ultra-high vacuum conditions and the cleaved samples were cooled down to a temperature of 4 K at which scanning tunneling microscopy (STM) and spectroscopy (STS) measurements were carried out. The cleaved bismuth crystal exhibits a (111) plane of the bismuth rhombohedral structure [which is the (001) plane of the bismuth hexagonal structure]. The topographic data and the differential conductance maps were. For STM measurements, a mechanically sharpened platinum-iridium tip was used, and electronic properties of the probe tip were characterized before the experiments on bismuth by checking a reference sample. Differential conductance maps [Figure 4.2 (b) and (d)] are taken simultaneously with topographic data at the van Hove singularity energy ($V = 183$ meV) of the bismuth edge states using a lock-in amplifier with an oscillation of 3 meV and with $I = 3.5$ nA. The data shown in this manuscript is reproduced on many step edges of Bi (111) with atomically different tips. All of the islands on the Bi (111) surface show the expected step height of 4 Å for bismuth bilayers and all of the extended edges are identified as zigzag structures of either A type or B type. A type and B type edges are equivalent in the hexagonal nanowire geometry as described in the main manuscript [Figure 4.1 (c)], however, the existence of the Bi (111) surface under the bismuth bilayer breaks the inversion symmetry, and A as well as B type edges can be identified in STM measurements. Only A type edges show the spectroscopic feature of a sharp peak

at 183 meV which is the van Hove singularity energy of the one-dimensional edge state. Quasi-particle interference (QPI) measurements reveal that this edge state is continuously dispersing down to the Fermi level and starts to merge with the surface states at the momentum where the surface gap closes [126]. This spectroscopic feature of geometric confinement only at A type edges resembles the topological hinge modes expected for the hexagonal nanowire, as discussed in the main text.

B.7 Transport experiment

The nanowires grew during slow sputtering deposition of high purity bismuth on a slightly heated silicon substrate. High resolution transmission electron microscopy (TEM) indicates high quality single crystals, of hexagonal or rhombohedral cross-sections, with clear facets. The facet widths are typically 50 to 300 nm wide. Resistance measurements show that transport in the normal state (i.e., when contacts to the nanowires are not superconducting) occurs predominately due to surface states, with an elastic mean free path of the order of 100 nm.

Appendix C

More on topoelectrical circuits

This is the appendix for Chapter 6.

C.1 Impedance response and Green's function

The signature of a nontrivial topological phase often lies in its response to an external perturbation. In electronic topological systems for instance, a nontrivial Chern number corresponds to a nonvanishing quantized Hall response, as epitomized by the Kubo formula. In circuits, however, the Kubo formula does not apply as there is no quantum excitation from a Fermi sea. Below, we shall derive the appropriate analog of the Kubo formula for circuits, which shall characterize the so-called *topoelectrical* response.

Define V_a and I_a to be the voltage and external input current on node a of a circuit. By Kirchhoff's law,

$$I_a = C_{ab} \ddot{V}_b + W_{ab} V_b \quad (\text{C.1})$$

where C_{ab} and W_{ab} are the Laplacian matrices of capacitances and inverse inductances, and the summation over repeated indices is implied. For a mode $V(t) \sim V(0)e^{i\omega t}$ at frequency ω , Equation (C.1) takes the form

$$I_a = \left(i\omega C_{ab} - \frac{i}{\omega} W_{ab} \right) V_b = J_{ab}(\omega) V_b \quad (\text{C.2})$$

where $J_{ab}(\omega)$ is the (grounded) circuit Laplacian.

The most natural measurement on a circuit is the impedance response $Z_{ab}(\omega)$, which is the ratio of the voltage between two nodes a and b due to a current

$I_j = I_0(\delta_{j,a} - \delta_{j,b})$ that enters through a and exits at b . Mathematically, $Z_{ab}(\omega)$ simply involves the inversion of Equation (C.2):

$$\begin{aligned} Z_{ab}(\omega) &= \frac{V_a - V_b}{I_0} \\ &= \sum_i \frac{G_{ai}(\omega)I_i - G_{bi}(\omega)I_i}{I_0} \\ &= G_{aa}(\omega) + G_{bb}(\omega) - G_{ab}(\omega) - G_{ba}(\omega) \\ &= \sum_n \frac{|\phi_n(a) - \phi_n(b)|^2}{j_n(\omega)} \end{aligned} \quad (\text{C.3})$$

where $J_{ab}(\omega) = \sum_n j_n(\omega) |\phi_n(a)\rangle\langle\phi_n(b)|$ is the expansion of the Laplacian into its eigenmodes (the ω dependence of the eigenmodes is left implicit), with the Green's function $G_{ab}(\omega) = \sum_n \frac{1}{j_n(\omega)} |\phi_n(a)\rangle\langle\phi_n(b)|$ being its inverse. When the circuit is ungrounded, an overall shift of the potential cannot be felt, and the corresponding zero eigenspace should be excluded in the definition of the Green's function.

Equation (C.3) describes the impedance between any two nodes purely in terms of the eigenmodes and eigenvalues of the Laplacian. Most notably, it suggests that circuit resonances (divergences of the impedance) occur whenever there are nontrivial zero eigenvalues j_n . In a realistic circuit with unavoidable disorder, the strength of such resonances depend on the density of such zero eigenmodes, as well as whether there is any mechanism that pins them to zero.

A quintessential example of a strong protected resonance is a *topoelectrical* resonance, which occurs due to topologically protected zero modes of the circuit Laplacian. Due to the localization of these modes at the boundary, such resonances can be easily identified through extremely large resonances at the boundary but not the interior of the circuit lattice. In this paper, the corner modes are such an example.

The circuit Laplacian in momentum space $\tilde{J}_\lambda(\omega_0, \mathbf{k})$ is given by

$$\begin{aligned} \tilde{J}_\lambda(\omega_0, \mathbf{k}) &= \sum_i e^{-i\mathbf{k}\cdot\mathbf{a}_i} J_{0a_i}(\omega_0) \\ &= i\sqrt{\frac{c}{l}} [(1 + \lambda \cos k_x)\sigma_1 \tau_0 + (1 + \lambda \cos k_y)\sigma_2 \tau_2 \\ &\quad - \lambda \sin k_x \sigma_2 \tau_3 + \lambda \sin k_y \sigma_2 \tau_1], \end{aligned} \quad (\text{C.4})$$

where \mathbf{a}_i are the unit cell lattice vectors of the model defined in Equation (C.2) via $a \equiv 0$ as the reference point and $b \equiv \mathbf{a}_i$, where intra unit cell degrees of freedom

are left implicit in the first line. It has, up to an overall factor of i , the same form as the model for an electric quadrupole insulator defined in Reference [86].

C.2 Effective Dirac problem and boundary modes

In Chapter 6, we showed that the admittance matrix $J(\omega_0)$ possesses the required symmetries to define the topological characteristics of a quadrupole insulator. In this section we demonstrate that in the corresponding dynamical matrix D , the same symmetry properties are emergent for frequencies near ω_0 , but globally realized. We derive the effective Dirac form of the matrix D and explicitly show that it implies the existence of corner modes.

We denote by $\tilde{C}(k_x, k_y)$ and $\tilde{W}(k_x, k_y)$ the Fourier components of the matrices C and W defined in Chapter 6 for a circuit with periodic boundary conditions. To show that \mathcal{M}_x and \mathcal{M}_y defined in Equation (6.8) are emergent symmetries of the dynamical matrix $\tilde{D}(k_x, k_y) = \tilde{C}^{-1/2}(k_x, k_y)\tilde{W}(k_x, k_y)\tilde{C}^{-1/2}(k_x, k_y)$ we note that the spectrum of $\tilde{D}(k_x, k_y)$ is gapless for $\lambda = 1$ with a linear band touching point near $(k_x, k_y) = (\pi, \pi)$, but is gapped for $\lambda \neq 1$. This motivates to expand $\tilde{D}(k_x, k_y)$ to linear order in $(1 - \lambda)$ and the deviations (p_x, p_y) of \mathbf{k} from $= (\pi, \pi)$. The resulting effective dynamical matrix $D(p_x, p_y)$ takes Dirac form

$$D(p_x, p_y) = \omega_0^2 \sigma_0 \tau_0 + \frac{\omega_0^2}{4} (p_x \sigma_2 \tau_3 - p_y \sigma_2 \tau_1) + \frac{\omega_0^2}{4} (1 - \lambda) (\sigma_1 \tau_0 + \sigma_2 \tau_2), \quad (\text{C.5})$$

where the term proportional to $(1 - \lambda)$ is a mass term. The spectrum of $D(p_x, p_y)$ is symmetric about ω_0^2 . This is a result of the chiral symmetry $\mathcal{C} = \sigma_3 \tau_0$ which anticommutes with $D(p_x, p_y)$. If this symmetry is not broken by a boundary in the range of frequencies near ω_0 , topological boundary modes will be pinned to the frequency ω_0 .

We are searching for an explicit analytical solution to the localized corner state within the respective Dirac equation. Without loss of generality we consider a corner to the upper right of the sample. To implement it in our formalism, we have to consider a real space dependence of the Dirac mass term in Equation (C.5). For simplicity, we set $\omega_0 = 2$ and remove the overall energy shift ω_0^2 from the Dirac operator. Further we substitute $(1 - \lambda)\sigma_1 \tau_0$ by $\Delta \sin \phi \sigma_1 \tau_0$ and $(1 - \lambda)\sigma_2 \tau_2$ by $\Delta \cos \phi \sigma_2 \tau_2$ so that the operator reads

$$D = p_x \sigma_2 \tau_3 - p_y \sigma_2 \tau_1 + \Delta (\sin \phi \sigma_1 \tau_0 + \cos \phi \sigma_2 \tau_2), \quad (\text{C.6})$$

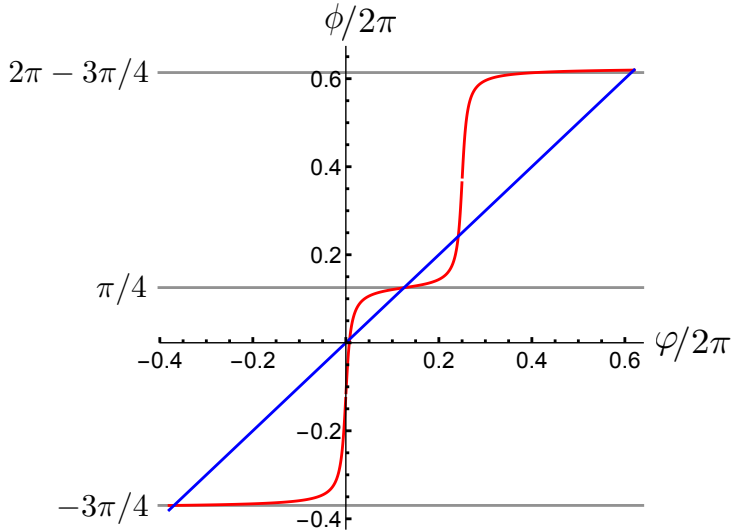


Figure C.1: Two dependencies of the operator D from Equation (C.6) on the angular variable φ that mimic a superconducting vortex (blue) and the corner of an electric quadrupole insulator (red). The existence of a zero mode in the former implies the existence of a corner mode in the latter.

where $\phi = \pi/4$ and $\phi = -3\pi/4$ holds inside and outside of the material, respectively. With these values for ϕ , we have merely implemented the sign change in the Dirac mass term across the sample boundary. We now equip ϕ with a position dependence to model a corner. A corner geometry requires that ϕ vary continuously from $\phi = \pi/4$ to $\phi = -3\pi/4$ and back again as we go once around the corner in real space (starting from within the sample). The form of this interpolation is constrained by symmetry arguments. Note that the bulk symmetries \mathcal{M}_x , \mathcal{M}_y and \mathcal{C}_4 are all broken locally by the corner. The only symmetry that leaves the corner invariant is the diagonal mirror symmetry $\mathcal{M}_{x\bar{y}} = \mathcal{C}_4\mathcal{M}_x$ that sends $(x, y) \rightarrow (y, x)$ and is represented by

$$\mathcal{M}_{x\bar{y}} = \frac{1}{2}(\sigma_0 + \sigma_3)\tau_3 + \frac{1}{2}(\sigma_0 - \sigma_3)\tau_1. \quad (\text{C.7})$$

Also, the system respects chiral symmetry for any choice of ϕ . We now endow ϕ with a spatial dependence and note that $\mathcal{M}_{x\bar{y}}$ symmetry is preserved if

$$\phi(x, y) = -\phi(y, x) + \pi/2 \bmod 2\pi. \quad (\text{C.8})$$

If we parametrize real space by $x = r\cos\varphi$, $y = r\sin\varphi$, the condition translates into one on the φ dependence of ϕ . Specifically

$$\phi(\varphi) = -\phi(-\varphi + \pi/2) + \pi/2 \bmod 2\pi. \quad (\text{C.9})$$

The choice $\phi_1(\varphi) = \varphi$ is consistent with this symmetry, and so is

$$\phi_2(\varphi) = \arctan\left(\frac{\varphi}{\lambda}\right) + \arctan\left(\frac{\varphi - \pi/2}{\lambda}\right) + \frac{\pi}{4}. \quad (\text{C.10})$$

In the limit $\lambda \rightarrow 0$, $\phi_2(\varphi)$ realizes a corner with the nontrivial part of the system located in the upper right quadrant. This can be seen by noting that in this limit, $\phi = \pi/4$ and $\phi = -3\pi/4$ holds as required inside and outside of the sample, respectively. For $\phi_1(\varphi)$, in contrast, the operator (C.6) is equivalent to the Hamiltonian that describes a vortex in an *s*-wave superconducting surface state of a three-dimensional topological insulator [223]. The latter supports a spectrally isolated zero energy mode localized at the origin. It is protected to lie at zero energy by the chiral symmetry. We can now choose any interpolation between $\phi_1(\varphi)$ and $\phi_2(\varphi)$ to connect these two situations: since chiral symmetry cannot be broken by the interpolation, the zero mode has to remain also in the system with a corner.

C.3 Mirror-graded winding number

Here we define the bulk topological invariant for a topological quadrupole insulator as a mirror-symmetry graded winding number. This index is valid if the model has diagonal mirror symmetry (e.g., $\mathcal{M}_{x\bar{y}}$) and chiral symmetry \mathcal{C} . The latter is in any case required to pin topological corner modes to eigenvalue zero (see the discussion of the Su-Schrieffer-Heeger model with chiral symmetry in Section 2.1.1.1). Our topological invariant, which was already employed in Reference [258] to characterize crystalline topological superconductors, is complementary to the characterization of multipole insulators in terms of Wilson loops that was given in Reference [86].

Consider a \mathbf{k} -dependent matrix (being for example a Bloch Hamiltonian, or an admittance matrix) $R(\mathbf{k})$ that both obeys \mathcal{C} , i.e., $\mathcal{C}R(\mathbf{k})\mathcal{C}^{-1} = -R(\mathbf{k})$, and $\mathcal{M}_{x\bar{y}}$, i.e., $\mathcal{M}_{x\bar{y}}R(k_x, k_y)\mathcal{M}_{x\bar{y}}^{-1} = -R(k_y, k_x)$ and let $[\mathcal{C}, \mathcal{M}_{x\bar{y}}] = 0$. The occupied bands of $R(k, k)$ can then be divided in a subspace with mirror eigenvalues ± 1 (or $\pm i$ for spinful mirror symmetry). Using this grading, we can bring $R(k, k)$ to the form

$$R(k, k) = \begin{pmatrix} 0 & q_+(k) & 0 & 0 \\ q_+(k)^\dagger & 0 & 0 & 0 \\ 0 & 0 & 0 & q_-(k) \\ 0 & 0 & q_-(k)^\dagger & 0 \end{pmatrix}, \quad (\text{C.11})$$

where the first half acts on the $+1$ mirror subspace, while the second half acts on the -1 mirror subspace. For $R(k, k)$ to be gapped, all eigenvalues of $q_\pm(k)$ need

to be nonzero. We can thus define a ‘spectrally flattened’ pair of unitary matrices $\tilde{q}_\pm(k)$ which share the eigenstates and phase of the eigenvalues with $q_\pm(k)$, but have eigenvalues of absolute value 1. We can now define the winding numbers

$$\nu_\pm := \frac{i}{2\pi} \int_0^{2\pi} dk \operatorname{tr} \tilde{q}_\pm^\dagger(k) \partial_k \tilde{q}_\pm(k), \quad (\text{C.12})$$

which are quantized to be integers. For a system with vanishing dipole moment, the net winding number $\nu_+ + \nu_-$ must vanish in any direction of momentum space. Hence, for the systems of interest to us $\nu_+ = -\nu_-$, and we can use

$$\nu := \frac{\nu_+ - \nu_-}{2} \in \mathbb{Z} \quad (\text{C.13})$$

as a topological invariant. The number of topological corner modes is equal to the parity of ν .

We now demonstrate this topological invariant for the admittance matrix realized in our electrical circuit. Up to prefactors, the matrix takes the form

$$R(\mathbf{k}) = (1 + \lambda \cos k_x) \sigma_1 \tau_0 + (1 + \lambda \cos k_y) \sigma_2 \tau_2 \\ - \lambda \sin k_x \sigma_2 \tau_3 + \lambda \sin k_y \sigma_2 \tau_1, \quad (\text{C.14})$$

and $\mathcal{C} = \sigma_3 \tau_0$, while $\mathcal{M}_{x\bar{y}} = \frac{1}{2}(\sigma_0 + \sigma_3)\tau_3 + \frac{1}{2}(\sigma_0 - \sigma_3)\tau_1$. The mirror-eigenvalue graded off-diagonal components of $R(k, k)$ are scalars in this case and can be computed as

$$q_\pm(k) = \sqrt{2} (1 + \lambda e^{\mp ik}). \quad (\text{C.15})$$

Clearly, for $\lambda > 1$, they have winding number $\nu_\pm = \pm 1$ and thus $\nu = +1$, corresponding to the topologically nontrivial phase with corner modes. In contrast, for $\lambda < 1$ we find $\nu_\pm = 0$ and thus $\nu = 0$, corresponding to the topologically trivial phase.

C.4 Octagonal sample geometry

To demonstrate the stability of corner-localized zeromodes under a \mathcal{M} , C_4 symmetric deformation of our rectangular sample, we study the circuit Laplacian given in Figure 6.1 (a) on an octagonal geometry. Note that an octagon preserves all protecting symmetries just like the square we studied previously, and should therefore also host zeromodes. Note that we do not modify the rectangular unit cell of the Laplacian, but rather tile a macroscopic octagon with these unit cells. We have to orient the octagon such that the mirror axes corresponding to \mathcal{M}_{xy} and $\mathcal{M}_{x\bar{y}}$

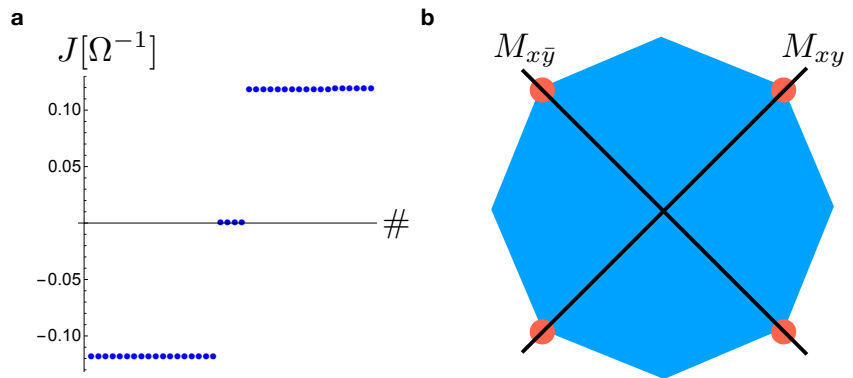


Figure C.2: Low-energy spectrum of the circuit Laplacian with unit cell structure given in Figure 6.1 (a) on an octagonal geometry. (a) There are, as for the square geometry considered in Chapter 6, four zero modes. (b) The zero modes are localized at the four corners that lie within the mirror axes corresponding to the nontrivial topological index of the model, the mirror-graded winding number.

each contain two corners rather than cutting halfway through two edges. This is because the nontrivial topological index of the model, the mirror-graded winding number introduced in the supplemental material, implies that edges perpendicular to the mirror axes noted above are gapless. In the prescribed orientation however all edges are generically gapped while the corners along the mirror axes should be gapless. This is indeed the case, see Figure C.2 for the resulting spectrum.

C.5 Grounding at the edge termination

In relating a quantum mechanical single-particle Hamiltonian to a topoelectrical circuit Laplacian, we have to take into account that there is a constraint on the circuit Laplacian which is not present in the quantum mechanical problem: The off-diagonal circuit Laplacian matrix elements, which describe a connection to and from a given site, necessarily also appear with opposite sign as diagonal elements for the respective site. Since the quantum mechanical Hamiltonian we want to model does not have any on-site terms at all, we need to eliminate these circuit Laplacian diagonal elements by a suitable choice of the grounding.

Working at a fixed resonance frequency, this can be achieved by making use of the fact that inductivities and capacitances enter the circuit Laplacian with opposite sign). Therefore, the total contribution arising from all inductivities at a given site can be cancelled by connecting this site to the ground with a capacitor, and vice

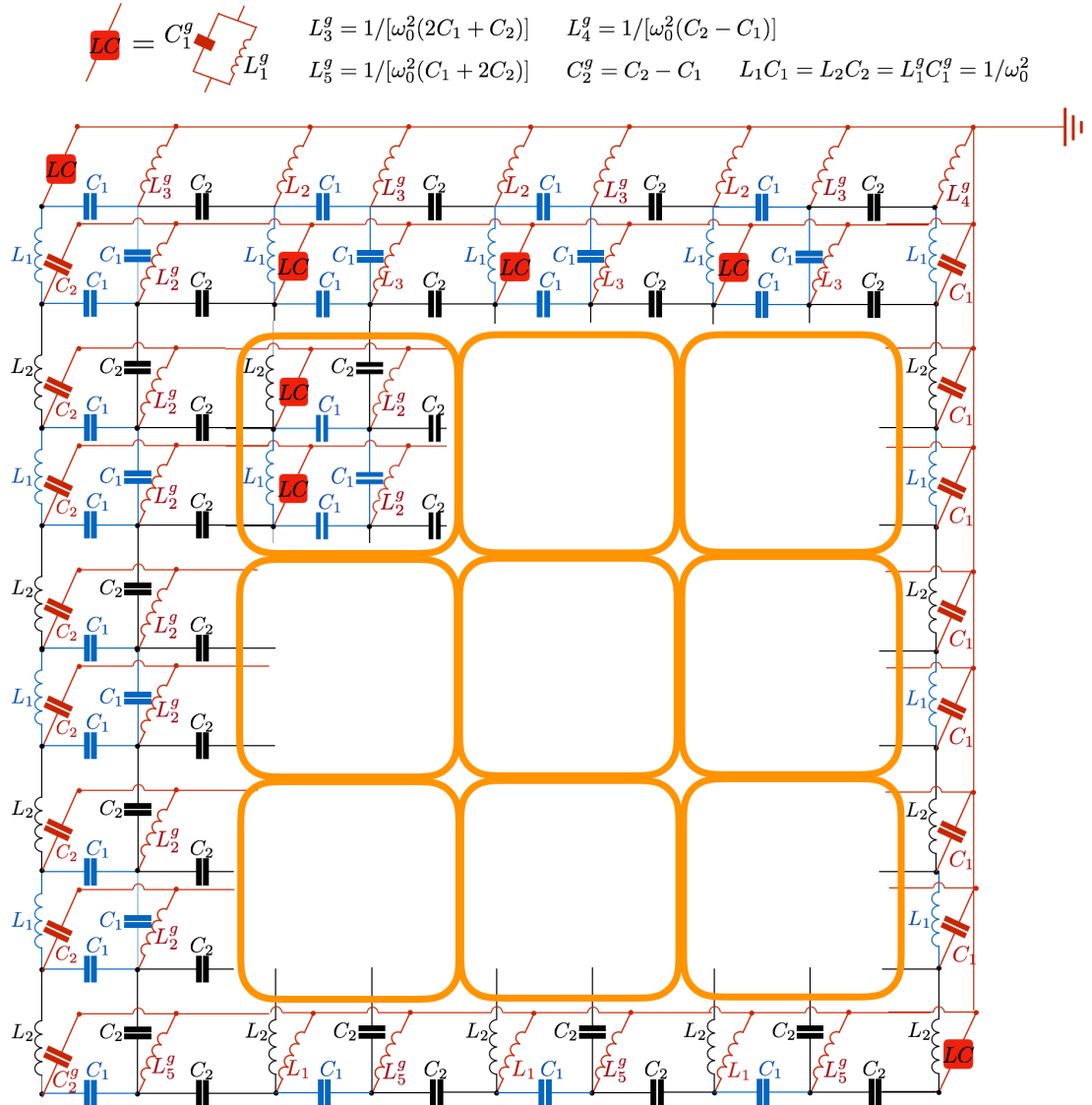


Figure C.3: Grounding used in the experimental realization of the open circuit with a single topological zero-energy mode located at the upper left corner. The bulk unit cell, corresponding to Figure 6.1 (a) in Chapter 6, is marked in orange, and only explicitly shown once.

versa. In the bulk of the circuit, this gives rise to the periodic grounding pattern that is depicted in Figure 6.1 (a) in Chapter 6.

In an open circuit, however, we cannot simply terminate our system with bulk unit cells as we would do it in the quantum mechanical case. The reason is that at the boundary of the system, some off-diagonal circuit Laplacian elements that encapsulate connections to other sites are missing, and thus we need to change our grounding respectively. Only then do also the diagonal elements that pertain to all boundary sites vanish. The resulting grounding pattern is shown in Figure C.3.

Appendix D

More on fractional corner charges

This is the appendix for Chapter 7.

D.1 Explicit mapping from spinless to spinful \mathcal{C}_3 eigenvalues

We start with the spinless indicators

$$[\tilde{K}_i^{(3)}] = \#\tilde{K}_i^{(3)} - \#\tilde{\Gamma}_i^{(3)}, \quad (\text{D.1})$$

where $\tilde{K}_{i=1,2,3}^{(3)}$, $\tilde{\Gamma}_{i=1,2,3}^{(3)} = \{1, e^{i2\pi/3}, e^{-i2\pi/3}\}$. Upon introducing spin, each spinless eigenvalue λ contributes two spinful eigenvalues $\lambda e^{\pm i\pi/3}$. From this we obtain the relations

$$\begin{aligned} [K_1^{(3)}] &= [\tilde{K}_1^{(3)}] + [\tilde{K}_2^{(3)}], \\ [K_2^{(3)}] &= [\tilde{K}_2^{(3)}] + [\tilde{K}_3^{(3)}], \\ [K_3^{(3)}] &= [\tilde{K}_3^{(3)}] + [\tilde{K}_1^{(3)}], \end{aligned} \quad (\text{D.2})$$

where the $[K_i^{(3)}]$, $i = 1, 2, 3$, are defined in Equation (7.25). Together with the constraints in Equation (7.27) this implies

$$\begin{aligned} [\tilde{K}_1^{(3)}] &= -[K_2^{(3)}], \\ [\tilde{K}_2^{(3)}] &= -[K_3^{(3)}], \\ [\tilde{K}_3^{(3)}] &= -[K_1^{(3)}], \end{aligned} \quad (\text{D.3})$$

providing a mapping between spinless and spinful \mathcal{C}_3 eigenvalues.

D.2 Corner charge classification of the layer groups

We consider the 80 layer groups labeled in Reference [259]. First we drop all layer groups that involve nonsymmorphic symmetries, since these are broken by any finite geometry with corners. Then we acknowledge that in some groups, only a subgroup is responsible for quantizing corner charges to fractional values, while the remaining symmetry operations at most pose constraints on the sample geometry and corner charge localization. The corner charge classification of these groups is therefore already determined by a minimal set S of layer groups that covers all possible ways of enforcing quantization. This set and its classification are given by Table D.1.

D.3 First-principle calculations

Fully relativistic DFT calculations were performed via the Vienna *ab initio* simulation package (VASP) [252, 260] by employing the Perdew-Burke-Ernzerhof (PBE) [255, 256] exchange-correlation functional and projected augmented-wave pseudopotentials [261, 251]. For the self-consistent calculations, we used a $19 \times 19 \times 1$ \mathbf{k} -point grid generated for the Monkhorst-Pack method in case of Bi and Sb, and a $17 \times 17 \times 1$ mesh for As. The plane wave basis cutoff was set to 400 eV (Bi and Sb) or 350 eV (As). A finer grid of $30 \times 30 \times 1$ \mathbf{k} -points was used later on in order to obtain the energy gaps and band representations.

For open flake calculations, we employed the Siesta code [221]. We used pseudoatomic orbitals (PAO) with a basis of double zeta plus polarization orbitals (DZP) and norm-conserving fully relativistic pseudopotentials from the PseudoDojo library [262]. The bulk crystal structure was terminated to obtain a hexagonal structure of 546 Sb atoms, and 30 Te atoms were added to the edges in order to passivate the edge states [as shown in Figure 7.5 (f)]. The distance between Te and edge Sb atoms was set to a value 3.02 Å, which was determined from the structure relaxation of an armchair Sb ribbon with Te adatoms at the edge. The DFT data post-processing was performed with the sisl Python package [263].

The irreducible representations of bands at high-symmetry points were obtained using the `irrep` code [264], which relies on the double space group character tables [133] published on the Bilbao Crystallographic server [265].

group	generators	classification	$Q_c \bmod 2$	same class.
1	-	\mathbb{Z}_1	{0}	4, 5, 8–13
				27–36
2	\mathcal{I}	\mathbb{Z}_2	{0, 1}	7, 14–18, 39, 43–46 52, 62, 64
3	\mathcal{C}_2^z	\mathbb{Z}_2	{0, 1}	19, 20, 21, 24, 25
6	$\mathcal{I}, \mathcal{C}_2^z$	\mathbb{Z}_2	{0, 1}	40
22	$\mathcal{C}_2^x, \mathcal{C}_2^y$	\mathbb{Z}_2	{0, 1}	
23	$\mathcal{M}_x, \mathcal{M}_y$	\mathbb{Z}_2	{0, 1}	26
37	$\mathcal{M}_x, \mathcal{M}_y, \mathcal{M}_z$	\mathbb{Z}_2	{0, 1}	47
38	$\mathcal{M}_x, \mathcal{I}$	\mathbb{Z}_2	{0, 1}	41, 42, 48
49	\mathcal{C}_4^z	\mathbb{Z}_4	{0, 1/2, 1, 3/2}	52, 54, 56
50	$\mathcal{C}_4^z \mathcal{I}$	\mathbb{Z}_4	{0, 1/2, 1, 3/2}	58, 60
51	$\mathcal{C}_4^z, \mathcal{I}$	\mathbb{Z}_4	{0, 1/2, 1, 3/2}	63
53	$\mathcal{C}_4^z, \mathcal{C}_2^x, \mathcal{C}_2^y$	\mathbb{Z}_4	{0, 1/2, 1, 3/2}	62
55	$\mathcal{C}_4^z, \mathcal{M}_x, \mathcal{M}_y$	\mathbb{Z}_4	{0, 1/2, 1, 3/2}	64
57	$\mathcal{C}_4^z \mathcal{I}, \mathcal{C}_2^x, \mathcal{C}_2^y$	\mathbb{Z}_4	{0, 1/2, 1, 3/2}	
59	$\mathcal{C}_4^z \mathcal{I}, \mathcal{M}_x, \mathcal{M}_y$	\mathbb{Z}_4	{0, 1/2, 1, 3/2}	
61	$\mathcal{C}_4^z, \mathcal{I}, \mathcal{C}_2^x, \mathcal{C}_2^y$	\mathbb{Z}_4	{0, 1/2, 1, 3/2}	
65	\mathcal{C}_3^z	\mathbb{Z}_3	{0, 2/3, 4/3}	
67	$\mathcal{C}_3^z, \mathcal{C}_2^x$	\mathbb{Z}_3	{0, 2/3, 4/3}	68
69	$\mathcal{C}_3^z, \mathcal{M}_x$	\mathbb{Z}_3	{0, 2/3, 4/3}	70
71	$\mathcal{C}_3^z, \mathcal{M}_x, \mathcal{I}$	\mathbb{Z}_6	{0, 1/3, 2/3, 1, 4/3, 5/3}	72
73	\mathcal{C}_6^z	\mathbb{Z}_6	{0, 1/3, 2/3, 1, 4/3, 5/3}	
74	$\mathcal{C}_6^z \mathcal{I}$	\mathbb{Z}_6	{0, 1/3, 2/3, 1, 4/3, 5/3}	
75	$\mathcal{C}_6^z, \mathcal{I}$	\mathbb{Z}_6	{0, 1/3, 2/3, 1, 4/3, 5/3}	
76	$\mathcal{C}_6^z, \mathcal{C}_2^x$	\mathbb{Z}_6	{0, 1/3, 2/3, 1, 4/3, 5/3}	
77	$\mathcal{C}_6^z, \mathcal{M}_x$	\mathbb{Z}_6	{0, 1/3, 2/3, 1, 4/3, 5/3}	
78	$\mathcal{C}_6^z \mathcal{I}, \mathcal{M}_x$	\mathbb{Z}_6	{0, 1/3, 2/3, 1, 4/3, 5/3}	79
80	$\mathcal{C}_6^z, \mathcal{I}, \mathcal{M}_x$	\mathbb{Z}_6	{0, 1/3, 2/3, 1, 4/3, 5/3}	

Table D.1: Corner charge classification and topological indices of S . The boundary classification of any layer group \mathfrak{l} is given by that of the group $s \in S$, where s is the largest possible subgroup of \mathfrak{l} contained in S . In the case where \mathfrak{l} contains nonsymmorphic operations, its classification is the same as that of the layer group \mathfrak{l}' that consists of the symmorphic part of \mathfrak{l} .

Appendix E

More on superconductors

This is the appendix for Chapter 8.

E.1 Quantization of the Berry phase

We here derive the quantization of the Berry phase due to particle-hole symmetry and a spectral gap. Take the M dimensional occupied subspace of bands to be spanned by the eigenstates $|\alpha_{k\xi}\rangle$, $\xi = 1 \dots M$. The action of a particle-hole symmetry \mathcal{P} with $\mathcal{P}^2 = 1$ is $\mathcal{P}\mathcal{H}_k\mathcal{P}^\dagger = -\mathcal{H}_{-k}$, which implies that

$$\mathcal{P}|\alpha_{k\xi}\rangle = \sum_{\zeta=1}^M S_{k\xi\zeta} |\tilde{\alpha}_{-\zeta}\rangle, \quad (\text{E.1})$$

where $|\tilde{\alpha}_{k\xi}\rangle$, $\xi = 1 \dots M$, denotes the set of eigenstates in the empty subspace and $S_{k\xi\zeta}$ is a unitary sewing matrix. The Berry connection is defined as

$$\mathbf{A}_{k\xi\zeta} = i\langle\alpha_{k\xi}|\nabla_k|\alpha_{k\zeta}\rangle. \quad (\text{E.2})$$

Note that it is Hermitian, that is, it satisfies $\bar{\mathbf{A}}_{k\zeta\xi} = \mathbf{A}_{k\xi\zeta}$. The Berry phase is defined as

$$\gamma_{k\perp} = \int_{-\pi}^{\pi} dk_{\parallel} \operatorname{Tr} A_{\parallel k}. \quad (\text{E.3})$$

Equation (E.1) implies that

$$\mathbf{A}_{k\xi\zeta} = S_{k\xi\tilde{\zeta}} \tilde{\mathbf{A}}_{-\tilde{k}\tilde{\xi}\tilde{\zeta}}^T S_{\tilde{k}\tilde{\xi}\zeta}^\dagger + i S_{k\xi\tilde{\zeta}} \nabla_k S_{\tilde{k}\tilde{\xi}\zeta}^\dagger, \quad (\text{E.4})$$

where summation over repeated indices is implicit, we denote by the Berry connection of the states of the empty subspace as $\tilde{\mathbf{A}}_{\mathbf{k}\xi\zeta}$, and by $\tilde{\gamma}_{\mathbf{k}_\perp}$ is its Berry phase. We therefore have

$$\begin{aligned}\tilde{\gamma}_{\mathbf{k}_\perp} &= \int_{-\pi}^{\pi} dk_\parallel \text{Tr} \tilde{\mathbf{A}}_{\parallel\mathbf{k}} \\ &= \int_{-\pi}^{\pi} dk_\parallel \text{Tr} \mathbf{A}_{\parallel -\mathbf{k}} - i \int_{-\pi}^{\pi} dk_\parallel \text{Tr} (S_{-\mathbf{k}} \nabla_{-\mathbf{k}} S_{-\mathbf{k}}^\dagger) \\ &= \int_{-\pi}^{\pi} dk_\parallel \text{Tr} \mathbf{A}_{\parallel(k_\parallel, -\mathbf{k}_\perp)} + 2\pi\nu, \quad \nu \in \mathbb{Z} \\ &= \gamma_{-\mathbf{k}_\perp} \mod 2\pi,\end{aligned}\tag{E.5}$$

where we recognized the definition of the winding number ν of the unitary matrix $S_{\mathbf{k}}$ in the second term of the second line. Since the combination of occupied and empty bands is necessarily trivial, we have the additional constraint $\gamma_{\mathbf{k}_\perp} + \tilde{\gamma}_{\mathbf{k}_\perp} = 0$. Note that this constraint holds only in the convention where $|\alpha_{\mathbf{k}\xi}\rangle$ is periodic in the Brillouin zone. See Section E.2 for a generalization to non-periodic BdG states. Thus, at all momenta $\bar{\mathbf{k}}_\perp$, where $\bar{\mathbf{k}}_\perp$ is equal to $-\mathbf{k}_\perp$ upon the addition of reciprocal lattice vectors, we obtain

$$\gamma_{\bar{\mathbf{k}}_\perp} = 0, \pi,\tag{E.6}$$

and the same for $\tilde{\gamma}_{\bar{\mathbf{k}}_\perp}$.

E.2 Constraints on the Berry phase for arbitrary atomic positions

In Chapter 8 and the previous section, we have used a convention where the BdG eigenfunctions $u_{\mathbf{k}\xi j}$ and $v_{\mathbf{k}\xi j}$ are periodic in the Brillouin zone. By this, we in effect placed all atomic orbitals that contribute to the quasiparticle spectrum at the origin of the unit cell. In general however, the BdG Hamiltonian is not periodic in the Brillouin zone, but rather satisfies

$$\mathcal{H}_{\mathbf{k}+\mathbf{G}ij} = V(\mathbf{G})_{im} \mathcal{H}_{\mathbf{k}mn} V^\dagger(\mathbf{G})_{nj},\tag{E.7}$$

with \mathbf{G} a reciprocal lattice vector, and summation over repeated indices implied. This unitary transformation is determined by the atomic positions \mathbf{r}_i , $i = 1 \dots M$:

$$V(\mathbf{G})_{ij} = \begin{pmatrix} 1 & 0 \\ 0 & 1 \end{pmatrix} e^{-i\mathbf{G}\cdot\mathbf{r}_i} \delta_{ij}.\tag{E.8}$$

This leads to the physically motivated gauge choice

$$\begin{pmatrix} v_{k+G\xi i} \\ u_{k+G\xi i} \end{pmatrix} = V(\mathbf{G})_{ij} \begin{pmatrix} v_{k\xi j} \\ u_{k\xi j} \end{pmatrix}, \quad (\text{E.9})$$

which encapsulates information about the atomic positions in the boundary conditions of the BdG functions. The quantization condition on the Berry phase, Equation (E.6), becomes modified in this convention. Crucially, the constraint $\gamma_{\mathbf{k}_\perp} + \tilde{\gamma}_{\mathbf{k}_\perp} = 0$ does not hold anymore. We can see this by noting that $\gamma_{\mathbf{k}_\perp} + \tilde{\gamma}_{\mathbf{k}_\perp}$ is insensitive to any kind of gap closing between the occupied and empty subspace. To calculate it conveniently, we may therefore use trivial eigenstates equal to the Hilbert space basis vectors, modulo phase factors stemming from the constraint (E.9). We obtain

$$\gamma_{\mathbf{k}_\perp} + \tilde{\gamma}_{\mathbf{k}_\perp} \bmod 2\pi = 4\pi \sum_i r_{\parallel i} \bmod 2\pi, \quad (\text{E.10})$$

where $r_{\parallel i}$ is the i th atom's coordinate along the direction corresponding to k_\parallel in Equation (E.3). On the other hand, the constraint in Equation (E.5) due to particle-hole symmetry is still valid (importantly, the matrix S_k used in its derivation is always periodic in the Brillouin zone). At high-symmetry momenta $\bar{\mathbf{k}}_\perp = -\bar{\mathbf{k}}_\perp$, we have

$$\gamma_{\bar{\mathbf{k}}_\perp} \bmod \pi = 2\pi \sum_i r_{\parallel i} \bmod \pi. \quad (\text{E.11})$$

Given the atomic positions \mathbf{r}_i , the occupied subspace Berry phase therefore distinguishes between two distinct classes: Either $\gamma_{\bar{\mathbf{k}}_\perp} = 2\pi \sum_i r_{\parallel i} \bmod 2\pi$ (the trivial case), or $\gamma_{\bar{\mathbf{k}}_\perp} = \pi + 2\pi \sum_i r_{\parallel i} \bmod 2\pi$ (the topological case). For a one-dimensional system, this refines our real-space picture in the Majorana basis. The $2M$ Majorana degrees of freedom originally stem from electrons at the atomic positions r_i , $i = 1 \dots M$. The Majorana Wannier center becomes

$$x_0 - \sum_i r_i \bmod 1 = \begin{cases} 0 & \text{trivial,} \\ \frac{1}{2} & \text{topological.} \end{cases} \quad (\text{E.12})$$

We thereby recover the generalization of the Majorana polarization discussed in Chapter 8.

E.3 Two-dimensional second-order topological superconductors

We next discuss our results in the context of two-dimensional second-order topological superconductors (second-order TSCs) [24, 236, 266]. These represent novel

topological phases of matter that host pointlike Majorana zeromodes at the corners of two-dimensional samples. In addition to particle-hole symmetry, they require crystalline symmetries for their topological protection (otherwise, the Majorana zeromodes could be adiabatically brought together along the sample edge and pairwise annihilated without a bulk gap closing). The most interesting case for our purposes is that of a second-order TSC protected by \mathcal{C}_4 rotations and spinful time-reversal symmetry (hosting four Kramers pairs of Majorana corner modes in a square sample geometry), as there are so far no bulk topological invariants available that allow to diagnose it. In particular, all symmetry indicators and (nested) Wilson loop indices are trivial [239]. We will now show that this phase can nevertheless be identified by the decay behavior of its Cooper pair wavefunctions in 2D. (Compare this with the 1D p -wave superconductor, which is also identifiable via the Berry phase, or the 2D chiral superconductor, which is also identifiable via the Chern number.)

For our purposes, it is in fact enough to show that our methods can diagnose the time-reversal broken model, which in principle also can be achieved via its nonzero \mathcal{C}_4 symmetry indicator invariants [32]: In contrast to other topological invariants, the real-space decay properties we consider survive the addition of spinful time-reversal symmetry [153, 154] (time-reversal acts locally in real space and merely implies a Kramers doubling of all Cooper pair wavefunctions). We use the following BdG Hamiltonian to model the \mathcal{C}_4 -protected second-order TSC:

$$H(k_x, k_y) = (M - \cos k_x - \cos k_y) \sigma_z \tau_z + \Delta \sin k_x \sigma_z \tau_x + \Delta \sin k_y \sigma_z \tau_y + \delta (\cos k_x - \cos k_y) \sigma_y \tau_0, \quad (\text{E.13})$$

where σ_i and τ_i , $i = 0, x, y, z$, are Pauli matrices and we abbreviate the Kronecker product $\sigma_i \otimes \tau_j$ by $\sigma_i \tau_j$. We interpret σ_i as acting on a sublattice index while τ_i acts on particle-hole space. \mathcal{C}_4 and particle-hole symmetry are represented by $\mathcal{C}_4 = \sigma_z e^{i\frac{\pi}{4}\tau_z}$ and $\mathcal{P} = \tau_x K$. $H(k_x, k_y)$ is equivalent to a time-reversal broken version of the second-order topological insulator model introduced in Reference [23]. For $|M| < 2$ and nonzero Δ, δ , the model is in the second-order topological phase and exhibits four corner Majorana zeromodes.

We now show that as long as we require \mathcal{C}_4 -symmetric Cooper pair wavefunctions (i.e., wavefunctions that are eigenfunctions of the \mathcal{C}_4 operator), the nontrivial second-order topological nature of $H(k_x, k_y)$ can be diagnosed by the real-space decay behavior of these wavefunctions. To decompose the ground state into \mathcal{C}_4 eigenspaces, we need to find a smooth and symmetric gauge in Bloch space. For this, we first diagonalize $H(k_x, k_y)$. Note that the term multiplying $(\cos k_x - \cos k_y)$ is proportional to the identity matrix in particle-hole space and so we can first independently diagonalize the other terms, arriving at the block-diagonal Hamiltonian

$$\tilde{H}(k_x, k_y) = \epsilon(k_x, k_y) \sigma_z \tau_z + (\cos k_x - \cos k_y) \sigma_y \tau_0, \quad (\text{E.14})$$

where we defined

$$\epsilon(k_x, k_y) = \sqrt{3 + 2(\cos k_x \cos k_y - \cos k_x - \cos k_y)}. \quad (\text{E.15})$$

The block-diagonal form of $\tilde{H}(k_x, k_y)$ allows us to find the following smooth negative-energy eigenstates:

$$\begin{aligned} |\Psi_1(k_x, k_y)\rangle &= \frac{1}{n(k_x, k_y)} \\ &\left[\cos k_y - \cos k_x, 0, i\sqrt{3 + \cos^2 k_x + \cos^2 k_y - 2(\cos k_x + \cos k_y)} + i\epsilon(k_x, k_y), 0 \right], \\ |\Psi_2(k_x, k_y)\rangle &= \frac{1}{n(k_x, k_y)} \\ &\left[0, i\sqrt{3 + \cos^2 k_x + \cos^2 k_y - 2(\cos k_x + \cos k_y)} + i\epsilon(k_x, k_y), 0, \cos k_x - \cos k_y \right], \end{aligned} \quad (\text{E.16})$$

where we introduced the normalization factor

$$\begin{aligned} n(k_x, k_y) &= \sqrt{8 - 4(\cos k_x + \cos k_y) + \cos 2k_x + \cos 2k_y + \epsilon(k_x, k_y)f(k_x, k_y)}, \\ f(k_x, k_y) &= \sqrt{16 - 8(\cos k_x + \cos k_y) + 2(\cos 2k_x + \cos 2k_y)}. \end{aligned} \quad (\text{E.17})$$

They satisfy

$$\begin{aligned} \langle \Psi_m(k_x, k_y) | \tilde{H}(k_x, k_y) | \Psi_n(k_x, k_y) \rangle &= \begin{pmatrix} -\tilde{\epsilon}(k_x, k_y) & 0 \\ 0 & -\tilde{\epsilon}(k_x, k_y) \end{pmatrix}_{mn}, \\ \tilde{\epsilon}(k_x, k_y) &= \sqrt{\epsilon(k_x, k_y)^2 + (\cos k_x - \cos k_y)^2}, \end{aligned} \quad (\text{E.18})$$

where $m, n = 1, 2$, and, crucially,

$$\langle \Psi_m(k_y, -k_x) | \mathcal{C}_4 | \Psi_n(k_x, k_y) \rangle = \begin{pmatrix} -e^{i\frac{\pi}{4}} & 0 \\ 0 & e^{-i\frac{\pi}{4}} \end{pmatrix}_{mn}, \quad (\text{E.19})$$

implying that our choice of gauge is not only smooth but also \mathcal{C}_4 -symmetric. Recall that $|\Psi_m(k_x, k_y)\rangle$ are the eigenstates of $\tilde{H}(k_x, k_y)$, not those of $H(k_x, k_y)$. To make a statement about the original model, we need to rotate back to the basis of $H(k_x, k_y)$. In practice, it is difficult to explicitly find a smooth unitary matrix $U(k_x, k_y)$ that achieves this (although such a choice of gauge is guaranteed to exist). We circumvent this problem by only considering gauge-invariant quantities from now on. In effect, Equation (E.16) achieves a \mathcal{C}_4 decomposition of the occupied

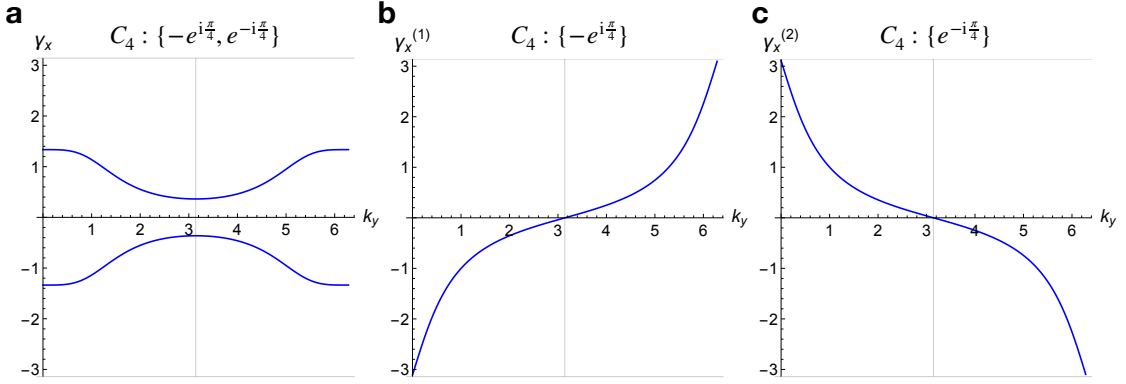


Figure E.1: Brillouin zone Wilson loops [85, 16] in the ground state of the second-order TSC model $H(k_x, k_y)$. (a) The total two-band Wilson loop is gapped and topologically trivial. Using a smooth \mathcal{C}_4 -preserving gauge, it becomes possible to calculate the Wilson loop (Berry phase) for each band separately, shown in (b),(c). The nontrivial second-order topology of $H(k_x, k_y)$ manifests itself via nonzero and opposite \mathcal{C}_4 -eigenspace Chern numbers ± 1 . Each \mathcal{C}_4 subspace is therefore topologically equivalent to a chiral TSC, and all \mathcal{C}_4 -preserving Cooper pair wavefunctions [appearing in Equation (8.7)] must decay polynomially.

subspace of $\tilde{H}(k_x, k_y)$ in the entire Brillouin zone. It therefore allows us to calculate the Chern number *per* \mathcal{C}_4 eigenspace. This Chern number can be evaluated in a gauge-invariant fashion, we may therefore use any (potentially non-smooth) unitary transformation $U(k_x, k_y)$ that satisfies

$$U(k_x, k_y)^\dagger H(k_x, k_y) U(k_x, k_y) = \tilde{H}(k_x, k_y), \quad (\text{E.20})$$

and preserves \mathcal{C}_4 symmetry, to rotate back to the original basis. We have obtained the transformation $U(k_x, k_y)$ by block-diagonalizing $H(k_x, k_y)$. Figure E.1 shows the Berry phase in x -direction $\gamma_x^{(m)}(k_y)$, labelled by the transverse momentum k_y , that we obtain for the $H(k_x, k_y)$ eigenstates $U(k_x, k_y) |\Psi_m(k_x, k_y)\rangle$, $m = 1, 2$. From the nontrivial Berry phase winding, we can immediately read off the Chern numbers ± 1 for the different \mathcal{C}_4 subspaces [267]. The Hamiltonian $H(k_x, k_y)$ can therefore be viewed as two copies of a 2D chiral TSC, one in each \mathcal{C}_4 subspace, that are coupled via a \mathcal{C}_4 -preserving potential. It follows that the Cooper pair wavefunctions belonging to individual \mathcal{C}_4 eigenvalue subspaces are those of a chiral TSC and therefore cannot be exponentially localized, and furthermore, that the Majorana Wannier functions cannot be exponentially localized *on atomic sites* (compare with Table 8.1). In fact, exploiting the equivalence of $H(k_x, k_y)$ with the model in Reference [23], we deduce that the Majorana Wannier functions for this system will be exponentially localized not at the origin (the 1a Wyckoff position), but halfway

along the diagonal of the \mathcal{C}_4 -invariant unit cell (the $1b$ Wyckoff position). Due to the \mathcal{C}_4 symmetry, the two Wannier functions are pinned to the $1b$ position – the only way for functions to move symmetrically away from the $1a$ or $1b$ position is in groups of 4. This pinning ensures that Majorana modes are paired across the diagonals of the unit cell, leading to the pairing obstruction noted above. Furthermore, we can see clearly in the Majorana picture that time-reversal symmetry does not qualitatively change this picture, since although time-reversal symmetry doubles the number of Majorana Wannier functions, it also imposes the constraint that the Wannier functions must come in pairs with the same center in real space.

Bibliography

- [1] Liang Fu, C. L. Kane, and E. J. Mele. Topological insulators in three dimensions. *Phys. Rev. Lett.*, 98:106803, 2007.
- [2] J. E. Moore and L. Balents. Topological invariants of time-reversal-invariant band structures. *Phys. Rev. B*, 75:121306, 2007.
- [3] D. Hsieh, Y. Xia, L. Wray, D. Qian, A. Pal, J. H. Dil, J. Osterwalder, F. Meier, G. Bihlmayer, C. L. Kane, Y. S. Hor, R. J. Cava, and M. Z. Hasan. Observation of unconventional quantum spin textures in topological insulators. *Science*, 323(5916):919–922, 2009.
- [4] Rahul Roy. Topological phases and the quantum spin Hall effect in three dimensions. *Phys. Rev. B*, 79:195322, 2009.
- [5] Liang Fu and C. L. Kane. Topological insulators with inversion symmetry. *Phys. Rev. B*, 76:045302, 2007.
- [6] Y. Xia, D. Qian, D. Hsieh, L. Wray, A. Pal, H. Lin, A. Bansil, D. Grauer, Y. S. Hor, R. J. Cava, and M. Z. Hasan. Observation of a large-gap topological-insulator class with a single dirac cone on the surface. *Nat Phys*, 5(6):398–402, 06 2009.
- [7] Y. L. Chen, J. G. Analytis, J.-H. Chu, Z. K. Liu, S.-K. Mo, X. L. Qi, H. J. Zhang, D. H. Lu, X. Dai, Z. Fang, S. C. Zhang, I. R. Fisher, Z. Hussain, and Z.-X. Shen. Experimental realization of a three-dimensional topological insulator, Bi_2Te_3 . *Science*, 325(5937):178–181, 2009.
- [8] Liang Fu. Topological crystalline insulators. *Phys. Rev. Lett.*, 106:106802, 2011.
- [9] Timothy H. Hsieh, Hsin Lin, Junwei Liu, Wenhui Duan, Arun Bansil, and Liang Fu. Topological crystalline insulators in the SnTe material class. *Nature Communications*, 3(1), 2012.

- [10] P. Dziawa, B. J. Kowalski, K. Dybko, R. Buczko, A. Szczerbakow, M. Szot, E. Ausakowska, T. Balasubramanian, B. M. Wojek, M. H. Berntsen, O. Tjernberg, and T. Story. Topological crystalline insulator states in Pb-SnSe. *Nat Mater*, 11(12):1023–1027, 12 2012.
- [11] Roger S. K. Mong, Andrew M. Essin, and Joel E. Moore. Antiferromagnetic topological insulators. *Phys. Rev. B*, 81:245209, 2010.
- [12] Y. Tanaka, Zhi Ren, T. Sato, K. Nakayama, S. Souma, T. Takahashi, Kouji Segawa, and Yoichi Ando. Experimental realization of a topological crystalline insulator in SnTe. *Nat Phys*, 8(11):800–803, 11 2012.
- [13] Su-Yang Xu, Chang Liu, N. Alidoust, M. Neupane, D. Qian, I. Belopolski, J. D. Denlinger, Y. J. Wang, H. Lin, L. A. Wray, G. Landolt, B. Slomski, J. H. Dil, A. Marcinkova, E. Morosan, Q. Gibson, R. Sankar, F. C. Chou, R. J. Cava, A. Bansil, and M. Z. Hasan. Observation of a topological crystalline insulator phase and topological phase transition in $\text{Pb}_{1-x}\text{Sn}_x\text{Te}$. *Nature Communications*, 3:1192 EP –, 11 2012.
- [14] Barry Bradlyn, L. Elcoro, Jennifer Cano, M. G. Vergniory, Zhijun Wang, C. Felser, M. I. Aroyo, and B. Andrei Bernevig. Topological quantum chemistry. *Nature*, 547(7663):298–305, 2017.
- [15] Hoi Chun Po, Haruki Watanabe, and Ashvin Vishwanath. Fragile topology and Wannier obstructions. *Phys. Rev. Lett.*, 121:126402, 2018.
- [16] Barry Bradlyn, Zhijun Wang, Jennifer Cano, and B. Andrei Bernevig. Disconnected elementary band representations, fragile topology, and Wilson loops as topological indices: An example on the triangular lattice. *Phys. Rev. B*, 99:045140, 2019.
- [17] Adrien Bouhon, Annica M. Black-Schaffer, and Robert-Jan Slager. Wilson loop approach to fragile topology of split elementary band representations and topological crystalline insulators with time-reversal symmetry. *Phys. Rev. B*, 100:195135, 2019.
- [18] Junyeong Ahn, Sungjoon Park, and Bohm-Jung Yang. Failure of nielsen-ninomiya theorem and fragile topology in two-dimensional systems with space-time inversion symmetry: Application to twisted bilayer graphene at magic angle. *Phys. Rev. X*, 9:021013, 2019.
- [19] Benjamin J. Wieder and B. Andrei Bernevig. The Axion Insulator as a Pump of Fragile Topology. *arXiv e-prints*, page arXiv:1810.02373, 2018.

- [20] María Blanco de Paz, Maia G. Vergniory, Dario Bercioux, Aitzol García-Etxarri, and Barry Bradlyn. Engineering fragile topology in photonic crystals: Topological quantum chemistry of light. *Phys. Rev. Research*, 1:032005, 2019.
- [21] Juan L. Mañes. Fragile Phonon Topology on the Time-Reversal Symmetric Honeycomb. *arXiv e-prints*, page arXiv:1904.06997, 2019.
- [22] Zhida Song, L. Elcoro, Nicolas Regnault, and B. Andrei Bernevig. Fragile Phases As Affine Monoids: Full Classification and Material Examples. *arXiv e-prints*, page arXiv:1905.03262, 2019.
- [23] Zhida Song, Zhong Fang, and Chen Fang. $(d - 2)$ -dimensional edge states of rotation symmetry protected topological states. *Phys. Rev. Lett.*, 119:246402, 2017.
- [24] Josias Langbehn, Yang Peng, Luka Trifunovic, Felix von Oppen, and Piet W. Brouwer. Reflection-symmetric second-order topological insulators and superconductors. *Phys. Rev. Lett.*, 119:246401, 2017.
- [25] Vladimir A. Benalcazar, B. Andrei Bernevig, and Taylor L. Hughes. Electric multipole moments, topological multipole moment pumping, and chiral hinge states in crystalline insulators. *Phys. Rev. B*, 96:245115, 2017.
- [26] Frank Schindler, Ashley M. Cook, Maia G. Vergniory, Zhijun Wang, Stuart S. P. Parkin, B. Andrei Bernevig, and Titus Neupert. Higher-order topological insulators. *Science Advances*, 4(6):eaat0346, 2018.
- [27] Max Geier, Luka Trifunovic, Max Hoskam, and Piet W. Brouwer. Second-order topological insulators and superconductors with an order-two crystalline symmetry. *Phys. Rev. B*, 97:205135, 2018.
- [28] Luka Trifunovic and Piet W. Brouwer. Higher-order bulk-boundary correspondence for topological crystalline phases. *Physical Review X*, 9(1), 2019.
- [29] Hoi Chun Po, Ashvin Vishwanath, and Haruki Watanabe. Symmetry-based indicators of band topology in the 230 space groups. *Nature Communications*, 8(1):50, 2017.
- [30] Eslam Khalaf, Hoi Chun Po, Ashvin Vishwanath, and Haruki Watanabe. Symmetry indicators and anomalous surface states of topological crystalline insulators. *Physical Review X*, 8(3), 2018.
- [31] Chen Fang and Liang Fu. New classes of topological crystalline insulators having surface rotation anomaly. *Science Advances*, 5(12), 2019.

- [32] Vladimir A. Benalcazar, Tianhe Li, and Taylor L. Hughes. Quantization of fractional corner charge in C_n -symmetric higher-order topological crystalline insulators. *Phys. Rev. B*, 99:245151, 2019.
- [33] Yoonseok Hwang, Junyeong Ahn, and Bohm-Jung Yang. Fragile topology protected by inversion symmetry: Diagnosis, bulk-boundary correspondence, and Wilson loop. *Physical Review B*, 100(20), 2019.
- [34] Eunwoo Lee, Rokyeon Kim, Junyeong Ahn, and Bohm-Jung Yang. Two-dimensional higher-order topology in monolayer graphdiyne. *npj Quantum Materials*, 5(1), 2020.
- [35] Maryam Taherinejad, Kevin F. Garrity, and David Vanderbilt. Wannier center sheets in topological insulators. *Physical Review B*, 89(11), 2014.
- [36] Flore K. Kunst, Guido van Miert, and Emil J. Bergholtz. Lattice models with exactly solvable topological hinge and corner states. *Physical Review B*, 97(24), 2018.
- [37] Sander H. Kooi, Guido van Miert, and Carmine Ortix. Inversion-symmetry protected chiral hinge states in stacks of doped quantum Hall layers. *Physical Review B*, 98(24), 2018.
- [38] Dumitru Călugăru, Vladimir Juričić, and Bitan Roy. Higher-order topological phases: A general principle of construction. *Physical Review B*, 99(4), 2019.
- [39] Flore K. Kunst, Guido van Miert, and Emil J. Bergholtz. Boundaries of boundaries: A systematic approach to lattice models with solvable boundary states of arbitrary codimension. *Physical Review B*, 99(8), 2019.
- [40] Kirill Plekhanov, Flavio Ronetti, Daniel Loss, and Jelena Klinovaja. Hinge states in a system of coupled rashba layers. *Physical Review Research*, 2(1), 2020.
- [41] Jinyu Zou, Zhuoran He, and Gang Xu. Higher-order topological insulators in a crisscross antiferromagnetic model. *Physical Review B*, 100(23), 2019.
- [42] M. Sitte, A. Rosch, E. Altman, and L. Fritz. Topological insulators in magnetic fields: Quantum Hall effect and edge channels with a nonquantized θ term. *Phys. Rev. Lett.*, 108:126807, 2012.
- [43] Eslam Khalaf. Higher-order topological insulators and superconductors protected by inversion symmetry. *Physical Review B*, 97(20):205136, 2018.

- [44] Chen Fang and Liang Fu. New classes of three-dimensional topological crystalline insulators: Nonsymmorphic and magnetic. *Physical Review B*, 91(16), 2015.
- [45] Heejae Kim, Ken Shiozaki, and Shuichi Murakami. Glide-symmetric magnetic topological crystalline insulators with inversion symmetry. *Physical Review B*, 100(16), 2019.
- [46] Yang Peng and Gil Refael. Floquet second-order topological insulators from nonsymmorphic space-time symmetries. *Physical Review Letters*, 123(1), 2019.
- [47] Alexei Kitaev. Periodic table for topological insulators and superconductors. *AIP Conference Proceedings*, 2009.
- [48] Shinsei Ryu, Andreas P Schnyder, Akira Furusaki, and Andreas W W Ludwig. Topological insulators and superconductors: tenfold way and dimensional hierarchy. *New Journal of Physics*, 12(6):065010, 2010.
- [49] Haruki Watanabe, Hoi Chun Po, and Ashvin Vishwanath. Structure and topology of band structures in the 1651 magnetic space groups. *Science Advances*, 4(8), 2018.
- [50] Ching-Kai Chiu, Hong Yao, and Shinsei Ryu. Classification of topological insulators and superconductors in the presence of reflection symmetry. *Phys. Rev. B*, 88:075142, 2013.
- [51] Takahiro Morimoto and Akira Furusaki. Topological classification with additional symmetries from clifford algebras. *Physical Review B*, 88(12), 2013.
- [52] Ken Shiozaki and Masatoshi Sato. Topology of crystalline insulators and superconductors. *Physical Review B*, 90(16), 2014.
- [53] Ching-Kai Chiu, Jeffrey C. Y. Teo, Andreas P. Schnyder, and Shinsei Ryu. Classification of topological quantum matter with symmetries. *Reviews of Modern Physics*, 88(3), 2016.
- [54] Ryan Thorngren and Dominic V. Else. Gauging spatial symmetries and the classification of topological crystalline phases. *Physical Review X*, 8(1), 2018.
- [55] Ken Shiozaki. The classification of surface states of topological insulators and superconductors with magnetic point group symmetry. *arXiv e-prints*, page arXiv:1907.09354, 2019.

- [56] Nobuyuki Okuma, Masatoshi Sato, and Ken Shiozaki. Topological classification under nonmagnetic and magnetic point group symmetry: Application of real-space Atiyah-Hirzebruch spectral sequence to higher-order topology. *Physical Review B*, 99(8), 2019.
- [57] Eyal Cornfeld and Adam Chapman. Classification of crystalline topological insulators and superconductors with point group symmetries. *Physical Review B*, 99(7), 2019.
- [58] Iñigo Robredo, Maia G. Vergniory, and Barry Bradlyn. Higher-order and crystalline topology in a phenomenological tight-binding model of lead telluride. *Physical Review Materials*, 3(4), 2019.
- [59] Jorge I. Facio, Sanjib Kumar Das, Yang Zhang, Klaus Koepernik, Jeroen van den Brink, and Ion Cosma Fulga. Dual topology in jacutingaite Pt_2HgSe_3 . *Physical Review Materials*, 3(7), 2019.
- [60] Alexey A. Soluyanov, Dominik Gresch, Zhijun Wang, QuanSheng Wu, Matthias Troyer, Xi Dai, and B. Andrei Bernevig. Type-II Weyl semimetals. *Nature*, 527(7579):495–498, 2015.
- [61] Zhijun Wang, Dominik Gresch, Alexey A. Soluyanov, Weiwei Xie, S. Kushwaha, Xi Dai, Matthias Troyer, Robert J. Cava, and B. Andrei Bernevig. MoTe_2 : A type-II Weyl topological metal. *Physical Review Letters*, 117(5), 2016.
- [62] Zhijun Wang, Benjamin J. Wieder, Jian Li, Binghai Yan, and B. Andrei Bernevig. Higher-order topology, monopole nodal lines, and the origin of large Fermi arcs in transition metal dichalcogenides XTe_2 ($\text{X}=\text{Mo},\text{W}$). *Physical Review Letters*, 123(18), 2019.
- [63] Feng Tang, Hoi Chun Po, Ashvin Vishwanath, and Xiangang Wan. Comprehensive search for topological materials using symmetry indicators. *Nature*, 566(7745):486–489, 2019.
- [64] Xiaoting Zhou, Chuang-Han Hsu, Tay-Rong Chang, Hung-Ju Tien, Qiong Ma, Pablo Jarillo-Herrero, Nuh Gedik, Arun Bansil, Vitor M. Pereira, Su-Yang Xu, Hsin Lin, and Liang Fu. Topological crystalline insulator states in the Ca_2As family. *Physical Review B*, 98(24), 2018.
- [65] Tan Zhang, Changming Yue, Tiantian Zhang, Simin Nie, Zhijun Wang, Chen Fang, Hongming Weng, and Zhong Fang. Topological crystalline insulators with C_2 rotation anomaly. *Physical Review Research*, 1(1), 2019.

- [66] Changming Yue, Yuanfeng Xu, Zhida Song, Hongming Weng, Yuan-Ming Lu, Chen Fang, and Xi Dai. Symmetry-enforced chiral hinge states and surface quantum anomalous Hall effect in the magnetic axion insulator $\text{Bi}_{2-x}\text{Sm}_x\text{Se}_3$. *Nature Physics*, 15(6):577–581, 2019.
- [67] Haijun Zhang, Chao-Xing Liu, Xiao-Liang Qi, Xi Dai, Zhong Fang, and Shou-Cheng Zhang. Topological insulators in Bi_2Se_3 , Bi_2Te_3 and Sb_2Te_3 with a single dirac cone on the surface. *Nature Physics*, 5(6):438–442, 2009.
- [68] Yuanfeng Xu, Zhida Song, Zhijun Wang, Hongming Weng, and Xi Dai. Higher-order topology of the axion insulator EuIn_2As_2 . *Physical Review Letters*, 122(25), 2019.
- [69] M. G. Vergniory, L. Elcoro, Claudia Felser, Nicolas Regnault, B. Andrei Bernevig, and Zhijun Wang. A complete catalogue of high-quality topological materials. *Nature*, 566(7745):480–485, 2019.
- [70] Tiantian Zhang, Yi Jiang, Zhida Song, He Huang, Yuqing He, Zhong Fang, Hongming Weng, and Chen Fang. Catalogue of topological electronic materials. *Nature*, 566(7745):475–479, 2019.
- [71] Anil Murani, Alik Kasumov, Shamashis Sengupta, Yu A. Kasumov, V. T. Volkov, I. I. Khodos, F. Brisset, Raphaëlle Delagrange, Alexei Chepelianskii, Richard Deblock, Hélène Bouchiat, and Sophie Guéron. Ballistic edge states in bismuth nanowires revealed by squid interferometry. *Nature Communications*, 8:15941, 2017.
- [72] Frank Schindler, Zhijun Wang, Maia G. Vergniory, Ashley M. Cook, Anil Murani, Shamashis Sengupta, Alik Yu. Kasumov, Richard Deblock, Sangjun Jeon, Ilya Drozdov, and et al. Higher-order topology in bismuth. *Nature Physics*, 14(9):918–924, 2018.
- [73] Abhay Kumar Nayak, Jonathan Reiner, Raquel Queiroz, Huixia Fu, Chandra Shekhar, Binghai Yan, Claudia Felser, Nurit Avraham, and Haim Beidenkopf. Resolving the topological classification of bismuth with topological defects. *Science Advances*, 5(11), 2019.
- [74] Chuang-Han Hsu, Xiaoting Zhou, Qiong Ma, Nuh Gedik, Arun Bansil, Victor M Pereira, Hsin Lin, Liang Fu, Su-Yang Xu, and Tay-Rong Chang. Purely rotational symmetry-protected topological crystalline insulator $\alpha\text{-Bi}_4\text{Br}_4$. *2D Materials*, 6(3):031004, 2019.

- [75] Feng Tang, Hoi Chun Po, Ashvin Vishwanath, and Xiangang Wan. Efficient topological materials discovery using symmetry indicators. *Nature Physics*, 15(5):470–476, 2019.
- [76] Ryo Noguchi, Masaru Kobayashi, Zhanzhi Jiang, Kenta Kuroda, Takanari Takahashi, Zifan Xu, Daehun Lee, Motoaki Hirayama, Masayuki Ochi, Tetsuroh Shirasawa, Peng Zhang, Chun Lin, Cédric Bareille, Shunsuke Sakuragi, Hiroaki Tanaka, So Kunisada, Kifu Kurokawa, Koichiro Yaji, Ayumi Harasawa, Viktor Kandyba, Alessio Giampietri, Alexei Barinov, Timur K. Kim, Cephise Cacho, Makoto Hashimoto, Donghui Lu, Shik Shin, Ryotaro Arita, Keji Lai, Takao Sasagawa, and Takeshi Kondo. A higher-order topological insulator built from the van der Waals stacking of bismuth bromide chains. *arXiv e-prints*, page arXiv:2002.01134, February 2020.
- [77] Liang Fu and C. L. Kane. Time reversal polarization and a Z_2 adiabatic spin pump. *Phys. Rev. B*, 74:195312, 2006.
- [78] Nicola Marzari, Arash A. Mostofi, Jonathan R. Yates, Ivo Souza, and David Vanderbilt. Maximally localized Wannier functions: Theory and applications. *Rev. Mod. Phys.*, 84:1419–1475, 2012.
- [79] W. P. Su, J. R. Schrieffer, and A. J. Heeger. Solitons in polyacetylene. *Phys. Rev. Lett.*, 42:1698–1701, 1979.
- [80] Nicola A. Spaldin. A beginner’s guide to the modern theory of polarization. *Journal of Solid State Chemistry*, 195:2 – 10, 2012. Polar Inorganic Materials: Design Strategies and Functional Properties.
- [81] R. Peierls. Zur Theorie des Diamagnetismus von Leitungselektronen. *Zeitschrift für Physik*, 80(11):763–791, 1933.
- [82] H.B. Nielsen and Masao Ninomiya. The Adler-Bell-Jackiw anomaly and Weyl fermions in a crystal. *Physics Letters B*, 130(6):389 – 396, 1983.
- [83] Lukasz Fidkowski, T. S. Jackson, and Israel Klich. Model characterization of gapless edge modes of topological insulators using intermediate Brillouin-zone functions. *Physical Review Letters*, 107(3), 2011.
- [84] Rui Yu, Xiao Liang Qi, Andrei Bernevig, Zhong Fang, and Xi Dai. Equivalent expression of \mathbb{Z}_2 topological invariant for band insulators using the non-abelian berry connection. *Phys. Rev. B*, 84:075119, 2011.

- [85] A. Alexandradinata, Xi Dai, and B. Andrei Bernevig. Wilson-loop characterization of inversion-symmetric topological insulators. *Phys. Rev. B*, 89:155114, 2014.
- [86] Vladimir A. Benalcazar, B. Andrei Bernevig, and Taylor L. Hughes. Quantized electric multipole insulators. *Science*, 357(6346):61–66, 2017.
- [87] R. D. King-Smith and David Vanderbilt. Theory of polarization of crystalline solids. *Physical Review B*, 47(3):1651–1654, 1993.
- [88] Nicola Marzari and David Vanderbilt. Maximally localized generalized Wannier functions for composite energy bands. *Physical Review B*, 56(20):12847–12865, 1997.
- [89] Raffaele Resta. Quantum-mechanical position operator in extended systems. *Physical Review Letters*, 80(9):1800–1803, 1998.
- [90] Guido van Miert and Carmine Ortix. Higher-order topological insulators protected by inversion and rotoinversion symmetries. *Phys. Rev. B*, 98:081110, 2018.
- [91] Zhida Song, Tiantian Zhang, Zhong Fang, and Chen Fang. Quantitative mappings between symmetry and topology in solids. *Nature Communications*, 9(1), 2018.
- [92] Jeffrey C. Y. Teo, Liang Fu, and C. L. Kane. Surface states and topological invariants in three-dimensional topological insulators: Application to $\text{Bi}_{1-x}\text{Sb}_x$. *Phys. Rev. B*, 78:045426, 2008.
- [93] Hoi Chun Po. Symmetry indicators of band topology. *Journal of Physics: Condensed Matter*, 32(26):263001, apr 2020.
- [94] Fan Zhang, C. L. Kane, and E. J. Mele. Surface state magnetization and chiral edge states on topological insulators. *Phys. Rev. Lett.*, 110:046404, 2013.
- [95] Akishi Matsugatani and Haruki Watanabe. Connecting higher-order topological insulators to lower-dimensional topological insulators. *Phys. Rev. B*, 98:205129, 2018.
- [96] Motohiko Ezawa. Magnetic second-order topological insulators and semimetals. *Phys. Rev. B*, 97:155305, 2018.
- [97] Nicodemos Varnava and David Vanderbilt. Surfaces of axion insulators. *Physical Review B*, 98(24), 2018.

- [98] Junyeong Ahn and Bohm-Jung Yang. Symmetry representation approach to topological invariants in C_2T -symmetric systems. *Physical Review B*, 99(23), 2019.
- [99] Andrew M. Essin, Joel E. Moore, and David Vanderbilt. Magnetoelectric polarizability and axion electrodynamics in crystalline insulators. *Phys. Rev. Lett.*, 102:146805, 2009.
- [100] Frank Wilczek. Two applications of axion electrodynamics. *Physical Review Letters*, 58(18):1799–1802, 1987.
- [101] Heqiu Li and Kai Sun. Pfaffian formalism for higher-order topological insulators. *Physical Review Letters*, 124(3), 2020.
- [102] Alexey A. Soluyanov and David Vanderbilt. Computing topological invariants without inversion symmetry. *Physical Review B*, 83(23), 2011.
- [103] Georg W. Winkler, Alexey A. Soluyanov, and Matthias Troyer. Smooth gauge and Wannier functions for topological band structures in arbitrary dimensions. *Phys. Rev. B*, 93:035453, 2016.
- [104] C. J. Bradley and A. P. Cracknell. *The Mathematical Theory of Symmetry in Solids*. Clarendon Press Oxford, Oxford, United Kingdom, 1972.
- [105] D. B. Litvin. *Magnetic Group Tables*. International Union of Crystallography, 2013.
- [106] K. v. Klitzing, G. Dorda, and M. Pepper. New method for high-accuracy determination of the fine-structure constant based on quantized Hall resistance. *Phys. Rev. Lett.*, 45:494–497, 1980.
- [107] F. D. M. Haldane. Model for a quantum Hall effect without Landau levels: Condensed-matter realization of the "parity anomaly". *Phys. Rev. Lett.*, 61:2015–2018, 1988.
- [108] C. L. Kane and E. J. Mele. \mathbb{Z}_2 topological order and the quantum spin Hall effect. *Phys. Rev. Lett.*, 95:146802, 2005.
- [109] Xiao-Liang Qi, Yong-Shi Wu, and Shou-Cheng Zhang. Topological quantization of the spin Hall effect in two-dimensional paramagnetic semiconductors. *Phys. Rev. B*, 74:085308, 2006.
- [110] B. Andrei Bernevig, Taylor L. Hughes, and Shou-Cheng Zhang. Quantum spin Hall effect and topological phase transition in HgTe quantum wells. *Science*, 314(5806):1757–1761, 2006.

- [111] B. Andrei Bernevig and Shou-Cheng Zhang. Quantum spin Hall effect. *Phys. Rev. Lett.*, 96:106802, 2006.
- [112] Oindrila Deb, Abhiram Soori, and Diptiman Sen. Edge states of a three-dimensional topological insulator. *Journal of Physics: Condensed Matter*, 26(31):315009, 2014.
- [113] R. Jackiw and C. Rebbi. Solitons with fermion number 1/2. *Phys. Rev. D*, 13:3398–3409, 1976.
- [114] Xiao-Liang Qi, Taylor L. Hughes, and Shou-Cheng Zhang. Topological field theory of time-reversal invariant insulators. *Phys. Rev. B*, 78:195424, 2008.
- [115] C. L. Kane and E. J. Mele. Quantum spin Hall effect in graphene. *Phys. Rev. Lett.*, 95:226801, 2005.
- [116] Hui Li and F. D. M. Haldane. Entanglement spectrum as a generalization of entanglement entropy: Identification of topological order in non-abelian fractional quantum Hall effect states. *Phys. Rev. Lett.*, 101:010504, 2008.
- [117] Ingo Peschel. Calculation of reduced density matrices from correlation functions. *Journal of Physics A: Mathematical and General*, 36(14):L205, 2003.
- [118] Lukasz Fidkowski. Entanglement spectrum of topological insulators and superconductors. *Phys. Rev. Lett.*, 104:130502, 2010.
- [119] Masashi Iizumi, Yoshikazu Hamaguchi, Kiichi F. Komatsubara, and Yoshiaki Kato. Phase transition in SnTe with low carrier concentration. *Journal of the Physical Society of Japan*, 38(2):443–449, 1975.
- [120] E. Plekhanov, P. Barone, D. Di Sante, and S. Picozzi. Engineering relativistic effects in ferroelectric SnTe. *Phys. Rev. B*, 90:161108, 2014.
- [121] Tian Liang, Satya Kushwaha, Jinwoong Kim, Quinn Gibson, Jingjing Lin, Nicholas Kioussis, Robert J. Cava, and N. Phuan Ong. A pressure-induced topological phase with large berry curvature in $Pb_{1-x}Sn_xTe$. *Science Advances*, 3(5), 2017.
- [122] Paolo Sessi, Domenico Di Sante, Andrzej Szczerbakow, Florian Glott, Stefan Wilfert, Henrik Schmidt, Thomas Bathon, Piotr Dziawa, Martin Greiter, Titus Neupert, Giorgio Sangiovanni, Tomasz Story, Ronny Thomale, and Matthias Bode. Robust spin-polarized midgap states at step edges of topological crystalline insulators. *Science*, 354(6317):1269–1273, 2016.

- [123] I. P. Rusinov, T. V. Menshchikova, A. Isaeva, S. V. Eremeev, Yu. M. Kortteev, M. G. Vergniory, P. M. Echenique, and E. V. Chulkov. Mirror-symmetry protected non-TRIM surface state in the weak topological insulator Bi_2Te_3 . *Scientific Reports*, 6:20734 EP –, 02 2016.
- [124] Kunjalata Majhi, Koushik Pal, Himanshu Lohani, Abhishek Banerjee, Pramita Mishra, Anil K. Yadav, R. Ganesan, B. R. Sekhar, Umesh V. Waghmare, and P. S. Anil Kumar. Emergence of a weak topological insulator from the Bi_xSe_y family. *Applied Physics Letters*, 110(16):162102, 2017.
- [125] Markus Eschbach, Martin Lanius, Chengwang Niu, Ewa Mlynaczak, Pika Gospodaric, Jens Kellner, Peter Schüffelgen, Mathias Gehlmann, Sven Döring, Elmar Neumann, Martina Luysberg, Gregor Mussler, Lukasz Plucinski, Markus Morgenstern, Detlev Grützmacher, Gustav Bihlmayer, Stefan Blügel, and Claus M. Schneider. Bi_1Te_1 is a dual topological insulator. *Nature Communications*, 8:14976, 2017.
- [126] Ilya K. Drozdov, A. Alexandradinata, Sangjun Jeon, Stevan Nadj-Perge, Huiwen Ji, R. J. Cava, B. Andrei Bernevig, and Ali Yazdani. One-dimensional topological edge states of bismuth bilayers. *Nat Phys*, 10:664–669, 08 2014.
- [127] Chuan Li, A. Kasumov, Anil Murani, Shamashis Sengupta, F. Fortuna, K. Napolskii, D. Koshkodaev, G. Tsirlina, Y. Kasumov, I. Khodos, R. Deblock, M. Ferrier, S. Guéron, and H. Bouchiat. Magnetic field resistant quantum interferences in josephson junctions based on bismuth nanowires. *Phys. Rev. B*, 90:245427, 2014.
- [128] J. W. Wells, J. H. Dil, F. Meier, J. Lobo-Checa, V. N. Petrov, J. Osterwalder, M. M. Ugeda, I. Fernandez-Torrente, J. I. Pascual, E. D. L. Rienks, M. F. Jensen, and Ph. Hofmann. Nondegenerate metallic states on $\text{Bi}(114)$: A one-dimensional topological metal. *Phys. Rev. Lett.*, 102:096802, 2009.
- [129] Shuichi Murakami. Quantum spin Hall effect and enhanced magnetic response by spin-orbit coupling. *Phys. Rev. Lett.*, 97:236805, 2006.
- [130] A. Takayama, T. Sato, S. Souma, T. Oguchi, and T. Takahashi. One-dimensional edge states with giant spin splitting in a bismuth thin film. *Phys. Rev. Lett.*, 114:066402, 2015.
- [131] F. Reis, G. Li, L. Dudy, M. Bauernfeind, S. Glass, W. Hanke, R. Thomale, J. Schäfer, and R. Claessen. Bismuthene on a SiC substrate: A candidate for a high-temperature quantum spin Hall material. *Science*, 357(6348):287–290, 2017.

- [132] M. G. Vergniory, L. Elcoro, Zhijun Wang, Jennifer Cano, C. Felser, M. I. Aroyo, B. Andrei Bernevig, and Barry Bradlyn. Graph theory data for topological quantum chemistry. *Phys. Rev. E*, 96:023310, 2017.
- [133] Luis Elcoro, Barry Bradlyn, Zhijun Wang, Maia G. Vergniory, Jennifer Cano, Claudia Felser, B. Andrei Bernevig, Danel Orobengoa, Gemma de la Flor, and Mois I. Aroyo. Double crystallographic groups and their representations on the Bilbao Crystallographic Server. *Journal of Applied Crystallography*, 50(5):1457–1477, 2017.
- [134] Jennifer Cano, Barry Bradlyn, Zhijun Wang, L. Elcoro, M. G. Vergniory, C. Felser, M. I. Aroyo, and B. Andrei Bernevig. Building blocks of topological quantum chemistry: Elementary band representations. *Phys. Rev. B*, 97:035139, 2018.
- [135] Barry Bradlyn, L. Elcoro, M. G. Vergniory, Jennifer Cano, Zhijun Wang, C. Felser, M. I. Aroyo, and B. Andrei Bernevig. Band connectivity for topological quantum chemistry: Band structures as a graph theory problem. *Phys. Rev. B*, 97:035138, 2018.
- [136] Jennifer Cano, Barry Bradlyn, Zhijun Wang, L. Elcoro, M. G. Vergniory, C. Felser, M. I. Aroyo, and B. Andrei Bernevig. Topology of disconnected elementary band representations. *Phys. Rev. Lett.*, 120:266401, 2018.
- [137] Yi Liu and Roland E. Allen. Electronic structure of the semimetals Bi and Sb. *Phys. Rev. B*, 52:1566–1577, 1995.
- [138] Yoshiyuki Ohtsubo and Shin ichi Kimura. Topological phase transition of single-crystal Bi based on empirical tight-binding calculations. *New Journal of Physics*, 18(12):123015, 2016.
- [139] Yuki Fuseya, Zengwei Zhu, Benoît Fauqué, Woun Kang, Bertrand Lenoir, and Kamran Behnia. Origin of the large anisotropic g factor of holes in bismuth. *Phys. Rev. Lett.*, 115:216401, 2015.
- [140] Sean Hart, Hechen Ren, Timo Wagner, Philipp Leubner, Mathias Mühlbauer, Christoph Brüne, Hartmut Buhmann, Laurens W. Molenkamp, and Amir Yacoby. Induced superconductivity in the quantum spin Hall edge. *Nature Physics*, 10:638–643, 08 2014.
- [141] M. L. Della Rocca, M. Chauvin, B. Huard, H. Pothier, D. Esteve, and C. Urbina. Measurement of the current-phase relation of superconducting atomic contacts. *Phys. Rev. Lett.*, 99:127005, 2007.

- [142] Ying Ran, Yi Zhang, and Ashvin Vishwanath. One-dimensional topologically protected modes in topological insulators with lattice dislocations. *Nature Physics*, 5:298 EP –, 2009. Article.
- [143] Benjamin J. Wieder, Zhijun Wang, Jennifer Cano, Xi Dai, Leslie M. Schoop, Barry Bradlyn, and B. Andrei Bernevig. Strong and fragile topological Dirac semimetals with higher-order Fermi arcs. *Nature Communications*, 11(1):627, 2020.
- [144] Shang Liu, Ashvin Vishwanath, and Eslam Khalaf. Shift insulators: Rotation-protected two-dimensional topological crystalline insulators. *Phys. Rev. X*, 9:031003, 2019.
- [145] N. D. Mermin. The topological theory of defects in ordered media. *Rev. Mod. Phys.*, 51:591–648, 1979.
- [146] Valerio Peri, Zhi-Da Song, Marc Serra-Garcia, Pascal Engeler, Raquel Queiroz, Xueqin Huang, Weiyin Deng, Zhengyou Liu, B. Andrei Bernevig, and Sebastian D. Huber. Experimental characterization of fragile topology in an acoustic metamaterial. *Science*, 367(6479):797–800, 2020.
- [147] Zhi-Da Song, Luis Elcoro, and B. Andrei Bernevig. Twisted bulk-boundary correspondence of fragile topology. *Science*, 367(6479):794–797, 2020.
- [148] Ari M. Turner and Ashvin Vishwanath. Chapter 11 - beyond band insulators: Topology of semimetals and interacting phases. In Marcel Franz and Laurens Molenkamp, editors, *Topological Insulators*, volume 6 of *Contemporary Concepts of Condensed Matter Science*, pages 293 – 324. Elsevier, 2013.
- [149] W. P. Su, J. R. Schrieffer, and A. J. Heeger. Soliton excitations in polyacetylene. *Phys. Rev. B*, 22:2099–2111, 1980.
- [150] M. J. Rice and E. J. Mele. Elementary excitations of a linearly conjugated diatomic polymer. *Phys. Rev. Lett.*, 49:1455–1459, 1982.
- [151] Alexander Altland and Martin R. Zirnbauer. Nonstandard symmetry classes in mesoscopic normal-superconducting hybrid structures. *Phys. Rev. B*, 55:1142–1161, 1997.
- [152] D. J. Thouless. Quantization of particle transport. *Phys. Rev. B*, 27:6083–6087, 1983.
- [153] Alexey A. Soluyanov and David Vanderbilt. Wannier representation of \mathbb{Z}_2 topological insulators. *Phys. Rev. B*, 83:035108, 2011.

- [154] Alexey A. Soluyanov and David Vanderbilt. Smooth gauge for topological insulators. *Phys. Rev. B*, 85:115415, 2012.
- [155] Daniel Bulmash, Pavan Hosur, Shou-Cheng Zhang, and Xiao-Liang Qi. Unified topological response theory for gapped and gapless free fermions. *Phys. Rev. X*, 5:021018, 2015.
- [156] D. J. Thouless, M. Kohmoto, M. P. Nightingale, and M. den Nijs. Quantized Hall conductance in a two-dimensional periodic potential. *Phys. Rev. Lett.*, 49:405–408, 1982.
- [157] Chen Fang, Matthew J. Gilbert, and B. Andrei Bernevig. Bulk topological invariants in noninteracting point group symmetric insulators. *Phys. Rev. B*, 86:115112, 2012.
- [158] Taylor L. Hughes, Emil Prodan, and B. Andrei Bernevig. Inversion-symmetric topological insulators. *Phys. Rev. B*, 83:245132, 2011.
- [159] Zohar Ringel, Yaakov E. Kraus, and Ady Stern. Strong side of weak topological insulators. *Phys. Rev. B*, 86:045102, 2012.
- [160] Jeffrey Goldstone and Frank Wilczek. Fractional quantum numbers on solitons. *Phys. Rev. Lett.*, 47:986–989, 1981.
- [161] A.J. Niemi and G.W. Semenoff. Fermion number fractionization in quantum field theory. *Physics Reports*, 135(3):99 – 193, 1986.
- [162] Guido van Miert and Carmine Ortix. Excess charges as a probe of one-dimensional topological crystalline insulating phases. *Phys. Rev. B*, 96:235130, 2017.
- [163] J. Zak. Berry’s phase for energy bands in solids. *Phys. Rev. Lett.*, 62:2747–2750, 1989.
- [164] Raquel Queiroz, Ion Cosma Fulga, Nurit Avraham, Haim Beidenkopf, and Jennifer Cano. Partial lattice defects in higher-order topological insulators. *Phys. Rev. Lett.*, 123:266802, 2019.
- [165] Xiao-Liang Qi and Shou-Cheng Zhang. Spin-charge separation in the quantum spin Hall state. *Phys. Rev. Lett.*, 101:086802, 2008.
- [166] Ying Ran, Ashvin Vishwanath, and Dung-Hai Lee. Spin-charge separated solitons in a topological band insulator. *Phys. Rev. Lett.*, 101:086801, 2008.
- [167] P. M. Ostrovsky, I. V. Gornyi, and A. D. Mirlin. Interaction-induced criticality in \mathbb{Z}_2 topological insulators. *Phys. Rev. Lett.*, 105:036803, 2010.

- [168] F. F. Assaad, M. Bercx, and M. Hohenadler. Topological invariant and quantum spin models from magnetic π fluxes in correlated topological insulators. *Phys. Rev. X*, 3:011015, 2013.
- [169] Jeffrey C. Y. Teo and C. L. Kane. Topological defects and gapless modes in insulators and superconductors. *Phys. Rev. B*, 82:115120, 2010.
- [170] Vladimir Juričić, Andrej Mesaros, Robert-Jan Slager, and Jan Zaanen. Universal probes of two-dimensional topological insulators: Dislocation and π flux. *Phys. Rev. Lett.*, 108:106403, 2012.
- [171] Ken-Ichiro Imura, Yositake Takane, and Akihiro Tanaka. Weak topological insulator with protected gapless helical states. *Phys. Rev. B*, 84:035443, 2011.
- [172] Robert-Jan Slager, Andrej Mesaros, Vladimir Juričić, and Jan Zaanen. Interplay between electronic topology and crystal symmetry: Dislocation-line modes in topological band insulators. *Phys. Rev. B*, 90:241403, 2014.
- [173] Itamar Kimchi, Yang-Zhi Chou, Rahul M. Nandkishore, and Leo Radzihovsky. Anomalous localization at the boundary of an interacting topological insulator. *Phys. Rev. B*, 101:035131, 2020.
- [174] M. V. Berry. Quantal phase factors accompanying adiabatic changes. *Proceedings of the Royal Society of London A: Mathematical, Physical and Engineering Sciences*, 392(1802):45–57, 1984.
- [175] F. D. M. Haldane. Path dependence of the geometric rotation of polarization in optical fibers. *Opt. Lett.*, 11(11):730–732, 1986.
- [176] Markus König, Steffen Wiedmann, Christoph Brüne, Andreas Roth, Hartmut Buhmann, Laurens W. Molenkamp, Xiao-Liang Qi, and Shou-Cheng Zhang. Quantum spin Hall insulator state in HgTe quantum wells. *Science*, 318(5851):766–770, 2007.
- [177] F. D. M. Haldane and S. Raghu. Possible realization of directional optical waveguides in photonic crystals with broken time-reversal symmetry. *Phys. Rev. Lett.*, 100:013904, 2008.
- [178] Zheng Wang, Yidong Chong, J. D. Joannopoulos, and Marin Soljačić. Observation of unidirectional backscattering-immune topological electromagnetic states. *Nature*, 461:772, 2009.
- [179] C. L. Kane and T. C. Lubensky. Topological boundary modes in isostatic lattices. *Nat Phys*, 10(1):39–45, 2014.

- [180] Roman Süsstrunk and Sebastian D. Huber. Observation of phononic helical edge states in a mechanical topological insulator. *Science*, 349(6243):47–50, 2015.
- [181] Zhaoju Yang, Fei Gao, Xihang Shi, Xiao Lin, Zhen Gao, Yidong Chong, and Baile Zhang. Topological acoustics. *Phys. Rev. Lett.*, 114:114301, 2015.
- [182] Jia Ningyuan, Clai Owens, Ariel Sommer, David Schuster, and Jonathan Simon. Time-and site-resolved dynamics in a topological circuit. *Phys. Rev. X*, 5(2):021031, 2015.
- [183] Victor V. Albert, Leonid I. Glazman, and Liang Jiang. Topological properties of linear circuit lattices. *Phys. Rev. Lett.*, 114:173902, 2015.
- [184] Mohammad Hafezi, Eugene A Demler, Mikhail D Lukin, and Jacob M Taylor. Robust optical delay lines with topological protection. *Nature Physics*, 7(11):907–912, 2011.
- [185] Ling Lu, Liang Fu, John D. Joannopoulos, and Marin Soljačić. Weyl points and line nodes in gyroid photonic crystals. *Nature Photonics*, 7:294, 2013.
- [186] Tena Dubček, Colin J. Kennedy, Ling Lu, Wolfgang Ketterle, Marin Soljačić, and Hrvoje Buljan. Weyl points in three-dimensional optical lattices: Synthetic magnetic monopoles in momentum space. *Phys. Rev. Lett.*, 114:225301, 2015.
- [187] Ling Lu, Zhiyu Wang, Dexin Ye, Lixin Ran, Liang Fu, John D. Joannopoulos, and Marin Soljačić. Experimental observation of Weyl points. *Science*, 349(6248):622–624, 2015.
- [188] D. Zeb Rocklin, Bryan Gin-ge Chen, Martin Falk, Vincenzo Vitelli, and T. C. Lubensky. Mechanical Weyl modes in topological Maxwell lattices. *Phys. Rev. Lett.*, 116:135503, 2016.
- [189] Jiho Noh, Sheng Huang, Daniel Leykam, Y. D. Chong, Kevin P. Chen, and Mikael C. Rechtsman. Experimental observation of optical Weyl points and Fermi arc-like surface states. *Nat Phys*, 13(6):611–617, 2017.
- [190] Ching Hua Lee, Stefan Imhof, Christian Berger, Florian Bayer, Johannes Brehm, Laurens W Molenkamp, Tobias Kiessling, and Ronny Thomale. Topoelectrical circuits. *Communications Physics*, 1(1):39, 2018.
- [191] Robert Keil, Charles Poli, Matthias Heinrich, Jake Arkinstall, Gregor Weihs, Henning Schomerus, and Alexander Szameit. Universal sign control of coupling in tight-binding lattices. *Phys. Rev. Lett.*, 116:213901, 2016.

- [192] Jihoo Noh, Wladimir A. Benalcazar, Sheng Huang, Matthew J. Collins, Kevin P. Chen, Taylor L. Hughes, and Mikael C. Rechtsman. Topological protection of photonic mid-gap defect modes. *Nature Photonics*, 12(7):408–415, 2018.
- [193] Ching Hua Lee, Guangjie Li, Gulixun Jin, Yuhan Liu, and Xiao Zhang. Topological dynamics of gyroscopic and Floquet lattices from Newton’s laws. *Phys. Rev. B*, 97:085110, 2018.
- [194] Guido van Miert, Carmine Ortix, and Cristiane Morais Smith. Topological origin of edge states in two-dimensional inversion-symmetric insulators and semimetals. *2D Materials*, 4(1):015023, 2016.
- [195] Jun-Won Rhim, Jan Behrends, and Jens H. Bardarson. Bulk-boundary correspondence from the intercellular Zak phase. *Phys. Rev. B*, 95:035421, 2017.
- [196] Motohiko Ezawa. Higher-order topological insulators and semimetals on the breathing kagome and pyrochlore lattices. *Phys. Rev. Lett.*, 120:026801, 2018.
- [197] Motohiko Ezawa. Minimal models for Wannier-type higher-order topological insulators and phosphorene. *Phys. Rev. B*, 98:045125, 2018.
- [198] Alexander Lau, Jeroen van den Brink, and Carmine Ortix. Topological mirror insulators in one dimension. *Phys. Rev. B*, 94:165164, 2016.
- [199] Robert-Jan Slager, Andrej Mesaros, Vladimir Juričić, and Jan Zaanen. The space group classification of topological band-insulators. *Nature Physics*, 9:98 EP –, 12 2012.
- [200] Wladimir A. Benalcazar, Jeffrey C. Y. Teo, and Taylor L. Hughes. Classification of two-dimensional topological crystalline superconductors and Majorana bound states at disclinations. *Phys. Rev. B*, 89:224503, 2014.
- [201] Jorrit Kruthoff, Jan de Boer, Jasper van Wezel, Charles L. Kane, and Robert-Jan Slager. Topological classification of crystalline insulators through band structure combinatorics. *Phys. Rev. X*, 7:041069, 2017.
- [202] Frank Wilczek and A. Zee. Appearance of gauge structure in simple dynamical systems. *Phys. Rev. Lett.*, 52:2111–2114, 1984.
- [203] Michael Victor Berry. Quantal phase factors accompanying adiabatic changes. *Proceedings of the Royal Society of London. A. Mathematical and Physical Sciences*, 392(1802):45–57, 1984.

- [204] J. Zak. Band center—a conserved quantity in solids. *Phys. Rev. Lett.*, 48:359–362, 1982.
- [205] Sander H. Kooi, Guido van Miert, and Carmine Ortix. Classification of crystalline insulators without symmetry indicators: Atomic and fragile topological phases in twofold rotation symmetric systems. *Phys. Rev. B*, 100:115160, 2019.
- [206] J. Zak. Symmetry specification of bands in solids. *Phys. Rev. Lett.*, 45:1025–1028, 1980.
- [207] J. Zak. Band representations and symmetry types of bands in solids. *Phys. Rev. B*, 23:2824–2835, 1981.
- [208] Gaoxue Wang, Ravindra Pandey, and Shashi P. Karna. Atomically thin group V elemental films: Theoretical investigations of antimonene allotropes. *ACS Applied Materials & Interfaces*, 7(21):11490–11496, 2015. PMID: 25955131.
- [209] Zhen Zhu, Jie Guan, and David Tománek. Strain-induced metal-semiconductor transition in monolayers and bilayers of gray arsenic: A computational study. *Phys. Rev. B*, 91:161404, 2015.
- [210] C. Kamal and Motohiko Ezawa. Arsenene: Two-dimensional buckled and puckered honeycomb arsenic systems. *Phys. Rev. B*, 91:085423, 2015.
- [211] S. Sharma, S. Kumar, and U. Schwingenschlögl. Arsenene and antimonene: Two-dimensional materials with high thermoelectric figures of merit. *Phys. Rev. Applied*, 8:044013, 2017.
- [212] Gang Li, Werner Hanke, Ewelina M. Hankiewicz, Felix Reis, Jörg Schäfer, Ralph Claessen, Congjun Wu, and Ronny Thomale. Theoretical paradigm for the quantum spin Hall effect at high temperatures. *Phys. Rev. B*, 98:165146, 2018.
- [213] Fernando Dominguez, Benedikt Scharf, Gang Li, Jörg Schäfer, Ralph Claessen, Werner Hanke, Ronny Thomale, and Ewelina M. Hankiewicz. Testing topological protection of edge states in hexagonal quantum spin Hall candidate materials. *Phys. Rev. B*, 98:161407, 2018.
- [214] Yan Shao, Zhong-Liu Liu, Cai Cheng, Xu Wu, Hang Liu, Chen Liu, Jia-Ou Wang, Shi-Yu Zhu, Yu-Qi Wang, Dong-Xia Shi, Kurash Ibrahim, Jia-Tao Sun, Ye-Liang Wang, and Hong-Jun Gao. Epitaxial growth of flat anti-

- monene monolayer: A new honeycomb analogue of graphene. *Nano Letters*, 18(3):2133–2139, 2018. PMID: 29457727.
- [215] Jianping Ji, Xiufeng Song, Jizi Liu, Zhong Yan, Chengxue Huo, Shengli Zhang, Meng Su, Lei Liao, Wenhui Wang, Zhenhua Ni, et al. Two-dimensional antimonene single crystals grown by van der Waals epitaxy. *Nature communications*, 7:13352, 2016.
- [216] M. Fortin-Deschênes, O. Waller, T. O. Menteş, A. Locatelli, S. Mukherjee, F. Genuzio, P. L. Levesque, A. Hébert, R. Martel, and O. Moutanabbir. Synthesis of antimonene on germanium. *Nano Letters*, 17(8):4970–4975, 2017. PMID: 28678509.
- [217] J Shah, W Wang, H M Sohail, and R I G Uhrberg. Experimental evidence of monolayer arsenene: an exotic 2D semiconducting material. *2D Materials*, 7(2):025013, 2020.
- [218] Feng-Chuan Chuang, Chia-Hsiu Hsu, Chia-Yu Chen, Zhi-Quan Huang, Vidvuds Ozolins, Hsin Lin, and Arun Bansil. Tunable topological electronic structures in Sb(111) bilayers: A first-principles study. *Applied Physics Letters*, 102(2):022424, 2013.
- [219] Ya ping Wang, Chang wen Zhang, Wei xiao Ji, Run wu Zhang, Ping Li, Pei ji Wang, Miao juan Ren, Xin lian Chen, and Min Yuan. Tunable quantum spin Hall effect via strain in two-dimensional arsenene monolayer. *Journal of Physics D: Applied Physics*, 49(5):055305, 2016.
- [220] Zhi-Quan Huang, Chia-Hsiu Hsu, Feng-Chuan Chuang, Yu-Tzu Liu, Hsin Lin, Wan-Sheng Su, Vidvuds Ozolins, and Arun Bansil. Strain driven topological phase transitions in atomically thin films of group IV and V elements in the honeycomb structures. *New Journal of Physics*, 16(10):105018, 2014.
- [221] José M Soler, Emilio Artacho, Julian D Gale, Alberto García, Javier Junquera, Pablo Ordejón, and Daniel Sánchez-Portal. The SIESTA method for ab initio order-N materials simulation. *Journal of Physics: Condensed Matter*, 14(11):2745–2779, 2002.
- [222] N. Read and Dmitry Green. Paired states of fermions in two dimensions with breaking of parity and time-reversal symmetries and the fractional quantum Hall effect. *Phys. Rev. B*, 61:10267–10297, 2000.
- [223] Liang Fu and C. L. Kane. Superconducting proximity effect and Majorana fermions at the surface of a topological insulator. *Phys. Rev. Lett.*, 100:096407, 2008.

- [224] Yukio Tanaka, Masatoshi Sato, and Naoto Nagaosa. Symmetry and topology in superconductors: Odd-frequency pairing and edge states. *Journal of the Physical Society of Japan*, 81(1):011013, 2012.
- [225] Yoichi Ando and Liang Fu. Topological crystalline insulators and topological superconductors: From concepts to materials. *Annual Review of Condensed Matter Physics*, 6(1):361–381, 2015.
- [226] Shun Tamura, Shintaro Hoshino, and Yukio Tanaka. Odd-frequency pairs in chiral symmetric systems: Spectral bulk-boundary correspondence and topological criticality. *Phys. Rev. B*, 99:184512, 2019.
- [227] A Yu Kitaev. Unpaired Majorana fermions in quantum wires. *Physics-Uspekhi*, 44(10S):131–136, 2001.
- [228] Alexei Kitaev. Anyons in an exactly solved model and beyond. *Annals of Physics*, 321(1):2 – 111, 2006. January Special Issue.
- [229] Roman M. Lutchyn, Jay D. Sau, and S. Das Sarma. Majorana fermions and a topological phase transition in semiconductor-superconductor heterostructures. *Phys. Rev. Lett.*, 105:077001, 2010.
- [230] Yuval Oreg, Gil Refael, and Felix von Oppen. Helical liquids and Majorana bound states in quantum wires. *Phys. Rev. Lett.*, 105:177002, 2010.
- [231] G. Strinati. Multipole wave functions for photoelectrons in crystals. III. the role of singular points in the band structure and the tails of the Wannier functions. *Phys. Rev. B*, 18:4104–4119, 1978.
- [232] J. Dubail and N. Read. Tensor network trial states for chiral topological phases in two dimensions and a no-go theorem in any dimension. *Phys. Rev. B*, 92:205307, 2015.
- [233] Frank Schindler, Barry Bradlyn, Mark H. Fischer, and Titus Neupert. Pairing Obstructions in Topological Superconductors. *arXiv e-prints*, page arXiv:2001.02682, 2020.
- [234] Christian Brouder, Gianluca Panati, Matteo Calandra, Christophe Mourougane, and Nicola Marzari. Exponential localization of Wannier functions in insulators. *Phys. Rev. Lett.*, 98:046402, 2007.
- [235] Doru Sticlet, Cristina Bena, and Pascal Simon. Spin and Majorana polarization in topological superconducting wires. *Phys. Rev. Lett.*, 108:096802, 2012.

- [236] Yuxuan Wang, Mao Lin, and Taylor L Hughes. Weak-pairing higher order topological superconductors. *Physical Review B*, 98(16):165144, 2018.
- [237] Chen-Hsuan Hsu, Peter Stano, Jelena Klinovaja, and Daniel Loss. Majorana Kramers pairs in higher-order topological insulators. *Physical review letters*, 121(19):196801, 2018.
- [238] Dominic V. Else, Hoi Chun Po, and Haruki Watanabe. Fragile topological phases in interacting systems. *Phys. Rev. B*, 99:125122, 2019.
- [239] Frank Schindler, Marta Brzezińska, Władimir A. Benalcazar, Mikel Iraola, Adrien Bouhon, Stepan S. Tsirkin, Maia G. Vergniory, and Titus Neupert. Fractional corner charges in spin-orbit coupled crystals. *Phys. Rev. Research*, 1:033074, 2019.
- [240] T. Senthil. Symmetry-protected topological phases of quantum matter. *Annual Review of Condensed Matter Physics*, 6(1):299–324, 2015.
- [241] Xie Chen, Zheng-Cheng Gu, Zheng-Xin Liu, and Xiao-Gang Wen. Symmetry protected topological orders and the group cohomology of their symmetry group. *Phys. Rev. B*, 87:155114, 2013.
- [242] Marc Serra-Garcia, Valerio Peri, Roman Süsstrunk, Osama R. Bilal, Tom Larsen, Luis Guillermo Villanueva, and Sebastian D. Huber. Observation of a phononic quadrupole topological insulator. *Nature*, 555:342–345, 01 2018.
- [243] Stefan Imhof, Christian Berger, Florian Bayer, Johannes Brehm, Laurens W. Molenkamp, Tobias Kiessling, Frank Schindler, Ching Hua Lee, Martin Greiter, Titus Neupert, and Ronny Thomale. Topoelectrical-circuit realization of topological corner modes. *Nature Physics*, 14(9):925–929, 2018.
- [244] Torsten Karzig, Christina Knapp, Roman M. Lutchyn, Parsa Bonderson, Matthew B. Hastings, Chetan Nayak, Jason Alicea, Karsten Flensberg, Stephan Plugge, Yuval Oreg, Charles M. Marcus, and Michael H. Freedman. Scalable designs for quasiparticle-poisoning-protected topological quantum computation with Majorana zero modes. *Phys. Rev. B*, 95:235305, 2017.
- [245] Feng Tang, Hoi Chun Po, Ashvin Vishwanath, and Xiangang Wan. Topological materials discovery by large-order symmetry indicators. *Science Advances*, 5(3), 2019.
- [246] Tomoki Ozawa, Hannah M. Price, Alberto Amo, Nathan Goldman, Mohammad Hafezi, Ling Lu, Mikael C. Rechtsman, David Schuster, Jonathan

Simon, Oded Zilberberg, and Iacopo Carusotto. Topological photonics. *Rev. Mod. Phys.*, 91:015006, 2019.

- [247] Yiruo Lin and Anthony J. Leggett. Towards a Particle-Number Conserving Theory of Majorana Zero Modes in p+ip Superfluids. *arXiv e-prints*, page arXiv:1803.08003, 2018.
- [248] Christina Knapp, Jukka I. Väyrynen, and Roman M. Lutchyn. Number-conserving analysis of measurement-based braiding with Majorana zero modes. *Phys. Rev. B*, 101:125108, 2020.
- [249] Matthew F. Lapa and Michael Levin. Rigorous results on topological superconductivity with particle number conservation, 2019.
- [250] I. C. Fulga, N. Avraham, H. Beidenkopf, and A. Stern. Coupled-layer description of topological crystalline insulators. *Phys. Rev. B*, 94:125405, 2016.
- [251] G. Kresse and D. Joubert. From ultrasoft pseudopotentials to the projector augmented-wave method. *Phys. Rev. B*, 59:1758–1775, 1999.
- [252] G. Kresse and J. Furthmüller. Efficiency of ab-initio total energy calculations for metals and semiconductors using a plane-wave basis set. *Computational Materials Science*, 6(1):15 – 50, 1996.
- [253] G. Kresse and J. Hafner. *Ab initio* molecular dynamics for open-shell transition metals. *Phys. Rev. B*, 48:13115–13118, 1993.
- [254] D. Hobbs, G. Kresse, and J. Hafner. Fully unconstrained noncollinear magnetism within the projector augmented-wave method. *Phys. Rev. B*, 62:11556–11570, 2000.
- [255] John P. Perdew, Kieron Burke, and Matthias Ernzerhof. Generalized gradient approximation made simple. *Phys. Rev. Lett.*, 77:3865–3868, 1996.
- [256] J. P. Perdew, K. Burke, and M. Ernzerhof. Perdew, Burke, and Ernzerhof reply. *Phys. Rev. Lett.*, 80:891–891, 1998.
- [257] Thomas Iadecola, Titus Neupert, and Claudio Chamon. Topological gaps without masses in driven graphene-like systems. *Phys. Rev. B*, 89:115425, 2014.
- [258] Fan Zhang, C. L. Kane, and E. J. Mele. Topological mirror superconductivity. *Phys. Rev. Lett.*, 111:056403, 2013.

- [259] M.I. Aroyo, J.M. Perez-Mato, D. Orobengoa, E. Tasci, G. De La Flor, and A. Kirov. Crystallography online: Bilbao crystallographic server. *Bulgarian Chemical Communications*, 43(2):183–197, 2011.
- [260] G. Kresse and J. Furthmüller. Efficient iterative schemes for ab initio total-energy calculations using a plane-wave basis set. *Phys. Rev. B*, 54:11169–11186, 1996.
- [261] P. E. Blöchl. Projector augmented-wave method. *Phys. Rev. B*, 50:17953–17979, 1994.
- [262] M.J. van Setten, M. Giantomassi, E. Bousquet, M.J. Verstraete, D.R. Hamann, X. Gonze, and G.-M. Rignanese. The pseudodojo: Training and grading a 85 element optimized norm-conserving pseudopotential table. *Computer Physics Communications*, 226:39 – 54, 2018.
- [263] Nick Papior. zerothi/sisl: v0.9.5, November 2018.
- [264] Stepan Tsirkin. `irrep` code. <https://github.com/stepan-tsirkin/irrep>.
- [265] Mois I. Aroyo, Asen Kirov, Cesar Capillas, J. M. Perez-Mato, and Hans Wondratschek. Bilbao crystallographic server. <http://www.cryst.ehu.eus>.
- [266] Xiaoyu Zhu. Second-order topological superconductors with mixed pairing. *Phys. Rev. Lett.*, 122:236401, 2019.
- [267] Maryam Taherinejad, Kevin F. Garrity, and David Vanderbilt. Wannier center sheets in topological insulators. *Phys. Rev. B*, 89:115102, 2014.